

From organelle over cell to tissue: Development of fluorescence-based methods to monitor the fate of model transporting structures

Dissertation

zur Erlangung des Grades eines

‘Doktor der Naturwissenschaften (Dr. rer. nat.)’

der Fachbereiche:

08 – Physik, Mathematik und Informatik

09 – Chemie, Pharmazie und Geowissenschaften

10 – Biologie

Universitätsmedizin

der Johannes Gutenberg-Universität Mainz

Inka Negwer

geboren in Frankfurt am Main

Mainz, April 2018



Max Planck **Graduate Center** 
mit der Johannes Gutenberg-Universität



Dekan: [REDACTED]

1. Berichterstatter: [REDACTED]

2. Berichterstatter: [REDACTED]

Datum der mündlichen Prüfung: 30. Mai 2018

D77 (Dissertation Mainz)

The present dissertation was composed between November 2014 and April 2018 at the Max Planck Institute for Polymer Research in Mainz and the Institute of Pharmacy and Biochemistry at the University of Mainz within the Max Planck Graduate Center (MPGC) under the supervision of [REDACTED] and [REDACTED].

Supervisors

[REDACTED]	[REDACTED]

Mentors

[REDACTED]	[REDACTED]

I hereby declare that I wrote the dissertation submitted without any unauthorized external assistance and used only sources acknowledged in the work. All textual passages which are appropriated verbatim or paraphrased from published and unpublished texts as well as all information obtained from oral sources are duly indicated and listed in accordance with bibliographical rules. In carrying out this research, I complied with the rules of standard scientific practice as formulated in the statutes of Johannes Gutenberg-University Mainz to insure standard scientific practice.

Inka Negwer

Für meine Familie.

Danksagung

This part was removed from the electronic version of the document.

Abstract

The field of nanotherapy engages in the development of nanometer-sized structures that enable or facilitate the transport of active compounds. By using the specific and non-destructive detection mode of fluorescence, this work set out to investigate the fate of fluorescent transporting structures based on small molecules and nanocarriers in biological environments. This was accomplished by the development and application of methods based on Förster resonance energy transfer (FRET) and fluorescence correlation spectroscopy (FCS) which enabled real-time monitoring at a scale below the optical resolution limit of confocal laser scanning microscopy (CLSM).

In the first project, the applicability of the small molecular cyanine dyes Cy3 and Cy5 as targeting moieties for the directed transport of reactive groups to mitochondria was investigated. Based on the accumulation of Cy3 and Cy5 in polarized mitochondria, a copper-free click reaction was performed which was traceable by FRET. The reaction yielded a Cy3-Cy5 conjugate with the synergistic property of an enhanced retention in the mitochondria as determined by CLSM. Moreover, the product could not be efficiently imported post-synthetically. This study could hence exemplify the prospect of combining targeted transport and *in organello* synthesis in order to assemble non-penetrating compounds directly inside mitochondria.

A widespread goal of nanocarrier research is to develop transporting structures that remain intact during circulation in the bloodstream but release their payload upon reaching the cell's interior. The question of studying nanocarrier stability *in situ* in blood and cells, which suffers from a lack of biocompatible methods, was addressed with FCS. Two independent FCS protocols were developed that enabled a diffusion-based size analysis in the respective biological environment and thus allowed to draw conclusions about the integrity state of the carrier systems.

In order to measure nanocarrier stability directly in blood, the second project focused on the development of an FCS method that employed near-infrared excitation and emission. By this, spectroscopic interferences with the high fraction of red blood cells could be minimized. The determination of accurate sizes in the presence of blood cells was furthermore enabled by the application of flow in conjunction with an appropriate analytical fit model. The method's applicability could be demonstrated on the example of premature dye release from polymeric micelles in blood.

In the third project, an FCS protocol on intracellular drug release was established based on the example of fluorescently labeled siRNA that was complexed with cationic lipids (lipoplexes). A great challenge arose from the heterogeneity of the cell's interior and the simultaneous presence of siRNA complexes and released siRNA. Nonetheless, intracellular FCS measurements yielded a qualitative insight into the incidence of release. Moreover, in a number of cells, which had been transfected either with lipoplexes or nanohydrogel particles and in which the onset of release could not be detected by CLSM, the highly sensitive method of FCS was able to provide evidence for the presence of released siRNA.

Zusammenfassung

Das Gebiet der Nanotherapie konzentriert sich auf die Entwicklung von Strukturen im Nanometerbereich, welche den Transport von Wirkstoffen bewerkstelligen oder der Diagnose dienen sollen. Mit Hilfe der Echtzeitdetektion spezifischer Fluoreszenzsignale wurden in der vorliegenden Dissertation sowohl niedermolekulare als auch nanopartikuläre, fluoreszierende Transportstrukturen in biologischer Umgebung nachverfolgt. Hierzu wurden Methoden basierend auf dem Förster-Resonanzenergietransfer (FRET) und der Fluoreszenzkorrelationsspektroskopie (FCS) entwickelt und angewendet, die einen Rückschluss auf das Verhalten und die Integrität der untersuchten Systeme bis in Bereiche unterhalb der mikroskopischen Auflösungsgrenze der konfokalen Laser-Scanning-Mikroskopie (CLSM) erlaubten.

In dem ersten Projekt wurde die Anwendbarkeit der niedermolekularen Cyanin-Farbstoffe Cy3 und Cy5 für den zielgerichteten Transport von reaktiven Gruppen zu den Mitochondrien untersucht. Basierend auf der Anreicherung von Cy3 und Cy5 in polarisierten Mitochondrien wurde eine kupferfreie Click-Reaktion durchgeführt, welche mittels FRET mikroskopisch nachverfolgt werden konnte. Das Reaktionsprodukt wurde stärker als die Edukte in den Mitochondrien zurückgehalten und konnte zudem nicht postsynthetisch in die Mitochondrien importiert werden. Diese Studie konnte somit veranschaulichen, wie eine Kombination von zielgerichtetem Transport und *In-organello*-Synthese zur Bildung einer membranundurchlässigen Verbindung direkt in den Mitochondrien führte.

Ein weit verbreitetes Ziel der Nanopartikelforschung ist es, Transportstrukturen zu entwickeln, die im Blut stabil bleiben, jedoch im Zellinneren ihre Wirkstoffladung freisetzen. Einem Mangel an geeigneten Nachweismethoden dieses Verhaltens konnte durch die Entwicklung zweier FCS-Protokolle entgegengewirkt werden, die eine diffusionsbasierte Größenbestimmung im Blut bzw. im Zellinneren und somit Rückschlüsse auf die Integrität der Partikel ermöglichten.

Um die Stabilität der Nanopartikel im Blut ermitteln zu können, wurde im zweiten Projekt dieser Arbeit eine FCS-Methode entwickelt, die auf Anregungs- und Emissionswellenlängen im Nahinfrarotbereich beruhte. Hierdurch konnte der störende Einfluss der roten Blutkörperchen minimiert werden. Für die Größenbestimmung in Gegenwart der Blutzellen war es weiterhin notwendig, die Blutprobe durch einen angelegten Fluss in Bewegung zu bringen und eine geeignete Fitfunktion zu entwickeln. Die Anwendbarkeit der Methode wurde anhand des Verlustes von nicht kovalent gebundenem Farbstoff aus Mizellen im Blut demonstriert.

Im dritten Projekt wurde ein FCS-Protokoll zur Ermittlung der intrazellulären Wirkstofffreisetzung anhand von Komplexen aus fluoreszenzmarkierter siRNA und kationischen Lipiden (Lipoplexe) erarbeitet. Hierbei stellten die Zellheterogenität und das gleichzeitige Auftreten von freigesetzter und komplexierter siRNA große Herausforderungen dar. Dennoch konnte FCS einen qualitativen Eindruck in die Freisetzungsmodalitäten gewähren. Für mehrere Zellen, die entweder mit Lipoplexen oder Nanohydrogelpartikeln behandelt worden waren und in denen eine Freisetzung mikroskopisch nicht erkennbar war, konnte die hochsensitive FCS-Methode einen Hinweis auf freigesetzte siRNA liefern.

Contents

Abstract	ix
Zusammenfassung	xi
I General introduction	1
1 Background and motivation	1
1.1 Assessing mitochondrial targeting with reactive model dyes by FRET	1
1.2 Monitoring the behavior of drug nanocarriers in blood and cells by FCS	3
2 Fundamentals	7
2.1 Principles of fluorescence	7
2.2 Confocal laser scanning microscopy	9
2.2.1 Principle and experimental setup of CLSM	9
2.2.2 Resolution limit	10
2.2.3 Super-resolution microscopy	12
2.3 Förster resonance energy transfer	13
2.4 Fluorescence correlation spectroscopy	14
2.4.1 Autocorrelation analysis of a freely diffusing single type of species	15
2.4.2 Autocorrelation analysis in multi-species FCS	19
2.4.3 Fast dynamic processes	20
2.4.4 Dual color fluorescence cross-correlation spectroscopy	21
2.4.5 Inverse FCS	24
2.4.6 FCS in living systems	25
II Modulation of mitochondriotropic properties of cyanine dyes by <i>in organello</i> copper-free click reaction	27
3 Introduction	27
3.1 Mitochondria	27
3.1.1 Mitochondrial structure	28
3.1.2 Mitochondrial energetics	28
3.1.3 Mitochondrial membrane potential	30
3.2 Mitochondria-localizing probes	31
3.2.1 Membrane passage of delocalized lipophilic cations	31
3.2.2 Mitochondrial accumulation depending on $\Delta\Psi_m$	32
3.2.3 Mitochondriotropic compounds: from small molecules to macromolecules	35
3.3 Intramitochondrial reactions	37

3.3.1	Reactions with an endogenous reaction partner	37
3.3.2	Reactions between two exogenous reaction partners	38
4	Results and discussion	41
4.1	Mitochondriotropism of Cy dyes	41
4.2	Copper-free click reaction of Cy dyes	43
4.2.1	SPAAC as a suitable reaction mechanism	43
4.2.2	Chromatographic analysis of SPAAC	45
4.2.3	Spectroscopic properties of Cy dyes	45
4.2.4	Reaction kinetics of SPAAC reaction pairs	47
4.3	<i>In organello</i> copper-free click reaction of Cy dyes	47
4.3.1	Mitochondrial accumulation of Cy dye reaction partners	47
4.3.2	Evaluation of spectral cross-talk	50
4.3.3	Co-incubation of Cy3 donor and Cy5 acceptor dye	50
4.3.4	Retention of the dicationic SPAAC product in mitochondria	51
4.3.5	LC-MS analysis confirms <i>in organello</i> SPAAC product formation	54
4.4	Comparative reaction kinetics	57
4.4.1	<i>In organello</i> reaction kinetics	57
4.4.2	Discussion	58
5	Materials and methods	60
5.1	Materials	60
5.2	Methods	63
III	Monitoring drug nanocarriers in human blood by near-infrared fluorescence correlation spectroscopy	71
6	Introduction	71
6.1	Blood	71
6.2	Transport of nanocarriers in the bloodstream	72
6.2.1	Adsorption of plasma proteins	72
6.2.2	Stability in blood	74
6.3	Methods to study nanocarrier stability in biological environment	74
6.3.1	<i>In vitro</i> techniques	75
6.3.2	<i>In vivo</i> techniques	76
7	Results and discussion	78
7.1	Calibration of the NIR-FCS setup in aqueous solution	78
7.2	NIR-FCS measurements in human blood	80
7.2.1	Static blood	80
7.2.2	Flowing blood	83

7.2.3	Increased viscosity explains diffusion slowdown	86
7.3	Applications	88
7.3.1	Sensitivity down to single dye molecules	88
7.3.2	Investigation of protein adsorption in flowing blood	89
7.3.3	Loading stability of micelles in flowing blood	90
8	Materials and methods	93
8.1	Materials	93
8.2	Methods	94
IV	Monitoring nanocarrier-based delivery and release of RNA molecules by fluorescence correlation spectroscopy	97
9	Introduction	97
9.1	Therapeutic strategy of RNA interference	97
9.1.1	Gene silencing by siRNA	97
9.1.2	Need for nanocarrier-based delivery of siRNA	98
9.1.3	siRNA delivery systems	99
9.2	From cellular uptake to release	100
9.2.1	Endocytosis and intracellular trafficking	100
9.2.2	Endosomal escape and release of payload	102
9.2.3	Analytical techniques to study intracellular trafficking	103
9.3	Applicability of FCS to study intracellular release	103
10	Results and discussion	105
10.1	General considerations for FCS measurements in living cells	105
10.1.1	Autofluorescent background	105
10.1.2	Control of measurement position	106
10.1.3	Heterogenous environment of cells	107
10.2	Lipoplex-mediated transfection	107
10.2.1	Lipoplex uptake and siRNA release in immortalized cells	108
10.2.2	Lipoplex uptake and siRNA release in primary macrophages	111
10.2.3	Integrity of intracellularly released siRNA	114
10.3	siRNA release from nanohydrogel particles	116
11	Materials and methods	120
11.1	Materials	120
11.2	Methods	122
V	Conclusion and Outlook	127

Bibliography	133
List of abbreviations	167
Publications	169
Appendices	171
Curriculum vitae	182

Part I

General introduction

1 Background and motivation

Complex pharmacological treatments owe a substantial share of their rise in the last decades to the increasing knowledge on pharmacokinetics and -dynamics in living systems. In order to gain a comprehensive understanding of human (patho-)physiology, researchers commonly employ methods with *in situ* detection modes that rely on a minimal disturbance of physiological processes. One such method that is ubiquitously applied for its selectivity and live cell compatibility is CLSM. [1,2] By introducing fluorescent labels to the structures of interest, real-time monitoring of intracellular behavior is enabled. With the extensive and ever-growing spectrum of fluorescent proteins, fluorescently tagged endogenous macromolecules and dyes with compartment-specific intracellular localization, almost every process can be explored. [1] One important drawback of fluorescence microscopy, however, is its diffraction-based resolution limit which prevents the distinction of objects which are separated by less than about 200 nm. Even super-resolution microscopy techniques with reported resolution limits of 20 to 50 nm do not allow for a spatial resolution of single molecules, proteins or small molecular associations. [3] Therefore, the complementation of CLSM with enhanced fluorescence-based methods is necessary in order to study biological processes at a molecular level. Two interesting possibilities are FRET and FCS. In the former case, sub-resolution information on the molecular interaction of two spectrally distinct fluorophores is made accessible by non-radiative energy transfer. [4,5] In the latter case, fluorescence intensity fluctuations provoked by the motion of fluorophores in a diffraction-limited observation volume are analyzed to extract information on *e.g.* the size and concentration of the fluorophores. [6,7] The applicability of both, FRET and FCS, has been demonstrated in a diverse set of biological applications (*e.g.* to study interactions between proteins and/or nucleic acids), often in combination with CLSM. [2,8–10]

This work is composed of three projects in which the fluorescence methods CLSM, FRET and FCS were combined, adapted and advanced to study processes at a sub-resolution scale. These processes reached from the reaction of individual dye molecules to the stability of nanometer-sized drug carrier systems. All investigations were performed in biological conditions. They differed, however, in their point of focus which shifted from an organelle to the eukaryotic cell's interior as such and to the connective tissue of blood.

1.1 Assessing mitochondrial targeting with reactive model dyes by FRET

The first project in this work addressed the concept of targeting small molecules to active mitochondria (Part II). Investigations on the delivery of small chemical probes to the mitochondria have been sparked by a fundamental desire to uncover the mechanisms of mitochondrial functioning. Moreover, this approach has been proposed as a therapeutic concept in the treat-

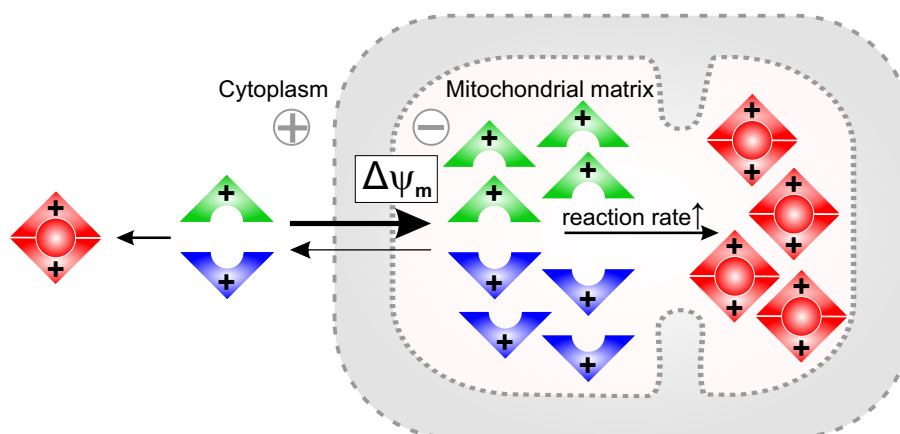


Figure 1: The concept of targeting mitochondria with two reactive mitochondriotropic compounds based on Cy3 (green) and Cy5 (blue) dye structures. The effective increase in concentration by a $\Delta\Psi_m$ -driven mitochondrial accumulation was supposed to enhance the reaction velocity. In consequence, it was postulated that the product (red) formation would be traceable by FRET.

ment of mitochondrial diseases. [11, 12] One possibility to achieve mitochondrial targeting of small molecules relies on their preferential intracellular distribution to the mitochondria. The property of localizing in mitochondria is termed “mitochondriotropism” and has been observed for a broad range of molecules. [13–16] Many of them, including several classes of fluorescent dyes, were found to comprise the common structural elements of a high lipophilicity and a positive net charge that led to their mitochondrial accumulation in response to the mitochondrial membrane potential ($\Delta\Psi_m$). This membrane potential is manifested in a gradient of charges and protons across the inner of the two mitochondrial membranes and is responsible for the more negatively charged environment of the mitochondrial matrix with respect to the cytoplasm. [17, 18]

The principle of $\Delta\Psi_m$ -driven accumulation of mitochondriotropics has been used for *in organello* reactions with endogenous mitochondrial components such as DNA, proteins, metals or reactive oxygen species (ROS). [16] Another promising approach involves the reaction between two exogenously introduced small molecules within the mitochondrial matrix. The main goal of this project was to investigate a bioorthogonal covalent reaction between two selectively enriched molecules within the mitochondria of living cells (Fig. 1). As targeting moieties for the transport of reactive groups the cyanine dyes Cy3 and Cy5 were employed. Evidence for the mitochondriotropic properties of Cy3 and Cy5 had been provided by previous studies in the Helm group. It was anticipated that the product formation between reactive Cy3 and Cy5 compounds would give rise to FRET and thereby enable to monitor the reaction process by CLSM. On the whole, the *in organello* reaction was assessed with the aim of evaluating potential advantages which the mitochondrial import of the building blocks might have over the direct administration of the product.

1.2 Monitoring the behavior of drug nanocarriers in blood and cells by FCS

The second and third project in this work focused on the topic of nanocarrier-based drug delivery. Nanocarriers are therapeutically applied delivery vehicles in the nanometer size range that can enable, direct or facilitate the transport of an active drug compound to its physiological target. [19] By packaging highly toxic (*e.g.* cytostatic compounds) or sensitive (*e.g.* nucleic acids such as siRNA) drug molecules into nanocarrier formulations a significant improvement of their efficacy, safety and tolerability can be achieved. [19] The nanotherapeutic concept is especially promising for cancer therapy where the occurrence of severe side effects has limited drug dosage and where an insufficient accumulation at the target site has lowered the therapeutic response. Therefore, the majority of nanotherapeutic formulations which are approved or currently in clinical development target various types of cancer. [20,21] However, nanocarrier-based treatments have also been approved for other diseases including, for instance, fungal and viral infections, multiple sclerosis and chronic kidney disease. [20] To meet the diverse requirements of the transported drugs and their targets, nanocarriers differ in their physicochemical properties, *e.g.* material, size, shape and surface functionalization. Moreover, nanocarriers can be of synthetic, semisynthetic or natural origin. The dominating fraction of approved and clinically investigated nanocarriers are either polymers, liposomes (or lipid nanocarriers) or nanocrystalline formulations. [20] However, micelles, polysaccharide- and peptide-based nanocarriers and inorganic nanoparticles are currently emerging.

In general, nanocarriers face a series of hurdles from their administration to the arrival at the target site. Most of the biological barriers are encountered by any nanocarrier irrespective of its therapeutic cargo or target site. As depicted in Figure 2, the pathway of a systemically applied nanocarrier system with an intracellular target commonly comprises the following steps: [19, 21, 22]

1. Circulation in the bloodstream: Blood is the first body fluid compartment encountered by an intravenously injected nanocarrier. To enhance the chances of reaching therapeutic levels at the diseased site, a long circulation half-life is aimed for. [19] On one hand, this implies that the nanocarrier should remain stable and retain its drug payload. [23] On the other hand, it should evade kidney filtration and sequestration by phagocytic immune cells.
2. Vascular extravasation: While the capillary endothelium prevents the translocation of molecules of > 5 nm size, some tissues such as spleen or liver but also tumors allow the entry of larger molecules (< 200 nm). [22] Tumors show an endothelial dysfunction characterized by a leaky microvasculature and reduced lymphatic drainage which leads to the enhanced permeability and retention (EPR) of nanocarriers. [24]
3. Extracellular matrix of tissues/tumors: The dense network of polysaccharides and proteins and an elevated interstitial fluid pressure hamper the diffusion of nanocarriers, especially towards remote regions. [25]

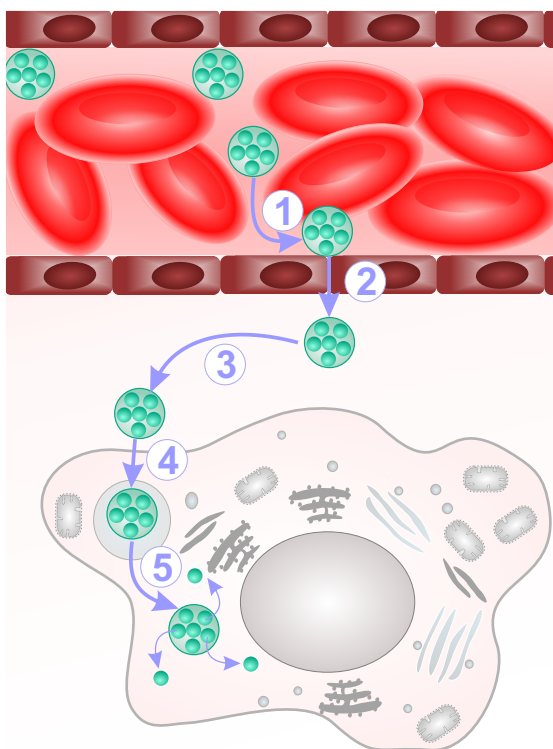


Figure 2: Physiological barriers encountered by a drug nanocarrier system upon its intravenous injection. Steps 1 to 5 are explained in the text. Adapted from Ref. [22].

4. Cell internalization: The uptake into specific cells can be enhanced by active targeting, *i.e.* the interaction of targeting structures (ligands) on the nanocarrier surface with cell-expressed counterparts (receptors). Internalization commonly proceeds *via* energy-consuming endocytic mechanisms. [26]
5. Endosomal escape and intracellular drug release: Trafficking within endomembrane compartments often culminates in the degradative environment of lysosomes which is fatal for sensitive drugs such as nucleic acids. [26] Endosomal escape and release of the drug from the nanocarrier are therefore considered pivotal. Potential triggers comprise internal (*e.g.* reductive environment, decreased pH, elevated enzyme levels) or external (*e.g.* heat, light, ultrasound) stimuli. [27]

To negotiate across these biological barriers, research efforts are focused on multifunctional carrier systems. Fine-tuning and the incorporation of stimuli-responsive cleavage sites are required to balance between drug retention in the bloodstream and an intracellular disintegration. [28] Thorough inspection on the functionality of these engineered properties in preclinical tests is crucial to prevent a dropout at later clinical stages. In this work, FCS-based protocols were developed that allow to investigate two of the above-mentioned potential hurdles in *ex vivo* biological environments.

The second project in this work addressed the question of nanocarrier stability during the

transport in human blood as described in step 1 of Figure 2. The high percentage of proteins, cells and other solutes in blood threatens the integrity of a nanocarrier system in multiple ways, *e.g.* by aggregation, disintegration or premature drug release. [23] However, profound knowledge on the stability of drug nanocarriers in blood was thus far missing due to a lack of methods that are directly compatible with blood. FCS is a well established method for the determination of size, loading efficiency and stability of drug nanocarriers in aqueous solutions. [29–35] However, it has not been applied for blood measurements. The reason for this lies within the interfering absorption and high scattering of blood which impedes FCS measurements at visible wavelengths. [36] In the near-infrared (NIR) range (700 - 1100 nm), disturbing absorption is at its minimum rendering an efficient detection of fluorescence signals possible - a concept that has already been explored in several NIR-imaging modalities. [37,38]

This project sought to implement NIR-FCS as a method to study nanocarrier stability in human blood (Part III). As the application of an FCS setup that was operated fully in the NIR range had not been described in the literature, the initial aim was to perform a comprehensive calibration in water. These calibration measurements were based on NIR fluorescent dyes and a well characterized NIR-labeled polymer brush. The main objective, however, was to establish a protocol that included a suitable mode of measuring in blood as well as an adequate data analysis and that yielded reliable sizes of fluorescent species in the presence of blood cells. Upon the successful implementation of such a protocol, it was planned to assess the stability of potential nanocarriers in blood.

The third project of this work focused on the last step of nanocarrier-based drug delivery, the intracellular release of the drug payload (Fig. 2, step 5). Exemplary, the delivery of siRNA molecules was investigated. Acting by an antisense-based recognition of target genes at the mRNA level, double-stranded siRNA fragments (≈ 22 nucleotides in length) are tested for potential therapeutic gene silencing in a number of genetic diseases. [39] However, in order to surmount the series of hurdles depicted in Figure 2, systemically applied siRNA molecules have to be packaged into nanocarrier systems. Ultimately, the fate of an siRNA-nanocarrier system is thought to depend on whether it is able to evade lysosomal degradation and to efficiently release the siRNA into the cytoplasm. During the *in vitro* investigation of potential carrier systems, CLSM is commonly applied to detect cellular uptake and intracellular trafficking, though not on a single particle level. [40–44] Furthermore, the quantification of gene knockdown yields information on the pharmacological efficiency of a system. Gene silencing can be quantified either on the protein (*e.g.* by flow cytometry or Western blots) or mRNA (*e.g.* by quantitative real-time polymerase chain reaction) level. [45,46] But neither of the above-mentioned methods can directly detect the release event.

The goal of this project was the development of an FCS protocol to detect the release of fluorescently labeled siRNA from nanocarrier systems within the cytoplasm of living cells (Part IV). It was postulated that release events would lead to the appearance of a fast diffusing species as opposed to the slow diffusion of loaded carriers. Particular focus of the investigations was

an *in vitro* transfection agent which consisted of electrostatic complexes between cationic lipids and negatively charged siRNA molecules. [40,47] The project furthermore aimed at answering central questions associated with siRNA release such as (i) when did release occur, (ii) what was the duration over which the diffusion of released molecules could be observed and (iii) how uniformly were cells affected by release. Lastly, it was planned to apply the FCS protocol in order to investigate if nanohydrogel particles were able to release their siRNA payload into the cytoplasm.

2 Fundamentals

2.1 Principles of fluorescence

The process of photoluminescence describes the emission of light from an excited molecule. [5] Photoluminescence is further subdivided into fluorescence and phosphorescence. In both cases, the emission is preceded by the absorption of a light quantum, termed a photon, with an absorption (“Abs”) energy of $E_{\text{Abs}} = h \cdot \nu_{\text{Abs}} = h \cdot c / \lambda_{\text{Abs}}$, where h is Planck’s constant, ν and λ are the frequency and wavelength of the incoming photon, respectively, and c is the speed of light. The energy amount that is necessary to provoke an electronic transition is contained in light of the ultraviolet, visible or near-infrared wavelength range. [48] The collision of an incident photon with an absorbing molecule leads to the excitation of an electron from its electronic ground state S_0 to the different vibrational energy levels of the excited singlet states S_1 or S_2 as depicted in the Jablonski diagram (Fig. 3A). Following the excitation of the electron, several competing processes can lead to its relaxation. [49] These processes proceed either non-radiatively or radiatively and if the latter case applies, determine the mode of photoluminescence. The by far fastest process (10^{-14} to 10^{-11} s) is the non-radiative vibrational relaxation (or internal conversion) of the electron to the lowest vibrational level of the excited singlet state S_1 . [2] From this state, the excited molecule will relax back into the various vibrational levels of the ground state. If such relaxation is accompanied by the emission of a photon with an energy of $E_{\text{F1}} = h \cdot \nu_{\text{F1}}$, it is termed fluorescence (“F1”). Before emitting fluorescence, however, the excited molecule will reside in the lowest vibrational level of S_1 for an average duration of 10^{-9} to 10^{-8} s. This duration defines the characteristic fluorescence lifetime. Furthermore, depopulation of S_1 can occur through a transition to the first excited triplet state T_1 . In the triplet state, the excited electron contains the same spin orientation as its ground state partner electron, a situation that is symmetry forbidden in quantum mechanics. Consequently, the probability of such intersystem crossing is very low. This is reflected in triplet lifetimes (10^{-6} to 10^{-5} s) that are orders of magnitude higher than fluorescence lifetimes. Energy dissipation from the lowest vibrational level of T_1 occurs either by phosphorescence in a time range of milliseconds to seconds or by a transition back to S_1 resulting in delayed fluorescence. Excited states can also get depopulated by various quenching processes, *e.g.* by collisional quenching upon contact with other molecules or by the attenuation of incident light by absorbing species, including the fluorescent molecule itself. [5] One of the processes, resonance energy transfer, will be detailed in Section 2.3.

A fluorescent molecule can undergo a large number of excitation and emission cycles until being irreversibly destroyed (named photobleaching). [5] Furthermore, a fluorescent molecule in solution containing several excitable electrons does not show discrete transitions but rather a probability distribution of all possible electronic transitions which is known as the absorption and emission spectra (Fig. 3B). These spectra contain several characteristic features. First of all, due to the initial energy loss by vibrational relaxations the emission spectrum is red-shifted with respect to the absorption spectrum. As this behavior was first described by Sir G. G.

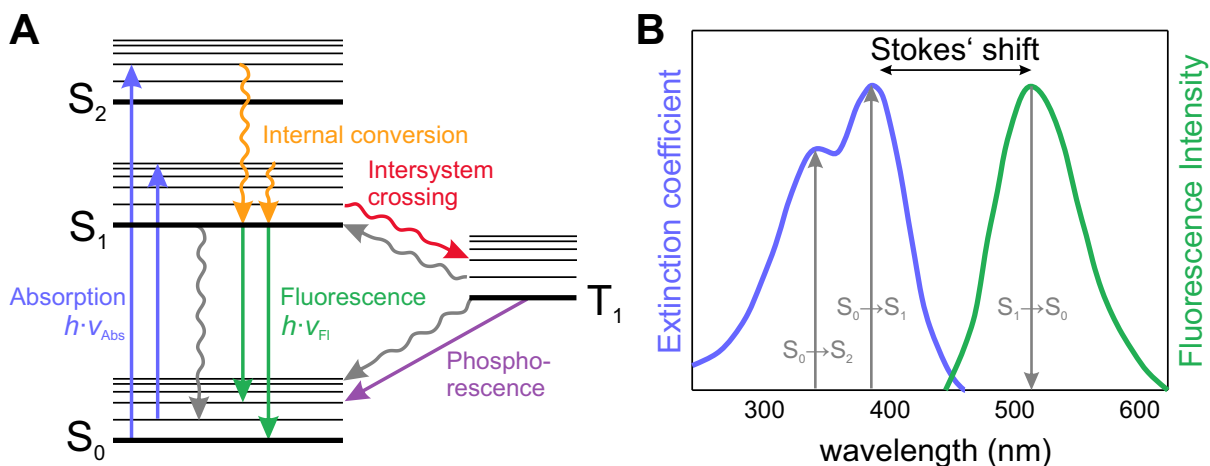


Figure 3: A) Jablonski diagram. Electron transitions from the ground state S_0 to the excited singlet states S_1 , S_2 and triplet state T_1 . All electronic states contain vibrational levels which are depicted as thin lines. Radiative and non-radiative relaxation mechanisms are drawn as straight and wavy arrows, respectively. Further details are given in the text. Adapted from Ref. [2]. B) Schematic representation of the absorption (blue) and emission (green) spectrum of quinine. Adapted from Ref. [49].

Stokes, the respective shift, distinct for each fluorescent molecule, is named after him (Stokes' shift). [50] Furthermore, fluorescence emission is independent of the excitation wavelength, a relation known as Kasha's rule. [51] The emission spectrum theoretically resembles a mirrored version of the absorption spectrum. In practice, many molecules deviate from the mirror image rule, for instance, because they are also excited to higher singlet states such as S_2 . This is also the case for quinine which was discovered by Herschel in 1845 and is regarded as the first reported fluorescent molecule (Fig. 3B). [52] In fluorescence applications, excitation instead of absorption spectra are typically utilized. Excitation spectra are recorded at a fixed emission wavelength while varying the excitation wavelength.

The fluorescence intensity at a certain wavelength is given by $I_\lambda = I_0 \cdot \varepsilon \cdot Q \cdot c \cdot k$ where I_0 is the excitation intensity, ε is the extinction coefficient, Q is the quantum yield, c is the concentration of the emitting molecule and k is an instrumental constant. [48] The quantum yield of the molecule describes the ratio of emitted to absorbed photons which depends on the rate constants of all non-radiative decays (k_{nr}) and the emissive rate (Γ) by $Q = \Gamma / (\Gamma + k_{nr})$. The extinction coefficient $\varepsilon_\lambda = A / (c \cdot d)$ (with the absorption $A = \log(I_0) / I$, the concentration c and the path length of the cuvette d) indicates how strongly a chromophoric molecule attenuates light at a given wavelength. [48]

Commonly, a molecule that is able to fluoresce is referred to as fluorescent probe, fluorochrome, dye or, if it is conjugated to a macromolecule, fluorophore. [2] Classical fluorescent molecules are of organic origin. They comprise small dyes (*e.g.* with xanthene or cyanine structure, see also Sections 3.2.3 and 4.1) and proteins (*e.g.* enhanced green fluorescent protein) which share the structural similarity of a highly conjugated polycyclic aromatic system. There are, however, also inorganic fluorochromes such as lanthanide ions or quantum dots. Quantum dots are tunable nanometer-scaled atom clusters of semiconductor material. [1] The fluorescence

emitted from quantum dots is not based on electronic transitions as described above but on the creation of an electron-hole pair which quickly recombines by the emission of a photon with less energy. Quantum dots have broad absorption spectra. The emission spectra, in contrast, are narrow and dependent on the size of the quantum dot which allows for tuning of the fluorescent properties. In general, fluorochromes are characterized by their maximum wavelengths of excitation and emission, their fluorescence lifetime, quantum yield, molar extinction coefficient and Stokes' shift. [1]

2.2 Confocal laser scanning microscopy

The invention of fluorescence microscopy by Köhler and Heimstädt dates back to the early 20th century. [2] Fluorescence microscopy, however, was crucially advanced through the discovery of the confocal principle by Minsky in the year of 1957. [53] In confocal microscopy, out-of-focus fluorescence light is blocked by the introduction of a pinhole aperture. [1] In contrast to widefield optical microscopy, it therefore offers the possibility to control a pinhole aperture in the image plane and thus perform an optical z -sectioning of thick specimen. [54] In CLSM, an image is acquired by raster scanning a tightly focused laser beam over a region of interest in the specimen and thereby illuminating the region point-by-point, concomitant with the fluorescence detection at each point. This scanning process reduces the light exposure of the specimen. But the full potential of CLSM could only be tapped by further advances in optics and electronics. [1] These milestones included the development of stable and powerful lasers, sensitive detectors, highly efficient scanning mirror units and high-throughput fiber optics. These improvements went hand-in-hand with a fast progress in computer technology that nowadays allows to handle large amounts of imaging data. At the same time, the spectrum of fluorophores was expanded to fluorochromes, fluorescent proteins and specific organellar stains with high quantum yields and high extinction coefficients that cover the whole wavelength range of ultraviolet, visible and near-infrared light. [1] Together, these improvements led to the emergence of CLSM as a valuable tool in biological studies on living and fixed cells.

2.2.1 Principle and experimental setup of CLSM

CLSM is typically performed with an epi-fluorescent inverted microscope. [1, 2, 55] As depicted in Figure 4, the excitation source, consisting of a laser, is reflected by a dichroic mirror and directed into the aperture of the microscope objective. The objective lens focuses the laser beam into a diffraction-limited spot in the specimen. Emitted fluorescence light from the illuminated spot is collected by the same objective, transmitted through the dichroic mirror and directed to the detection unit. Here, the fluorescent light is first filtered by an emission filter which blocks scattered excitation light and which can be adapted to select a desired detection wavelength range. The emitted fluorescence is then focused as a confocal point into the pinhole which prevents the passage of out-of-focus light rays that stem from above and below the focal plane and are thus not confocal (meaning in a conjugate plane) with the pinhole. [1] A detec-

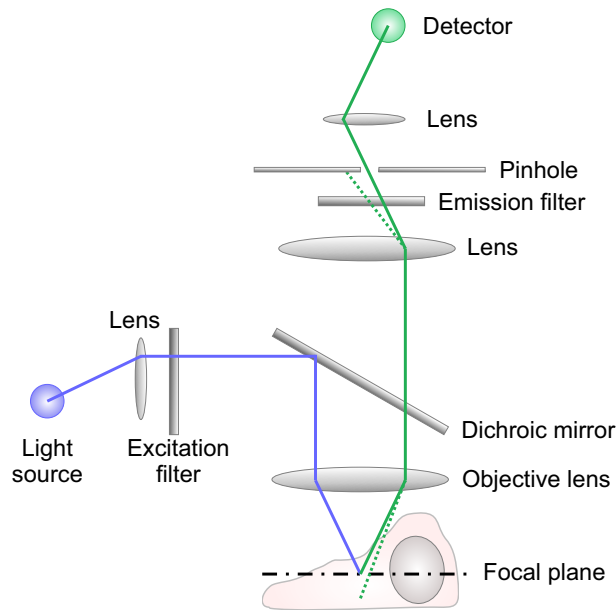


Figure 4: Basic setup of a confocal microscope. The blue and green lines indicate excitation and fluorescence emission light, respectively. Fluorescence light that does not originate from the focal plane (dotted green line) is not confocal with the pinhole and does not reach the detector. Further details are given in the text. Adapted from Ref. [55].

tor, typically a photomultiplier tube (PMT), then captures the incident photons. This beam path is then repeated multiple times by raster scanning the specimen in order to compose a pixel-based x,y -image. By adjusting the focal plane, a 3D image stack with thin optical slices can be acquired. The intensity information of each pixel is recorded by a computer and used to assemble the confocal image and to perform image processing and analysis.

In variation to the beam path displayed in Figure 4, it is possible to apply more than one laser at a time. By using acousto-tunable filters, the wavelength and intensity of multiple lasers from one or multiple excitation sources can be simultaneously modulated. [1] The individual lasers are thus fiber-coupled, expanded and colinearized into the scanning unit of the confocal microscope. Usually, the confocal image is assembled through beam scanning rather than a movement of the sample stage. For scanning, a galvanometer-based mirror system is typically used. A further variation includes the placement of a diffraction grating or prism coupled with slits in front of the PMT. This allows to separate the emitted fluorescence in smaller wavelength integrals which enables the performance of spectral imaging.

2.2.2 Resolution limit

A limitation inherent to all optical microscopy techniques is resolution. Resolution is defined as “the ability of an imaging system to reproduce details in the object as separate entities in the image”. [56] The resolution limit is thus the minimal distance below which two objects cannot be resolved. Resolution is determined by fundamental physical factors and instrument limitations such as optical aberrations caused by imperfect objective lenses. Furthermore, in

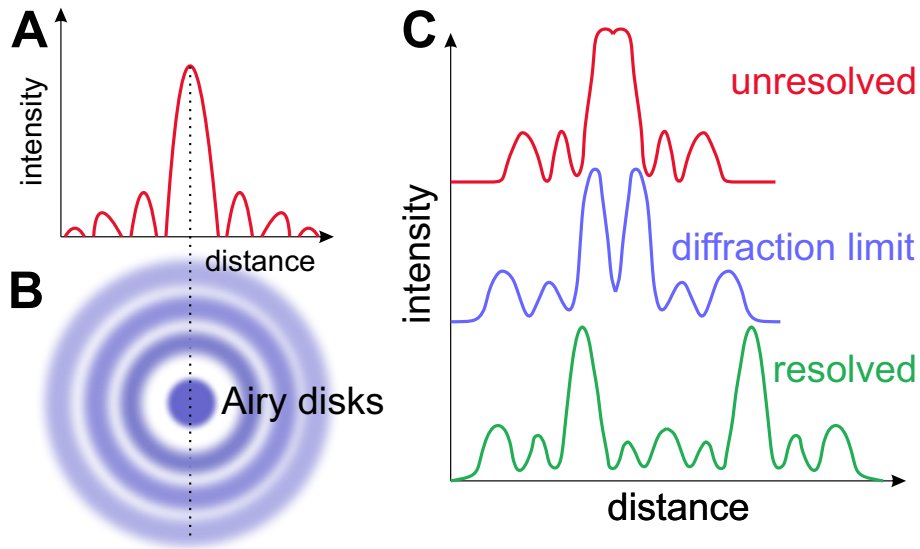


Figure 5: A) The intensity PSF in the focal plane as a function of lateral distance from the optical axis. B) Top view on the Airy disk diffraction pattern of a point source. C) Intensity PSF of two approaching point sources. At a distance $>$ diffraction limit the two points are resolved (green). The distance between both points that equals the diffraction limit is displayed in blue. When the distance is further reduced, the two points can no longer be resolved (red). Adapted from Ref. [2].

order to enhance contrast and thus resolution power a high signal-to-noise ratio is aimed for. Therefore, as much light as possible has to be captured by the objective. This relation was first described by E. Abbe who derived the numerical aperture (NA), meaning light capturing capacity, of an objective: [57]

$$NA = n \cdot \sin(\alpha) \quad (2.1)$$

Here, n is the refractive index of the surrounding medium and α is the half opening angle of the objective. With dry objectives, the numerical aperture is limited to values of about 0.95. Therefore, in order to enhance the detection efficiency, either oil or water immersion objectives with high numerical apertures of up to ≈ 1.4 are commonly used in CLSM. [58]

In physical terms, resolution is inseparable from the wave-like nature of light which causes its diffraction upon contact with an object. Due to diffraction, the illuminated point source is projected as a bright central spot (termed Airy disk) with surrounding concentric rings of successively decreasing maximum and minimum intensity (Airy pattern) (Fig. 5A,B). [2] This phenomenon is characterized by a system parameter which is called the intensity point spread function (PSF). The Airy pattern thus describes the intensity distribution of the intensity PSF in the focal plane. [2]

In order to specify the contrast that is necessary to visually resolve two closely spaced points, the Rayleigh criterion is used. [1] The Rayleigh criterion states that two points are resolved when the first minimum of one Airy disk overlaps with the central maximum of the second Airy disk

(Fig. 5C). The following relation for lateral resolution has been postulated: [56]

$$r_{\text{lateral}} = \frac{1.22\lambda}{2NA} = \frac{0.61\lambda}{NA} \quad (2.2)$$

As the intensity PSF in confocal microscopy is about 30% narrower than in widefield microscopy, the lateral resolution limit is reduced to: [1]

$$r_{\text{lateral}} = \frac{0.4\lambda}{NA} \quad (2.3)$$

The intensity PSF distribution has a similar shape in the axial dimension. However, its resolution is worse than in lateral dimension: [1]

$$r_{\text{axial}} = \frac{1.4\lambda n}{(NA)^2} \quad (2.4)$$

Here, confocal microscopy leads to an only marginal improvement with respect to widefield microscopy. However, its main advantage is its optical sectioning capability which effectively increases resolution as compared to widefield imaging. During image acquisition, the choice of an appropriate sampling rate (pixel size), meaning the number of pixels per resolved distance r , is of practical relevance. The Nyquist sampling theorem states that the pixel size should be about half (or less) of the lateral distance to be resolved. [59]

2.2.3 Super-resolution microscopy

The ability of a confocal or widefield fluorescence microscope to separate two distinct objects is limited to approximately half of the applied wavelength (average of excitation and emission wavelengths) and ranges from about 200 to 350 nm for visible light. [1, 60] In order to resolve details that are closer together than the diffraction limit, several super-resolution microscopy techniques have been developed in the past two decades. [3] The formula of success for these techniques is that they do not rely exclusively on the focusing strength of the objective lens. Instead they exploit nonlinear behavior and light-induced fluorescent state on- and off-switching (compare Section 2.4.3) in order to localize individual fluorochromes at a high spatial accuracy. [2] Two basic approaches can be distinguished. The first approach comprises methods such as PALM (photo-activated localization microscopy) [61, 62] or STORM (stochastic optical reconstruction microscopy) [63] where fluorochromes are singled out by their stochastic on- and off-switching and by their precise localization at single molecule detection efficiency. This process is repeated until the spatial arrangement of all fluorochromes could be reconstructed. In contrast, in the second approach light-induced transitions between an on- and off-state are provoked. The techniques of STED (stimulated emission depletion) [64, 65] and RESOLFT (reversible saturable/switchable optical linear (fluorescence) transitions) [66, 67] are examples for this approach. Here, a second, superimposed and red-shifted beam spot depletes excited state fluorochromes. This second diffraction spot contains a doughnut shape with a zero light intensity minimum at the center at which an off-switching of the fluorochromes does not oc-

cur. This means that only fluorescence light from the inner circle, whose effective size is below the resolution limit, is detected. Besides the mentioned techniques, several other techniques have been reported (reviewed in Ref. [3, 60, 68, 69]). With the application of super-resolution microscopy, a spatial separation of objects at a 20 to 50 nm distance could be reached. [3] By the alternative approach of FRET, an effective resolution enhancement down to a level of < 10 nm is achieved. However, FRET does not break the diffraction limit. Rather, it is based on the detection of molecular interactions as described in the following section. [2, 56]

2.3 Förster resonance energy transfer

The photophysical process of Förster (or fluorescence) resonance energy transfer was first described by Theodor Förster. [4] The energy transfer occurs among two spectrally distinct fluorophores which are termed donor (“D”) and acceptor (“A”). The excited state energy from the donor is transferred to a less energetic excited state of the acceptor by a non-radiative mechanism (Fig. 6A). [5] The mechanism depends on a long-range dipole-dipole coupling of both fluorophores. The excited acceptor will then, after vibrational relaxation, either emit a photon or decay non-radiatively in the case of a non-fluorescent quencher. Effectively, FRET leads to the diminution of donor fluorescence and the concomitant appearance of acceptor fluorescence upon donor excitation. Three key requirements need to be fulfilled in order to observe FRET:

Spectral overlap of donor and acceptor: Although the energy transfer proceeds non-radiatively, FRET depends on a spectral overlap of donor emission and acceptor excitation spectra as depicted in Fig. 6B. [5]

Orientation of donor emission and acceptor absorption dipole: Efficient FRET only occurs if the dipole moments of donor and acceptor are oriented in a parallel fashion. A perpendicular orientation, in contrast, will lead to a minimized FRET efficiency. [5]

Spatial proximity of donor and acceptor: The distances by which both fluorophores are separated are typically in the single-digit nanometer range (< 10 nm). [70] The FRET efficiency (E_{FRET}) depends on the inverse of the sixth power of the distance r between donor and acceptor:

$$E_{\text{FRET}} = \frac{1}{1 + \left(\frac{r}{R_0}\right)^6} \quad (2.5)$$

R_0 , also known as the Förster radius, denotes the distance at which the FRET efficiency is at its half maximum (Fig. 6C). [4] R_0 depends on the spectral overlap J_λ , the donor quantum yield Q_D , the acceptor extinction coefficient ε_A and dipole orientation factor κ^2 ($\kappa^2 \approx 2/3$ for freely rotating dyes). [2, 5]

$$R_0 = (2.8 \cdot 10^{17} \cdot \kappa^2 \cdot Q_D \cdot \varepsilon_A \cdot J_\lambda) \quad (2.6)$$

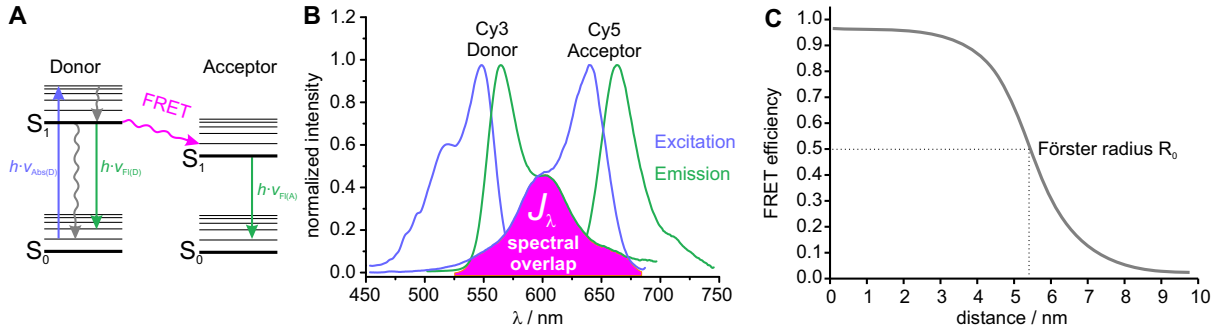


Figure 6: A) Electronic transitions in the process of FRET. Straight and wavy arrows indicate radiative and non-radiative relaxation mechanisms, respectively. Adapted from Ref. [2]. B) Excitation and emission spectra of the FRET pair Cy3/Cy5. The spectral overlap J_λ between donor emission and acceptor excitation is highlighted. C) FRET efficiency in relation to the distance between donor and acceptor at the example of Cy3-Cy5 with $R_0 = 5.4$ nm as reported in Ref. [72].

The small organic dyes Cy3 and Cy5, which were employed in Part II, are a widely applied FRET pair with an R_0 that ranges between 4.7 and 6.5 nm depending on the (biological) environment. [71]

FRET can serve as a so-called spectroscopic ruler. [70] In combination with CLSM, the information delivered by FRET can be allocated in a spatial map, the confocal image. [73] Special attention, however, has to be paid to the introduction of cross-talk artifacts. Cross-talk can occur *via* a direct excitation of the acceptor at donor excitation wavelength (termed cross-excitation). The second type of cross-talk (termed bleed-through) occurs if donor emission adds to the signal intensity in the acceptor detection channel.

2.4 Fluorescence correlation spectroscopy

FCS is a noninvasive technique applicable to investigate the dynamic properties and interactions of fluorescent molecules in various environments. [6, 9, 74] It is based on monitoring the motion of fluorescent species in a very small observation volume (V_{obs}) (Fig. 7A). The conceptual principle of FCS was introduced by Madge, Elson and Webb in the early 1970s who initially applied FCS to measure DNA-drug intercalation. [75–77] However, drawbacks such as a poor signal-to-noise ratio, unstable laser emission and inefficient detectors limited the applicability of FCS in its early days. The breakthrough of FCS for widespread applications in life sciences and biophysics was achieved when Rigler proposed the combination of FCS with a confocal microscope in the 1990s. [78] The introduction of a pinhole ensured a small observation volume (≈ 1 fL) and thus a high signal-to-noise ratio. [7, 54] Furthermore, the development of temporally stable laser sources and single photon detectors contributed to the resurgence of FCS. [10] The present-day FCS setup has therefore adapted the main components and configuration of CLSM, making it typically extendable from commercial confocal microscopes (Section 2.2). Contrary to CLSM, in FCS the diffraction-limited confocal observation volume remains stably parked in one position throughout the measurement. Furthermore, FCS requires detectors with single photon counting efficiency such as avalanche photodiodes (APD) which are not routinely

integrated into CLSM setups.

FCS is based on the analysis of spontaneous fluctuations of fluorescence intensity stemming from an ensemble of fluorescent molecules at thermal equilibrium. [6] Fluctuations in the local equilibrium concentration originate from the motion of fluorophores in and out of the observation volume. In a statistical, time-correlating analysis a great number of these single molecule events is averaged and delivers information about dynamics in a time scale from nanoseconds to seconds. Such dynamics span, for instance, rotational and translational diffusion, laminar flow and binding kinetics. Consequently, biophysical parameters such as the diffusion coefficient, flow velocity, rate or binding constant and concentration can be obtained. [7] In this respect, the typical scope of FCS expands to concentrations ranging from $< 10^{-9}$ to 10^{-6} M and diffusion coefficients ranging from 10^{-15} to 10^{-9} $\text{m}^2 \text{s}^{-1}$ corresponding to sizes of the fluorescent molecules from less than 1 nm to 500 nm. [10, 74]

2.4.1 Autocorrelation analysis of a freely diffusing single type of species

The temporal fluctuations around the equilibrium state are analyzed by the normalized second-order autocorrelation function: [7, 10]

$$G(\tau) = \frac{\langle \delta F(t) \delta F(t + \tau) \rangle}{\langle F(t) \rangle^2} \quad (2.7)$$

Here, deviations of the fluorescence intensity, $\delta F(t)$, from the temporal average of the signal, $\langle F(t) \rangle$, are defined as $\delta F(t) = F(t) - \langle F(t) \rangle$. The autocorrelation function describes the self-similarity of the signal at time point t compared to a later time point $t + \tau$ in relation to the average fluorescence signal of all times (Fig. 7B,C). [10] The mean residence time of the fluorophore in V_{obs} , *e.g.* governed by Brownian motion, hereby determines the level of self-similarity. While at short lag times τ , the molecule is still likely to reside in V_{obs} , this probability decreases with increasing lag times. Concomitant with the reduced probability of self-similarity, the autocorrelation curve decays to zero.

The thermodynamic concentration fluctuations of the fluorophore are governed by a Poissonian distribution. [7, 10] In a Poissonian system, the variance is equal to the average number of fluorescent molecules. Therefore, under the assumption that the fluorescence intensity is proportional to the average number of fluorophores in V_{obs} , the autocorrelation function at $\tau = 0$ converges to: [9]

$$G(0) = \frac{\langle \delta F(t) \rangle^2}{\langle F(t) \rangle^2} = \frac{\langle \delta N \rangle^2}{\langle N \rangle^2} = \frac{1}{\langle N \rangle} \quad (2.8)$$

The amplitude G_0 is hence inversely proportional to the average number of molecules $\langle N \rangle$ in the observation volume. Importantly, contributions from single molecules to the relative fluctuations become significant only when $\langle N \rangle$ is kept low, *i.e.* at a temporal average of $\langle N \rangle$ that ranges from 0.1 and 1000. [10]

The derivation of biophysical parameters is rendered possible by fitting the autocorrelation curve with an appropriate analytical expression. Under the assumption that V_{obs} adapts a

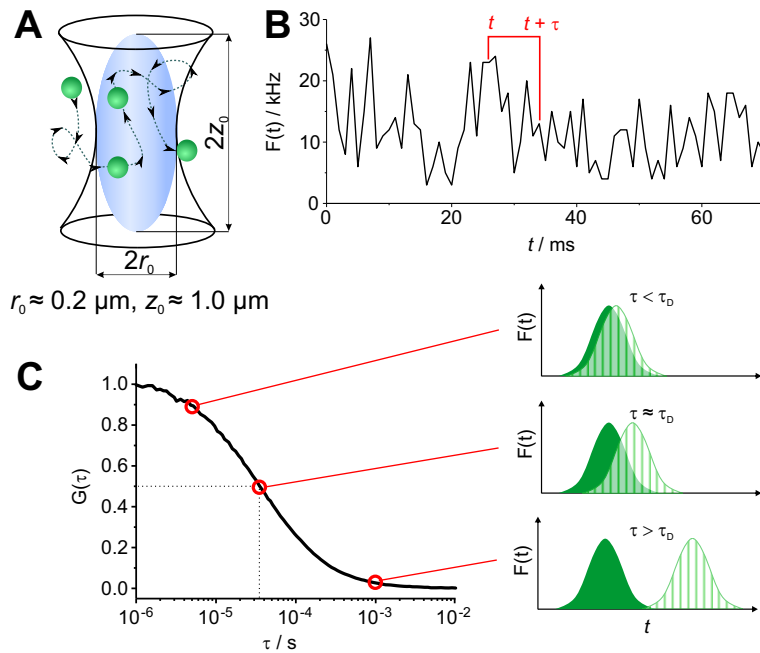


Figure 7: Principle of FCS. A) In FCS, the motion of fluorescent molecules (green) through a femtoliter-sized, diffraction-limited observation volume (V_{obs}) is assessed. Adapted from Ref. [74]. B) Photons, emitted during the transit through V_{obs} , are recorded in an intensity time trace which reveals concentration-based relative fluctuations of the fluorescence intensity signal. C) The signal is analyzed by an autocorrelation function (eq. 2.7) which compares the fluorescence signal at $t = 0$ with itself shifted by different lag times ($t + \tau$). To visualize the principle of autocorrelation, the burst of a single molecule is depicted (right panel, C) and compared with a time-shifted version of itself. The overlapping fraction of the signals decreases with increasing lag time. The half-decay of the autocorrelation curve yields the mean residence time (τ_D) of the fluorescent molecule in V_{obs} from which further physical parameters are deduced. The correlation is computationally calculated by a multiple tau algorithm where the lag time is binned and the size of the integration time (bin time) is increased with increasing sampling time. [79] Adapted from Ref. [80].

3D ellipsoidal Gaussian shape, the autocorrelation curve derived from free three-dimensional diffusion of one single type of species can be fitted with: [6, 7, 10]

$$G(\tau) = \frac{1}{N} \frac{1}{(1 + \frac{\tau}{\tau_D}) \sqrt{(1 + \frac{\tau}{S^2 \tau_D})}} \quad (2.9)$$

Here, S denotes the structure parameter of V_{obs} . S relates the e^{-2} decay of the beam waist in the axial (z_0) and radial (r_0) dimension by $S = z_0/r_0$. The diffusion time τ_D reflects the mean residence time of the fluorescent species in V_{obs} (Fig. 8A). It is linked to the diffusion coefficient D by:

$$\tau_D = \frac{r_0^2}{4D} \quad (2.10)$$

The calculation of D requires knowledge on the dimensions of V_{obs} . These are determined by calibration measurements using reference dyes with known diffusion coefficients. Eventually, the diffusion coefficient of the fluorescent species can be inserted into the Stokes-Einstein equation in order to retrieve its hydrodynamic radius R_H . [10] The Stokes-Einstein equation hereby applies to diluted systems and delivers R_H of an equivalent globular structure.

$$R_H = \frac{k_B T}{6\pi\eta D} \quad (2.11)$$

Here, k_B refers to Boltzmann's constant, T is the temperature and η is the viscosity of the solvent. For species that are larger than tens of nanometers, Equation 2.10 should be substituted for: [81]

$$\tau_D = \frac{r_0^2 + R_H^2}{4D} \quad (2.12)$$

The fit with Equation 2.9 furthermore yields $\langle N \rangle$, the average number of molecules residing in the observation volume. By relating $\langle N \rangle$ to V_{obs} , whereby $V_{\text{obs}} = \pi^{\frac{3}{2}} r_0^2 z_0$, the concentration of the fluorescent species can be calculated (Fig. 8B):

$$\langle c \rangle = \langle N \rangle / V_{\text{obs}} \quad (2.13)$$

Another parameter that can be derived is the molecular brightness ε . The molecular brightness is defined as the ratio between the detected average fluorescence intensity and $\langle N \rangle$: $\varepsilon = \langle F(t) \rangle / \langle N \rangle$. The unit of molecular brightness is Hertz ($\text{Hz} = \text{s}^{-1}$), referring to the number of photons detected from a single dye molecule per second. The physical parameters that determine ε are the detection efficiency of the system, the fluorescence quantum yield of the dye and its excitation cross-section. [7] A higher molecular brightness improves the signal-to-noise ratio of the measurement. It is thus beneficial to optimize the molecular brightness by choosing photostable dyes with high quantum yields, by employing highly efficient detectors and by adapting the pinhole size. [9] In the case of a fluorescent particle that is labeled with several fluorophores, the more general term ‘‘fluorescence brightness’’ is suitable. A comparison of the

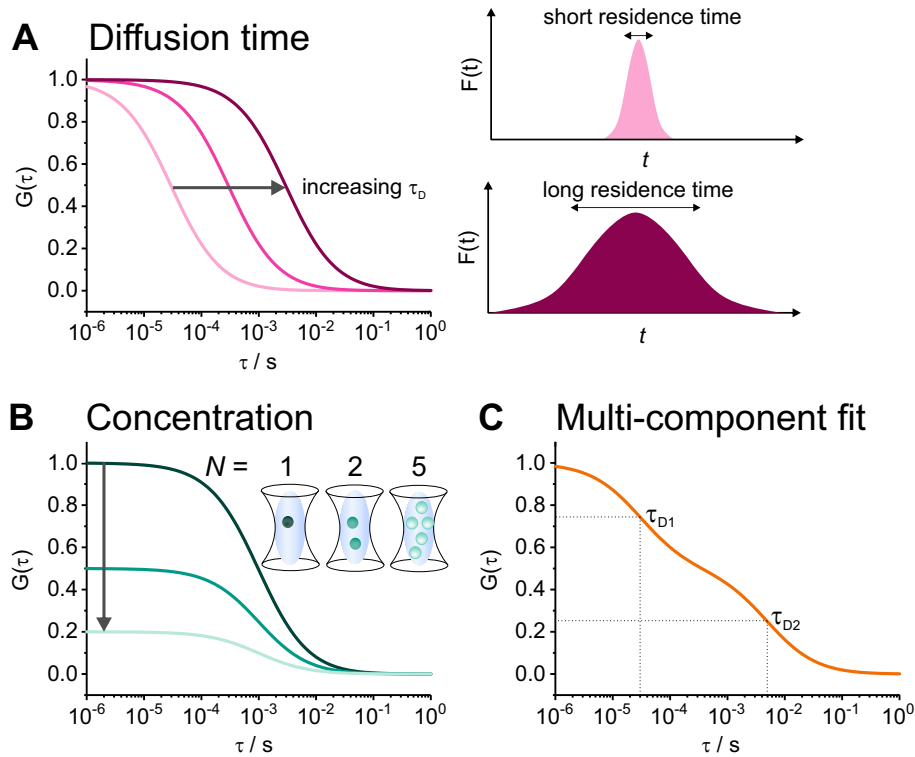


Figure 8: Information extracted from an autocorrelation analysis of freely diffusing fluorescent species. A) The diffusion time increases with the size of the fluorescent species (Eq. 2.10 and 2.11). The larger the molecule, the longer its residence time in V_{obs} . Adapted from Ref. [80]. B) The amplitude of the autocorrelation curve is inversely proportional to the average number of molecules in V_{obs} and thus the concentration. C) Differently sized fluorescent molecules can be distinguished by their diffusion times if the latter differ by at least a factor of 1.6. [82]

fluorescence brightnesses of the individual fluorophore and the multi-labeled particle yields an indication on the number of labels per particle. This, however, implies that the fluorophores in the particle are not quenched.

2.4.2 Autocorrelation analysis in multi-species FCS

FCS measurements are not limited to solutions that contain one single type of fluorescent species. Mixtures of multiple types of fluorescent species can be analyzed. Importantly, Meseth *et al.* theoretically and experimentally determined that in order to distinguish two fluorescent species based on their diffusion they were required to have diffusion times that differed by a factor of ≥ 1.6 (Fig. 8C). [82] If the quantum yields, for instance, differed or if one species was present in excess, an even greater factor applied. As the diffusion time of a species scales to the inverse third power with its molecular weight, $\tau_D \propto M^{1/3}$, an at least four-fold difference in molecular weight is required. On that condition, multiple types of non-interacting species can be fitted with the general expression: [7]

$$G(\tau) = \frac{\sum_{i=1}^n M_i(\tau; \tau_{Di}) \langle N_i \rangle \varepsilon_i^2}{(\sum_{i=1}^n \langle N_i \rangle \varepsilon_i^2)} \quad (2.14)$$

$M_i(\tau; \tau_{Di})$ considers the motion type by which an individual species i traverses V_{obs} . Four different motion types will be discussed in the following. τ_{Di} and ε_i are the diffusion times and fluorescence brightnesses of the individual species i , respectively. Importantly, the relative contribution of each component $\langle N_i \rangle / \sum_{i=1}^n \langle N_i \rangle$ is weighted by the square of its fluorescence brightness. [7] Therefore, absolute fractions are cumbersome to extract and require knowledge on the exact fluorescence brightness of each species.

2D diffusion: Two-dimensional diffusion is observed within structures that can be considered planar, *e.g.* lipid bilayer membranes. [75, 83–85]

$$M_i(\tau; \tau_{Di}) = \frac{1}{1 + \frac{\tau}{\tau_{Di}}} \quad (2.15)$$

3D diffusion: To consider Brownian motion in the three-dimensional space, the 2D diffusion term has to be extended (see also Eq. 2.9). [7, 75–77]

$$M_i(\tau; \tau_{Di}) = \frac{1}{(1 + \frac{\tau}{\tau_{Di}}) \sqrt{(1 + \frac{\tau}{S^2 \tau_{Di}})}} \quad (2.16)$$

Anomalous diffusion: In complex environments such as living cells, deviations from Brownian motion lead to a restricted movement. [86, 87] This motion type is termed anomalous diffusion. It accounts for the local confinement of fluorescent molecules that encounter obstacles such as cellular organelles or that are immobilized by nonspecific interactions with biomolecules. In anomalous diffusion, the mean-square displacement is not linearly proportional to time t but to t^α so that $\langle \Delta r^2 \rangle \propto t^\alpha$. α is the anomaly parameter and adopts values < 1 . It yields information

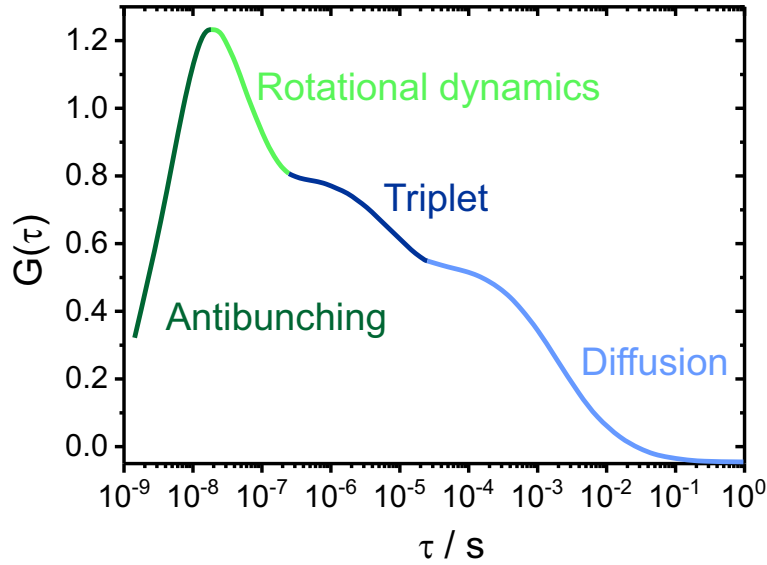


Figure 9: An autocorrelation analysis yields information on the indicated processes occurring at different time scales. Adapted from Ref. [10].

on the degree of restriction in motion. The smaller α , the higher the degree of binding or obstruction. In the fit model, α is implemented by $(\tau/\tau_D)^\alpha$. [88]

$$M_i(\tau; \tau_{Di}) = \frac{1}{(1 + (\frac{\tau}{\tau_D})^\alpha) \sqrt{(1 + \frac{1}{S^2} (\frac{\tau}{\tau_D})^\alpha)}} \quad (2.17)$$

Diffusion and flow: Furthermore, diffusion can be combined with laminar flow. [89, 90] The theoretical derivation as well as experimental validation roots back to Magde and coworkers who described the motion dynamics of particles governed by diffusion and laminar flow. [91] Here, τ_F denotes the flow residence time which is related to the flow velocity v by $v = r_0/\tau_F$.

$$M_i(\tau; \tau_{Di}) = \frac{1}{(1 + \frac{\tau}{\tau_D}) \sqrt{(1 + \frac{\tau}{(S^2 \tau_D)})}} \exp \left[\frac{(\frac{\tau}{\tau_F})^2}{1 + \frac{\tau}{\tau_D}} \right] \quad (2.18)$$

2.4.3 Fast dynamic processes

So far, mathematical fit models have been introduced that considered alterations in the fluorescence intensity signal caused by concentration fluctuations. These concentration fluctuations were derived from motion processes such as diffusion and/or flow. However, there are further sources of fluorescence fluctuations which are in principle accessible by FCS. They are caused by photophysical processes or dynamics and affect time scales which are faster than diffusion (Fig. 9). [10]

One photophysical process that affects most of the fluorescent dyes is photoblinking. It originates from a transition of the dye from the excited singlet state to the first excited triplet state (Section 2.1). [5] Triplet lifetimes (τ_T) of fluorescent dyes typically range from 10^{-6} to

10^{-5} s. [10] During the time that the fluorophore spends in the triplet state, it cannot be excited and appears to be dark. At each time point throughout an experiment, a certain fraction of fluorophores (f_T) resides in the triplet state. This leads to an apparent reduction in concentration which is reflected by a rise of the amplitude of the autocorrelation curve. [7] The exponential decay caused by photoblinking can be resolved with the following expression: [92,93]

$$G_T(\tau) = 1 + \frac{f_T}{1 - f_T} \exp\left[-\frac{\tau}{\tau_T}\right] \quad (2.19)$$

Other bright-to-dark transitions that fluorescent molecules are prone to comprise photoinduced isomerization (*e.g.* cyanine dyes) and reversible protonation reactions (*e.g.* enhanced green fluorescent protein). If these light-induced transitions are irreversible, they are considered under the term “photobleaching”. Photobleaching can also be brought upon by photo-oxidation in the presence of molecular oxygen.

Two further processes on fast time scales are rotational diffusion and photon-antibunching (Fig. 9). These two phenomena occur within the dead-time (30 to 60 ns) of standard APDs. [9] They are therefore not accessible by a conventional FCS setup with a single APD. Instead, their investigation requires the cross-correlation of the time-resolved signals from two APDs. [94] Rotational dynamics (10^{-8} to 10^{-7} s) occur due to photoselection as the probability of excitation depends on the orientation of the fluorophore. Light that is oscillating parallel to the absorption dipole of the chromophoric structure is preferentially absorbed. [10, 95, 96] Photon-antibunching ($< 10^{-8}$ s) appears as an initial rise in the autocorrelation curve. It describes the finite probability for a chromophore to absorb a second photon at time point t after it has absorbed a first photon at time point $t = 0$. [6, 10, 95, 97]

The setup employed in this work accessed lag times from about 50 ns. Therefore, only the concatenation of the fitting model with a multiplicative triplet term was of practical relevance. The triplet-rectified fit model for n fluorescent species ($1 \leq i \leq n$) moving by free 3D diffusion is thus presented as:

$$G(\tau) = G_T(\tau) \cdot G_D(\tau) = \left(1 + \frac{f_T}{1 - f_T} \exp\left[-\frac{\tau}{\tau_T}\right]\right) \frac{1}{N} \sum_{i=1}^n \frac{f_i}{\left(1 + \frac{\tau}{\tau_{Di}}\right) \sqrt{\left(1 + \frac{\tau}{S^2 \tau_{Di}}\right)}} \quad (2.20)$$

The respective fraction f_i of species i scales with the square root of the fluorescence brightness of species i (see also Eq. 2.14). Therefore, if two or more fluorescent species show different brightnesses, f_i does not reflect an absolute fraction and is termed “apparent” fraction throughout this work.

2.4.4 Dual color fluorescence cross-correlation spectroscopy

A modification of the conventional autocorrelation analysis involves the cross-correlation of two different signals. In general, a cross-correlation analysis requires two independent fluorescence intensity traces. These can be obtained either by hardware (*e.g.* two independent

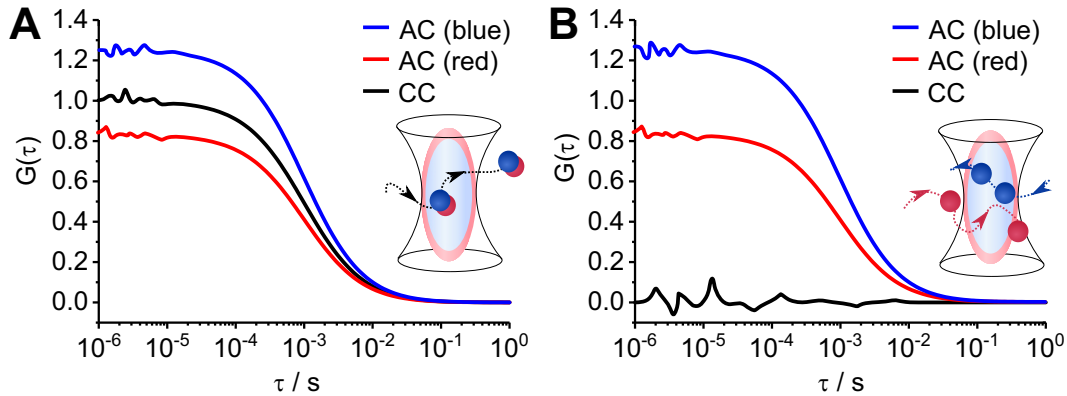


Figure 10: Principle of dual color FCCS (autocorrelation (AC), cross-correlation (CC)). A) The interaction of “blue” and “red” molecules leads to their simultaneous diffusion. Here, cross-correlation analysis yields a high cross-correlation amplitude. B) A cross-correlation amplitude which fluctuates around zero is indicative for the independent diffusion of two types of non-interacting fluorescent species. Adapted from Ref. [100].

detectors) or software (*e.g.* distinction of species based on their fluorescence lifetimes) cross-correlation. [98] In FCS, a cross-correlation analysis can help to suppress artifacts introduced by the detectors (“afterpulsing”) or illumination source. [10] However, the most common cross-correlation techniques are dual beam and dual color fluorescence cross-correlation spectroscopy (FCCS). The first technique is applied in the presence of flow and analyzes fluctuations from two separate observation volumes by performing a spatial cross-correlation analysis. [99] The second application will be explained in more detail in the following paragraphs.

Dual color FCCS is employed to study the interactions of two different species. This is especially important when their dynamics do not lead to a large change in mass and are thus not accessible by single color FCS. [9] It requires the labeling of the two reaction partners with dyes that are spectrally different. The instrumental realization resembles that of conventional FCS with the difference that two excitation laser at different wavelengths and two spectrally separated detection elements are utilized. The excitation lasers are collimated and focused into the sample so that they illuminate the same spot. [101] The fluorescence emitted from the two dyes is passed through the same pinhole and then divided into two detection channels by a dichroic mirror. The signals from both detectors are cross-correlated and analyzed by the following cross-correlation (CC) function: [101]

$$G_{CC}(\tau) = \frac{\langle \delta F_b(t) \delta F_r(t + \tau) \rangle}{\langle F_b(t) \rangle \langle F_r(t) \rangle} \quad (2.21)$$

For simplicity, the two dyes are abbreviated with the letters “b” and “r” indicating the colors blue and red, respectively. Thus, F_b and F_r are the signals from the two detection channels. Considering the dependence of the diffraction limit on wavelength, it is important to highlight that the two observation volumes $V_{\text{obs},b}$ and $V_{\text{obs},r}$, created by different excitation lasers, have different dimensions (r_i, z_i). [101] In the ideal case of a perfect overlap, $V_{\text{obs},b}$ lies entirely within $V_{\text{obs},r}$. The effective observation volume that needs to be considered in cross-correlation analysis

is described as follows:

$$V_{\text{obs.br}} = \pi^{\frac{3}{2}} \cdot \frac{(r_b^2 + r_r^2)}{2} \cdot \sqrt{\frac{(z_b^2 + z_r^2)}{2}} \quad (2.22)$$

In the case where the two detection channels can perfectly separate the two species, the general auto- and cross-correlation functions read: [102]

Autocorrelation: with $i = \text{b, r}$

$$G_{\text{AC}.i}(\tau) = \frac{\langle c_i \rangle M_i(\tau; \tau_{\text{D}.i}) + \langle c_{\text{br}} \rangle M_{\text{br}}(\tau; \tau_{\text{D}.br})}{V_{\text{obs}.i}(\langle c_i \rangle + \langle c_{\text{br}} \rangle)^2} \quad (2.23)$$

Cross-correlation:

$$G_{\text{CC}}(\tau) = \frac{\langle c_{\text{br}} \rangle M_{\text{br}}(\tau; \tau_{\text{D}.br})}{V_{\text{obs.br}}(\langle c_b \rangle + \langle c_{\text{br}} \rangle)(\langle c_r \rangle + \langle c_{\text{br}} \rangle)} \quad (2.24)$$

Here, $M_i(\tau; \tau_{\text{D}.i})$ indicates the motion type (Eq. 2.15, 2.16, 2.17 or 2.18). The concentration of the double-labeled species c_{br} is directly proportional to the amplitude of the cross-correlation curve and can be calculated by:

$$c_{\text{br}} = \frac{G_{\text{CC}}(0)V_{\text{obs.br}}}{V_{\text{obs.b}}V_{\text{obs.r}}G_{\text{AC}.b}(0)G_{\text{AC}.r}(0)} \quad (2.25)$$

Figure 10 depicts the two extreme cases of complete (A) and no (B) interaction. In the first case, the two species are interacting with each other and are concomitantly diffusing together, thereby yielding a correlated motion. This behavior will lead to the appearance of a cross-correlation curve whose amplitude lies between those of the autocorrelation curves. In the second case, there is no interaction between the two species and thus no cross-correlation. All intermediate binding events can be derived from the concentration of the double-labeled species relative to the concentrations of the individual interaction partners.

Dual color FCCS measurements require a careful calibration. [103, 104] Misplaced observation volumes lead to a reduced cross-correlation while the leakage of blue dye fluorescence into the red dye emission channel leads to an artificial cross-correlation. To ensure that the observation volumes overlap perfectly, commercially available positive controls are employed. Spectral cross-talk, in contrast, is typically assessed by comparing the signals in the blue and red detection channel emitted from a construct that is labeled only with the blue dye. Another possibility to eliminate spectral cross-talk is pulsed interleaved excitation. [105] In this mode, two pulsed lasers asynchronously excite the two fluorescent species so that each detected photon can be assigned to the respective excitation source and therefore counted as cross-talk or positive signal. Such excitation mode furthermore allows the application of only a single detector or the combination of FCCS with FRET.

2.4.5 Inverse FCS

As implied by the name “inverse FCS”, this modality is based on an inversion of the detection mode of FCS. Instead of monitoring fluorescent species in an unstained solution, inverse FCS analyzes the mobility and concentration of unlabeled particles in a strongly fluorescent medium. [106,107] When an unlabeled particle diffuses through the observation volume, it occupies a certain volume fraction and therefore displaces a certain number of dye molecules. This leads to a decrease in the fluorescence intensity signal apparent by transient dips. Wennmalm *et al.*, who introduced the concept of inverse FCS, derived that the obtained autocorrelation function could be fitted with a similar model (Eq. 2.9) as applied for standard FCS. [106] Thus, accurate diffusion parameters of the unlabeled particles could be obtained. While standard FCS can monitor the motion of single dye molecules, inverse FCS was reported to be limited to a minimum particle size of about 100 nm. A further condition for sufficient sensitivity in inverse FCS is a high concentration of background molecules (*e.g.* 400 μM dye) which should not give rise to an autocorrelation curve themselves. [106,107]

In inverse FCS the concentration of particles relates differently to the amplitude of the autocorrelation curve than in standard FCS. [107] In order to calculate accurate concentrations the particle-occupied volume V_{part} relative to the observation volume V_{obs} , given by $V_{\text{q}} = V_{\text{part}}/V_{\text{obs}}$, has to be determined. The amplitude of the autocorrelation curve at $\tau = 0$ is then related to the average number of particles in V_{obs} by:

$$G(0) = \frac{N}{\left(\frac{1}{V_{\text{q}}} - N\right)^2} \quad (2.26)$$

If $1/V_{\text{q}} \gg N$, the simplified relation, $G(0) \approx V_{\text{q}}^2 \cdot N$, can be assumed in which case the amplitude of the autocorrelation curve is directly proportional to N . [107] This relation, however, was proposed to be invalid for larger particles that are equal to or exceed the dimensions of V_{obs} . [106] Such particles were expected to show an amplitude that is lower than estimated.

Inverse FCS furthermore offers the possibility of cross-correlation. [108] Two different modes of inverse FCCS have been reported. Both of them rely on the introduction of a label that is spectrally different from the fluorescent dye in the surrounding medium. In the first mode, the signal of a differentially labeled particle is analyzed in two ways: by its own fluorescence intensity trace and by its “negative” signal in the intensity trace of the surrounding fluorescent medium. Cross-correlation of both fluorescence intensity traces gives rise to an anti-correlation and yields information about the proportions of the particle and the detection volume. [107] If the size of either the particle or detection volume is known, the respective other size can be derived. The second mode investigates the binding of a small differentially labeled molecule to an unlabeled particle. The authors suggested an advantage of this approach over standard FCS because the cross-correlation of the two intensity traces (standard and inverse FCS) would yield the relative fraction of bound *vs.* unbound particle.

2.4.6 FCS in living systems

Features like (i) noninvasiveness, (ii) the default combination with confocal microscopes and (iii) a working range of nanomolar concentrations render FCS inherently suitable for measurements in living systems. [9, 10] Already the first applications of FCS were situated in biological context and targeted on the question of receptor transport in cellular membranes. [109, 110] Since then, FCS has been applied to study biomolecular interactions in the cytoplasm, nucleus, membrane and cellular organelles. The diversity of these studies is covered in a number of comprehensive reviews. [8–10, 80, 83, 111] Model systems of interest have thus far spanned bacteria, yeast, mammalian and plant cells. But also living organisms or united cell structures such as the embryos of zebrafish and medaka, nematodes, fruit flies and the human skin have been investigated. Thus, these studies have greatly contributed to the elucidation of *e.g.* membrane and chromatin organization, protein dynamics, directed transport and receptor translocation. However, such intracellular measurements are challenging due to the increased complexity of the underlying systems. [9] In contrast to FCS measurements in solution, the pool of fluorescent molecules is limited by the finite volume of an individual cell. Furthermore, the intracellular mobility is reduced due to an increased fluid-phase viscosity, binding events with biomolecules and molecular crowding. The concomitantly increased residence time in V_{obs} also raises the degree of photobleaching which, by the limited capabilities of dye replenishment, are likely to appear in the autocorrelation curve. Further effects such as a background signal brought upon by autofluorescent molecules, movement of the sample and cell viability have to be accounted for. [9] The practical implications of these effects as well as strategies to either prevent or consider them during analysis will be discussed in Section 10.1.

Part II

Modulation of mitochondriotropic properties of cyanine dyes by *in organello* copper-free click reaction

3 Introduction

Mitochondria with their specialized physiology offer the unique possibility of being targeted by a well-balanced distribution of positive charge and lipophilicity in a small molecule's scaffold. Here, the structural and functional conditions of mitochondria relevant to this principle of targeting will be explained (Section 3.1). Furthermore, molecular properties that convey mitochondrial uptake and accumulation will be covered and classes of molecules with these properties will be introduced (Section 3.2). The last part will focus on externally mediated reactions that take place in the mitochondria (Section 3.3).

3.1 Mitochondria

Mitochondria are semiautonomous organelles that fulfill a diverse set of cellular functions. The production of adenosine triphosphate (ATP) *via* the coupled processes of citric acid cycle and oxidative phosphorylation (OXPHOS) is considered one of the major functions. Mitochondria are also the sites for biochemical pathways that include fatty acid oxidation, mitochondrial purine and pyrimidine metabolism, urea cycle, biosynthesis of heme, ubiquinone (coenzyme Q) and iron-sulfur centers as well as biosynthesis and metabolism of cardiolipin and lipids. [112] Further major functions include the regulation of Ca^{2+} homeostasis, the production and regulation of ROS and the regulation of programmed cell death. [113, 114] However, mitochondrial tasks extend beyond these functions and biochemical processes mentioned here. [115]

Mitochondria contain their own genome which is placed on a multi-copy, circular and double-stranded DNA molecule (mtDNA). [12, 116] The mtDNA encodes all 22 tRNA and two rRNA genes that are required for mitochondrial translation. Furthermore, 13 mitochondrial proteins, involved in the respiratory chain, are encoded. However, only a subfraction of mitochondrial functions is sustained by these proteins thus rendering the mitochondria only partially autonomous. Genomic information for the main fraction of proteins (≈ 1500) is contained in the nuclear genome. Upon their cytoplasmic synthesis, these proteins are imported into the mitochondria. [116]

3.1.1 Mitochondrial structure

The complex structure of the mitochondria ensures a regulated interface between the cytoplasm and the mitochondrial matrix. This compartmentalization is vital to mitochondrial functions. [17] Each mitochondrion contains a pair of lipid bilayer membranes (Fig. 11). The outer mitochondrial membrane is highly permeable to most small molecules (< 5 kDa). This permeability is suggested to be caused by the abundant mitochondrial protein VDAC (voltage-dependent anion channel, also called porin) which forms pores in the outer membrane and regulates the passage of cations and anions by variations of its selective functional states. [112] The terminology “voltage-dependent”, however, is misleading as no mechanism that would generate a physiologically relevant potential across the outer membrane has been described. [18] The outer mitochondrial membrane encloses the intermembrane space which is the compartment that lies between outer and inner membrane. It has been postulated to be “chemically equivalent” to the cytoplasm with respect to small molecules. [17] In contrast to the outer membrane, the inner mitochondrial membrane is impermeable to nearly all ions and polar molecules. This is achieved through a densely packed bilayer of hydrophobic phospholipids with a high proportion of the bisphosphatidylglycerol cardiolipin. [18] Transport of proteins, ions and metabolites into the mitochondrial matrix is accomplished through specialized carrier proteins. The inner mitochondrial membrane is furthermore the site of the electron transport chain which will be explained in more detail in the following paragraph. The inner mitochondrial membrane is folded in so-called cristae. The surrounded volume, the mitochondrial matrix, is thus covered by a large membrane surface. [17] Mitochondria are not isolated from each other but are connected in a network. This network is not rigid. Rather, mitochondria are mobile and plastic organelles which constantly change their morphology by fusion and fission. [18]

3.1.2 Mitochondrial energetics

Mitochondria play a key role in cellular energetics by synthesizing ATP (Fig. 11). [17, 113, 117] Fuel in the form of reducing equivalents is provided by degradation of nutrients such as carbohydrates, fatty acids and amino acids. In the cytosol, glucose is subjected to glycolysis which generates pyruvate and reduced nicotinamide dinucleotide ($\text{NADH} + \text{H}^+$). [117] In a next step, pyruvate is shuttled across the inner mitochondrial membrane by pyruvate carrier proteins. In the mitochondrial matrix, pyruvate is oxidatively decarboxylated by the pyruvate dehydrogenase forming acetyl coenzyme A (acetyl CoA). Fatty acids are transported into the mitochondrial matrix with the help of an associated transport protein (carnitine-acylcarnitine translocase). In a process termed β -oxidation, they are then degraded to acetyl CoA, $\text{NADH} + \text{H}^+$ and reduced flavine adenine dinucleotide (FADH_2). The degradation product acetyl CoA (from glucose and fatty acid metabolism) enters the citric acid cycle where further oxidation leads to the generation of $\text{NADH} + \text{H}^+$ and FADH_2 , the reducing equivalents. The degradation products of amino acids are fed into the citric acid cycle as various intermediate products and thus contribute to the formation of reducing equivalents. [118] In the process of OXPHOS,

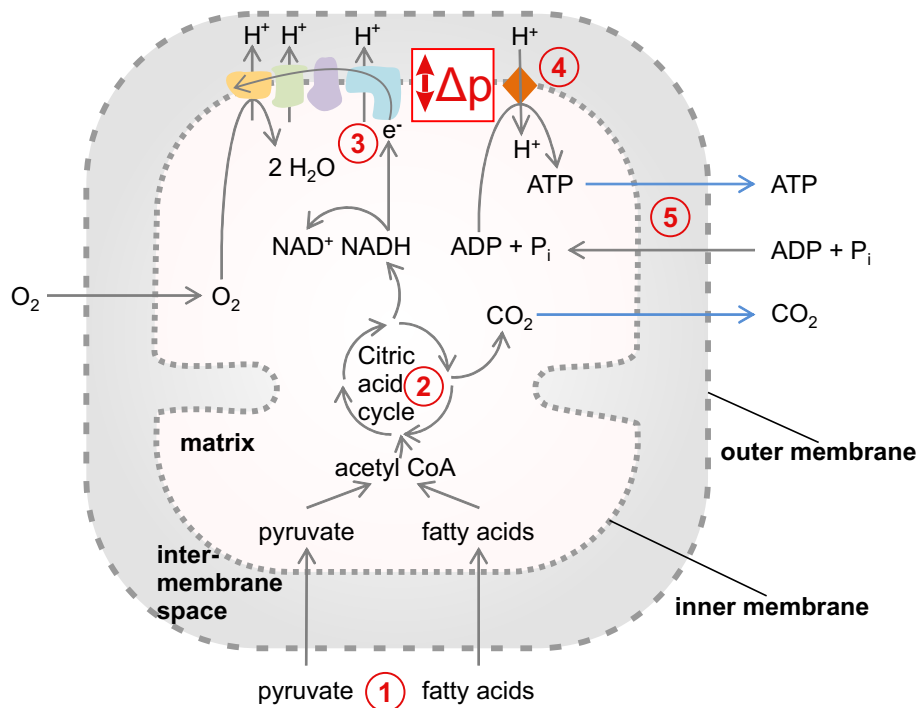


Figure 11: ATP synthesis in the mitochondria. 1) Nutrients such as pyruvate, derived from glucose, and fatty acids are transported to the mitochondrial matrix where they are degraded to acetyl CoA. 2) In the citric acid cycle, acetyl CoA reacts with oxaloacetate to form citrate. Starting from citrate, two subsequent decarboxylation reactions take place in each of which one molecule of NADH + H⁺ is formed. During the following regeneration of oxaloacetate further energy is harvested in the form of reducing equivalents. 3) OXPHOS: the electron carriers NADH and FADH₂ are oxidized and thereby release electrons. The free enthalpy that is gained when the electrons flow down the electron transport chain is used to pump protons across the inner mitochondrial membrane thereby establishing an electrochemical proton motive force Δp . 4) The proton gradient is used by the ATP synthase to generate ATP from ADP + P_i. 5) In exchange with ADP, ATP is transported to the cytosol. Adapted from Ref. [17]

electrons are passed from NADH and FADH₂ along the electron transport chain to O₂ to yield H₂O. The electron transport occurs through the four large respiratory protein complexes I - IV which are situated in the inner mitochondrial membrane (detailed in Ref. [119, 120]). Within these complexes flavines, iron-sulfur clusters, quinones (*e.g.* ubiquinone), copper ions and prosthetic heme groups of cytochromes serve as electron carriers. [120] During the successive exergonic redox reactions the released free enthalpy is utilized to drive the endergonic transport of protons from the matrix to the intermembrane space. This proton transport occurs in complex I, III and IV. Complex II constitutes a direct link to the citric acid cycle which passes on electrons from FADH₂ without pumping protons to the intermembrane space. The thus established electrochemical proton gradient Δp leaves the mitochondrial matrix both alkaline and electrically negative and serves as a storage for free enthalpy. The potential energy stored in Δp is used for ATP synthesis by the inner-membrane ATP synthase. The flow of protons along their electrochemical potential releases free enthalpy that leads to the rotation of the γ -subunit of the ATP synthase. This rotation induces structural changes within the β -subunit of the ATP synthase and thus drives the reaction of adenosine diphosphate and orthophosphate (ADP + P_{*i*}) towards ATP. [120] In exchange with cytosolic ADP, ATP is then transported out of the matrix by inner-membrane adenine nucleotide transporters.

3.1.3 Mitochondrial membrane potential

The function of the electrochemical gradient Δp as a driving force in ATP synthesis has been described above. The electrochemical gradient, also called proton-motive force, is composed of two contributions: the mitochondrial membrane potential $\Delta\Psi_m$ and the pH gradient ΔpH_m . At 37°C, the following relation has been postulated:

$$\Delta p \text{ (mV)} = \Delta\Psi_m + 61.5\Delta\text{pH}_m \quad (3.1)$$

Note, that the factor “61.5” derives from the use of a simplified Nernst equation to convert ΔpH_m into a potential. [121] The potential $\Delta\Psi_m$ is related to the separation of charges between the intermembrane space and the mitochondrial matrix. It is thus an electrical gradient. Typical values range between 120 mV and 180 mV and vary depending on the cell type as well as mitochondrial condition, *e.g.* diseased cells *vs.* actively respiring cells. [122, 123] The pH difference ΔpH_m describes a chemical gradient and is established through the net accumulation of protons in the intermembrane space. Typically, ΔpH_m is 0.5 - 1.0 units thus contributing 30 - 60 mV to Δp . [121] The two factors add up to a Δp of 150 - 240 mV, of which $\Delta\Psi_m$ is the dominant fraction. $\Delta\Psi_m$ sensitively describes the balance between ATP synthesis and consumption and is thus an important indicator for abnormal conditions. A decrease of $\Delta\Psi_m$, for instance, occurs concomitant with an increase in ATP synthesis, thermogenesis or mitochondrial dysfunction. [12, 122] Thermogenesis is a protective mechanism to release energy in the form of heat exerted by some mammals as well as infants who contain mitochondria-rich brown adipose tissue. [120] By transporting protons into the mitochondrial matrix with the

help of an uncoupling protein (UCP-1), OXPHOS and ATP synthesis are uncoupled and the free enthalpy of the proton gradient is transformed to heat. Elevated levels of $\Delta\Psi_m$ are found in the mitochondria of many types of cancer cells. [124,125] This is, however, just one of several alterations of OXPHOS that were reported for cancer cells. [126] Furthermore, an increase in $\Delta\Psi_m$ is considered to lead to an augmented ROS production. [127]

In summary, the impermeability of the inner mitochondrial membrane to ions, many small molecules and proteins is essential for the maintenance of an electrochemical gradient which drives ATP synthesis. The mitochondrial membrane potential $\Delta\Psi_m$ is the prevalent determining factor of this gradient. The tightly regulated partitioning into a mitochondrial matrix and an intermembrane space results in a unique chemical environment of the matrix. Explicitly, the matrix is alkaline and contains an excess of negatively charged molecules. These conditions can be exploited to selectively accumulate probes with certain properties as will be outlined in Section 3.2.

3.2 Mitochondria-localizing probes

The aim of overcoming the barrier of the inner mitochondrial membrane with molecular probes is motivated by several perspectives. First of all, important structural and dynamic parameters of mitochondrial physiology can be assessed with the help of probes that intracellularly distribute to the mitochondria. These probes thus serve as sensors for mitochondrial function *vs.* dysfunction. Secondly, probes were transferred to the mitochondria in order to investigate a potential therapeutic intervention with mitochondrial metabolism. In both cases, uptake into the mitochondrial matrix is often followed by a selective and specific intramitochondrial reaction as detailed in Section 3.3. But how is a selective distribution of probes in the mitochondria achieved? The answer is found in specific molecular characteristics, so-called mitochondriotropic properties, that lead to the mitochondrial localization of the probes. [15,128] Naturally, cations are attracted towards the negatively charged environment of the matrix which is caused by the potential difference between intermembrane space and matrix. However, only those which are lipophilic enough to permeate membranes can actually reach the matrix. Consistently, the structural prerequisites for mitochondriotropism include a net cationic charge (which should be delocalized as will be explained below) and a lipophilic character, often together with a certain proportion of aromatic character. In this section, the membrane passage of certain lipophilic cations as the barrier to mitochondrial uptake will be described. Then, the high accumulation of mitochondriotropics in dependence of $\Delta\Psi_m$ as means of mitochondrial targeting will be detailed and lastly, different classes of mitochondria-localizing probes will be presented.

3.2.1 Membrane passage of delocalized lipophilic cations

In the following, the translocation of lipophilic cations across lipid bilayer membranes is elucidated. The membrane passage consists of a multi-step process which involves the binding of the cation at the membrane surface, its rapid transport through the lipid bilayer and desorption

from the other side of the membrane. The total potential energy profile as depicted in Figure 12 is a sum of electrostatic and nonelectrical terms. [129] With regard to the latter, the hydrophobic force plays the most important role. When transferring the cation from the aqueous milieu to the hydrophobic interior of a lipid bilayer membrane a first energy barrier has to be surmounted. [130–132] The main electrostatic component of this activation energy derives from the removal of the solvation layer of the cation. The enthalpy input needed for this desolvation is inverse proportional to the ionic radius as described by the Born energy (Appendix 1). [130,132] This means that the enthalpy input is reduced if the charge is dispersed over a large surface area, *e.g.* due to the delocalization of the charge across a conjugated π -electron system. A delocalized positive net charge, prominent for mitochondriotropics, thus facilitates the membrane passage. Further but less influential electrostatic components comprise the image and dipole energy. [133] The image energy describes the attraction of the ion towards water as a result of the higher dielectric constant of water (≈ 80) *vs.* the interior of the membrane (≈ 2). The membrane dipole energy presumably originates from the dipole moments of the polar moieties of the membrane lipids (*e.g.* lipid head groups, surface water molecules, and lipid carbonyls) and increases the activation energy of the cation. [129,132] This electrostatic energy demand is counteracted by a hydrophobic force. [134] Formally, the hydrophobic force is described for the corresponding uncharged analog of the cation with a similar size and hydrophobicity. Attraction of the lipophilic molecule into the lipid bilayer leads to an increase in entropy (loss of water structure [132]) and is thus the driving force of membrane binding. As the effect is strongest close to the membrane surface the characteristic potential energy wells depict the binding sites of the lipophilic cation (Fig. 12). [130] Movement through the lipophilic interior of the membrane is impeded by another energy barrier which again composes the counteracting forces of an attractive hydrophobic energy and a repulsive electrostatic energy (Born, image and dipole energy). The gradual increase of the latter rapidly drives the ion towards the potential minimum at the other side of the membrane. [132] From there, a last activation energy has to be summoned in order for the lipophilic cation to desorb into the aqueous environment. The rate of movement of the lipophilic cation through the membrane is proportional to the Arrhenius rate equation $e^{-E/RT}$ with R denoting the universal gas constant and T denoting the absolute temperature. By inserting the particular free energy of activation (E) the rate for each step (adsorption, transfer, desorption) can be derived. [130]

3.2.2 Mitochondrial accumulation depending on $\Delta\Psi_m$

The mechanism of membrane passage of lipophilic cations as described above applies to all phospholipid bilayers and occurs in the absence of a membrane potential. There is, however, a selective accumulation of cations in the mitochondrial matrix that works against their concentration gradient. This increased transport across the inner mitochondrial membrane is driven

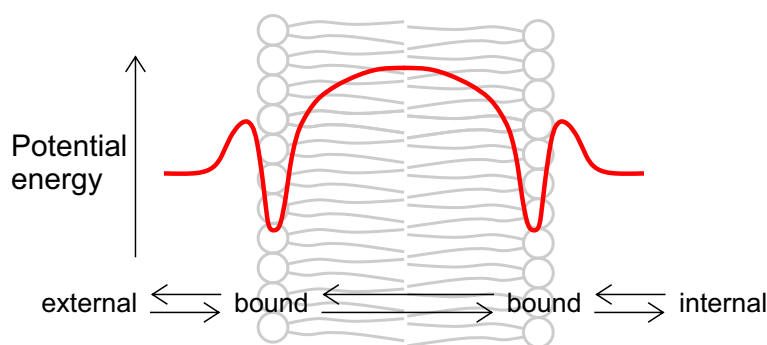


Figure 12: Energy profile for the translocation of a lipophilic monocation through a lipid bilayer membrane. Figure adapted from Ref. [132]

by $\Delta\Psi_m$. [123] At equilibrium, the extent of accumulation is described by the Nernst equation:

$$\Delta\Psi_m = \frac{RT}{nF} * \ln \frac{c_{in}}{c_{out}} \quad (3.2)$$

where R denotes the universal gas constant, T is the absolute temperature, n is the valence of the charged molecule and F is Faraday's constant. The concentration of the cation in the mitochondria and outside of the mitochondria are denoted by c_{in} and c_{out} , respectively. In case of a monocationic molecule that accumulates in the mitochondria at 37 °C, the equation can be simplified as follows: [123]

$$\Delta\Psi_m = 61.5 * \log \frac{c_{in}}{c_{out}} \quad (3.3)$$

The accumulation ratio is thus expressed by:

$$\frac{c_{in}}{c_{out}} = 10^{\Delta\Psi_m/61.5} \quad (3.4)$$

As easily apparent from the above equation, the accumulation ratio increases ten-fold with every change in $\Delta\Psi_m$ of 61.5 mV. [128] Therefore, at a $\Delta\Psi_m$ of 140 mV, the compound would be almost 200-fold enriched in concentration within the mitochondrial matrix (Fig. 13).

Triphenylphosphonium alkyl cations (TPP⁺) comprise a class of molecules whose accumulation in dependence of $\Delta\Psi_m$ has been extensively studied. [132,135–137] Due to their Nernstian behavior, TPP⁺ compounds are commonly applied to measure $\Delta\Psi_m$ either by use of a TPP-specific ion-selective electrode or by determination of the external *vs.* mitochondrial distribution of ³H-labeled TPP⁺ probes. [122,137,138]

In intact cells, an externally applied probe first has to cross the plasma membrane. Similar to the inner mitochondrial membrane, the plasma membrane exhibits a negative membrane potential. An accumulation of cations inside the cytoplasm with respect to the extracellular concentration can be likewise calculated with the Nernst equation (Eq. 3.4). The plasma membrane potential $\Delta\Psi_p$ is, however, much lower than $\Delta\Psi_m$ (typical values of 30 - 60 mV are reported) which leads to enrichment factors in the cytoplasm of three- to ten-fold (Fig.

13). [139] It should be stressed that accumulation factors calculated by Nernst equation apply to equilibrium conditions. Hereby, equilibration in dependence of $\Delta\Psi_m$ requires much less time than equilibration across the plasma membrane. This is due to the large surface-to-volume ratio of the folded inner mitochondrial membrane. Every intervention into one of the parameters that enter the Nernst equation (Eq. 3.2) leads to an adjustment of the equilibrium conditions (re-equilibration). For instance, a modulation of $\Delta\Psi_m$ or $\Delta\Psi_p$, *e.g.* by the application of pharmacologicals, would alter the accumulation ratio. In contrast, if the extracellular probe concentration was diminished the accumulation ratio itself would not change. In this case, the mitochondrial and cytoplasmic concentrations would be decreased accordingly until the system would reach equilibrium again.

Importantly, the dynamics of the equilibration process depend on the energy barrier (Section 3.2.1). A reduction in the energy barrier for the translocation of a lipophilic cation across membranes (*i.e.* the higher its lipophilicity and the greater its ionic radius) should hence go along with an increase in the uptake and efflux rates. Evidence for such behavior was provided by Ross and coworkers who compared the uptake rates of three TPP⁺ alkyl derivatives with differing lipophilicity. [137] The lipophilic compounds decyl-TPP⁺ and MitoQ (contains an additional ubiquinone moiety) reached steady state levels considerably faster than methyl-TPP⁺. Moreover, mitochondria incubated with MitoQ showed a large fraction of membrane-bound probe. This fraction evades Nernstian equilibrium which only considers free and unbound molecules. Thus, in addition to the increased uptake rate highly lipophilic molecules can also be taken up to a greater extent than calculated by the Nernst relation (Eq. 3.2) due to non-negligible membrane binding.

The number of positive charges of the molecule also influences the extent and rate of mitochondrial uptake. So far, monocationic molecules have been discussed. In theory, dications should accumulate to the square of values calculated for monocations (*e.g.* 700,000-fold at a $\Delta\Psi_m$ of 180 mV). The primary requirement, however, is that the dication is able to permeate membranes. [139] A divalent charge leads to an increase in enthalpy (Born energy) and thus a higher activation energy (Appendix 1). To still achieve efficient uptake (rates), this elevated enthalpy contribution must be compensated by an increased lipophilicity. To study the correlation of divalency and lipophilicity, a series of bis-TPP dications were incubated with isolated mitochondria. [140] The constructs consisted of two TPP⁺ moieties linked by an alkyl chain which varied in length. TPP-based dications with C₅- and C₆-linkers were able to accumulate in the mitochondrial matrix, while constructs with shorter linkers were not enriched. The accumulation, however, was found to comply with Nernstian behavior only at $\Delta\Psi_m$ values of up to 100 mV, showing deviations from the calculated accumulation at higher $\Delta\Psi_m$. [140] Although C₅- and C₆-bis-TPP dications were able to accumulate in isolated mitochondria, they were precluded from cellular uptake in cell culture experiments. The authors of the study explain this observation by an overall higher activation energy of the plasma membrane which differs from the inner mitochondrial membrane in terms of its lipid and protein composition. [140]

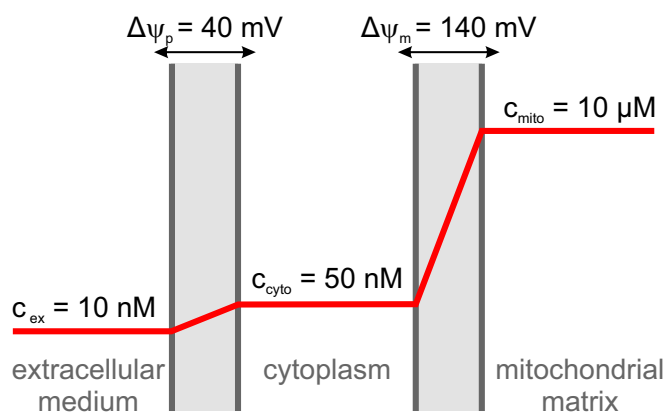


Figure 13: Distribution of a lipophilic, monovalent cation among extracellular medium, cytoplasm and mitochondrial matrix in dependence of $\Delta\Psi_p$ and $\Delta\Psi_m$. Equilibrium concentrations were calculated by the Nernst equation.

3.2.3 Mitochondriotropic compounds: from small molecules to macromolecules

Triphenylphosphonium alkyl cations were among the first reported compounds whose extent of mitochondrial uptake was linked to $\Delta\Psi_m$ (Section 3.2.2). [135, 136] Their discovery played a major role in the verification of membrane potentials whose existence had been postulated by Mitchell's chemiosmotic model. [141] Shortly after investigations took up speed in the 1970s, fluorescent dyes based on rhodamine and cyanine structures joined the group of mitochondriotropic probes. [142, 143] Selective fluorescent staining of mitochondria had been practiced since the 1890s by application of the dye Janus Green. [144] However, the link to $\Delta\Psi_m$ had not been established at this time. Widely applied fluorescent dyes with mitochondriotropic properties comprise the rhodamine dyes rhodamine 123, [142] tetramethylrhodamine methyl (TMRM) and ethyl (TMRE) esters and the cyanine dyes JC-1 [145, 146] and DiOC₆ (Fig. 14). [114, 121] The accessibility of the dyes by fluorescence-based methods such as fluorescence microscopy and cytometry justifies their comprehensive use as sensors for $\Delta\Psi_m$ -dependent (patho-)biochemical processes. [147] However, there are some cationic dyes which do not accumulate $\Delta\Psi_m$ -dependently. Some members of the MitoTracker[®] series, for instance the cyanine dye MitoTracker Green FM, [148] contain chloromethyl groups which lead to covalent binding of the dye to cysteine residues of mitochondrial proteins. *N*-Nonyl acridine orange, on the contrary, binds non-covalently to cardiolipin in the inner mitochondrial membrane. [149] Along with these monocationic probes, dequalinium, a lipophilic dication, was reported for its mitochondrial accumulation. Dequalinium was found to selectively target cancer cells, to impair carcinoma cell proliferation, migration and invasion and to inhibit the tumor growth of bladder and colon cancer. [150–153] Its mechanism of action was postulated to involve the inhibition of a calmodulin-stimulated phosphodiesterase. [154]

It should be mentioned that mitochondrial localization was also observed for negatively charged and electrically neutral molecules. In order to predict mitochondriotropic properties, Horobin *et al.* developed a quantitative structure-activity relationship model. Their algorithm

takes into account the molecule's structure, amphiphilicity and lipophilicity ($\log P$), conjugated domains, electric charge and its acidic or basic properties (pKa). [14, 155]

Apart from small molecular mitochondriotropics, macromolecules have also been found to localize to the mitochondria. Peptides such as mitochondria-penetrating peptides, [156, 157] Szeto-Schiller peptides [158–160] or a probe based on the partial sequence of the antibiotic gramicidin (hemigramicidin-TEMPO) [161, 162] have been designed to target mitochondria. These peptides are either of natural or synthetic origin. Their common structural motif comprises basic (*e.g.* arginine, lysine) and hydrophobic (*e.g.* phenylalanine, tyrosine, isoleucine, cyclohexylalanine) amino acid residues. There are also several non-peptidic probes that take advantage of the delocalized positive charge of the guanidinium moiety. For instance, a tetraguanidinium oligomer [163] as well as lactose- or sorbitol-based guanidinium conjugates [164, 165] have been successfully accumulated in mitochondria. Another approach consists of utilizing the natural pathway for cellular proteins to reach mitochondria. Such mitochondria-transported proteins contain a mitochondrial target sequence (MTS) of 20 to 40 amino acids which is recognized by the protein import machinery. [166, 167] The translocation is implemented by the carrier proteins TOM (outer mitochondrial membrane) and TIM (inner mitochondrial membrane) and mitochondrial heat shock protein mthsp70. [18, 168] After transfer to the matrix, the MTS is cleaved off by peptidases and the protein activity is restored.

While some of the above-mentioned probes show an inherent pharmacological activity (*e.g.* dequalinium, [151] Szeto-Schiller peptides [158]), many of them are used as targeting structures to bring reactive compounds to the mitochondria (reviewed in Ref. [11, 16, 123, 169]). A diverse set of cargos has been conjugated to TPP. [170] A straightforward conjugation chemistry as well as good stability and low reactivity towards cellular components render TPP an attractive choice. However, the balance of charge and lipophilicity of the TPP-cargo conjugate should be maintained so that cellular uptake and distribution to the mitochondria are still guaranteed (Section 3.2.2). [11, 123] Attachment to mitochondriotropic peptides or an MTS sequence are a further possibility to achieve biocompatible mitochondrial targeting. The former present a versatile tool to access a wide array of possible cargos. [171] For large and non-penetrating cargos the use of drug carrier vesicles has been suggested. [172] Transport of these vesicles to the mitochondria is aimed at by the decoration with small molecular mitochondriotropics, such as TPP⁺, or short peptides. A few examples are TPP⁺-decorated liposomes (MITO-Porter) [173] or dequalinium-modified liposomes (DQAsomes), [174] iron oxide nanoparticles (Mito-CIO, SPION) [175–177] or dendrimers. [178] In most cases, evidence for the mitochondrial delivery of the fluorescent model cargo has been provided by a colocalizing fluorescent signal with a mitochondriotropic dye. [123] Still, in future studies it should be critically evaluated if the vesicles are able to pass lipid bilayer membranes and reach the matrix or if they are only associated to the mitochondrial membrane or degraded beforehand. Figure 14 gives an overview of different classes of mitochondria-localizing probes and their application for mitochondrial targeting.

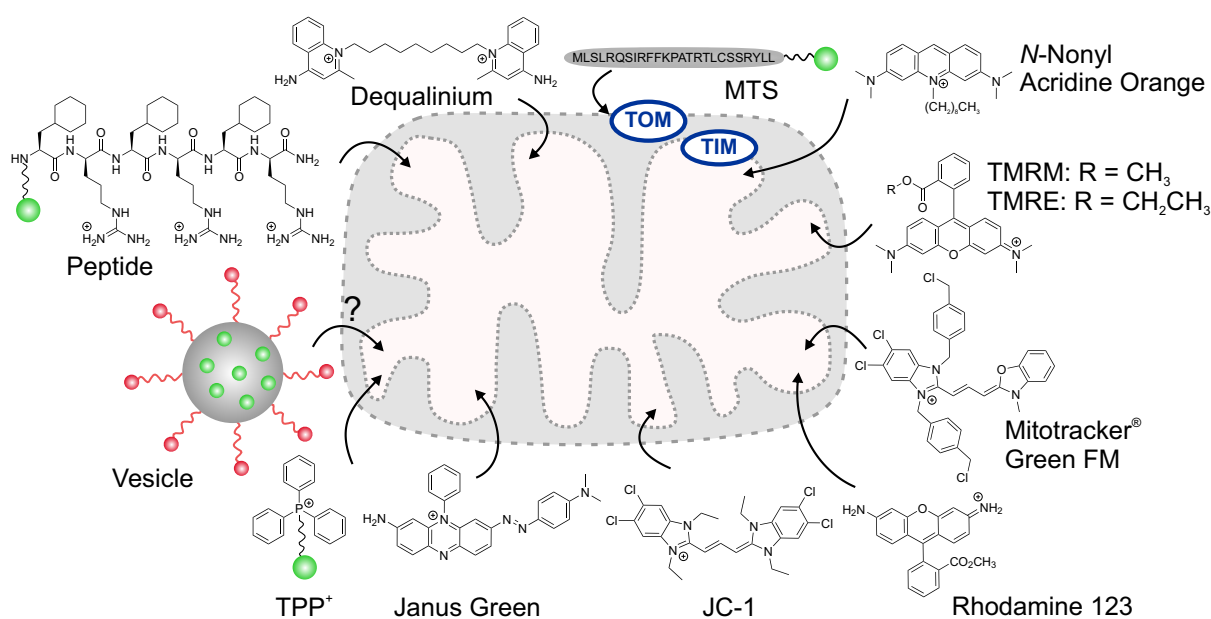


Figure 14: Mitochondria-localizing probes. Small molecular compounds (such as TPP⁺, dequalinium and fluorescent dyes) and peptides (such as mitochondria-penetrating peptides) accumulate in the mitochondria. Proteins with MTS use the mitochondrial import machinery (TOM/TIM) to access the matrix. Drug delivery strategies (cargo in green) comprise *e.g.* TPP⁺, peptides, MTS and vesicles decorated with mitochondriotropics (in red).

3.3 Intramitochondrial reactions

Research on the topic of mitochondriotropic probes is driven by the desire to gain information on mitochondrial processes. The identification of mitochondrial pathomechanisms is a crucial step in the design of selective and specific drug molecules which can intervene with abnormal processes. Because many of such drugs lack mitochondriotropism, they often rely on mitochondrial drug delivery systems (Section 3.2.3). Drug targets include mtDNA and mitochondrial proteins whereas sensors are used to measure reactive oxygen species and metal ion concentrations. [16] Each intervention, regardless if detection or pharmacological treatment is aimed for, is based on an intramitochondrial reaction either with an endogenous reaction partner or, as recently introduced, between two exogenous compounds.

3.3.1 Reactions with an endogenous reaction partner

Many of the reaction mechanisms for pharmacological modulation of mtDNA and mitochondrial proteins are not unique to the mitochondria but were reported in the cytoplasm and other cellular compartments. Selectivity is therefore achieved by the conjunction of the active compound with a mitochondriotropic which is accumulated depending on $\Delta\Psi_m$ (Section 3.2.2). For instance, alkylation (chlorambucil: mtCbl [179]), topoisomerase II inhibition (doxorubicin: mtDox [180]) and crosslinking (cisplatin: mtPt [181, 182]) of mtDNA have been reported. Furthermore, a more precise DNA modulation was realized with restriction enzymes. [183–185] Manipulation of mitochondrial proteins was accomplished following the detection of specific in-

hibitors that intervene in processes such as mitochondrial translation and transcription as well as protein folding. [186–188]

A broad area of mitochondrial research focuses on ROS which are tightly linked to mitochondrial dysfunction and a great number of diseases. [189] ROS are byproducts of normal respiration when O_2 is incompletely reduced during OXPHOS. [113] Starting from the superoxide anion ($O_2^{\bullet-}$), other ROS such as hydrogen peroxide (H_2O_2), hydroxyl radical ($\bullet OH$) and peroxynitrite ($OONO^-$) are generated. The predominant principle of ROS detection relies on a redox-based off- to on-switch of a fluorescent signal which is triggered selectively by a particular ROS species (reviewed in Ref. [123]). Conversely, the destruction of a Cy5 fluorophore upon oxidation by $OONO^-$ has been reported. The subsequent collapse of FRET from a Cy3-Cy5 conjugate (PnCy3Cy5) upon Cy5 oxidation was monitored by CLSM. [190] An example for ROS detection by a nonredox reaction is given by Hu and colleagues. [191] Their probe consists of a tetrafluorofluorescein derivative whose fluorescence is quenched because of the formation of a lactone ring stabilized by trifluoromethanesulfonate groups. Upon nucleophilic attack of the superoxide anion radical, the trifluoromethanesulfonate groups are cleaved to yield free phenol which recovers the fluorescent form of the tetrafluorofluorescein derivative.

In order to prevent ROS induced damage, ROS scavenging therapies with antioxidants such as dimethyltyrosine [159] and ubiquinone (MitoQ) [192] have been proposed. On the contrary, a selective induction of ROS in cancer cells has been reported to effectively induce cell death. [193] Mitochondrial metal concentrations also serve as indicators of mitochondrial health. [16] Their selective determination is often based on redox reactions or the formation of ligation complexes coupled to a fluorescent readout. A comprehensive overview of mitochondrial therapeutics comprising antioxidative, antiproliferative and antitumoral activities is provided in recent reviews. [12, 16, 123, 169]

3.3.2 Reactions between two exogenous reaction partners

Only recently, the great potential of mitochondria as selective reaction chambers for exogenously introduced reaction partners has been recognized. Once more, selectivity is reached through the high accumulation of mitochondriotropic building blocks in the mitochondrial matrix in dependence of $\Delta\Psi_m$. A several-hundred-fold higher concentration inside the mitochondria compared to the external and cytoplasmic levels of the building blocks thus greatly enhances reaction kinetics.

A prerequisite for such an intramitochondrial reaction is a reaction mechanism which proceeds at intraorganellar pH and salt concentrations and is independent of other reaction partners. Furthermore, the reactants should be inert towards biomolecules. These requirements are fulfilled by the strain-promoted azide-alkyne cycloaddition (SPAAC), a commonly applied bioorthogonal reaction. [194–198] In this [3+2]-dipolar cycloaddition, a 1,3-dipole (azide) reacts with a dipolarophile (strained alkyne) to form a stable and aromatic 1,2,3-triazole (Fig. 15). [199] The strain of the latter reaction partner results from the incorporation of the alkyne

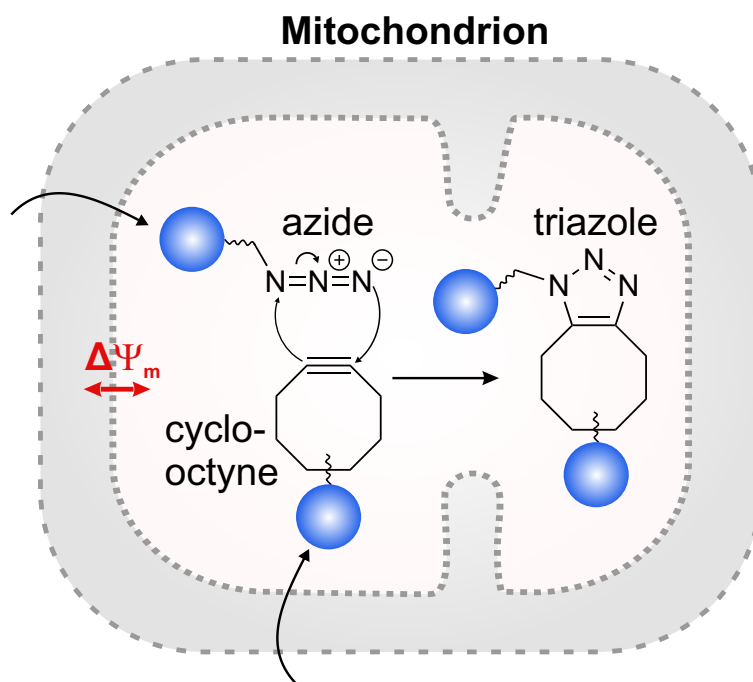


Figure 15: The strain-promoted azide-alkyne cycloaddition proceeds in a concerted fashion. Exploitation of mitochondria as reaction chambers is achieved by covalently attaching the reactive moieties to mitochondriotropic compounds (in blue) such as TPP which convey selective enrichment in dependence of $\Delta\Psi_m$ as described by the Nernst equation (Eq. 3.2). [122]

in a ring. This leads to massive bond angle deformations of the sp-hybridized carbon atoms (163° instead of 180°). [200] The enthalpic release of ring strain is thus energetically favorable leading to high reactivity without the requirement for catalysts. This is in contrast to the Huisgen [3+2]-cycloaddition, [201] which proceeds at elevated temperatures, or the Cu(I)-catalyzed click reaction. [202, 203] Due to the similarity of the reactive groups (azide and alkyne) between the Cu(I)-catalyzed click reaction and the SPAAC reaction, the SPAAC reaction is referred to as a copper-free click reaction.

In 2016, Logan and coworkers were the first to apply the SPAAC reaction for the assembly of a new compound in the mitochondrial matrix. [122] For this, they exploited the selective enrichment of their mitochondriotropic building blocks, a TPP⁺-conjugated azide and a TPP⁺-conjugated cyclooctyne (Fig. 15). The reaction rate of the intramitochondrial SPAAC reaction, and hence amount of product formation in a given time, corresponded to the extent of mitochondrial accumulation in response to $\Delta\Psi_m$. To quantify the intramitochondrial reaction progression, the product was isolated from the mitochondria and quantified by liquid chromatography mass spectrometry (LC-MS). By comparing the detected amounts of product, the authors were able to determine small changes in $\Delta\Psi_m$. Of note, the uptake and thus reaction rate of TPP⁺-azide and TPP⁺-cyclooctyne were also affected by $\Delta\Psi_p$. Changes in the reaction rate were therefore linked to both membrane potentials, $\Delta\Psi_m$ and $\Delta\Psi_p$, whose relative contributions could not be disentangled. The applicability of this approach for determination of changes in $\Delta\Psi_m$ and $\Delta\Psi_p$ was demonstrated for *in organello*, *in vitro* and *in vivo*

measurements.

Since its initial report as a sensor for changes in the plasma and mitochondrial membrane potentials, the intramitochondrial SPAAC reaction was advanced to unambiguously detect mitochondrial matrix localization. [204,205] The concept was demonstrated for an azide-modified peptide nucleic acid probe which was directed to the mitochondria by an MTS peptide. Inside the mitochondrial matrix, the probe reacted with TPP⁺-cyclooctyne. Upon isolation from mitochondria and analysis by LC-MS, the detection of product revealed that the probe had reached the mitochondrial matrix. Furthermore, the successful removal of the MTS by cleavage activity of the mitochondrial processing peptidase could be shown by this approach.

Next to the intramitochondrial SPAAC reaction, a metal-catalyzed mechanism for the reaction of two exogenous compounds inside the mitochondria has been reported in 2016 as well. Tomas-Gamasa and coworkers introduced a ruthenium complex into cells. [206] For selective mitochondrial enrichment of the Ru-complex, a TPP⁺-containing ligand was employed. Inside the mitochondria, the catalytic activity of the Ru-complex was utilized to uncage a second mitochondriotropic probe by a π -allyl-mediated mechanism. This probe was a quenched rhodamine dye which regained its fluorescence properties after cleavage of two allylcarbamate groups by Ru. These residues served as protective groups for two aromatic amines and stabilized the nonfluorescent form of the rhodamine derivative. The reaction could thus be followed by means of an increase in the fluorescence signal.

4 Results and discussion

In order to carry out and monitor a bioorthogonal covalent reaction in the mitochondria of living cells, small molecular fluorescent compounds were required that could transport reactive groups to mitochondria and simultaneously serve as imaging reporters.¹

4.1 Mitochondriotropism of Cy dyes

Cationic cyanine dyes are fluorescent small molecules that contain structural elements commonly found in mitochondriotropics (Section 3.2.3). [114, 208, 209] However, cyanine dyes had never been systemically evaluated for their mitochondriotropism. As introduced in Section 3.2, mitochondriotropic properties include a delocalized positive net charge, an overall lipophilic character, and a certain proportion of aromaticity. [132] Cyanine dyes are composed of two terminal heterocyclic nitrogen groups which are linked by a polymethine chain. [71] The polymethine chain consistently contains an odd number of carbon atoms. This allows for resonance stabilization of the positive charge between the two nitrogen atoms across the polymethine bridge. Different subclasses are distinguished by the incorporated heterocycles such as indoles, quinolines, benzoxazoles or benzothiazoles (Fig. 16).

This project focused on indocarbocyanines and their derivatives, which are widely used in life sciences and for which the term Cy dye was introduced. [210] The nomenclature of Cy dyes denotes the number of carbon atoms in the polymethine chain. For instance, Cy3 and Cy5 derivatives contain three ($n = 1$) and five ($n = 2$) carbon atoms, respectively. Cy dyes have several positions to which reactive groups can be attached. These positions include the indoline nitrogen atom, the polymethine chain or the benzene ring of indoline.

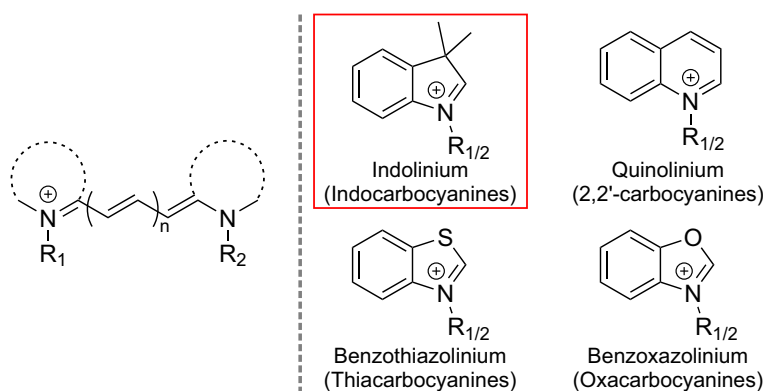


Figure 16: General chemical structure of cyanine dyes (left) and different classes of cyanines (right). R_1 and R_2 denote sites of alkylic substituents. Symmetrical ($R_1 = R_2$) and unsymmetrical ($R_1 \neq R_2$) substitutions are distinguished.

In order to determine if Cy dyes were unexceptionally mitochondriotropic, a series of lipophilic Cy dyes with Cy3 and Cy5 scaffolds, derivatized with small functional groups at

¹Results of this Part are partially published in Ref. [207]. Permission for reproduction has been granted by John Wiley & Sons.

different positions, [211] were tested in a cell culture experiment (Appendix 2). To this end, rat brain endothelial (RBE4) cells were co-incubated with a Cy dye and the mitochondria-localizing dye MitoTracker Green FM. The cells were then imaged on a confocal microscope.² A high colocalization with MitoTracker was observed for all derivatives. An example for the colocalization of a Cy3 and Cy5 dye with MitoTracker is given in Figure 17. Here, a mixed color (*i.e.* yellow and white) upon superimposition of the single channel images indicates colocalization.

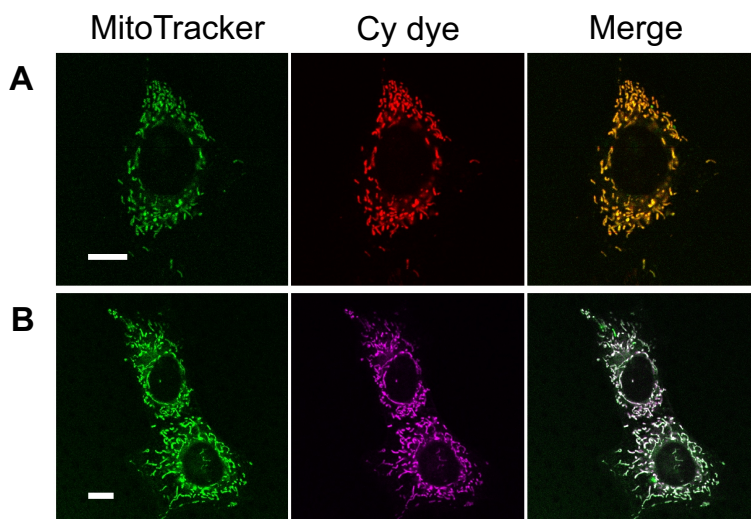


Figure 17: Confocal images for co-incubation of RBE4 cells with Cy3 dye (A) or Cy5 dye (B) with MitoTracker Green FM. Incubation with the Cy dyes (500 nM) lasted for four hours. MitoTracker Green FM (150 nM) was added 30 min prior to imaging. Experiment was performed on the Leica TCS SP5 confocal microscope. MitoTracker channel: $\lambda_{\text{exc}} = 488$ nm and $\lambda_{\text{em}} = 500 - 540$ nm. Cy3 channel: $\lambda_{\text{exc}} = 561$ nm and $\lambda_{\text{em}} = 570 - 620$ nm. Cy5 channel: $\lambda_{\text{exc}} = 633$ nm and $\lambda_{\text{em}} = 650 - 700$ nm. The chemical structures of *N*-pentynyl Cy3 and Cy5 propyl azide can be found in Appendix 2. Merged images indicate colocalization. Scale bar: 10 μm

To support the visual analysis of colocalizing pixels the quantitative correlation methods of Pearson and Manders were applied. [59, 212] Both methods rely on a correlation of the pixel intensity values in the two investigated channels. Pearson's coefficient yields a measure for the strength of linearity between corresponding pixels in both channels (see Methods 5.2.6). In contrast to Pearson's, Manders' analysis excludes average intensity values in its mathematical expression and delivers separate colocalization coefficients for each channel. [59] In both cases, coefficients close to a value of 1 indicate high correlation (*i.e.* a high percentage of colocalizing pixels) between the signals of the two channels. The series of tested Cy dyes revealed high coefficient values (Appendix 2).

It should be stressed that the tested dyes complied with the general structure in Figure 16 and did not contain any sulfonic acid groups. The attachment of two or more sulfonic acid groups to the indoline moiety, however, is a common practice to increase the water solubility of the dyes and can be found in numerous commercially available Cy dye derivatives. [213] The presence of these sulfonic acid groups shields the positive charge of the Cy dyes and conveys

²Colocalization data in Appendix 2 were acquired and analyzed by Dr. Markus Hirsch.

an overall negative charge. Hence, mitochondrial staining as prevalent for cationic Cy dye derivatives could not be observed as exemplary tested for sulfonated Cy5 (Appendix 3).

In conclusion, the systemic investigation of cationic Cy dyes with Cy3 and Cy5 scaffolds revealed their inherent mitochondriotropic properties which were unaffected by the attachment of a small reactive moiety (in this case a terminal alkyne or azide) and the site of this modification. The mitochondriotropism of Cy3 and Cy5 dyes was additionally reported by another group during the work on this project. [190] Thus, it was concluded that Cy dyes were promising candidates to transport reactive groups into the mitochondria in order to perform an *in organello* reaction.

4.2 Copper-free click reaction of Cy dyes

After the Cy dyes were found suitable to lead reactive groups to the mitochondria, a corresponding reaction mechanism had to be found and tested.

4.2.1 Strain-promoted azide-alkyne cycloaddition as a suitable reaction mechanism

Covalent reaction of two Cy dyes inside the mitochondria relies on a reaction mechanism that is compatible with physiological conditions and does not require auxiliary reagents. The SPAAC reaction meets these requirements (Section 3.3.2). The reactive groups that take part in this cycloaddition are an azide and a strained alkyne. The electronic and steric properties of the molecules that incorporate these reactive moieties critically influence the reactivity of the reaction partners. For instance, in comparison to unsubstituted cyclooctyne the aza-dibenzoannulated cyclooctyne (DBCO) exhibits an increased ring strain leading to enhanced reaction kinetics. [200]

In this work, two SPAAC reaction pairs were investigated (Fig. 18). The first reaction pair consisted of a DBCO-functionalized Cy3 dye (Cy3-DBCO) and an azide-modified Cy5 chromophore (Cy5-azide). For the second reaction pair, the functionalities were switched between the Cy3 and Cy5 dye, yielding the reactive fluorophores Cy3-azide and Cy5-DBCO.³ In all cases, the reactive groups were attached to one of the indolinic nitrogen atoms *via* a linker. They were thus spatially separated from the chromophoric parts of the molecules and did not interfere with their spectroscopic properties (Section 4.2.3). As the building blocks were unsymmetrically substituted, the SPAAC reaction was expected to yield a mixture of two regioisomeric triazoles. In general, regioselectivity is determined by the steric and electronic properties of the reactants. [214] In this work, the regioisomers were not distinguished and compositely referred to as SPAAC product **1** or **2** depending on their precursor molecules (Fig. 18).

³DBCO-functionalized Cy3 dye was synthesized by Dr. Stefka Kaloyanova. Cy3-azide, Cy5-azide and Cy5-DBCO were commercially available.

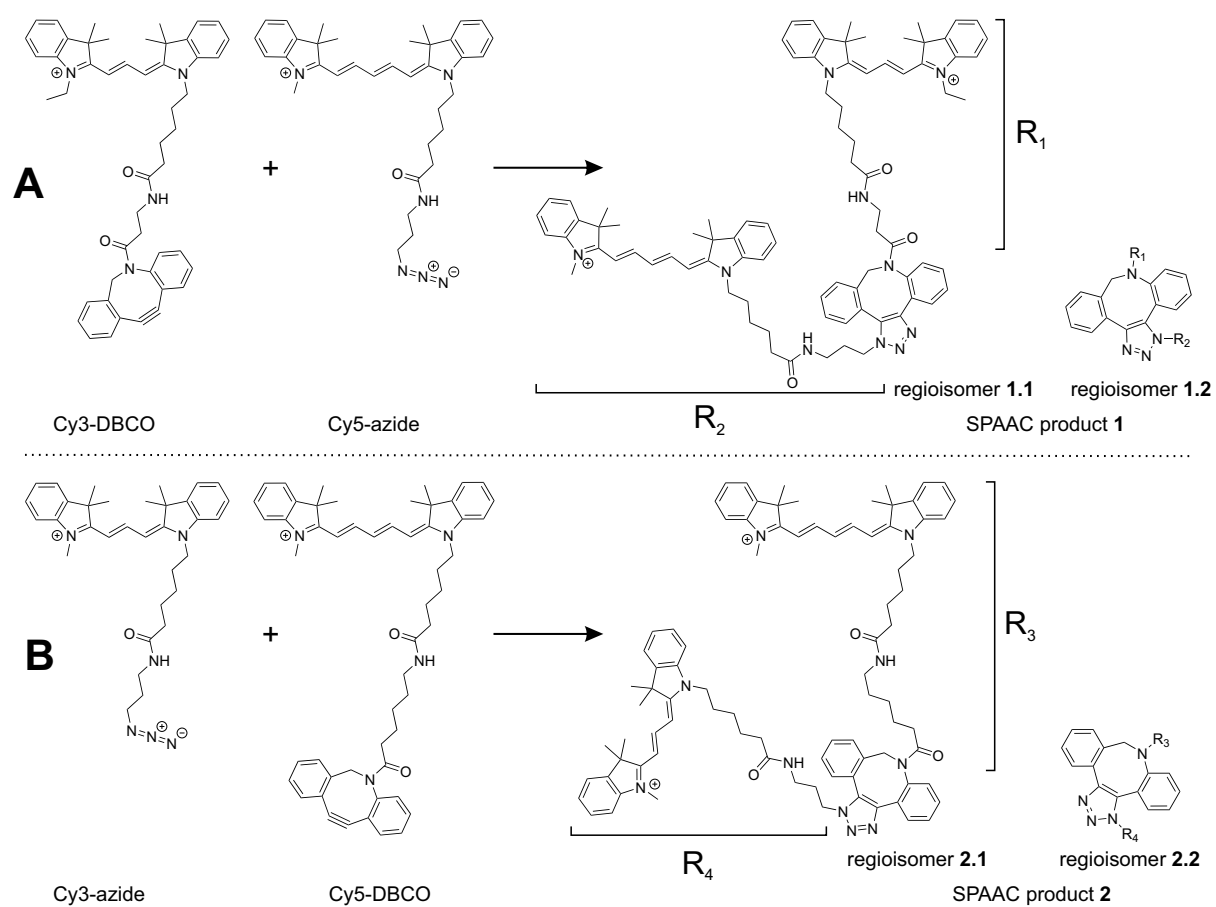


Figure 18: SPAAC reaction of reaction pair 1 consisting of Cy3-DBCO and Cy5-azide (A) and reaction pair 2 consisting of Cy3-azide and Cy5-DBCO (B). The full chemical names of SPAAC product 1 and 2 are given in Appendix 4.

4.2.2 Chromatographic analysis of SPAAC

In order to prove the successful coupling of the reaction partners, the individual Cy dyes as well as the corresponding reaction mixture were analyzed by reversed phase high performance liquid chromatography (RP-HPLC). The instrument was coupled to an absorbance detector (diode array detector) and an electrospray ionization mass spectrometry (ESI-MS) detector (Methods 5.2.9). In order to keep the reaction conditions close to physiological salt concentration and pH value, measurements were performed in phosphate-buffered saline (PBS), pH 7.4. The non-sulfonated Cy dyes, however, showed poor water solubility and could not be completely dissolved in pure PBS (Section 4.1). Therefore, in a preliminary solubilization experiment with Cy3-DBCO, the organic solvent dimethyl sulfoxide (DMSO) was added step by step. At a volume fraction of 40% DMSO, Cy3-DBCO (at 200 μ M concentration) was completely dissolved. In all subsequent experiments, the four Cy dyes were dissolved and applied in PBS substituted with 40% DMSO, unless otherwise indicated. Although injected as a solution from the solvents mentioned above, different eluent compositions occurred during RP-HPLC separation (Methods 5.2.9).

Figure 19 shows the RP-HPLC analysis of Cy3-DBCO and Cy5-azide. Cy3-DBCO eluted with a retention time of 5.7 min and was identified by its signal in the absorbance trace at 542 nm and its m/z of 729.4 ($[M]^+$, calcd. 729.42). Cy5-azide was identified with an m/z of 565.4 ($[M]^+$, calcd. 565.36) at a retention time of 3.6 min, as also apparent by the signal in the absorbance trace at 632 nm. The reaction of Cy3-DBCO and Cy5-azide and subsequent RP-HPLC analysis confirmed the formation of the dicationic SPAAC product **1** with a signal at m/z 647.4 ($[M]^{2+}$, calcd. 647.39, retention time 6.8 min). The elution of SPAAC product **1** was furthermore registered by a signal in both absorbance traces (542 nm and 632 nm) indicative for the co-presence of a Cy3 and Cy5 fluorophore. Of note, upon SPAAC reaction unknown Cy3 and Cy5 side products were detected. These side products were assumed to be responsible for the incomplete turnover of starting material, apparent by the remaining Cy5-azide peak in the reaction mixture.

A chromatographic analysis of Cy3-azide and Cy5-DBCO and their reaction mixture can be found in Appendix 5.

4.2.3 Spectroscopic properties of Cy dyes

The spectroscopic properties of Cy dyes render them accessible to a wide range of fluorescence-based methods. In Figure 20A, the excitation and emission spectra of Cy3-DBCO and Cy5-azide are displayed. The spectral overlap of Cy3-DBCO and Cy5-azide dyes enabled FRET as demonstrated by the spectroscopic analysis of isolated SPAAC product **1** (Fig. 20B). Here, excitation at 488 nm led to near-complete quenching of the donor emission and high acceptor emission with a maximum at 667 nm.

The detection of mitochondrial FRET from a Cy3-Cy5 conjugate by confocal microscopy was recently demonstrated by Jia and coworkers. [190] The authors measured the decrease in FRET

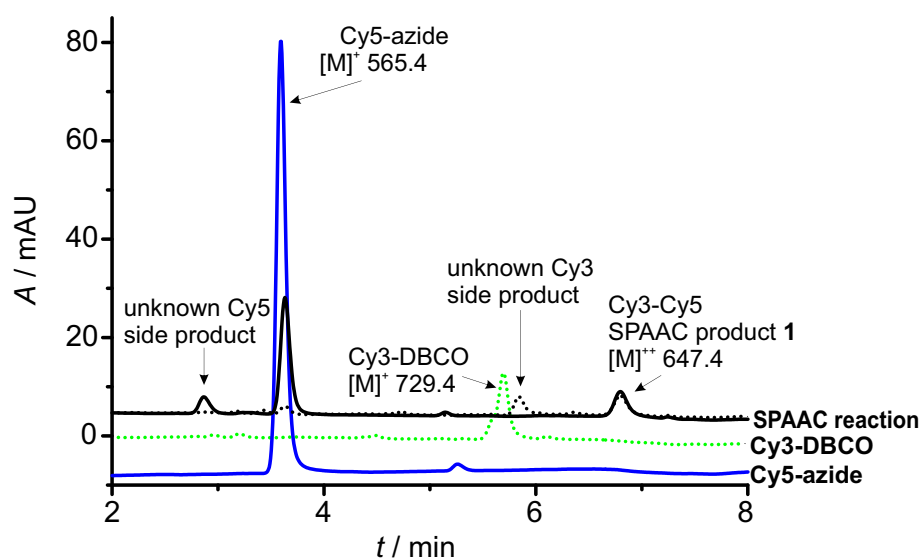


Figure 19: HPLC analysis of Cy3-DBCO (green), Cy5-azide (blue) and the reaction mixture (black) for which Cy3-DBCO and Cy5-azide (final concentration $10 \mu\text{M}$) were reacted in PBS, 40% DMSO at room temperature for 36 hours. Solid and dotted lines represent absorbance detection at 632 nm and 542 nm, respectively. Coupling to ESI-MS allowed the assignment of peaks to Cy5-azide, Cy3-DBCO and SPAAC product 1.

signal indicative of an oxidative destruction of Cy5 in the presence of a specific ROS. Contrary to that study, the present work relied on the appearance of FRET resulting from successful coupling of a Cy3 and Cy5 dye by copper-free click reaction rather than its destruction.

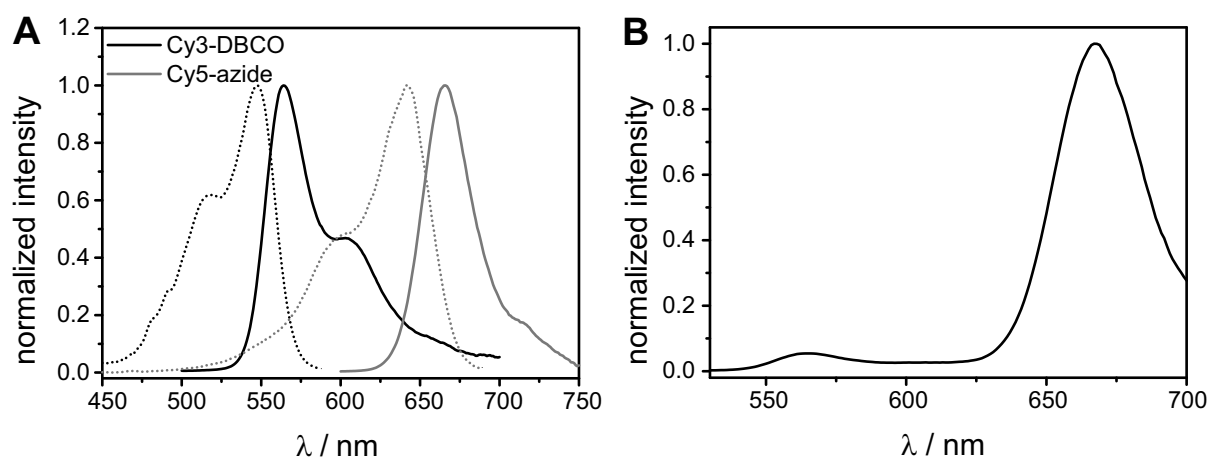


Figure 20: A) Excitation (dotted lines) and emission (solid lines) spectra of Cy3-DBCO and Cy5-azide in PBS containing 40% DMSO. The maxima of excitation and emission were $\lambda_{\text{exc}}^{\text{max}} = 547 \text{ nm}$ and $\lambda_{\text{em}}^{\text{max}} = 564 \text{ nm}$ for Cy3 and $\lambda_{\text{exc}}^{\text{max}} = 641 \text{ nm}$ and $\lambda_{\text{em}}^{\text{max}} = 666 \text{ nm}$ for Cy5. These values are in accordance with the literature. [71] B) Emission spectrum of SPAAC product 1 at $\lambda_{\text{exc}} = 488 \text{ nm}$. The SPAAC product 1 had been isolated following RP-HPLC separation.

4.2.4 Reaction kinetics of SPAAC reaction pairs

In order to determine the reaction kinetics of Cy3-DBCO and Cy5-azide, the decrease in donor emission caused by FRET upon formation of SPAAC product **1** was monitored (Fig. 21). The reactants were mixed in PBS / 40% DMSO either at a high concentration of 10 μ M or at a lower concentration of 250 nM and incubated at 37°C. For the 10 μ M concentration, a 55% decrease in donor emission, followed by saturation, was observed within the first hour. A further decrease in donor emission was not detected. The saturation presumably marked the point where Cy3-DBCO had been mostly used up. Based on the previous analysis as shown in Figure 19, it seemed likely that unreactive Cy3 side products were still present in the reaction mixture and prevented quenched levels of donor emission as observed for the isolated product in Figure 20B. At a concentration of 250 nM, no appreciable decrease occurred within the time frame of twelve hours. Solely, an initial small drop in donor emission was observed. A possible cause for this drop was the adaption of the temperature of the reaction mixture to the measurement conditions of 37°C after initialization of the reaction. The lack of a substantial decrease in donor emission was important as a 250 nM concentration of reaction partners was to be utilized for the incubation of cells (Section 4.3). Thus, the detection of an appreciable FRET signal in the mitochondria was to be indicative for an increased reaction rate due to the accumulation of reactants (concentration \gg 250 nM) inside the mitochondrial matrix.

The spectroscopic details of the second reaction pair, Cy3-azide and Cy5-DBCO, and its reaction kinetics monitored by fluorimetric analysis were likewise obtained and are depicted in Appendix 5.

4.3 *In organello* copper-free click reaction of Cy dyes

In Section 4.2, the reactivity of the two Cy dye reaction pairs in buffer was demonstrated. It was shown that reaction kinetics could be successfully monitored by taking advantage of FRET occurring between a Cy3 donor and Cy5 acceptor. Next, the reactive Cy dyes were tested for mitochondrial accumulation in cultured RBE4 cells - first by individual incubation and then in combination with their respective reaction partners.

4.3.1 Mitochondrial accumulation of Cy dye reaction partners

The inherent mitochondriotropism of Cy dyes was demonstrated in Section 4.1. However, the colocalization study (Appendix 2) did not comprise the four SPAAC reactive Cy dyes (Cy3-DBCO, Cy5-azide, Cy3-azide and Cy5-DBCO). Their intracellular distribution needed to be closely examined prior to their synchronous administration. Therefore, RBE4 cells were treated with either Cy3-DBCO or Cy5-azide separately and imaged on a Zeiss LSM 880 confocal microscope (Section 2.2 and Methods 5.2.7).

The extent of accumulation of the Cy dyes was expected to be driven by the plasma membrane potential $\Delta\Psi_p$ (30 - 60 mV) and the inner mitochondrial membrane potential $\Delta\Psi_m$ (\approx 140 mV) which attract positively charged molecules first into the cytoplasm and with even greater

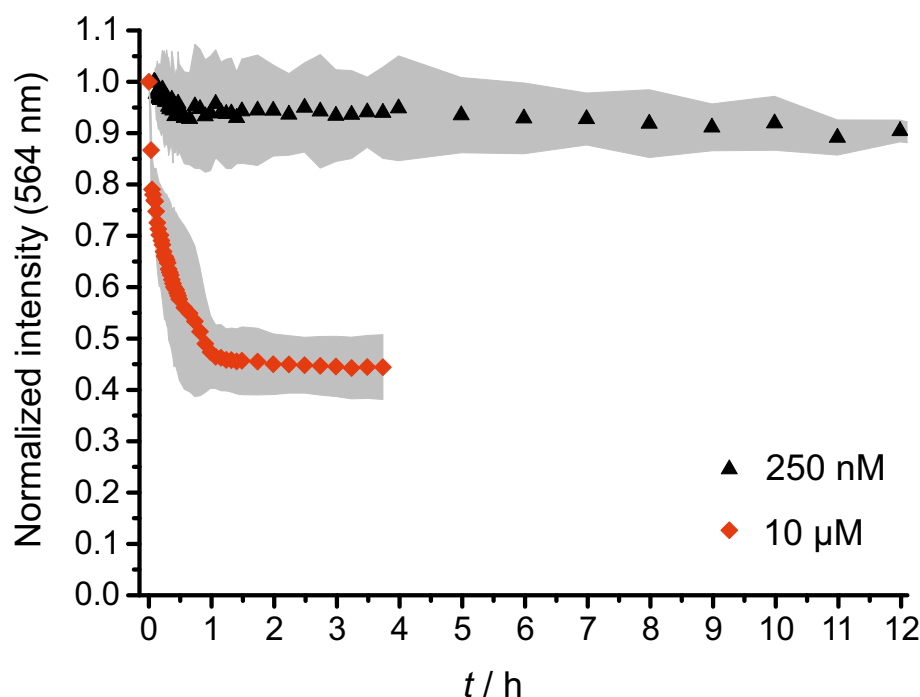


Figure 21: Kinetics of Cy3-DBCO and Cy5-azide reaction. Reactants were mixed at high (10 μM , red diamonds) and low (250 nM, black triangles) concentration. Donor emission at 564 nm upon $\lambda_{\text{exc}} = 488$ nm was normalized to the intensity at the starting concentration and plotted as mean \pm SD (in gray) of three independent experiments. PMT detector gain was adapted for high and low concentrations.

driving force towards the mitochondrial matrix (Section 3.2.2). [139] At first, it was therefore determined which concentration of the dyes had to be added to the extracellular medium in order to achieve an efficient signal readout, *e.g.* intensity per pixel, of stained mitochondria. The tested concentration series comprised three orders of magnitude and ranged from 12.5 nM to 1 μM . Best results were obtained with a concentration of 250 nM where high mitochondrial specificity was combined with a good signal detection. At concentrations higher than 250 nM a diffusive cytosolic fluorescence became apparent in addition to the mitochondrial staining. In subsequent experiments, Cy dyes were therefore added to the cell culture medium in a 250 nM concentration (Fig. 22). It was furthermore observed that mitochondrial fluorescence intensity reached steady-state levels after about two hours of incubation. Thus, abiding by this time regime ensured that an equilibrium between extracellular, cytoplasmic and mitochondrial dye concentration had been reached.

The fluorescence intensity of mitochondria differed among individual cells. This observation was in good agreement with several reports on mitochondrial heterogeneity. [114, 215–218] A heterogeneous distribution has been reported for mitochondrial morphologies as well as dynamics such as $\Delta\Psi_{\text{m}}$. It was hence suggested that such heterogeneity would have led to varying enrichment factors of the mitochondriotropic Cy dyes (Fig. 22A,B). The dependence of mitochondrial accumulation on $\Delta\Psi_{\text{m}}$ was probed by the addition of a respiratory uncoupler. Carbonyl cyanide *p*-trifluoromethoxyphenylhydrazone (FCCP) causes depolarization by uncoupling

OXPHOS through an increased proton flux across the membrane. [121, 219] Co-incubation of Cy3-DBCO or Cy5-azide with 5 μM FCCP led to a loss of fluorescent signal and thus confirmed that the extent of mitochondrial uptake depended on $\Delta\Psi_m$ (Fig. 22C,D).

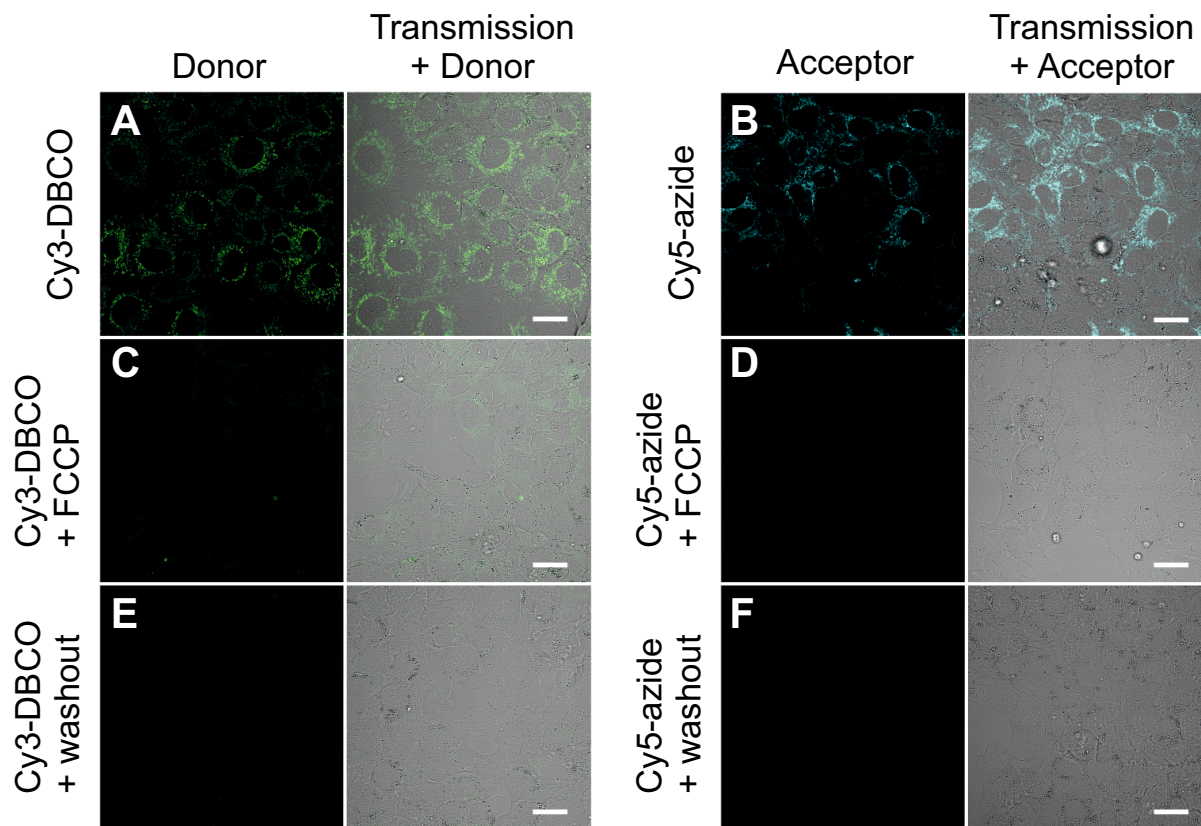


Figure 22: Confocal images for incubation with the single dyes Cy3-DBCO (A,C,E) or Cy5-azide (B,D,F). RBE4 cells were incubated with the dyes (final concentration 250 nM) for two hours. Co-treatment with FCCP (5 μM) (C,D) led to dissipation of $\Delta\Psi_m$ and reduced the fluorescent signal. Performing two washing cycles (E,F) led to a loss of fluorescent signal. Cy3 channel: $\lambda_{\text{exc}} = 488$ nm and $\lambda_{\text{em}} = 544 - 598$ nm. Cy5 channel: $\lambda_{\text{exc}} = 633$ nm and $\lambda_{\text{em}} = 659 - 696$ nm. Scale bar: 25 μm .

As demonstrated above, abolition of $\Delta\Psi_m$ changed the accumulation ratio between cytoplasmic and mitochondrial dye concentration and therefore led to destaining of the mitochondria. It was postulated, however, that there was a possibility to alter mitochondrial dye concentration without influencing either membrane potential, $\Delta\Psi_p$ or $\Delta\Psi_m$. By modulation of dye concentration in one of the three compartments (extracellular medium, cytoplasm, mitochondria) the system was to be brought in disequilibrium (Section 3.2.2). In succession, the two unmodified concentrations were expected to adapt until reaching equilibrium again. Such an effect of re-equilibration was deliberately provoked by complete removal of extracellular dye. This was procured through washing of the cells with PBS and subsequent incubation in fresh dye-free cell medium. The extracellular medium comprised the by far largest volume of the three compartments. Its dye depletion was therefore expected to force an increased flux of Cy dyes by reversed membrane passage from the mitochondria through the cytoplasm out of the cells. Correspondingly, a time-dependent decrease in mitochondrial fluorescence was observed.

In order to reduce the fluorescence intensity to levels below signal detection, various washing schemes were tested. These schemes involved several washing steps with re-equilibration periods of 30 min or one hour in between. Best results, also with regard to time consumption and feasibility, were obtained by an alternation of two washing cycles with one-hour equilibration periods (Fig. 22E,F).

An equal set of experiments was performed with Cy3-azide and Cy5-DBCO (Appendix 6). In consistency with their counterparts, both dyes showed accumulation in polarized mitochondria. Upon depolarization by FCCP, mitochondrial levels of dye were greatly reduced, stressing the dependence of accumulation on $\Delta\Psi_m$. The washing process also led to a re-equilibration of the dye from the mitochondria into the extracellular environment and thus reduced the fluorescence signal.

These results confirmed that i) the staining of mitochondria by Cy dyes depended on the polarization state of the mitochondria ($\Delta\Psi_m$), (ii) the mitochondrial translocation of Cy dyes was reversible and (iii) the dynamics of mitochondrial enrichment and diffusion from mitochondria fell within a time frame of several hours and were therefore accessible by the here presented protocol.

4.3.2 Evaluation of spectral cross-talk

A careful evaluation of spectral cross-talk is important when performing FRET experiments. Cross-excitation of the acceptor (Cy5) dye as well as bleed-through from the donor (Cy3) dye would give false positive FRET signals and lead to a misinterpretation of results (Section 2.3). To avoid cross-excitation of Cy5, Cy3 was excited with the 488 nm line of the argon laser. This excitation wavelength differed from λ_{exc}^{max} of 547 nm. However, as apparent from the spectrum in Figure 20A, Cy3 was still efficiently excited at 488 nm. In contrast, Cy5 could not be excited at this wavelength. A falsification by bleed-through was circumvented by a red shift of the detection range. Consequently, at an excitation wavelength of 488 nm and a detection range of 659 to 696 nm no spectral cross-talk was detected in the FRET channel (Fig. 23). In line with these settings, Cy3 dyes were consistently excited at 488 nm, even for the single channel experiments in Sections 4.3 and 4.4.

4.3.3 Co-incubation of Cy3 donor and Cy5 acceptor dye

In the previous sections, the $\Delta\Psi_m$ -dependent accumulation has been demonstrated for all four reactive Cy dyes. To evaluate if they would be able to react after enrichment inside mitochondria, RBE4 cells were incubated with a 250 nM solution of Cy3-DBCO and Cy5-azide each. Figure 24A shows the detection of a mitochondria-localized FRET signal following a two-hour incubation period. Importantly, in cuvette reaction kinetics performed at this reactant concentration (Fig. 21) had not shown any detectable product formation (Section 4.2.4). This finding precluded a substantial formation of product in the extracellular medium. Hence, the detection of a mitochondrial FRET signal gave a first hint for the successful reaction in the

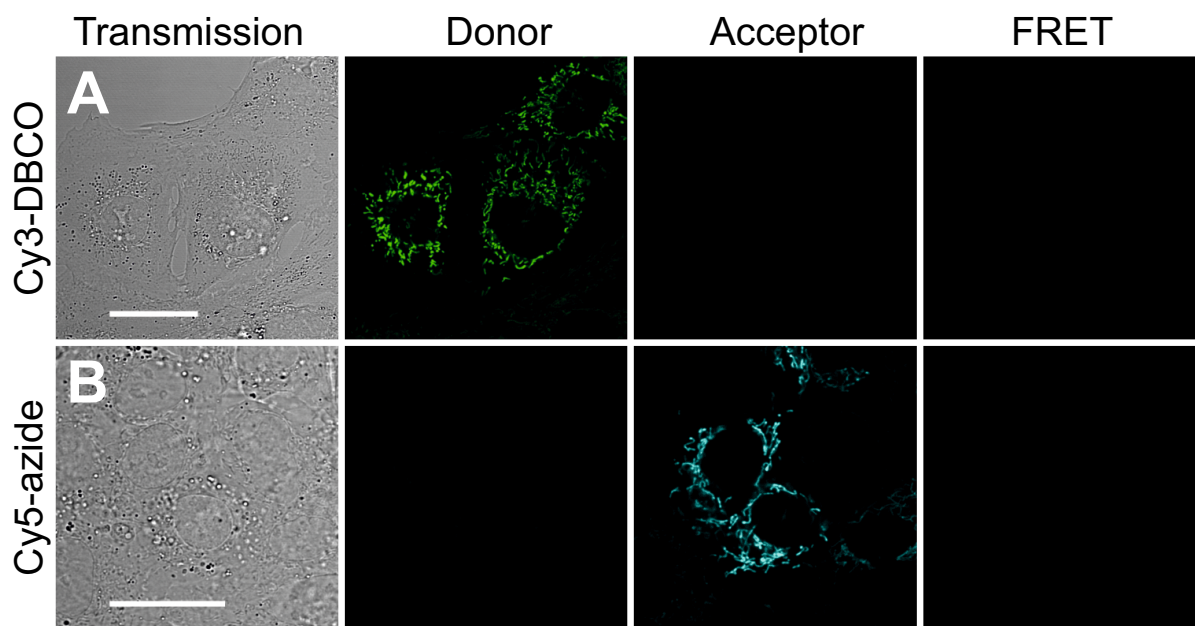


Figure 23: Evaluation of cross-talk for Cy3-DBCO (A) and Cy5-azide (B). Cells were treated for two hours at 250 nM dye concentration. Excitation at 488 nm with simultaneous detection from 544 - 598 nm (donor) and 659 - 696 nm (FRET). Acceptor channel recorded upon $\lambda_{\text{exc}} = 633$ nm and $\lambda_{\text{em}} = 659$ - 696 nm. Scale bar: 25 μm .

mitochondria. Nonetheless, confocal imaging *per se* does not permit to draw any definite conclusions about a covalent coupling of Cy3 and Cy5. An appropriate control reaction of two unreactive Cy dyes (Cy3-azide and Cy5-azide) with similar fluorescent properties was therefore conducted. Strikingly, a fluorescent signal in the FRET channel was again observed (Fig. 24B). In this case, however, it was not plausible that the FRET signal originated from a covalent product as the two dyes did not show any reactivity against each other. It was therefore assumed that FRET occurred due to the steric proximity of donor and acceptor as a result of increased mitochondrial concentrations of both dyes. In summary, co-incubation of cells with Cy3-DBCO and Cy5-azide led to the appearance of a mitochondrial FRET signal. A reliable conclusion about a successful SPAAC reaction could still not be drawn as the control experiment with Cy3-azide and Cy5-azide delivered a comparable result (Fig. 24).

4.3.4 Retention of the dicationic SPAAC product in mitochondria

In order to unambiguously distinguish between covalent product formation and mere mitochondrial enrichment of co-incubated Cy3 and Cy5 dyes, the incubation procedure was extended by an additional step. In Section 4.3.1, it was shown that monocationic Cy dyes were able to freely cross lipid bilayer membranes and equilibrate according to $\Delta\Psi_p$ and $\Delta\Psi_m$. In contrast, Ross *et al.* had reported that the membrane passage of dicationic lipophilic molecules strongly depended on the charge distribution in conjunction with the degree of lipophilicity. [140] An unfavorable charge to surface ratio was shown to greatly reduce the rate of membrane translocat-

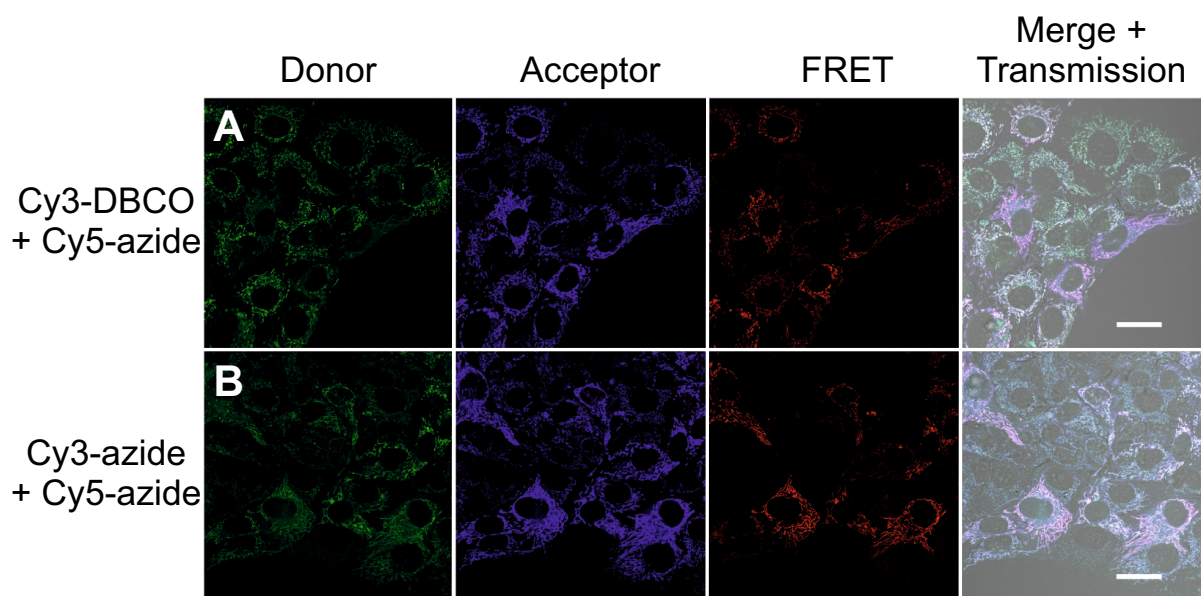


Figure 24: Co-incubation of RBE4 cells with a Cy3 donor and Cy5 acceptor at 250 nM concentration for two hours. A) Cy3-DBCO and Cy5-azide. B) Mock experiment with the unreactive dyes Cy3-azide and Cy5-azide. Donor (544 - 598 nm) and FRET (659 - 696 nm) channel were simultaneously recorded upon $\lambda_{\text{exc}} = 488$ nm. Acceptor (659 - 696 nm) channel was recorded upon $\lambda_{\text{exc}} = 633$ nm. Scale bar: 25 μm .

tion or even completely impede it (Section 3.2.2). To test whether this applied to the dicationic SPAAC product **1** and could be used for distinction, two washing steps were appended to the co-incubation of Cy3-DBCO and Cy5-azide (Fig. 25A). A mitochondrial FRET signal was still observed after washing. However, when the mock incubation of Cy3-azide and Cy5-azide was followed by washing, no appreciable fluorescence signal in any of the detection channels (donor, acceptor, FRET) prevailed (Fig. 25B). This indicated that the unreacted monocationic dyes in the mock incubation were driven out of the mitochondria in a fast equilibration process. The different outcome in the SPAAC reaction (Fig. 25A) pointed towards an altered membrane permeability as the result of a covalent product formation. SPAAC product **1** with its increased molecular size and two cationic charges was presumably unable to re-equilibrate in a similar time frame as the monocationic dyes upon the washing pulse. It was therefore concluded that the addition of washing steps enabled a clear identification of the proceedings of the covalent reaction (Fig. 26). The adapted protocol was applied for all subsequent experiments, unless otherwise indicated.

Further control incubations, firstly in the presence of a respiratory uncoupler and secondly with the preformed SPAAC product **1**, were performed. As apparent from Figure 25C, there was only a faint FRET signal when $\Delta\Psi_{\text{m}}$ was diminished by the addition of FCCP. In other words, depolarized mitochondria accumulated the starting material to a smaller extent. This then led to only small amounts of product **1** being formed in the mitochondria in the investigated time interval of two hours and therefore negligible FRET readout. In the second control reaction, treatment of RBE4 cells with the externally preformed product **1** did not result in detectable

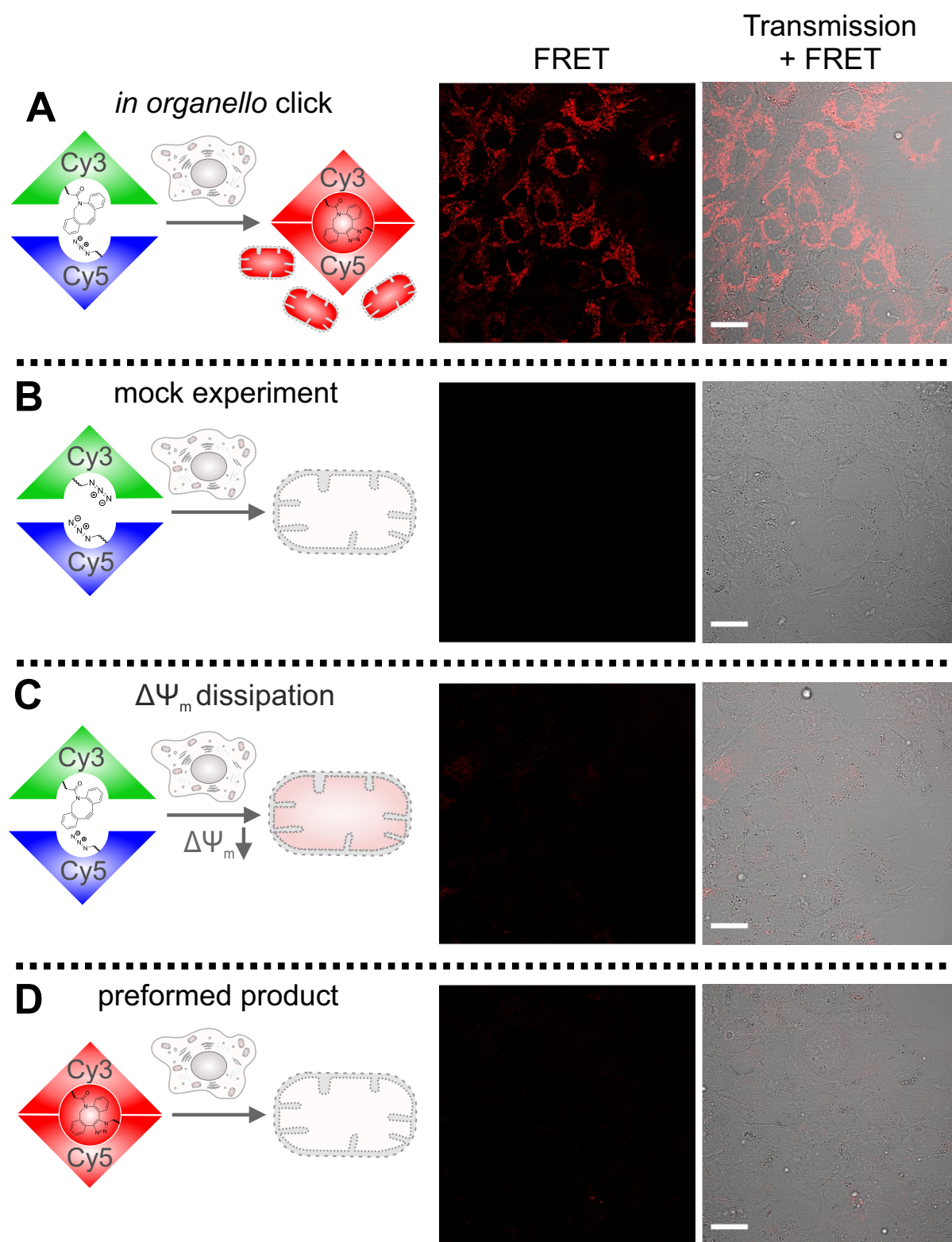


Figure 25: Confocal images for synchronous Cy3 and Cy5 incubation (250 nM each). Cells were treated for four hours followed by two washing cycles. FRET channel: Cy5 signal (659 - 696 nm) upon $\lambda_{exc} = 488$ nm. A) *In organello* SPAAC with Cy3-DBCO and Cy5-azide. B) Mock experiment with Cy3-azide and Cy5-azide. C) *In organello* SPAAC in the presence of 5 μ M FCCP. D) Preformed product **1** (250 nM). Scale bar: 25 μ m.

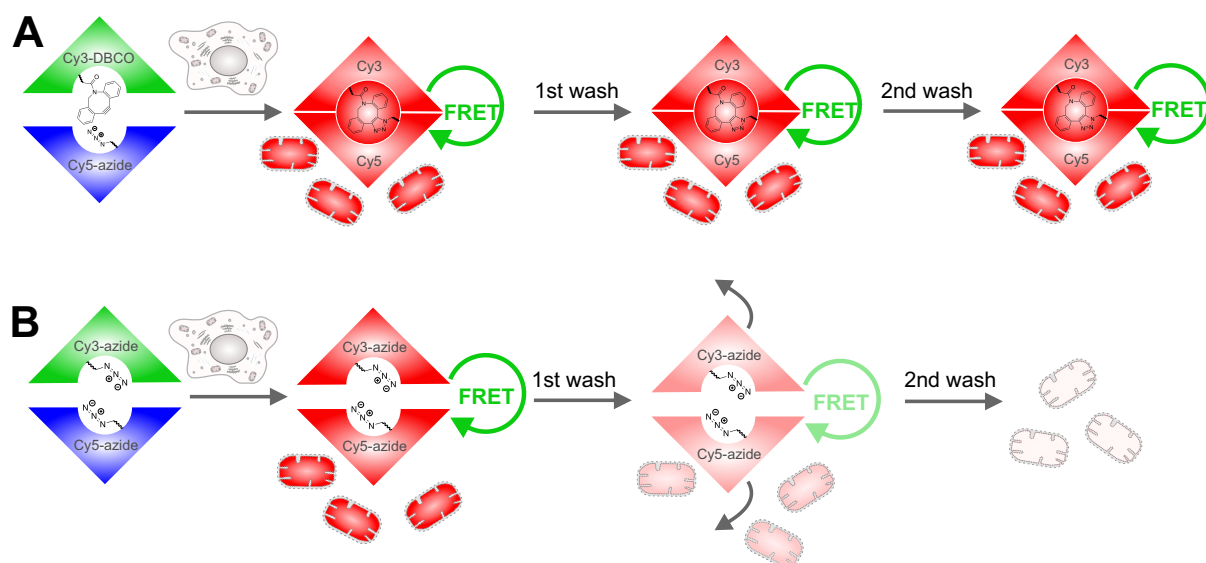


Figure 26: Scheme of the washing procedure to distinguish between a covalent SPAAC product formation (A) and a mere accumulation in the mitochondria resulting in a FRET signal due to the immediate vicinity of a Cy3 and Cy5 chromophore (B). Upon washing, the monocationic Cy3 and Cy5 dyes re-equilibrate across the mitochondrial and plasma membrane. This results in fainting of the FRET signal which becomes undetectable after a second washing step. In contrast, due to its altered membrane permeability, the SPAAC product is trapped in the mitochondria thus maintaining a high FRET signal (A).

levels of mitochondrial FRET signal (Fig. 25D). This observation supported the assumption of a low membrane permeability for the dicationic product **1**. In conclusion, SPAAC product **1** could not be efficiently imported into the mitochondria and, in its function as a mitochondrial stain, needed to be formed by an *in organello* reaction.

In order to support the individual confocal images from Figure 25 with a more quantitative analysis, several images were subjected to a manual cell segmentation (Methods 5.2.7). Hereby, approximately 50 cells were outlined and their total intensities in the FRET channel were averaged and plotted (Fig. 27). The *in organello* SPAAC reaction (Fig. 25A) showed a significantly higher FRET intensity ($p \leq 0.001$; Student's two-sample t-test) than any of the control experiments (Fig. 25B-D).

The *in organello* click reaction of two Cy dyes was shown here for reaction pair **1**. A mitochondrial formation of SPAAC product **2** (Fig. 18B) from Cy3-azide and Cy5-DBCO was comparably observed and is presented in Appendix 7 along with the corresponding controls.

4.3.5 LC-MS analysis confirms *in organello* SPAAC product formation

The results in Section 4.3.4 strongly hinted towards an *in organello* SPAAC reaction. To unambiguously demonstrate that the detected FRET signal derived from the covalent Cy3-Cy5 product, compounds were re-isolated from cells after a reaction time of four hours. The extraction protocol was adapted from Logan *et al.* [122] and a detailed description can be found in Methods 5.2.8. In short, after Cy dye incubation and two washing cycles, RBE4 cells

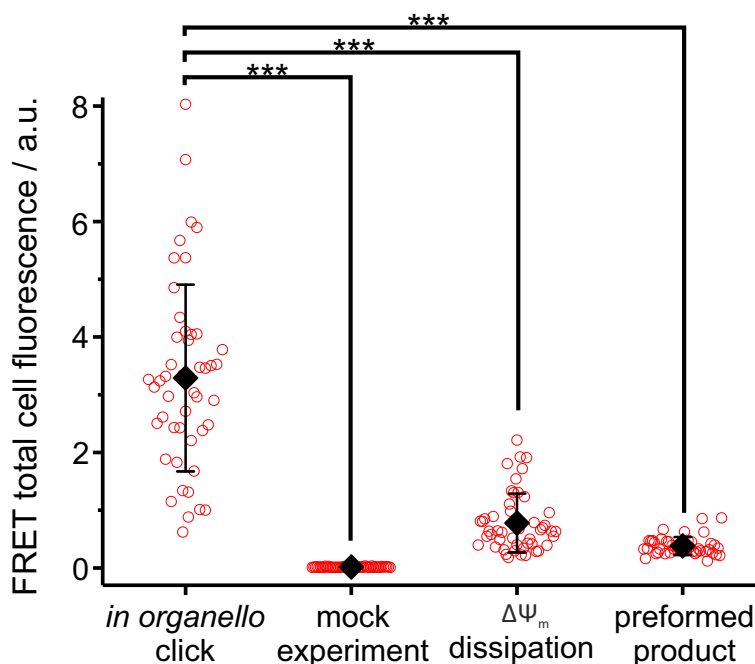


Figure 27: FRET total cell fluorescence for manually segmented cells treated with conditions A)–D) as shown in Figure 25. $N \approx 50$ cells, mean \pm SD. Statistical analysis by Student’s two-sample t-test: *** $p \leq 0.001$.

were detached, washed again and vigorously vortexed in acetonitrile. The supernatant was subjected to RP-HPLC analysis and analyzed by absorbance and ESI-MS detection. SPAAC product **1** was identified by its m/z of 647.4 ($[M]^{2+}$, calcd. 647.39, retention time 6.9 min). The corresponding peak was detected in the 542 nm and 632 nm absorbance traces close to the excitation maxima of Cy3 and Cy5, respectively. This rendered the identification of SPAAC product **1** unambiguous (Figure 28A).

Similarly, the reaction of Cy3-azide and Cy5-DBCO was analyzed (Fig. 28B). Control experiments, comprising the synchronous treatment with FCCP and the incubation with preformed product **2**, were included. In all three experiments, SPAAC product **2** with its m/z of 661.8 ($[M]^{2+}$, calcd. 661.41, retention times 4.2 min and 4.4 min) was detected. As observed for the RP-HPLC analysis in buffer (Appendix 5), SPAAC product **2** eluted as a double peak presumably because the two regioisomers **2.1** and **2.2** showed slightly shifted retention times (Fig. 18B). Importantly, a reduced amount of product was extracted from the cells in conditions where $\Delta\Psi_m$ was abolished. The reduction in product formation was attributed to a decreased mitochondrial accumulation of the starting material. Even less product was detected when the cells were incubated with the preformed product **2**. This finding was ascribed to the greatly reduced membrane permeability of preformed product **2**. It should be mentioned that all experiments in Figure 28B were performed in comparable conditions. However, neither an external nor internal LC-MS standard was added and therefore differences in cell number or viability, although not microscopically apparent, could not be completely ruled out. Nonetheless, these results were in good agreement with Figures 25 and 27 where significantly lower FRET signals

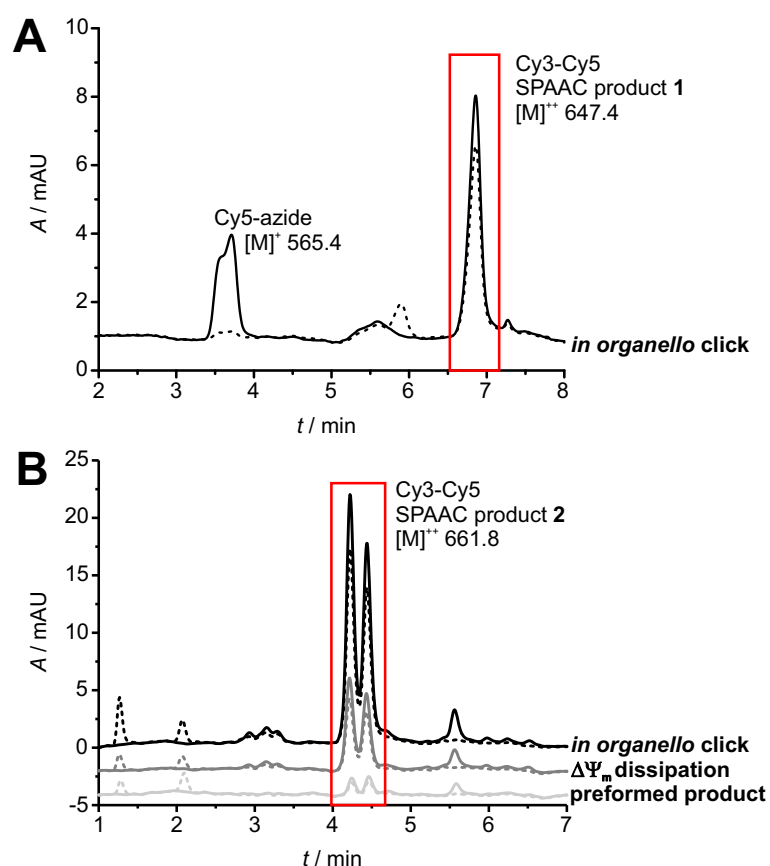


Figure 28: RP-HPLC analysis of compounds that were extracted from cells after *in organello* SPAAC, followed by two washing cycles. Quenching of precursor molecules prior to the extraction was omitted as the predominant proportion of precursor molecules had been washed out. Assignment of compounds by absorbance (dotted line: $\lambda_{\text{abs}} = 542$ nm; solid line: $\lambda_{\text{abs}} = 632$ nm) and ESI-MS detection. A) Reaction between Cy3-DBCO and Cy5-azide (two hours of incubation). SPAAC product **1** and unreacted, residual Cy5-azide were detected by their m/z . The peak (5.9 min) in the absorbance trace at 542 nm is an unknown side product of Cy3. B) Reaction between Cy3-azide and Cy5-DBCO and control experiments of the reaction at dissipated $\Delta\Psi_m$ and uptake of the preformed product **2** (four hours of incubation). The double peak eluting between 4.2 - 4.4 min was assigned to SPAAC product **2**. Traces of unreacted Cy3-azide and Cy5-DBCO were identified with retention times of 1.3 min ($\lambda_{\text{abs}} = 542$ nm) and 5.6 min ($\lambda_{\text{abs}} = 632$ nm), respectively.

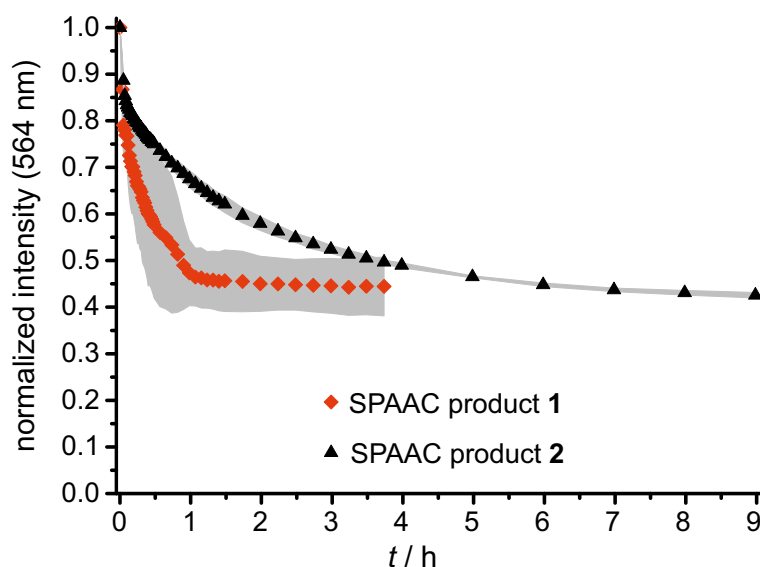


Figure 29: In cuvette kinetics of the formation of products **1** and **2**. Reactants were mixed at concentrations of $10 \mu\text{M}$. Donor emission at $\lambda_{\text{em}} = 564 \text{ nm}$ (upon $\lambda_{\text{exc}} = 488 \text{ nm}$) was normalized to the intensity at the starting concentration and plotted as mean \pm SD (in gray) of three independent experiments.

were imaged in the corresponding control experiments for SPAAC reaction pair **1**.

It was concluded that the *in organello* SPAAC reaction depended on (i) the presence of mitochondriotropic Cy dye structures for organellar targeting, (ii) a $\Delta\Psi_{\text{m}}$ as exhibited by polarized mitochondria and (iii) that the dicationic product was retained in the mitochondria due to its low membrane permeability.

4.4 Comparative reaction kinetics

The in cuvette kinetics of SPAAC reaction **1** and **2** as analyzed by a decrease in donor emission have already been described in Section 4.2.4 (Fig. 21 and Appendix 5). A direct comparison revealed that both reactions at $10 \mu\text{M}$ concentration proceeded with different velocities (Fig. 29). For the reaction between Cy3-DBCO and Cy5-azide a steep decrease in donor emission was observed within the first hour. This steep decrease was followed by saturation at levels of about 45% of the initial donor intensity. The kinetics of SPAAC reaction **2** between Cy3-azide and Cy5-DBCO, however, proceeded much slower. Here, a reduction in donor emission to about 50%, followed by saturation, took as long as four hours. From these comparative kinetics, it was apparent that the dynamic range spanned only one hour for SPAAC reaction **1** but four hours for SPAAC reaction **2**.

4.4.1 *In organello* reaction kinetics

To examine whether this difference in the dynamic range translated to the *in organello* reaction, the intensity of mitochondrial FRET signal for reaction **1** and **2** was evaluated after three different incubation intervals (two, four and twelve hours). Figure 30 displays the semi-

quantitative analysis of the FRET signal by manual cell segmentation. Representative confocal images for each time point can be found in Appendix 8. The strongest increase in FRET for the *in organello* formation of product **1** occurred within the first four hours (Fig. 30A). At the twelve-hour time point, there was no further, statistically significant increase in FRET compared to the four-hour time point. Kinetics of the reaction of Cy3-azide and Cy5-DBCO, however, behaved differently. Here, a statistically significant increase ($p \leq 0.001$; Student's two-sample t-test) in mitochondrial FRET was observed between four and twelve hours (Fig. 30B). It thus became clear that the *in organello* reactions of both reaction pairs showed different reaction rates. Of note, the investigated time frame spanned only twelve hours. Therefore, it remained open whether the dynamic range of SPAAC reaction **2** was within this time period or exceeded the incubation period of twelve hours.

4.4.2 Discussion

Despite a similar trend in reaction kinetics for both reaction pairs, the dynamic range of the *in organello* reaction was still found to be considerably more slowly than in buffer. It should be taken into account that additional time was required for the Cy dyes to reach the mitochondria. But this effect by itself could not serve as a satisfying explanation. While for the *in cuvette* kinetics the concentration of reactants was set to $10 \mu\text{M}$, the mitochondrial concentrations could only be estimated. Values reported experimentally and theoretically (calculated by Nernst equation 3.2) describe accumulation factors of 100- to 1,000-fold for monocationic mitochondriotropic compounds. [122,132,139] This would translate into mitochondrial concentrations of $25 \mu\text{M}$ to $250 \mu\text{M}$ for the applied conditions of 250 nM extracellular concentration. However, the observed slowdown for the *in organello* kinetics pointed towards effective mitochondrial concentrations of less than $10 \mu\text{M}$. One reason for this apparent discrepancy might be rooted in a difference between actual and effective concentrations. It is likely that the reactive Cy dyes bind to a certain extent to proteins and membrane lipids. For instance, a high membrane interaction factor was reported for Cy3 in comparison to other fluorescent dyes. [220] Thus, although the Cy dyes could have been enriched by a factor of $\approx 1,000$ -fold, the amount that was accessible to the click reaction might have been substantially lower. Furthermore, the reactants might show a reduced reactivity due to unfavorable orientations of their functional groups when free rotation is inhibited, *e.g.* due to interactions with the mitochondrial membrane. Additionally, the influence of an altered solute diffusion on the reaction dynamics should not be neglected. [221] The mitochondrial matrix exhibits an increased effective viscosity, partly due to the presence of nanostructures such as cristae and partly due to macromolecular crowding. [222] This confines the motion of molecules and leads to smaller diffusion coefficients. It was therefore likely that the *in organello* SPAAC reaction became diffusion controlled in the confined environment of the mitochondrial matrix. [223]

Lastly, differences between the experimental method presented here and the ones applied by other groups [122,137,138] need to be pointed out. The latter used either a TPP-specific ion-

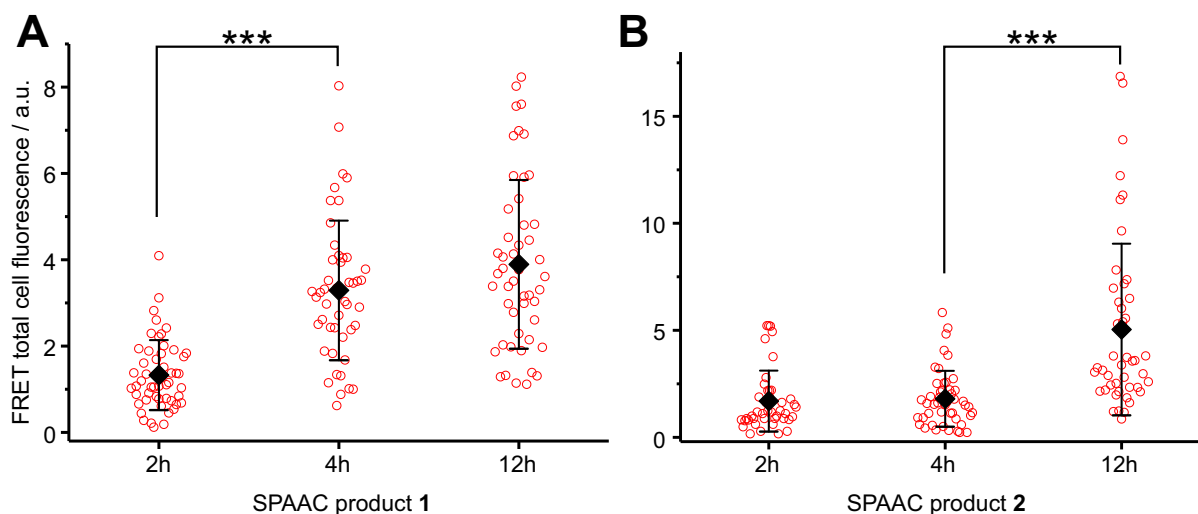


Figure 30: FRET total cell fluorescence for manually segmented cells; $N \approx 50$ cells, mean \pm SD. RBE4 cells were treated with 250 nM concentrations of SPAAC reaction partners A) Cy3-DBCO and Cy5-azide, leading to SPAAC product **1**; and B) Cy3-azide and Cy5-DBCO, leading to SPAAC product **2** for two, four and twelve hours followed by two washing cycles. Statistical analysis by Student's two-sample t-test: *** $p \leq 0.001$.

selective electrode [122, 138] or compared the external *vs.* mitochondrial distribution of TPP^+ ^3H -labeled probes. [122, 137, 138] And in most cases, these methods were applied to isolated mitochondria thus neglecting effects by $\Delta\Psi_p$ and the cytoplasmic milieu. Except for Logan *et al.*, the studies did not involve an intramitochondrial reaction but looked at the accumulation of single compounds. [122] And while Logan *et al.* reported Nernstian behavior for the ratio of mitochondrial and external concentrations of their precursors, they did not comment on the conformity of their SPAAC reaction kinetics with the mitochondrial concentrations of the reactants. In the end, it remained open whether the slowdown of the *in organello* reaction kinetics was caused by a deviation from Nernstian behavior of the four reactive Cy dyes or by the highly complex reaction environment in living cells.

5 Materials and methods

5.1 Materials

5.1.1 Chemicals

Acetic acid (LC-MS grade)	Sigma Aldrich (St. Louis, MO, USA)
Acetonitrile (LC-MS grade)	Sigma Aldrich
bFGF, human recombinant	Thermo Fisher Scientific (Waltham, MA, USA)
Carbonyl cyanide	Enzo Life Sciences (Lörrach, Germany)
p-trifluoromethoxyphenylhydrazine	
Dimethyl sulfoxide (spectroscopy grade)	Acros Organics (Thermo Fisher, Geel, Belgium)
Disodium hydrogen phosphate	Carl Roth (Karlsruhe, Germany)
DMEM, #61965	Thermo Fisher Scientific
DMEM:F-12 (1:1) indicator free, #21041	Thermo Fisher Scientific
DMEM:F-12 (1:1) indicator free, 15 mM	Thermo Fisher Scientific
HEPES, #11039	
DPBS, #14190	Thermo Fisher Scientific
Fetal bovine serum (FBS), #10500	Thermo Fisher Scientific
Formic acid, eluent additive for LC-MS	Sigma Aldrich
Ham's F-10, #41550	Thermo Fisher Scientific
Penicillin-streptomycin liquid, #15140	Thermo Fisher Scientific
Potassium chloride	AppliChem (Darmstadt, Germany)
Potassium dihydrogen phosphate	Carl Roth
Sodium chloride	Carl Roth
Trimethyl amine (LC-MS grade)	Sigma Aldrich
Trypan blue solution 0.4%, sterile-filtered	Sigma Aldrich
Trypsin-EDTA 0.05%, #25300	Thermo Fisher Scientific

5.1.2 Fluorophores

These dyes were applied for the colocalization study with the mitochondria localizing dye MitoTracker Green FM (see Methods 5.2.6). Alkynylated Cy dyes were a kind gift of Prof. Dr. Tom Brown (University of Oxford, UK). [211]

Table 4: Alkyne-functionalized Cy dyes, Cy5 propyl azide and MitoTracker Green FM. Spectroscopic data and CLSM settings.

Name	Full chemical name/ Supplier*	$\lambda_{\text{exc}}^{\text{max}}$ /nm	$\lambda_{\text{em}}^{\text{max}}$ /nm	Leica SP5 settings	
				Laser /nm	Detection /nm
<i>N</i> - pentynyl- Cy3	2-[3-(2,3-dihydro-3,3-dimethyl-1-(4-pentynyl)-1H-indol-2-ylidene)-1-propenyl]-1,3,3-trimethyl-3H-indolium iodide	550	563	561	570 - 620
Ethynyl- Cy3.25	2-[3-(2,3-Dihydro-1,3,3-trimethyl-1H-benz[e]indol-2-ylidene)-1-propenyl]-5-ethynyl-1,3,3-trimethyl-3H-indolium iodide	580	598	561	570 - 620
<i>N</i> - pentynyl- Cy3.5	2-[3-(2,3-Dihydro-1,3,3-trimethyl-1H-benz[e]indol-2-ylidene)-1-propenyl]-3,3-dimethyl-1-(4-pentynyl)-3H-benz[e]indolium iodide	590	607	561	570 - 620
Ethynyl- Cy5	2-[5-(2,3-Dihydro-1,3,3-trimethyl-1H-indol-2-ylidene)-1,3-pentadienyl]-1-butyl-3,3-dimethyl-5-ethynyl-3H-indolium iodide	655	675	633	650 - 700
<i>N</i> - pentynyl- Cy5	2-[5-(2,3-Dihydro-1-(4-pentynyl)-3,3-dimethyl-1H-indol-2-ylidene)-1,3-pentadienyl]-1,3,3-trimethyl-3H-indolium iodide	645	664	633	650 - 700
Ethynyl- Cy5.25	2-[5-(2,3-Dihydro-1,3,3-trimethyl-1H-benz[e]indol-2-ylidene)-1,3-pentadienyl]-5-ethynyl-1,3,3-trimethyl-3H-indolium iodide	673	693	633	650 - 700
Phenyl- ethynyl- Cy5.25	2-[5-(2,3-Dihydro-1,3,3-trimethyl-1H-benz[e]indol-2-ylidene)-1,3-pentadienyl]-5-(4-ethynylphenyl)ethynyl-1,3,3-trimethyl-3H-indolium iodide	680	703	633	650 - 700
<i>N</i> - pentynyl- Cy5.5	2-[5-(2,3-Dihydro-1,3,3-trimethyl-1H-benz[e]indol-2-ylidene)-1,3-pentadienyl]-3,3-dimethyl-1-(4-pentynyl)-3H-benz[e]indolium iodide	682	704	633	650 - 700

Cy5 propyl azide	Jena Bioscience* (Jena, Germany) (#CLK-CCA-9295-1)	649 [†]	670 [†]	633	650 - 700
Mito- Tracker [®] Green	Thermo Fisher Scientific* (#M7514)	490 [†]	516 [†]	488	500 - 560

*Commercially available. [†]Data from supplier.

With the exception of Cy3-DBCO, Cy dyes for the SPAAC reaction were commercially available as a dry substance. They were dissolved in DMSO at 2 mM concentration, aliquoted, stored at -20°C and thawed prior to use.

Table 5: Cy dyes for SPAAC reaction. Spectroscopic data and CLSM settings.

Name	Supplier	$\lambda_{\text{exc}}^{\text{max}}$ /nm	$\lambda_{\text{em}}^{\text{max}}$ /nm	LSM 880 settings	
				Laser /nm	Detection /nm
Cy3- azide	Jena Bioscience (#CLK-046-1)	546	563	488	544 - 598
Cy3- DBCO	see Methods 5.2.2	547	564	488	544 - 598
Cy5- azide	Jena Bioscience (#CLK-047-1)	641	666	633	659 - 696
Cy5- DBCO	Lumiprobe (Hannover, Germany) (#A30F0)	643	667	633	659 - 696
Sulfo- Cy5	Jena Bioscience (#CLK-AZ118-1)	641 [†]	666 [†]	633	659 - 696

[†]Data from supplier.

5.1.3 Buffers and Media

PBS 10x: 1.4 M NaCl, 27 mM KCl, 15 mM KH₂PO₄, 80.6 mM Na₂HPO₄ in MilliQ-H₂O (Millipore, Merck, Darmstadt, Germany) resulting in a pH of 6.8.

PBS: Dilution of PBS 10x with MilliQ-H₂O resulting in a pH of 7.4. Final concentrations of 140 mM NaCl, 2.7 mM KCl, 1.5 mM KH₂PO₄ and 8.06 mM Na₂HPO₄.

RBE4 growth medium: 45% v/v DMEM, 45% v/v Ham's F-10, 10 % v/v FBS, 100 U mL⁻¹ penicillin, 100 μ g mL⁻¹ streptomycin, 1 ng mL⁻¹ bFGF

RBE4 incubation medium: 90% v/v DMEM:F-12 indicator free, 10% v/v FBS, 100 U mL⁻¹ penicillin, 100 μ g mL⁻¹ streptomycin, 1 ng mL⁻¹ bFGF

RBE4 microscopy medium: 90% v/v DMEM:F-12 indicator free + 15 mM HEPES, 10% v/v FBS, 100 U mL⁻¹ penicillin, 100 μg mL⁻¹ streptomycin, 1 ng mL⁻¹ bFGF

RBE4 freezing medium: 35% v/v DMEM, 35% v/v Ham's F-10, 20% v/v FBS, 10% DMSO

5.1.4 Glassware and Disposables

8-well μ-slide, ibiTreat, #1.5 polymer coverslip	Ibidi (Martinsried, Germany)
8-well glass-bottomed polystyrene Nunc TM chambers	Thermo Fisher Scientific
Cell culture flask, 75 cm ² / 175 cm ² , ventilated cap, tissue culture treated	Sarstedt (Nümbrecht, Germany)
Filter top vacuum bottles, PES, pore size 0.2 μm, 250 mL / 500 mL	Sarstedt
Pipet tips, with filter, sterile	Greiner (Frickenhausen, Germany)
Pipet tips, without filter	Eppendorf (Wesseling-Berzdorf, Germany)
Reaction tube, 1.5 mL and 2.0 mL	Carl Roth Eppendorf
Screw cap vials, 2.0 mL	Carl Roth
Serological pipettes, sterile, disposable	Sarstedt
Syringe filter units, cellulose, pore size 0.2 μm	Carl Roth

5.2 Methods

5.2.1 Software and data analysis

Analysis and processing of confocal images was performed with the open-source software ImageJ. [224] Colocalization analysis was performed with the open-source software BioImageXD. [225] Charts and plots were prepared with OriginPro 9.1 (OriginLab, Northampton, MA, USA). Figures were prepared with Corel Draw X7 (Corel Corporation, Ottawa Canada). Analysis of chromatograms was performed with Agilent ChemStation (Santa Clara, CA, USA).

5.2.2 Synthesis of Cy3-DBCO

Cy3-DBCO was synthesized and characterized by Dr. Stefka Kaloyanova (Max Planck Institute for Polymer Research, Mainz, Germany). A detailed description can be found in Ref. [207].

Prior to use, Cy3-DBCO was HPLC purified once more. Upon lyophilization and dissolution in DMSO, the stock concentration was determined by its fluorescence intensity relative to a known concentration of Cy3-azide. The thus calculated stock concentration was 46.4 μM.

5.2.3 Fluorimetry

The spectroscopic analysis was performed on an FP-6500 fluorimeter (Jasco, Tokyo, Japan) equipped with an ETC-273T Peltier temperature controller using a 1.5 mm path length quartz cell. The following settings were applied:

Table 7: Fluorimetry settings.

Instrument parameter	Setting
data pitch (exc / em)	1 nm
response time	0.5 s
scanning speed	1000 nm min ⁻¹
bandwidth (exc / em)	5 nm

Spectral corrections for PMT and illumination lamp were included.

Fluorescence spectra: Excitation and emission spectra of Cy dyes were acquired for a 10 μM dye concentration in PBS, 40% DMSO at 25°C.

Fluorescence kinetics: Kinetics of product formation was measured by recording emission spectra from 500 nm to 720 nm upon excitation at 488 nm. Here, SPAAC reaction partners (Cy3-DBCO and Cy5-azide or Cy3-azide and Cy5-DBCO) were mixed at 10 μM or 250 nM concentration in PBS, 40% DMSO and were measured at 37°C for up to twelve hours. The PMT gain was adapted to 500 V for the 10 μM concentration and 800 V for the 250 nM concentration.

5.2.4 Cell culture

An immortalized cell line derived from rat brain endothelial (RBE4) cells was used. [226] The cells were a kind gift of Prof. Dr. Gert Fricker (University of Heidelberg, Germany). Buffers and media that were used in cell culture were sterile and prewarmed to 37°C prior to use. Cells were cultured in 75 cm² tissue culture flasks at 37°C under humidified 95% air / 5% CO₂ atmosphere in a HeraCell 150 incubator (Heraeus, Thermo Fisher Scientific). Sterile handling was performed in a HeraSafe KS12 laminar flow bench (Thermo Fisher Scientific).

Thawing: Cells from a liquid nitrogen stock were rapidly thawed in a water bath of 37°C and then transferred into 10 mL of RBE4 growth medium. After centrifugation (300 \times g, 5 min), the cell pellet was resuspended in prewarmed RBE4 growth medium and cultivated in a 75 cm² tissue culture flask.

Passaging: Cells were passaged when reaching 70 - 90% confluency (two to three times per week). Cells were lifted from the tissue culture flask by incubation with trypsin-EDTA (5 min at 37°C). After inactivation of trypsin by FBS, the cell suspension was centrifuged and

resuspended in RBE4 growth medium. Cells were then cultivated at a 1:5 or 1:10 ratio of the confluent cell suspension diluted with RBE4 growth medium.

Cell seeding: A 70 - 90% confluent flask of cells was trypsinated until the cells were detached (≈ 5 min). Following deactivation by addition of FBS and centrifugation, the cell pellet was resuspended in a small volume of RBE4 incubation medium (typically 1 - 2 mL). This cell suspension was diluted with trypan blue solution in a ratio of 1:5 and 1:10 and the cells were counted with a Neubauer Improved counting chamber (Marienfeld, Lauda-Königshofen, Germany). Upon adjustment to the desired cell number by further dilution with RBE4 incubation medium, 300 μ L of cell suspension were distributed per well of the Ibidi or Nunc chamber.

Freezing: Cells were detached by trypsinization. The centrifuged cell pellet was then resuspended in RBE4 freezing medium and aliquoted. The aliquots were stored at -80°C and then transferred to the liquid nitrogen tank for long-term storage.

5.2.5 Confocal laser scanning microscopy

Microscopy experiments were performed on two different confocal microscopes, a Leica TCS SP5 and a Zeiss LSM 880. The Leica TCS SP5 microscope was applied for the colocalization study of alkynylated Cy dyes with MitoTracker Green FM. All remaining experiments were conducted on the Zeiss LSM 880 microscope.

Leica TCS SP5: The confocal microscope (Leica, Wetzlar, Germany) was equipped with an argon laser of which the 488 nm laser line was used. Furthermore, helium-neon lasers with 561 nm and 633 nm were applied. Fluorescence emission was detected by PMTs. Temperature control was achieved with an Okolab heated stage H301 (Okolab, Pozzuoli, Italy). Images were acquired using the Leica Application Suite (LAS AF). The TCS SP5 was provided by the Confocal Laser Scanning Microscope Core Facility at the Institute of Molecular Biology (Mainz, Germany).

Zeiss LSM 880: The LSM 880 confocal laser scanning microscope (Carl Zeiss, Jena, Germany) was equipped with an incubator PM 2000 RBT (Pecon, Erbach, Germany) and supplied with CO_2 (95% air / 5% CO_2). In this project, the 488 nm argon laser line as well as the 633 nm helium-neon laser were used. Emission was detected by a spectral detection unit (Quasar, Carl Zeiss). Images were acquired sequentially switching between the different excitation wavelengths line by line. Image acquisition as well as pre-sorting of image data was performed using the built-in ZEN software (Carl Zeiss, Jena, Germany).

The detector gain was set to voltages that minimized the incidence of saturated pixels and it was kept constant for the respective channels throughout experiments. Further microscope settings are listed here:

Table 8: Microscopy parameters

Instrument parameter	Leica SP5	Zeiss LSM 880
image size (pixel)	512 x 512	1024 x 1024
pixel depth	8 bit	8 bit
objective	63x oil / 1.4	40x water / 1.2
pinhole (diameter)	136 μm	74 μm

5.2.6 Colocalization of alkynylated Cy dyes with MitoTracker Green FM

The colocalization study was conducted and interpreted by Dr. Markus Hirsch (Helm Group, JGU, Mainz, Germany) as described in and reproduced from Ref. [207].

Protocol: One day prior to the live cell experiment, RBE4 cells were seeded in antibiotics-free RBE4 growth medium in eight-well Ibidi slides at a density of 10,000 cells/well. At the day of the experiment, Cy dyes (final concentration 100 nM) and MitoTracker Green FM (100 nM) were added to the cells for three hours. Before confocal imaging, cells were rinsed with DPBS and supplied with fresh, indicator-free medium (DMEM/F-12).

Colocalization analysis: Employing the analysis tool BioImageXD [225], micrographs of corresponding Mitotracker Green FM and Cy dye channels were subjected to Gaussian noise reduction. Automatic threshold determination was performed and output statistics included Pearson’s coefficient as well as Manders’ coefficients. [59, 212]

Pearson’s coefficient is derived from a pixel distribution diagram of the colocalization data. To create such a scatter plot, the pixel intensity in the first channel (x-coordinate) is plotted against the intensity of the same pixel in the second channel (y-coordinate). Pearson’s coefficient is then calculated as follows:

$$r_p = \frac{\sum_i (A_i - a)(B_i - b)}{\sqrt{\sum_i (A_i - a)^2 \sum_i (B_i - b)^2}}$$

Here, A_i and B_i are the intensity values of pixel i in the first and second channel, while a and b are the average intensities in the respective channel. The spread of the distribution with respect to the fitted line is described by Pearson’s coefficient. The output values range from -1 to 1 with 1 indicating full colocalization, 0 indicating no correlation and negative values pointing towards a mutually exclusive presence of pixel intensity > 0 in the two channels.

Manders’ coefficient is an advancement of Pearson’s coefficient in the way that it excludes

average intensity values.

$$M_1 = \frac{\sum_i (A_{i,coloc})}{\sum_i (A_i)} \text{ and } M_2 = \frac{\sum_i (B_{i,coloc})}{\sum_i (B_i)}$$

M_1 relates the 'summed intensities in the first channel for which the intensity in the second channel is above 0' to the 'total intensity in the first channel' ($A_{i,coloc}$) and *vice versa* for the second channel (M_2). This results in output values ranging from 0 to 1 with values close to 1 indicating colocalization.

5.2.7 Incubation of cells with Cy dyes

One to two days prior to the live cell experiment, RBE4 cells were seeded in 300 μ L RBE4 incubation medium in eight-well Nunc chambers reaching 70 - 80% confluency on the day of the experiment. Dye stocks in DMSO were diluted with indicator-free DMEM/F-12 (+ 15 mM HEPES) medium to 3 μ M. Prior to the dye incubation, cells were rinsed and supplied with fresh RBE4 microscopy medium. Cy dyes (final concentration 250 nM), and where indicated FCCP (final concentration 5 μ M), were added to the wells for the designated time span (two to twelve hours). The incubation was performed at 37°C. At the end of the incubation period, the cells were either directly imaged on the confocal microscope or a washing procedure was inserted before imaging.

Washing procedure: In some experiments, the dye incubation was followed by washing. To this end, the dye containing medium was removed and the cells were once rinsed with DPBS. Afterwards, fresh RBE4 microscopy medium was added and the cells were incubated at 37°C for another hour allowing for re-equilibration of the dyes. This procedure was repeated. After a total of two washing cycles, the cells were subjected to imaging.

Image processing: Confocal images were analyzed with ImageJ. [224] For representation, the transmission channel was contrast enhanced and fluorescence channels were consistently arithmetically enhanced throughout one experiment. From a z -stack of five sections, CLSM images show representative slices in which mitochondria were best in focus.

Cell segmentation and analysis: On the basis of the transmission and fluorescence data, the outlines of approximately 50 cells from four different positions were manually segmented with ImageJ ROI manager. For each cell the total cell fluorescence (integrated cell density) in the FRET channel was measured. Box plotting and statistical analysis were performed with OriginPro 9.1.

5.2.8 Re-isolation of compounds after cellular incubation

For the re-isolation of the SPAAC product after formation in the mitochondria, an extraction protocol as described by Logan *et al.* was adapted. [122] Two days prior to the experiment, RBE4 cells were seeded in 175 cm² tissue culture flasks. At the day of the experiment, cells were washed with DPBS and supplied with 10 mL of fresh RBE4 growth medium. The Cy dye DMSO stock was diluted with indicator-free DMEM/F-12. The dilution was added to the cells resulting in a final concentration of 250 nM. Where indicated, a 5 μ M concentration of FCCP was additionally included. This step was followed by an incubation at 37°C for the indicated time span, either two or four hours. Afterwards, two washing cycles with re-equilibration periods of one hour in between were performed. Next, cells were detached by the addition of 2.5 mL trypsin-EDTA. Trypsin was quenched with RBE4 growth medium and the cell suspension was centrifuged (300 \times g, 5 min). The supernatant was removed and the cell pellet was resuspended in 1.5 mL DPBS, transferred to fresh reaction tubes and centrifuged (16,000 \times g, 3 min). Compounds were extracted by resuspending the cell pellet in 100 μ L acetonitrile (supplemented with 0.1% formic acid) and vigorous vortexing for 5 min. After a final centrifugation step (16,000 \times g, 15 min), the supernatant, containing the extracted compounds, was subjected to LC-MS analysis (Methods 5.2.9).

5.2.9 Liquid chromatography coupled to absorbance and mass spectrometry detection

Chromatographic separation was performed on an Agilent 1100 instrument equipped with a quaternary pump, autosampler, DAD detector and mass selective detector (LC-MSD-Trap-SP10180). An Agilent Poroshell EC-C18 120 Å column (3.0 x 50 mm, 2.7 μ m) with a guard column was used. RP-HPLC separation took place at a temperature of 30°C. The mobile phase consisted of MilliQ-H₂O (solvent A) and acetonitrile (solvent B). 1 M triethylammonium acetate pH 7.0 (solvent C) was constantly kept at 10%.

For RP-HPLC separation of Cy3-DBCO, Cy5-azide and the corresponding SPAAC product **1**, the following gradient was applied:

Table 9: Gradient of solvents A - C for the chromatographic separation of SPAAC reaction pair **1**.

Time / min	Solvent A	Solvent B	Solvent C
0	45%	45%	10%
5	30%	60%	10%
6	0%	90%	10%
7	0%	90%	10%
8	45%	45%	10%
12	45%	45%	10%

For analysis of Cy3-azide, Cy5-DBCO and the corresponding SPAAC product **2**, the method

was adapted as follows:

Table 10: Gradient of solvents A - C for the chromatographic separation of SPAAC reaction pair **2**.

Time / min	Solvent A	Solvent B	Solvent C
0	40%	50%	10%
7	20%	70%	10%
8	0%	90%	10%
9	0%	90%	10%
10	40%	50%	10%
14	40%	50%	10%

In both cases, the flow rate was 0.7 mL min⁻¹. Absorbance detection was set to 542 nm for Cy3 dyes and 632 nm for Cy5 dyes. Additionally, detection by ESI-MS in positive ion mode was employed. The following instrument settings were applied:

Table 11: MS settings.

Instrument parameter	Setting
dry temperature	350°C
nebulizer pressure	70 psi
dry gas	12 L min ⁻¹
trap drive	56.9
Octapole RF amplitude	200 V _{pp}
capillary exit	100.8 V
skimmer	40.0 V
Oct 1 DC	12.0 V
Oct 2 DC	1.87 V
scan range	250 - 900 m/z
max accumulation time	200 ms
ICC target	30,000

Analysis of dyes and SPAAC reaction in buffer: Cy dyes and the SPAAC reaction mixture were analyzed at final concentrations of 10 μM or 25 μM in PBS, 40% DMSO. In order to detect the formation of SPAAC product, the reaction mixture was incubated at room temperature for the indicated time span prior to LC-MS analysis.

Analysis of SPAAC products isolated from cells: Upon incubation of the RBE4 cells with the SPAAC reaction partners as described in Section 4.3.3, the re-isolated compounds, dissolved in acetonitrile / 0.1% formic acid, were subjected to an LC-MS analysis. The plotted chromatograms (Fig. 28) were modified by a baseline subtraction of cellular background.

Part III

Monitoring drug nanocarriers in human blood by near-infrared fluorescence correlation spectroscopy

6 Introduction

Depending on the type of administration and the target site nanocarriers have to overcome specific biological barriers (Section 1.2). [28] This project dealt with the development of method to monitor nanocarrier stability in blood, the first environment encountered after intravenous injection. To this end, the composition of blood will be outlined (Section 6.1) and possible processes which threaten the stability of nanocarriers in the blood will be described (Section 6.2). Lastly, current methods for the evaluation of nanocarrier stability *in vitro* and *in vivo* will be introduced (Section 6.3).

6.1 Blood

Blood is considered a connective tissue. It is composed of a fluid part, termed the plasma, and a corpuscular part consisting of three cell types: the red blood cells (erythrocytes), white blood cells (leukocytes) and platelets (thrombocytes). Its main functions are (i) the transport of respiratory gases (oxygen, carbon dioxide), nutrients, metabolites and signaling compounds, (ii) the maintenance of homeostasis with regard to dissolved substances, temperature and pH, (iii) the counteraction of bleeding by coagulation and (iv) immune defense. [227, 228]

With a volume of 4 to 6 L, blood accounts for 7 to 8% of an adult's body weight and is one of the most important body fluid compartments along with interstitial and intracellular fluids. The mature, anuclear erythrocytes are the main cellular fraction (≈ 5 million μL^{-1}) and occupy almost half of the blood volume (0.47 for males, 0.42 for females). [229] This volume fraction is called hematocrit. Erythrocytes contain large amounts of hemoglobin, a multi-subunit protein which is responsible for the transport of oxygen. Each of the four hemoglobin subunits carries heme, a protoporphyrin with a coordinatively bound iron atom whose free binding position can be occupied by oxygen. [229] The chromophoric heme conveys the red color of blood. Carbon dioxide, in contrast, is transported either as a physically dissolved gas, bound to amino groups of hemoglobin or as dissolved bicarbonate. Leukocytes (4,000 to 10,000 μL^{-1}) play an important role in the specific and unspecific immune defense and are further subdivided in granulocytes (neutrophils, basophils and eosinophils), monocytes and lymphocytes. The third cellular fraction, the thrombocytes (160,000 to 300,000 μL^{-1}), is essential for the initiation of

coagulation as well as the formation of a platelet plug during primary hemostasis. All cellular components derive from pluripotent stem cells.

Blood plasma contains water (900 - 910 g L⁻¹), proteins (65 - 80 g L⁻¹) and to a lesser extent electrolytes, carbohydrates, lipids and amino acids. [228] Plasma proteins are synthesized in the liver. They fulfill specific and unspecific transport functions and contribute to the buffering capacity of blood. [229] Together with the electrolytes, plasma proteins are responsible for the maintenance and regulation of osmotic pressure. The most abundant plasma protein is albumin (35 - 45 g L⁻¹) which acts as a transport vehicle for many biomolecules including fatty acids and steroids but also small drug molecules. Further highly abundant proteins are globulins (subdivided in α_1 , α_2 , β and γ) and fibrinogen. The latter is activated by clotting factors to form a fibrin network which leads to wound closure (secondary hemostasis). The liquid fraction isolated from coagulated blood is called serum. In contrast to plasma, serum is devoid of fibrinogen and clotting factors.

6.2 Transport of nanocarriers in the bloodstream

Blood can be considered a transport medium that brings a nanocarrier to its target site. The *in vivo* fate of the nanocarrier thus depends critically on its ability to remain intact while dispersed in blood. [230] Equally important, and prerequisite for the circumvention of further obstacles, is the successful deposition of the nanocarrier at the target site. Such deposition is perfusion controlled and the propensity of accumulation is directly linked to the blood circulation half-life of the nanocarrier. [19] Therefore, one of the fundamental goals in nanotherapeutic research is to ensure a prolonged circulation half-life without aggregation, decomposition or substantial loss of drug cargo.

6.2.1 Adsorption of plasma proteins

The blood circulation of nanocarriers is counteracted by a rapid blood clearance which is induced by the adsorption of plasma proteins. The adsorbed protein layer(s) are commonly referred to as “protein corona”. [231] Plasma proteins exhibit a high affinity especially towards hydrophobic surfaces. They bind to nanocarriers and grant them a biological identity. [21] Consequently, it was suggested that the biological identity of the nanocarrier and not its “bare” chemical surface determines its biological distribution and physiological reaction. [232] Several effects were deduced from nanocarrier-protein interactions.

First, the coating with certain plasma proteins termed opsonins (*e.g.* immunoglobulins, complement proteins, fibrinogen) is reported to target the nanocarrier for sequestration by the mononuclear phagocyte system (MPS). [19, 21] The effector cells of the MPS, scavenging monocytes and macrophages, are part of the immune system and reside in the reticuloendothelial tissues which are found in liver, spleen, lung and bone marrow. Opsonization triggers the receptor-mediated uptake into phagocytic cells followed by lysosomal degradation of the nanocarrier. This process is thus held responsible for a rapid clearance of nanocarriers from

the bloodstream and a short circulation half-life. Second, the colloidal stability of a nanocarrier dispersion can be compromised upon protein adsorption. [21] Thus an aggregation of the nanocarrier in the blood may occur. Third, an adsorbed protein layer can mask attached ligands from receptor recognition employed for means of active targeting. [233] Fourth, it was found that nanocarrier-protein interactions influence not only the fate of the nanocarrier but also that of the adsorbed proteins. A conformational change in protein structure, for instance, can lead to a loss of functionality and can trigger an immune response. [234] Furthermore, interactions can also perturb the blood coagulation system by acting either pro- or anti-coagulative. [235] The incidence of thrombotic complications has been reported for several nanocarrier systems.

Several strategies are pursued to control nanocarrier-protein interactions and to prevent aggregation. One strategy relies on the reduction of protein adsorption by the addition of a protein-repellent stealth layer on the nanocarrier's surface. [19] The most commonly employed polymer which is grafted onto nanocarrier surfaces is polyethylene glycol (PEG). PEGylation of liposomal doxorubicin (Doxil[®]) was shown to prolong circulation half-life from minutes up to two days. [236] The steric repulsion of proteins by PEG is believed to root in the formation of a hydrating layer. However, a complete elucidation of the underlying mechanism is still missing. [237] Furthermore, by now it has been generally acknowledged that PEGylation does not completely prevent protein binding but rather leads to the adsorption of specific, opsonization-counteracting proteins such as clusterin. [234, 238] Therefore, other molecular structures (*e.g.* zwitterionic sulfobetaines) are investigated with the aim of developing corona-free nanocarriers. [239] A second strategy involves the deliberate alteration of corona compositions. To this end, nanocarriers are precoated by incubation with either whole plasma protein pools, enriched fractions or isolated proteins. [240–242] In *in vitro* studies, this pre-treatment was reported to reduce aggregation and to decrease phagocytic uptake. Further strategies involve the chemical conjugation of nanocarriers with so-called self-markers (*e.g.* CD47 peptide) which are commonly expressed by cells to evade the MPS. [243] A similar outcome is anticipated by coating nanocarriers with membranes of erythrocytes, leukocytes or thrombocytes. [244–246] Both approaches led to a reduction in phagocytic uptake and an increase in circulation half-life as reported for murine *in vivo* models.

Vast research efforts have been mobilized to resolve the thermodynamic and -kinetic process of protein adsorption (high *vs.* low affinity binding). Parameters such as the composition, density, conformation and thickness of the protein corona were found to depend on the physicochemical properties of the nanocarrier. [232, 247] The exposure time, protein source and relative ratio of physiological fluid to nanocarrier dispersion were identified as further influencing factors. [248] Additionally, differences in corona compositions between *in vitro* and *in vivo* investigations were reported. [249] Both findings indicate a limited transferability from *in vitro* to *in vivo* data and emphasize the necessity of *in vivo* investigations on nanocarrier-protein interactions.

6.2.2 Stability in blood

Besides aggregation, other events such as dissociation, degradation or premature drug release threaten the stability of a nanocarrier system when transported in the bloodstream. Especially, spontaneously formed nanocarriers such as some polymeric nanoparticles or micelles are susceptible to destabilization when transferred to blood. [23] Their self-assembly into polymeric structures occurs above a certain concentration threshold, the critical micellar concentration (CMC). In order to convey *in vivo* stability, the CMC should be low so that disassembly does not occur upon dilution in the blood. [230] Although some micellar formulations (*e.g.* poly(caprolactone)-b-PEG, poly(benzyl aspartic acid)-PEG or poly(D,L-lactic acid)-PEG micelles) proved to be stable at low concentrations in buffered saline, the interaction with plasma proteins led to dissociation and premature drug release. [250–252] These stability issues restrained the therapeutic potential of self-assembled systems in (pre-)clinical studies and led to the evolution of a new generation of micelles. Currently investigated micelles are stabilized either by physical interactions or by chemical crosslinking of the micellar structure. [253] However, stabilization of the micellar structure alone is often insufficient to prevent rapid partitioning of the payload from its carrier in the blood. [254] Drug retention can be achieved by π - π -stacking between drug molecules and polymers [255], by coordinative binding [256] and by pH- or redox-labile covalent bonding of drug molecules to micelles. [257, 258]

In general, the mere physical entrapment of a drug payload holds the potential of insufficient drug retention as observed for poly(lactic-co-glycolic acid) nanoparticles loaded with paclitaxel. Here, the nanoparticle-based formulations offered no advantage over the systemic administration of the free cytotoxic drug. [259, 260] A careful *in vitro* and *in vivo* evaluation is also requested when stimuli-responsiveness is aimed at. Often, a sharp transition is required to retain sufficient stability in the blood flow but triggered disintegration at the target site. For instance, doxorubicin-loaded liposomes with the temperature-sensitive compound poly[2-(2-ethoxy)ethoxyethyl vinyl ether] showed high stability at physiological temperature and drug release upon heating of the tumor to $> 40^\circ\text{C}$. [261] Another thermoresponsive liposomal doxorubicin formulation (ThermoDox[®]) is currently tested in a phase III study on hepatocellular carcinoma. [262]

6.3 Methods to study nanocarrier stability in biological environment

Typically, a nanocarrier will leave the chemist's bench with a comprehensive physicochemical characterization with regard to size, size distribution, surface properties, composition, purity *etc.* [23, 28] Such properties are usually determined in the aqueous buffer conditions at which the nanocarrier was prepared. Buffers such as PBS mimic the physiological composition of blood with respect to ionic strength and pH. However, the absence of proteins and blood cells and the possible negligence of *in vivo* dilution factors impede meaningful conclusions for the behavior of the nanocarrier in blood.

6.3.1 *In vitro* techniques

As a first approach towards *in vivo* conditions, the nanocarrier's stability is often evaluated in blood plasma or serum. Many analytical techniques can yield information on size and can thus detect instabilities due to aggregation or decomposition. However, some techniques require a sample workup (*e.g.* centrifugation, dialysis, precipitation, deposition on a specific probing surface) following the plasma/serum incubation. They are hence performed in conditions that deviate from the biological environment. Such techniques include, for instance, transmission electron microscopy, gel electrophoresis, atomic force microscopy or chromatography. [230,247,263]

Other techniques, in contrast, are compatible with high concentrations of proteins. One of these techniques is FCS. In aqueous solution, FCS has been broadly applied to study the formation of nanocarriers [29–32], their drug loading efficiency [33,34], stability [35], leakage [264] and triggered release [265,266]. On the subject of protein corona formation, FCS has been applied to determine kinetic parameters on the binding affinities of proteins as well as the thickness of the adsorbed protein layer(s). [267–270] Furthermore, *in vitro* studies on the stability of nanocarriers in plasma or serum have been performed by FCS. For instance, Novo *et al.* could confirm that significant proportions of siRNA remained entrapped in targeted decationized polyplexes upon plasma dispersion. [271] In another study, different biological media ranging from serum to intraperitoneal and ascites fluid were tested for their effect on siRNA leakage from PEGylated *vs.* non-PEGylated lipoplexes. [264] The authors found that in all tested environments the non-PEGylated lipoplexes revealed less siRNA leakage. In addition, FCS has been employed to monitor temperature-triggered release from thermosensitive liposomes. [272] The authors developed an assay that allowed the quantification of released dye in the presence of intact dye-loaded liposomes. For this, they encapsulated a quenched dye (fluorescein di- β -D-galactopyranoside) into the liposomes that regained its fluorescence by enzymatic cleavage after the release. The authors reported that different plasma sources and individual proteins led to differentiating transition temperatures. Consequently, they hypothesized that the adsorbed proteins partially penetrated into the membrane and affected the liposomal integrity.

Another method that is applicable to *in situ* plasma measurements is dynamic light scattering (DLS). DLS is based on measuring the scattering intensity fluctuations caused by Brownian motion of nanocarriers. Similarly to FCS, the intensity fluctuations are autocorrelated and fitted in order to retrieve the diffusion parameters of the nanocarrier or its degradation products. [263] In contrast to FCS, DLS is more sensitive to polydispersity as the analyzed intensity scales with the sixth power of the species' diameter. This relation explains the low sensitivity of DLS for small molecules such as released drug molecules. However, the main difference to FCS is that DLS is not specific for fluorescently labeled species. Therefore, a multi-exponential fit is required in order to account for the diversity of proteins and lipids that interfere with DLS measurements in serum or plasma. Nevertheless, DLS was successfully applied to determine protein-induced aggregation of zwitterionic poly-L-lysine, nanohydrogel particles and

siRNA-loaded liposomes. [273–275]

6.3.2 *In vivo* techniques

There is, however, a considerable lack of techniques that monitor blood-induced nanocarrier instabilities directly *in vivo* or, as the closest approximation to *in vivo* conditions, in a blood sample. [23] This shortcoming is rooted in the increased complexity of whole blood and biological tissues (such as the skin) that causes incompatibilities with many techniques. Optical methods, for instance, suffer from a loss in resolution and penetration depth due to high scattering and absorption in the aforementioned biological environments. [276,277] The main components of red blood cells, hemoglobin and oxyhemoglobin, show high absorption in the visible wavelength range ($\lambda < 600$ nm) (Fig. 31). Water, in contrast, strongly absorbs at $\lambda > 1150$ nm. But the disturbing influence of these major absorbers is at its minimum in the NIR wavelength range. [36] The exploitation of this low absorption window has been implemented in several NIR imaging techniques. These techniques employ NIR dyes (*e.g.* indocyanine green) or quantum dots which are excited and emit in the range of ≈ 700 to 1100 nm. [37,38,278] Thus, penetration depths of 0.5 - 1 mm for microscopy and > 1 cm for macroscopy have been reported. [38] NIR imaging and other techniques such as computed tomography, magnetic resonance imaging, positron emission tomography or photoacoustic imaging have been broadly applied to study the biodistribution of nanocarriers either for diagnosis, image-guided surgery or the evaluation of pharmacokinetics in (pre-)clinical studies. [28,36] These approaches yield a quantitative and time-resolved overview of the biodistribution. However, they do not allow to gain insight into the integrity state in which the nanocarrier and/or its drug payload distribute and accumulate in the different body compartments.

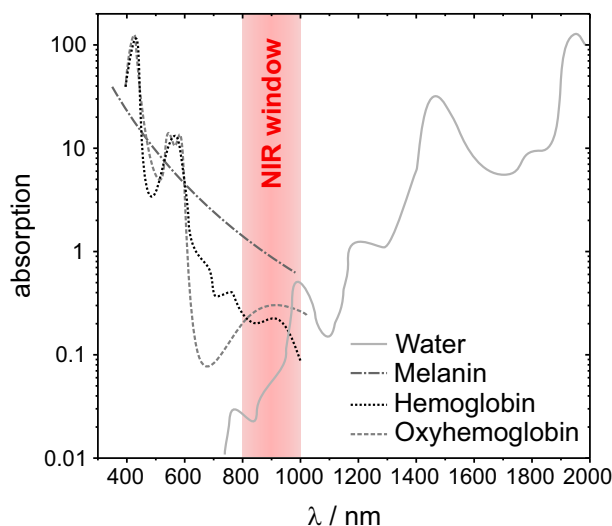


Figure 31: Absorption spectra of water, melanin, hemoglobin and oxyhemoglobin which are the main absorbers in blood and other tissues. The NIR window between 800 and 1000 nm depicts the wavelength range of the highest optical transmission. Adapted from Ref. [36].

To avoid the stability-related failure of a nanocarrier at late stages in clinical development, it

is necessary to advance particle-sizing methods towards application in blood or at best *in vivo*. While DLS is hampered by the high background scattering in blood, FCS with its fluorescence-based detection mode is adaptable to the NIR range. For instance, the applicability of two-photon FCS for measurements in human skin at penetration depths of up to 10 μm has been demonstrated. [279] Two-photon FCS is conducted with dyes whose excitation and emission maxima lie within the visible wavelength range. The excitation wavelength is, however, shifted to the NIR range by relying on the coincidental simultaneous absorption of two NIR photons. [10] Emitted photons, however, are still susceptible to an absorption by (oxy-)hemoglobin and other chromophores on their way from the emitter through the tissue towards the detector. This potential interference can be circumvented by using NIR dyes and by employing a fully NIR-FCS setup as described in this work.

7 Results and discussion

7.1 Calibration of the NIR-FCS setup in aqueous solution

To perform FCS measurements in the NIR range, *i.e.* at NIR excitation and emission wavelengths, a commercial microscope was combined with a Ti-sapphire laser and an NIR-sensitive APD.⁴ The setup is schematically illustrated in Figure 32A and is explained in more detail in Methods 8.2.2. In order to obtain the accurate size of a fluorescent species by FCS, the dimensions of the observation volume V_{obs} have to be known (Section 2.4.1). These dimensions reflect the radial and axial resolution which are determined by the properties of the confocal microscope as well as the applied excitation and emission wavelengths. As the diffraction limit adopts larger values with increasing wavelengths (Section 2.2.2), it was expected that the dimensions of V_{obs} in the NIR range would be increased as compared to the visible range. As a first step, it was therefore necessary to conduct test and calibration measurements with the NIR-FCS setup in aqueous solution. Commonly, calibration measurements are performed with fluorescent tracers, often dye molecules, with known diffusion coefficients. Fitting the autocorrelation curves of these reference dyes with the appropriate fit function then yields the structural parameter S and the diffusion time τ_D . The obtained τ_D is used to calculate the lateral size of V_{obs} by $r_0 = \sqrt{\tau_D \cdot 4D}$, while S delivers the axial dimension $z_0 = S \cdot r_0$ (Section 2.4.1).

For calibrating the NIR-FCS setup, three different fluorescent species were utilized. The two commercial dyes, Alexa Fluor 790 and IRDye 800CW, were measured in order to retrieve S which was found to range around a value of 5. Owing to the novelty of performing FCS measurements in the NIR range, however, the diffusion coefficients of the two NIR dyes had not been published and were thus not known in advance. Therefore, a third fluorescent species was employed whose diffusion coefficient could be reliably determined by an alternative method, in this case multi-angle DLS. This species was a cylindrical polymer brush (**PB1**) with poly-L-lysine main chain and polysarcosine side chains, labeled with IRDye 800CW (Fig. 32B).⁵ **PB1** showed a diffusion coefficient of $D_{\text{PB1, water}} = 20.4 \mu\text{m}^2 \text{s}^{-1}$ (23°C, DLS) which was translated into a hydrodynamic radius of 11.4 nm by Stokes-Einstein equation (Eq. 2.11) (Appendix 9). The diffusion time of **PB1** in water was measured by NIR-FCS and related to its known diffusion coefficient ($D_{\text{PB1, water}}$). This yielded the dimensions of V_{obs} with $r_0 \approx 0.35 \mu\text{m}$ and, with $S \approx 5$, $z_0 \approx 1.75 \mu\text{m}$. With these parameters at hand, the diffusion coefficients for the dyes were determined to be $280 \pm 9 \mu\text{m}^2 \text{s}^{-1}$ for Alexa Fluor 790 and $245 \pm 14 \mu\text{m}^2 \text{s}^{-1}$ for IRDye 800CW in water at 23°C (Appendix 10).

The Ti-sapphire laser was operated at 780 nm and delivered femtosecond pulses with high power (≈ 1 W) at a frequency of 80 MHz. In principal, the use of such powerful femtosecond laser for linear excitation in NIR-FCS experiments was not necessary. In fact, the application of low power picosecond or continuous wave lasers would reduce the risk of photodestruction and

⁴Results of this Part are partially contained in Ref. [[280], in preparation]

⁵Polymer brushes were synthesized and characterized by Meike Schinnerer.

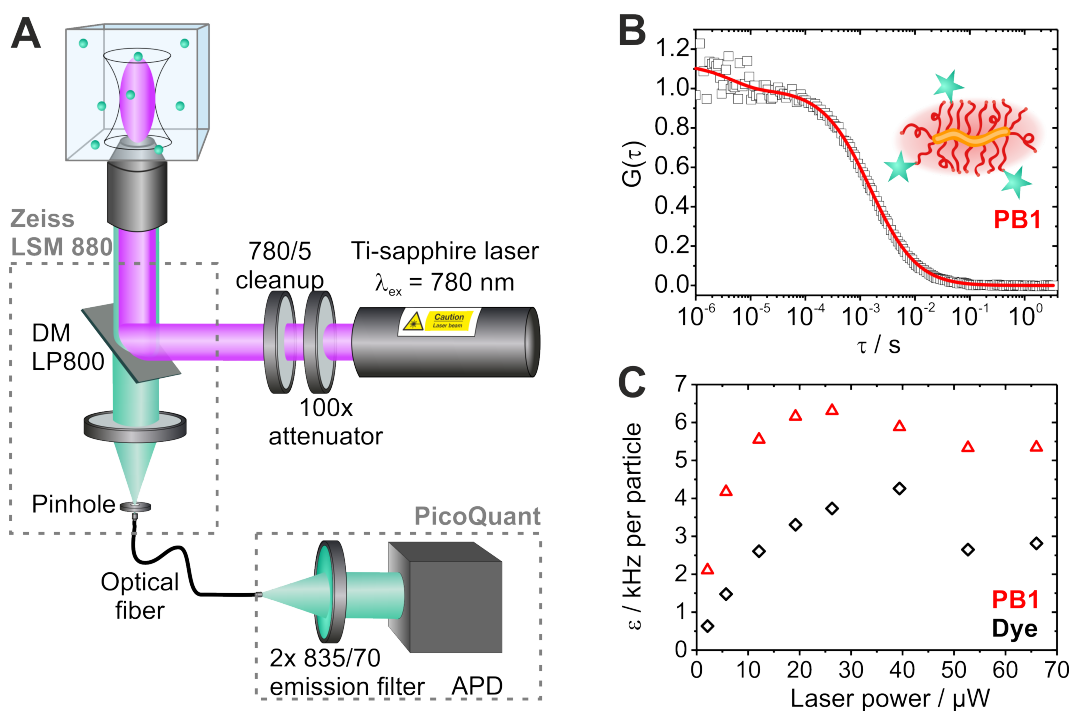


Figure 32: A) Schematic of the NIR-FCS setup. B) Autocorrelation curve (squares) of **PB1** measured in water. The curve was fitted with an analytical model for 3D diffusion of one fluorescent species including triplet (Eq. 2.20) (line). The inset shows a schematic of **PB1** with the poly-L-lysine backbone (yellow), polysarcosine side chains (red) and dye (turquoise stars). C) Fluorescence brightness (ϵ) of **PB1** (red triangles) and IRDye 800CW (black diamonds) at increasing laser power.

saturation and could therefore replace the Ti-sapphire laser in the future. The Ti-sapphire laser, however, offered the convenience of tuning the excitation wavelength in a range from 780 to 920 nm. Despite its strong attenuation, the individual pulses retained a high power and could easily saturate or photodestruct fluorescent molecules. To avoid this, it was important to adjust the laser power to values for which the photon emission of the fluorescent molecules (fluorescence brightness) scaled linearly with the applied laser power. At the same time, reliable, noise-free autocorrelation curves required a certain number of emitted photons per time interval. As such, the laser power was adjusted as a trade-off between saturation and an efficient signal-to-noise ratio. Figure 32C shows the relation of fluorescence brightness (ϵ) for IRDye 800CW and **PB1** with laser power (Section 2.4.1). The linear range for ϵ of IRDye 800CW was found to span laser powers of ≈ 2 to $12 \mu\text{W}$. **PB1**, in contrast, deviated from linearity at lower laser powers. To remain well within the linear range, laser power was thus restricted to $6 \mu\text{W}$ for IRDye 800CW and to $2 \mu\text{W}$ for **PB1**. As a side note, by dividing ϵ of **PB1** and IRDye 800CW both measured at $2 \mu\text{W}$, it was determined that **PB1** was labeled with an average of three dye molecules, assuming that no quenching effects took place.

7.2 NIR-FCS measurements in human blood

7.2.1 Static blood

After calibration of the NIR-FCS setup in aqueous solution, the measurements were extended to heparin-stabilized human blood. During the development of a particle-sizing protocol for measurements in blood, the model NIR fluorescent species **PB1** was continuously applied. This allowed for a direct comparison of **PB1** behavior in the different conditions of water and blood. At first, **PB1** was dispersed in blood at a 3 nM concentration. A droplet of the **PB1**-containing blood was placed onto a cover slip in a chambered microscopy slide and analyzed. Initial measurements in such static conditions led to the following observations: i) at some positions a very low average fluorescence signal was recorded which could not be adequately autocorrelated, ii) other positions, by contrast, showed a considerably higher fluorescence signal and delivered autocorrelation curves that could be fitted with an analytical model of one or two diffusing species (Eq. 2.20) and iii) the incidence of finding the latter positions decreased with increasing depth of penetration, *i.e.* the distance between cover slip surface and V_{obs} .

It was assumed that these position-dependent changes in the average signal intensity were related to the high number of cells in the blood. Due to the high cell content, the free volumetric space in which unhindered Brownian diffusion of **PB1** could occur was strongly restricted. The assumption of such an exclusion effect requested further analysis. Therefore, in order to correlate acquired autocorrelation curves with the precise position of V_{obs} with respect to cells, red blood cells (RBC) were stained with the green-fluorescing membrane dye DiI. During the staining procedure, the plasma was removed and substituted with PBS to which **PB1** was added at nanomolar concentration. A high percentage of RBC (hematocrit of $\approx 30\%$) was retained. In this dispersion confocal images were taken at an excitation of 543 nm and an emission detection from 553 to 633 nm. This provided a first impression of the 3D configuration of the cells. However, in the visible spectrum the main components of RBCs oxy- and deoxyhemoglobin show strong absorption leading to a dramatic loss in signal intensity already at the first micrometers (compare also Fig. 31). [36] High scattering additionally reduced image resolution with the effect that a clear distinction of cellular structures at imaging depths $> 10 \mu\text{m}$ was not possible. Within the first $10 \mu\text{m}$ a close network of packed, sedimented cells was observed (Fig. 33A). FCS measurements were then performed at every micrometer depth of penetration, starting from the cover slip surface and going up to a distance of $10 \mu\text{m}$. When V_{obs} was positioned in a cell-free spot clear off the glass-sample interface, the corresponding autocorrelation curves could be fitted with an analytical model for one freely diffusing species (Eq. 2.20) (Figure 33B). With $21.5 \mu\text{m}^2 \text{s}^{-1}$ the obtained diffusion coefficient only marginally differed from $D_{\text{PB1, water}} = 20.4 \mu\text{m}^2 \text{s}^{-1}$, assuming that the dimensions of V_{obs} were equal in both cases. When the measurement was performed at a location occupied by a cell, the fluorescence signal was greatly reduced and the fit of the autocorrelation curve did not provide reliable values for D (Fig. 33C). It was concluded that free Brownian diffusion occurred only in the liquid blood fraction and that the complete or partial obstruction of V_{obs} resulted in a loss of signal intensity.

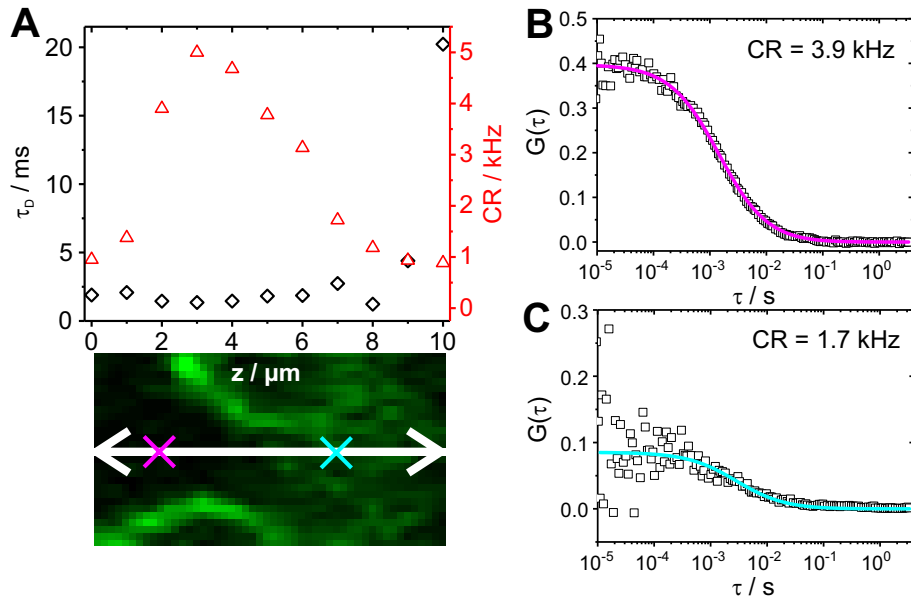


Figure 33: NIR-FCS measurements of **PB1** in the stained blood cell suspension (BCS). A) Diffusion time (τ_D) and fluorescence intensity (count rate, CR) for FCS measurements of **PB1** performed at z -positions ranging from 0 to 10 μm depth of penetration. The x, z -confocal image below the graph depicts whether a corresponding z -position was occupied or not. B) Autocorrelation curve recorded at a cell-free position (pink crosshairs in A)) in 2 μm penetration depth. The fitting yielded $D_{\text{PB1, BCS}} = 21.5 \mu\text{m}^2 \text{s}^{-1}$. C) Autocorrelation curve measured at an occupied spot (cyan crosshairs in A)) in 7 μm penetration depth. CR was decreased and fitting yielded $D_{\text{PB1, BCS}} = 11.4 \mu\text{m}^2 \text{s}^{-1}$. Fitting with a model for one type of freely diffusing species (Eq. 2.9) was performed from a lag time of 10 μs and did not include a triplet contribution. Diffusion coefficients were calculated assuming that V_{obs} did not depend on the measurement position.

FCS is extremely sensitive to spherical aberrations caused by a mismatch of refractive indices especially as the objective lens is optimized for water with $n_{\text{water}} = 1.33$. [281] Red blood cells were reported to show a refractive index of $n_{\text{RBC}} = 1.399$. [282] Thus, passing the laser beam through a cell might lead to an increase in V_{obs} rendering the transfer of its dimensions from aqueous calibration measurements inapplicable (Section 7.1). Consequently, the calculation of accurate diffusion coefficients would be impossible. Such a scenario in which V_{obs} was positioned above a cell was therefore investigated. In accordance with Figure 33C, a measurement performed at a cell-occupied spot yielded a low average fluorescence signal and a noisy autocorrelation curve (Fig. 34A-C). At an unoccupied measurement position above this very cell, in contrast, a good autocorrelation curve was measured (Fig. 34D-F). Here, the diffusion coefficient of $19.3 \mu\text{m}^2 \text{s}^{-1}$, calculated with dimensions of V_{obs} as obtained from the calibration in water, closely matched $D_{\text{PB1, water}}$. It was hence concluded that laser penetration through one layer of cells did not distort the observation volume.

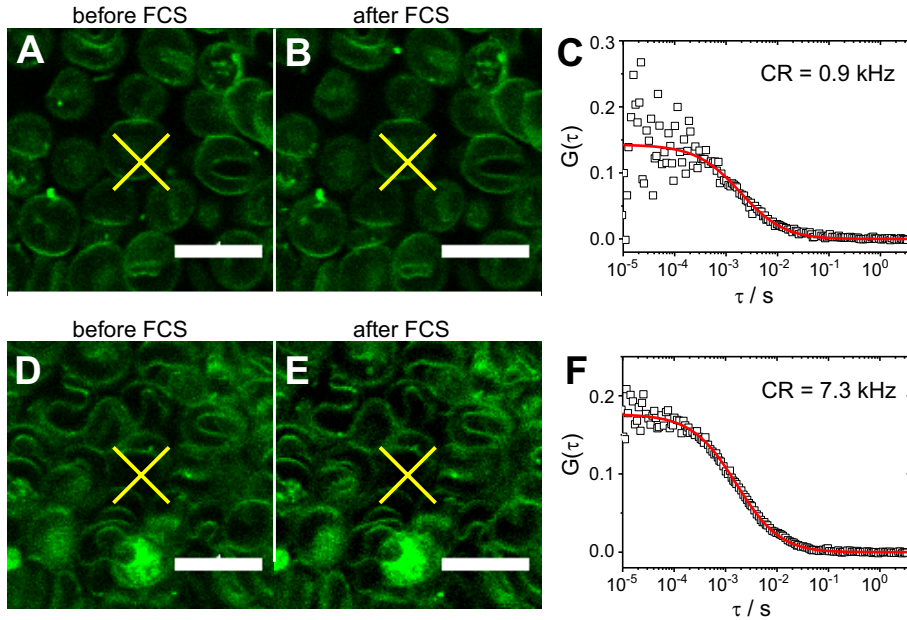


Figure 34: Confocal images with indicated FCS measurement positions (yellow crosshairs) at $1 \mu\text{m}$ (A, B) and $4 \mu\text{m}$ (D, E) depth of penetration. A) and D) were recorded before the FCS measurement and B) and E) were recorded after the FCS measurement. C) The autocorrelation curve shows a low CR and fitting yielded $D_{\text{PB1, BCS}} = 16.6 \mu\text{m}^2 \text{s}^{-1}$. F) The fit applied to the autocorrelation curve above one layer of cells yielded $D_{\text{PB1, BCS}} = 19.3 \mu\text{m}^2 \text{s}^{-1}$ at a high CR. Fitting with a model for one type of freely diffusing species (Eq. 2.9) was performed from a lag time of $10 \mu\text{s}$ and did not include a triplet contribution. Diffusion coefficients were calculated assuming that V_{obs} did not depend on the measurement position. Scale bar: $10 \mu\text{m}$.

In summary, NIR-FCS measurements in static human blood i) required positioning of V_{obs} in a cell-free spot, ii) were still reliable if this spot was located above one layer of cells and iii) were best performed close to the cover slip surface, *i.e.* at a depth of penetration of up to $10 \mu\text{m}$. Abiding by these criteria yielded autocorrelation curves that could be fitted with one type of freely diffusing fluorescent species (Eq. 2.9) as represented by Figure 35. Nonetheless, the

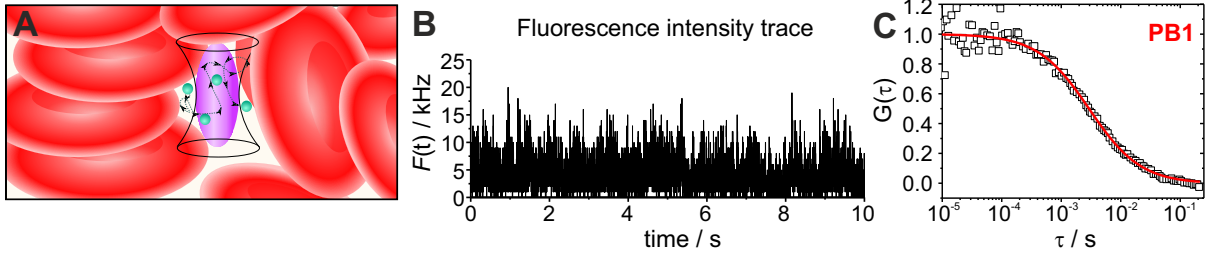


Figure 35: NIR-FCS measurements of **PB1** in static human blood. A) In the crowded environment of blood cells, V_{obs} has to be positioned in a cell-free spot in order to monitor the diffusion of **PB1**. B) Excerpt of the fluorescence intensity trace in a cell-free position of V_{obs} . C) For analysis, small time fragments (120 repetitions of 1 s each) were autocorrelated and averaged. The average autocorrelation curve was fitted with a model for one type of freely diffusing species (Eq. 2.9) without triplet contribution and yielded $\tau_D \approx 3000 \mu\text{s}$. Under the assumption that V_{obs} shows identical dimensions as determined in the calibration measurement, $D_{\text{PB1, static blood}} = 10.2 \mu\text{m}^2 \text{s}^{-1}$ was determined.

time-consuming and tedious search for appropriate positions greatly hampered the feasibility of such measurements.

7.2.2 Flowing blood

It was hypothesized that the requirement of searching for appropriate measurement positions could be circumvented by introducing a directed movement to the blood. By applying a flow, a dependence on measurement position should be abrogated since the cells would occupy V_{obs} only temporarily. To test this hypothesis, **PB1** was mixed with heparin-treated human blood at a concentration of 8 nM. With the help of a syringe pump, the **PB1** containing blood was then let through a microchannel at an extremely low flow velocity of $50 \mu\text{L h}^{-1}$. The microchannel contained a cover glass bottom through which the laser was focused into the sample. NIR-FCS measurements were performed at a depth of penetration of $10 \mu\text{m}$ (Fig. 36A). The analysis of the fluorescence intensity time trace revealed an alternation between high and low intensity segments (Fig. 36B). The high intensity segments lasted for durations of 0.5 to several seconds. They were interrupted by low signal intervals. A similar reduction in signal intensity had been observed when V_{obs} was positioned within a cell in static blood. Thus, it was assumed that the low intensity segments constituted times in which V_{obs} was occupied by a cell. In consequence, during the high intensity segments V_{obs} was presumably free of cells and accessible for the fluorescent species.

The experimental autocorrelation curve recorded under these conditions showed two decays (Fig. 36C). The first one was at around a few milliseconds and was presumably caused by the diffusion and flow of **PB1** through the FCS observation volume. The second decay was at a few hundred milliseconds and thus in line with the alternation of high and low intensity segments. It was therefore likely to be caused by the movement of blood cells. Under the assumption that the two decay times derived from the contributions of **PB1** and the blood cells, an analytical model was derived that took into account the diffusion and flow of these two differently sized species. The basis of this model was an independent expression for each

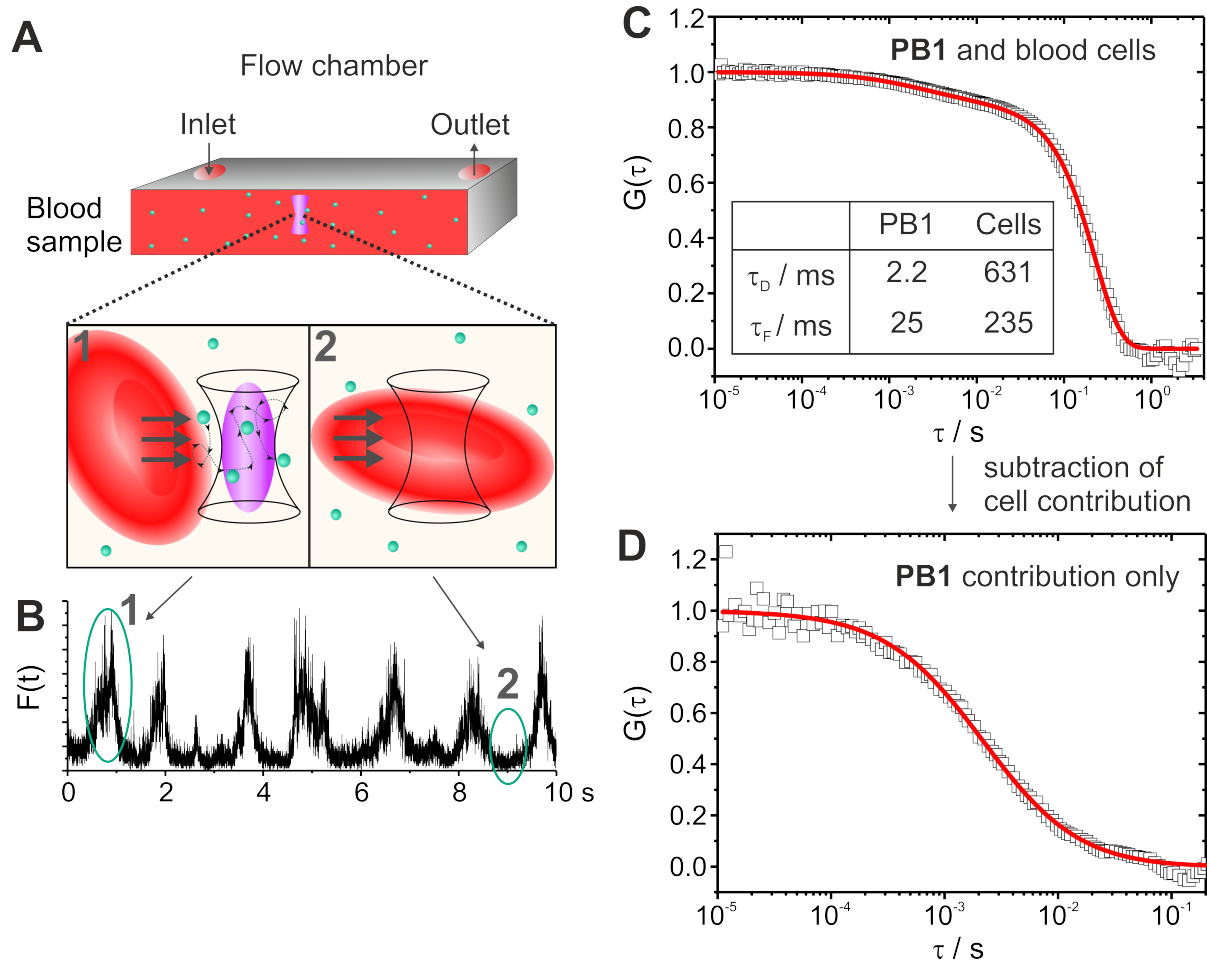


Figure 36: A) Setup and scheme of NIR-FCS measurements in flowing blood. The FCS observation volume was either free (1) or occupied (2) by a blood cell. B) Correspondingly, the fluorescence intensity time trace revealed high (1) and low (2) intensity time segments. C) The experimental autocorrelation curve (squares) of **PB1** in the blood flow was fitted (line) with an analytical model (Eq. 7.1) combining standard and inverse FCS thus taking into account contributions of fluorescent species and blood cells. The inset shows the diffusion and flow residence times of **PB1** and cells as derived from the fit. D) The extracted fit parameters were used to subtract the cells' contribution and obtain an autocorrelation curve (squares) resembling that of a standard FCS experiment. A fit with Equation 2.18 (line) yielded the diffusion properties of the fluorescent species.

species which considered the combined motion by diffusion and flow as introduced in Section 2.4.2 (Eq. 2.18). The contribution of the fluorescent species **PB1** could hence be directly resolved. The second contribution had to be thoroughly considered as it stemmed from an unlabeled species, the blood cells. Typically, unlabeled molecules do not appear as a separate contribution in FCS autocorrelation curves. In this case, however, the large size of a red blood cell ($\approx 8 \mu\text{m}$ in diameter, $\approx 2 \mu\text{m}$ in thickness), which exceeded the dimensions of V_{obs} , and their high percentage led to a complete expulsion of the fluorescent species in certain time segments. Thus, their contribution could not be ignored.

In inverse FCS, a modification of standard FCS, unlabeled species are resolved by autocorrelating the negative dips that their movement through V_{obs} introduces in the fluorescence intensity trace of a strongly fluorescent medium (Section 2.4.5). [106] Inverse FCS autocorrelation curves can be fitted with a classical fit function (Eq. 2.9) and thereby yield correct values for the size of the unlabeled particle. Following this argument, the passage of the blood cells through V_{obs} should be treated similarly to that of a fluorescent species, *i.e.* with a term for diffusion and flow as represented by Equation 2.18. Therefore, the following combined expression was derived:

$$G_{\text{total}}(\tau) = \frac{1}{N} (f_1 \cdot G_{\text{D1}}(\tau) \cdot G_{\text{F1}}(\tau) + f_2 \cdot G_{\text{D2}}(\tau) \cdot G_{\text{F2}}(\tau)) =$$

$$\frac{1}{N} \left(\frac{f_1}{\left(1 + \frac{\tau}{\tau_{\text{D1}}}\right) \sqrt{1 + \frac{\tau}{(S^2 \tau_{\text{D1}})}}} \exp \left[\frac{\left(\frac{\tau}{\tau_{\text{F1}}}\right)^2}{1 + \frac{\tau}{\tau_{\text{D1}}}} \right] + \frac{f_2}{\left(1 + \frac{\tau}{\tau_{\text{D2}}}\right) \sqrt{1 + \frac{\tau}{(S^2 \tau_{\text{D2}})}}} \exp \left[\frac{\left(\frac{\tau}{\tau_{\text{F2}}}\right)^2}{1 + \frac{\tau}{\tau_{\text{D2}}}} \right] \right) \quad (7.1)$$

$G_{\text{D}}(\tau)$ and $G_{\text{F}}(\tau)$ denote the diffusion and flow terms of the fluorescent species **PB1** (“1”) and blood cells (“2”), respectively. f_1 and f_2 are the fractional contributions. Although blood cells and **PB1** flowed with the same velocity v , their tremendous size mismatch resulted in different flow residence times τ_{F1} and τ_{F2} . The size of the fluorescent species was much smaller than the lateral dimension (r_0) of the FCS observation volume. The flow residence time of **PB1** was thus related to the flow velocity by $\tau_{\text{F1}} = r_0/v$. On the contrary, the average size of red blood cells exceeded r_0 by a factor of about 5 to 10. Therefore, the flow residence time τ_{F2} was approximated by $\tau_{\text{F2}} = (r_0 + R_{\text{H}})/v$ and dominated by R_{H} rather than r_0 . The experimental autocorrelation curve measured for **PB1** in the blood flow could be fitted with Equation 7.1 (Fig. 36C). The fit parameters (inset in Fig. 36C) revealed that diffusion and flow times of the cells were orders of magnitude larger than those of the fluorescent **PB1**.

However, as apparent from Figure 36C, the second decay dominated the autocorrelation curve so that the first relevant decay was barely visible. Thus, a mathematical operation was performed to subtract the cell contribution from the experimental curve in Figure 36C. The obtained autocorrelation curve contained only the first decay and resembled autocorrelation

curves of standard FCS measurements.

$$G_{\text{processed}}(\tau) = G_{\text{D1}}(\tau) \cdot G_{\text{F1}}(\tau) = \frac{G_{\text{total}}(\tau) \cdot N - f_2 \cdot G_{\text{D2}}(\tau) \cdot G_{\text{F2}}(\tau)}{f_1} =$$

$$\left(\frac{1}{f_1}\right) \left(G_{\text{total}}(\tau) \cdot N - \frac{f_2}{\left(1 + \frac{\tau}{\tau_{\text{D2}}}\right) \sqrt{\left(1 + \frac{\tau}{S^2 \tau_{\text{D2}}}\right)}} \exp\left[\frac{\left(\frac{\tau}{\tau_{\text{F2}}}\right)^2}{1 + \frac{\tau}{\tau_{\text{D2}}}}\right] \right) \quad (7.2)$$

Values for f_1 , f_2 , τ_{D2} and τ_{F2} were derived from the previous fit of the original autocorrelation curve with Equation 7.1. Figure 36D shows the autocorrelation curve of **PB1**, devoid of cell effects. The processed autocorrelation curve could be fitted with Equation 2.18 and yielded a diffusion time for **PB1** of 2.2 ms. Using the lateral dimension of the observation volume r_0 as obtained from the calibration in aqueous solution, a diffusion coefficient of $D_{\text{PB1, blood}} = 14.4 \mu\text{m}^2 \text{s}^{-1}$ was calculated.

In summary, the applicability of the fit model in Equation 7.1 and the values of the derived fit parameters strongly supported the postulated hypothesis that the two decay times were indeed caused by the motion of **PB1** and the blood cells. The advantage of applying flow to the blood sample in order to continuously move the blood cells through V_{obs} and thereby create cell-free time segments could hence be confirmed.

7.2.3 Increased viscosity explains diffusion slowdown

A comparison of the diffusion coefficients of **PB1** in blood ($D_{\text{PB1, blood}} = 14.4 \mu\text{m}^2 \text{s}^{-1}$) and water ($D_{\text{PB1, water}} = 20.4 \mu\text{m}^2 \text{s}^{-1}$) showed a deviation that undoubtedly went beyond the measurement uncertainty. Since the diffusion of **PB1** was limited to the liquid blood fraction, the cause for this deviation had to be related to the properties of the plasma. A direct effect of the blood cells on $D_{\text{PB1, blood}}$ was assumed to be unlikely as the derivation of accurate diffusion coefficients in the presence of blood cells could be demonstrated in Section 7.2.1. Therefore, the diffusion behavior of **PB1** in undiluted human plasma was investigated (Fig. 37A). The obtained diffusion coefficient of $D_{\text{PB1, plasma}} = 14.3 \mu\text{m}^2 \text{s}^{-1}$ matched $D_{\text{PB1, blood}}$. Importantly, this indicated that the FCS measurements of **PB1** in the blood flow delivered accurate results. Nevertheless, three possible effects were examined to determine the cause of the effective slowdown by a factor of 1.43 ($D_{\text{PB1, water}}/D_{\text{PB1, plasma}}$).

First, the possible occurrence of a refractive index mismatch between water and plasma was analyzed. Due to a high concentration of proteins, ions and other solutes, plasma might exhibit a slightly increased refractive index with respect to water. Furthermore, plasma proteins might lead to enhanced scattering. The combination of both effects could lead to an increased size of V_{obs} , especially at higher depths of penetration. A relative size increase of V_{obs} would then lead to prolonged diffusion times, which, without a proper correction, would result in erroneously reduced diffusion coefficients. To address this issue, FCS autocorrelation curves were recorded

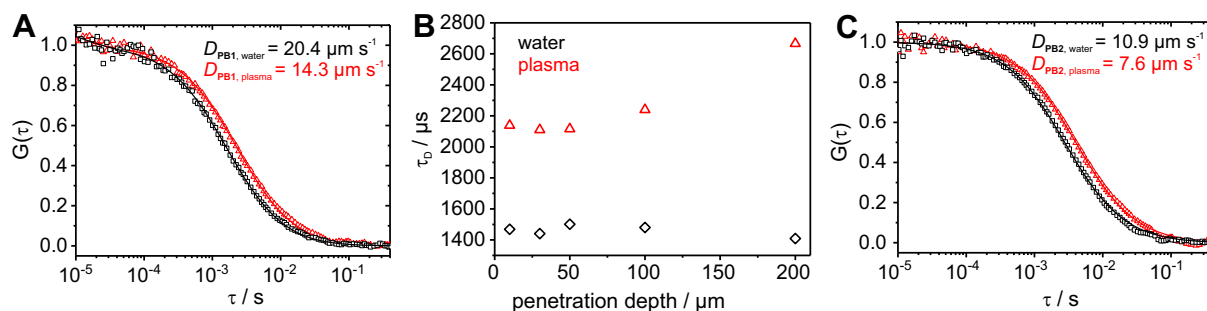


Figure 37: A) Normalized autocorrelation curves of **PB1** in water (black squares) and plasma (red triangles). Fitting (line) was performed with a one component fit (Eq. 2.20) including triplet. B) The diffusion times (τ_D) of **PB1** measured at different depths of penetration in water (black diamonds) and plasma (red triangles) are plotted. An increase in τ_D indicates an increase of V_{obs} due to a refractive index mismatch or scattering effects. C) Normalized autocorrelation curve of **PB2** in water (black squares) and plasma (red triangles). Fitting (line) was performed with a one component fit (Eq. 2.20). The diffusion coefficients for panel (A) and (C) were calculated assuming equally sized V_{obs} in water and plasma and are depicted in the respective insets.

at different depths of penetration in water and plasma (Fig. 37B). The results showed no change in the diffusion time of **PB1** for a depth of penetration of up to 50 μm in plasma. Thus, at a measurement position in 30 μm penetration depth in plasma the observation volume remained unaltered and equal dimensions of V_{obs} as determined by calibration in water could be assumed.

Second, many nanocarriers are reported to show an immediate adsorption of plasma proteins upon contact with blood (Section 6.2.1). The presence of a tightly bound protein corona would increase the hydrodynamic radius of **PB1** and thus its diffusion time in plasma compared to water. Using Stokes–Einstein relation (Eq. 2.11), the diffusion coefficient of **PB1** in plasma ($D_{PB1, plasma} = 14.3 \mu m^2 s^{-1}$) yielded a hydrodynamic radius of 16.2 nm assuming that **PB1** experienced the same viscosity in plasma as in water. That translated to an increase of $\Delta R_H = 4.8$ nm as compared to the value in water ($R_H = 11.4$ nm). In order to further investigate the possibility of an adsorbed protein layer, a second larger polymer brush (**PB2**) was employed. The diffusion coefficient of **PB2** in water was $10.9 \mu m^2 s^{-1}$ (23°C) as determined by multi-angle DLS and yielded a respective R_H of 21.3 nm (Appendix 9). In plasma, the diffusion coefficient was reduced by a factor of 1.43 ($D_{PB2, plasma} = 7.6 \mu m^2 s^{-1}$) translating into $\Delta R_H = 9.4$ nm (Fig. 37C). Considering the analogous synthetic identity of both brushes a protein adsorption layer would be expected to consist of the same proteins and therefore yield a similar ΔR_H . However, since ΔR_H was almost twice as large for **PB2** in comparison to **PB1** the formation of a tightly bound protein corona seemed unlikely.

Third, the viscosity difference between plasma and water was evaluated as a potential cause for diffusion slowdown. Due to its high protein content, plasma has a higher macroscopic viscosity than water. The macroscopic viscosity was determined with rolling ball viscometer measurements and yielded $\eta_{plasma} = 1.48$ mPa·s at 22°C and 1.35 mPa·s at 25°C.⁶ Certainly,

⁶Rolling ball viscosimetry measurements were performed by Dr. Svenja Morsbach using a LOVIS 2000 M microviscosimeter (Anton Paar, Graz, Austria).

these values could not be directly transferred to the viscosity experienced by small species such as **PB1** and **PB2**. Their diffusion slowdown was presumably caused by an increase in the local viscosity (microviscosity). The question whether micro- or macroviscosity affect the diffusion of a certain tracer is not trivial. Several reports suggest that a transition between micro- and macroviscosity occurs, depending on the size and nature of the studied tracer and the surrounding medium. [283,284] For the practical application in blood and plasma measurements, however, it was sufficient to correct for an effective viscosity increase. The fact that both brushes showed the same diffusion slowdown of 1.43 in plasma compared to water strongly suggested that the effective viscosity was increased by this very factor.

In summary, neither a size increase of the brushes due to protein adsorption nor a refractive index mismatch took effect at the applied measurement conditions. It was thus concluded that the relative slowdown in plasma and blood with respect to water was caused by a higher effective viscosity in plasma. To account for the altered viscosity when deriving the hydrodynamic radius with Stokes-Einstein equation (Eq. 2.11), the ratio $D_{\mathbf{PB1}, \text{water}}/D_{\mathbf{PB1}, \text{plasma}}$ was used to determine $\eta_{\text{plasma}} = 1.34 \text{ mPa}\cdot\text{s}$ (23°C) based on $\eta_{\text{water}} = 0.94 \text{ mPa}\cdot\text{s}$ (23°C).

7.3 Applications

In the previous section, a protocol for NIR-FCS measurements in flowing blood was established. By fitting the autocorrelation data with the analytical expression in Equation 7.1 and by accounting for an increased effective viscosity of the blood, the diffusion properties of the polymer brush **PB1** could be accurately determined. This protocol was hence applied to measure the diffusion of single dye molecules as well as of a protein adsorbing particle and to investigate the loading stability of micelles in blood.

7.3.1 Sensitivity down to single dye molecules

One important trademark of FCS is its ability to monitor diffusion with a sensitivity down to the level of single dye molecules. What is nowadays regarded as state-of-the-art in aqueous media is not guaranteed in a complex and crowded medium such as blood. However, with the goal of applying NIR-FCS to study the stability of nanocarriers in blood such sensitivity to weakly fluorescing single dye molecules was required. The thus far measured polymer brush **PB1** was relatively large ($R_{\text{H}} = 11.4 \text{ nm}$) and labeled with approximately three dye molecules. A single dye molecule such as DBCO-functionalized IRDye 800CW, however, exhibited a hydrodynamic radius of 1.0 nm ($D_{\text{NIR dye, water}} = 236 \mu\text{m}^2 \text{ s}^{-1}$) and a three times lower fluorescence brightness (Fig. 38A).

Prior to the investigation of IRDye 800CW in blood, the dye was measured in undiluted human plasma (Fig. 38A). The obtained diffusion coefficient yielded $D_{\text{NIR dye, plasma}} = 38.1 \mu\text{m}^2 \text{ s}^{-1}$ which translated to $R_{\text{H}} = 4.3 \text{ nm}$ assuming an increased viscosity of $\eta_{\text{plasma}} = 1.34 \text{ mPa}\cdot\text{s}$ (23°C). This marked size increase was not surprising as NIR dyes with cyanine structures such as IRDye 800CW were reported to bind to albumin and other plasma proteins. [285,286]

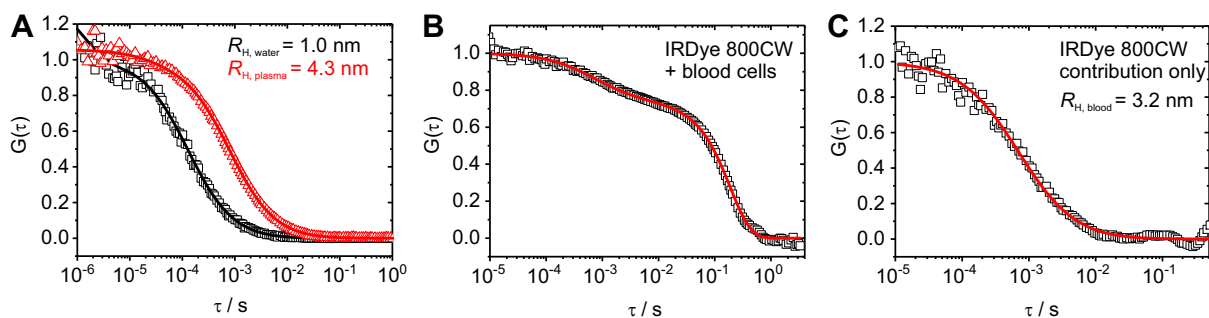


Figure 38: A) Normalized autocorrelation curves of DBCO-functionalized IRDye 800CW in water (black squares) and plasma (red triangles). Fitting (line) was performed with a one component fit (Eq. 2.20) including triplet. B) The NIR-FCS measurement of IRDye 800CW-DBCO in the blood flow (velocity of $50 \mu\text{L h}^{-1}$) yielded an experimental autocorrelation curve (black squares) that was fitted with Equation 7.1, comprising contributions from the fluorescent dye and blood cells. C) Processed autocorrelation curve showing the contribution of IRDye 800CW-DBCO (Eq. 7.2). The fit yielded $D_{\text{NIR dye, blood}} = 50.0 \mu\text{m}^2 \text{s}^{-1}$.

Accordingly, the detection of a fluorescent species with $R_{\text{H}} = 4.3 \text{ nm}$ in plasma strongly indicated a dye-protein complex formation. This could be confirmed by measuring a mixture of IRDye 800CW and human serum albumin (HSA), the most abundant plasma protein. Upon viscosity correction with the intrinsic viscosity of HSA ($4.2 \text{ cm}^3 \text{ g}^{-1}$, see Ref. [267]), a species with a hydrodynamic radius of 4.0 nm was detected which matched the size of a dye-albumin complex.

The dye was then diluted with blood at 10 nM concentration and its diffusion was measured in the presence of flow. Figure 38B and C show the original and processed autocorrelation data that were fitted with Equation 7.1 and Equation 7.2, respectively. The calculated R_{H} of 3.2 nm , though slightly smaller than that of the species observed in plasma, indicated the diffusion of protein-bound dye molecules. Of note, it was reported that albumin contains at least two binding sites for NIR cyanine dyes that differ in their affinities towards the dyes. [287] However, the several-fold molar excess of plasma proteins with respect to dye molecules in blood or plasma rendered the simultaneous binding at both binding sites unlikely. Thus, it was concluded that NIR-FCS measurements allowed the detection of weakly fluorescing species (*e.g.* single dye-protein complexes) in flowing blood.

7.3.2 Investigation of protein adsorption in flowing blood

The formation of a protein corona on a nanocarrier's surface influences its *in vivo* fate as it can induce aggregation, shield attached ligands and attract phagocytic cells (Section 6.2.1). To test whether the NIR-FCS approach could yield information on the protein corona directly from a blood sample, a protein adsorbing quantum dot was measured. The employed quantum dot exhibited an anionic surface and showed an emission maximum at 800 nm (Qdot 800). In water, Qdot 800 revealed a hydrodynamic radius of 9.4 nm ($D_{\text{Qdot 800, water}} = 24.5 \mu\text{m}^2 \text{s}^{-1}$) as determined by NIR-FCS (Fig. 39A). To evaluate the interaction with proteins, the size of Qdot 800 in undiluted human plasma was determined. Fitting of the autocorrelation data yielded $D_{\text{Qdot 800, plasma}} = 6.3 \mu\text{m}^2 \text{s}^{-1}$ which was translated into $R_{\text{H}} = 25.8 \text{ nm}$ assuming a viscosity

of $\eta_{\text{plasma}} = 1.34 \text{ mPa}\cdot\text{s}$ (23°C) (Fig. 39A). The protein corona thus showed a thickness of $\Delta R_{\text{H}} = 16.4 \text{ nm}$. This value differed from findings from the Nienhaus group who employed FCS to measure protein adsorption on differently functionalized quantum dots. [268,269] They reported on the adsorption of a protein monolayer with a thickness of $\approx 6 - 7 \text{ nm}$ in serum and $\approx 3 \text{ nm}$ in the sole presence of HSA. In order to determine if ΔR_{H} could have been caused by the aggregation of several particles, the fluorescence brightnesses in water and plasma were compared. In both conditions, ε was found to be identical. Thus, it was concluded that the determined ΔR_{H} of 16.4 nm did not derive from aggregation and instead indicated the adsorption of more than one protein layer on the particle's surface (Fig. 39B).

The particle was then analyzed by NIR-FCS in flowing blood at a concentration of 3 nM . The original autocorrelation curve showing contributions of fluorescent particles and cells was fitted with Equation 7.1 and yielded $D_{\text{Qdot 800, blood}} = 8.4 \mu\text{m}^2 \text{ s}^{-1}$ from which $R_{\text{H}} = 19.3 \text{ nm}$ was retrieved. For ease of visualization, the processed autocorrelation curve with its corresponding fit (Eq. 7.2) is depicted in Figure 39D. Clearly, the size of Qdot 800 dispersed in blood was markedly larger than in water which strongly hinted at the simultaneous diffusion with adsorbed proteins. The thickness of the protein corona, however, was found to be reduced to $\Delta R_{\text{H}} = 9.9 \text{ nm}$. This reduction could have been caused by variations in the composition of the applied protein sources, citrate-containing plasma *vs.* heparin-treated full blood. In addition, shear stress exerted by the application of flow, though extremely low, could have had an effect on the protein corona, especially on loosely bound proteins. [288] Accordingly, the different corona thicknesses found in plasma and blood emphasized the importance of conducting experiments under conditions as close as possible to *in vivo* conditions, *e.g.* in blood rather than plasma and in the presence of flow rather than in static liquids.

7.3.3 Loading stability of micelles in flowing blood

To demonstrate the applicability of the NIR-FCS method to study the behavior of nanocarriers in blood, the loading stability of a potential nanocarrier system was investigated. [289] The system consisted of core-crosslinked micelles which were assembled from amphiphilic block copolypept(o)ides made of polysarcosine and poly-S-alkylsulfonyl cysteine.⁷ The micelles were loaded with IRDye 800CW, which was used as a model for a small drug molecule. The dye was either covalently (**PM1**) or non-covalently (**PM2**) attached to the micelles. A first NIR-FCS characterization in water revealed hydrodynamic radii for **PM1** and **PM2** of 51 nm and 44 nm , respectively (Fig. 40A). These values were in accordance with the multi-angle DLS data of the unloaded micelles ($R_{\text{H, PM}} = 45 \text{ nm}$) and indicated that the IRDye 800CW molecules were indeed loaded to the micelles (Appendix 9). Nonetheless, the obtained autocorrelation data could only be accurately fitted with a model for two diffusing fluorescent species (Eq. 2.20). As the second type of fluorescent species revealed an $R_{\text{H}} \approx 1 \text{ nm}$, it was attributed to the free dye. The apparent fractions of the free dye in water were 6% for **PM1** and 23% for **PM2**.

⁷Core-crosslinked micelles were synthesized and characterized by Olga Schäfer.

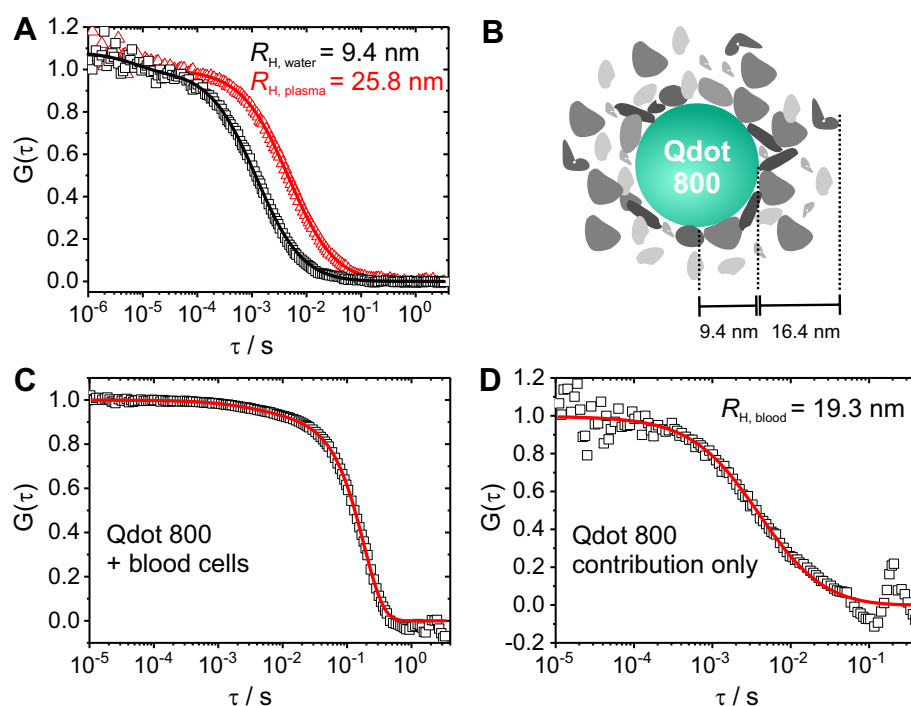


Figure 39: A) Normalized autocorrelation curves of carboxyl-functionalized Qdot 800 in water (black squares) and plasma (red triangles). Fitting (line) was performed with a one component fit (Eq. 2.20) including triplet. The obtained hydrodynamic radii are presented in the inset. B) Schematic of Qdot 800 covered with proteins. The hydrodynamic radius of Qdot 800 and the thickness of its protein corona are indicated. The NIR-FCS measurement of Qdot 800 in the blood flow (velocity of $50 \mu\text{L h}^{-1}$) yielded C) an experimental autocorrelation curve (black squares), fitted with Equation 7.1 (line), from which D) a processed autocorrelation curve devoid of cell contribution was extracted.

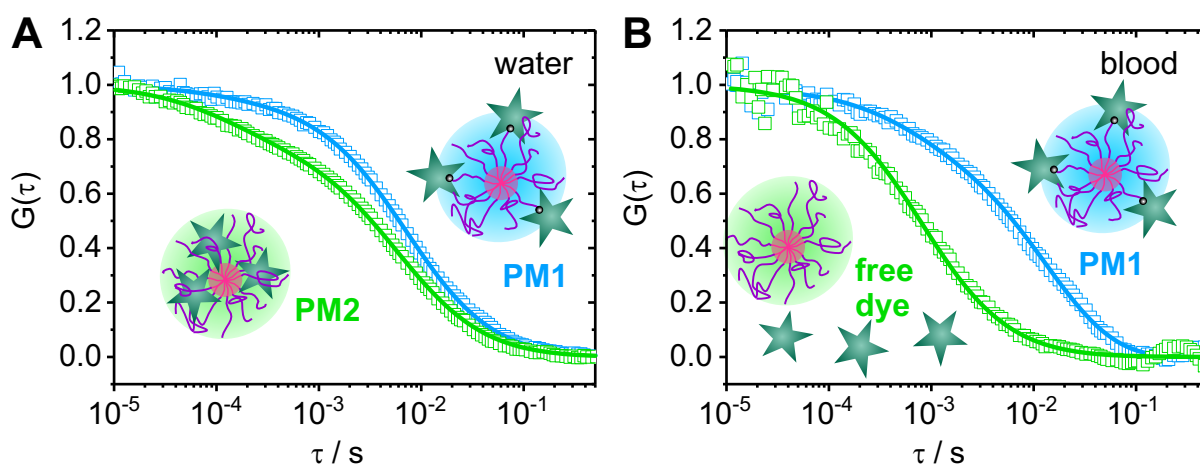


Figure 40: NIR-FCS studies on the loading stability of core-crosslinked micelles in blood. Normalized autocorrelation curves (symbols) and the corresponding fits (lines) are shown for micelles that were either covalently (**PM1**, blue color) or non-covalently (**PM2**, green color) loaded with IRDye 800CW. A) Measurements in water. The dye was mainly loaded to the micelles and only a small fraction of free dye was detected for both systems. B) Measurements in the blood flow (velocity of $50 \mu\text{L h}^{-1}$) upon incubation with blood for 30 h (at 4°C). The dye was fully released from **PM2** but still loaded to **PM1**.

PM1 and **PM2** were then diluted with heparin-treated human blood and incubated for 30 hours. Afterwards, the micelles were subjected to NIR-FCS measurements in flowing blood. The processed autocorrelation curves devoid of cell contributions are shown together with their corresponding fits in Figure 40B. After subtraction of the cell contribution it became clear that the processed autocorrelation curve for **PM1** showed two decay times. Fitting with Eq. 8.1 yielded two types of fluorescent species with different hydrodynamic radii of 55 nm and 2.9 nm for **PM1**. The larger species corresponded to dye-loaded micelles and the smaller one to free dye molecules that have formed complexes with plasma proteins (Section 7.3.1). Furthermore, the apparent fraction of free dye had increased to 18%. Two causes for this increase were possible. Either it was the result of a partial degradation of the peptide-dye bond and/or it indicated the presence of a small fraction of dye molecules that were non-covalently attached and thus dissociated from the micelles in blood. The dominant fraction of the dye cargo, however, was still loaded on the micelles. The identical size of the micelles in water and blood pointed towards their retained integrity upon the extended incubation in blood. The fit to the processed autocorrelation curve measured for **PM2** in blood (Fig. 40B) revealed the presence of only one type of fluorescent species with R_H of 3.4 nm. This indicated a complete loss of the non-covalently attached dye cargo from the micelles. This finding was in line with observations on the loss of encapsulated dexamethasone from core-crosslinked polymeric micelles *in vivo* and stressed the necessity to carefully consider the mode of cargo loading with respect to stability and controlled release. [290]

8 Materials and methods

8.1 Materials

8.1.1 Chemicals

Further chemicals that were also employed in Part II are listed in Materials 5.1.1.

Albumin from human serum, lyophilized, globulin-free (purity $\geq 99\%$)	Sigma Aldrich
Alexa Fluor 790 succinimidyl ester, #A30051	Thermo Fisher Scientific
Dil stain, #D282	Thermo Fisher Scientific
D(+)-glucose, anhydrous	Carl Roth
IRDye 800CW dibenzocyclooctyne, #929-50000	LI-COR Biotechnology (Lincoln, NE, USA)
Qdot 800 ITK, carboxylated quantum dots, #Q21371MP	Thermo Fisher Scientific

8.1.2 Glassware and Disposables

Further glassware and disposables that were also employed in Part II are listed in Materials 5.1.4.

Braun Injekt 5 mL, luer, #4606051V	B. Braun (Melsungen, Germany)
coverslips for sticky-Slides, #1.5H ($170 \pm 5 \mu\text{m}$, D 263 M Schott glass)	Ibidi
Luer fitting, 0.8 mm barb to female, #7318221	BioRad (Hercules, CA, US)
Luer fitting, 0.8 mm barb to male, #7318224	BioRad
S-Monovette, 4.5 mL, lithium heparin	Sarstedt
sticky-Slide I luer (0.1 x 5 x 48.2 mm)	Ibidi
Tygon tubing E-3603 (inner diameter 1.6 mm, outer diameter 3.2 mm, wall 0.8 mm)	Saint-Gobain Performance (Courbevoie, France)

8.1.3 Biological material

Human blood plasma: Plasma was received from ten healthy donors in the Mainz University Medical Center in accordance with the local ethics guidelines. After addition of sodium citrate the donated blood was separated by centrifugation. The plasma was pooled and aliquots were stored at -80°C . After thawing, the plasma was centrifuged at $20,000 \times g$ for 30 min to remove any residual protein precipitates. The protein concentration was estimated to lie between 65 to 70 g L^{-1} .

Human blood: For FCS measurements in full human blood, a male healthy donor volunteered to donate blood. The blood was collected in a heparin-coated tube to prevent clotting and was

either immediately used or stored at 4°C for up to one day. For FCS and CLSM measurements in the stained blood cell suspension, human blood from a buffy coat preparation (working group of Prof. Dr. K. Landfester, MPI-P, Mainz) was used and further treated as described in Section 8.2.5.

8.1.4 Nanocarriers obtained from cooperation partners

Polymer brushes: The brushes were obtained from Meike Schinnerer from the working group of Prof. Dr. M. Schmidt (Institute of Physical Chemistry, Johannes Gutenberg University, Mainz). Information on the synthesis route and characterization can be found in Ref. [[280], in preparation] and in Appendix 9.

Polymeric micelles: The micelles were obtained from Olga Schäfer from the working group of Dr. M. Barz (Institute of Organic Chemistry, Johannes Gutenberg University, Mainz). Information on the synthesis route and characterization can be found in Ref. [[280], in preparation] and in Appendix 9.

8.2 Methods

8.2.1 Software and data analysis

Autocorrelation analysis of FCS data was performed with ZEN 2.1 SP3 software (Carl Zeiss, Jena, Germany) or with OriginPro 9.1. Confocal images were processed with the open-source software ImageJ. [224] Charts and plots were prepared with OriginPro 9.1. Figures were prepared with Corel Draw X7.

8.2.2 NIR-FCS setup

The NIR-FCS experimental setup is based on an LSM 880 confocal microscope (Carl Zeiss, Jena, Germany)(compare Fig. 32A). Fluorescence was excited by a Ti-sapphire laser (Mai Tai, Newport) tunable in the range 780 - 920 nm and delivering ≈ 125 fs pulses at 80 MHz repetition rate with ≈ 1 W average power. The laser was operated at 780 nm and strongly ($\approx 10,000$ times) attenuated using neutral density filters and an acousto-optical attenuator. The excitation laser beam was passed through a clean-up filter and a dichroic mirror and focused into the sample by a high numerical aperture water immersion objective (C-Apochromat 40x / 1.2 W, Carl Zeiss, Jena, Germany). The fluorescence was collected with the same objective and after passing through the dichroic mirror (LP800) and a confocal pinhole (54 μm) delivered to the detection unit. After passing through two stacked band pass emission filters from 800 - 870 nm, the fluorescence was detected by an avalanche photodiode detector (Excelitas, Waltham, MA, USA), integrated in a PicoQuant FLIM and FCS upgrade kit and fiber coupled to the microscope.

8.2.3 NIR-FCS static measurements

FCS measurements in static conditions (water, plasma and blood) were performed in an eight-well chambered Nunc microscopy slide at 23°C. Measurements were performed at 30 - 60 μm (water), 30 μm (plasma) and 10 μm (blood) depth of penetration. The total measurement time per sample ranged between 60 and 900 s and consisted of time segments (repetitions) of 10 to 30 s each. The time-dependent fluctuations of the fluorescence intensity caused by the diffusion of the fluorescent species through the observation volume were recorded and autocorrelated (Eq. 2.7). Fitting of these experimental autocorrelation curves was performed with ZEN 2.1 SP3 software. Hereby, repetitions which revealed the occasional presence of large aggregates were deselected prior to the fitting.

8.2.4 NIR-FCS flow measurements

Flow was generated with a syringe pump (kdScientific, Holliston, MA, USA). The syringe containing the diluted fluorescent sample was connected by a tube to a microchannel assembled from a single channel sticky slide and a glass cover slip. The dimensions of the channel were 0.1 \times 5 \times 48.2 mm in height, width and length. In order to calibrate the system, autocorrelation curves for **PB1** and IRDye 800CW were recorded in the same channels in the absence of flow.

For blood flow measurements, 3 mL of heparin-treated human blood containing fluorescent molecules/particles at low nanomolar concentrations were loaded into the syringe and a flow rate of 50 $\mu\text{L h}^{-1}$ was applied. The observation volume was positioned at 10 μm depth of penetration and the fluorescence signal was detected for 300 s in repetitions of 10 s each. The fitting of the experimental autocorrelation curves was performed with OriginPro 9.1 using the analytical expression for two types of species τ_{D1} (fluorescent molecules/particles) and τ_{D2} (cells) with their independent flow residence times τ_{F1} and τ_{F2} (Eq. 7.1). For the representation of the autocorrelation curve and respective fitting without cell contribution, the experimental data was processed with Equation 7.2, hereby substituting f_1 , f_2 , τ_{D2} and τ_{F2} with values from the previous fit with Equation 7.1. The processed autocorrelation curve was then fitted with Equation 2.18 delivering parameters for the diffusion and flow of the fluorescent species. In case of blood dispersed **PM1**, the processed autocorrelation curve was fitted with an analytical model for two types of fluorescent species τ_{D1} and τ_{D2} moving at one flow velocity:

$$G_{\text{processed}}(\tau) = \frac{1}{N} (f_1 \cdot G_{D1}(\tau) \cdot G_F(\tau) + f_2 \cdot G_{D2}(\tau) \cdot G_F(\tau)) =$$

$$\frac{1}{N} \left(\frac{f_1}{(1 + \frac{\tau}{\tau_{D1}}) \sqrt{(1 + \frac{\tau}{S^2 \tau_{D1}})}} \exp \left[\frac{(\frac{\tau}{\tau_F})^2}{1 + \frac{\tau}{\tau_{D1}}} \right] + \frac{f_2}{(1 + \frac{\tau}{\tau_{D2}}) \sqrt{(1 + \frac{\tau}{S^2 \tau_{D2}})}} \exp \left[\frac{(\frac{\tau}{\tau_F})^2}{1 + \frac{\tau}{\tau_{D2}}} \right] \right) \quad (8.1)$$

8.2.5 Staining of red blood cell membrane

Human blood was diluted with DPBS and centrifuged at $3,000 \times g$ for 3 min. The supernatant was carefully removed, including a viscous layer of leukocytes, and the remaining red blood cells were washed three times with 10 mL of DPBS. After the last washing step, 50 μL of packed red blood cells were dispersed in 4 mL DPBS and 1 mL of 5% glucose solution. To this dispersion, 50 μL of DiI (0.5 mg mL^{-1}) were added and the mixture was incubated at room temperature for 30 min. Next, the red blood cells were sedimented by centrifugation as described above and washed three times with DPBS. At the last step, 100 μL of DPBS were added to the packed red blood cells resulting in a hematocrit of $\approx 30\%$. For confocal imaging on the LSM 880 microscope, DiI was excited at 543 nm and the emission was detected with the integrated Quasar detector in the range from 553 to 633 nm. The pinhole was set to 38 μm . The average pixel dwell time was 1.5 μs and image resolution was 512 x 512 pixels.

Part IV

Monitoring nanocarrier-based delivery and release of RNA molecules by fluorescence correlation spectroscopy

9 Introduction

Nanocarrier-based drug delivery has opened up new avenues for the directed transport of sensitive or toxic drug payloads to target sites. However, the success of nanocarrier systems does not only depend on their long blood circulation time and accumulation at the diseased site, but also on their intracellular performance (Section 9.2). In this regard, efficient cellular uptake of the nanocarrier as well as intracellular release of the active compound are pivotal. With the sole requirement of a fluorescently labeled payload, intracellular FCS studies can potentially provide valuable information on the release process (Section 9.3). In this work, "proof-of-principle" experiments for the detection of intracellular release were performed on the example of siRNA molecules. The concept of RNA interference (RNAi), by which siRNA molecules work, will be elucidated and the need for nanocarrier-aided transport will be explained in Section 9.1.

9.1 Therapeutic strategy of RNA interference

The possibility of repressing gene activity on a post-transcriptional level by using long double-stranded (ds) RNA molecules was reported in 1998 by Fire and Mello who knocked down several genes in the nematode worm *Caenorhabditis elegans*. [291] However, it was only after Tuschl and his team realized that gene silencing could be achieved with a synthetic, 21-23 nucleotide long ds RNA sequence, the so-called siRNA, that RNAi could be adapted for genetic research and therapeutic interventions. [292, 293]

9.1.1 Gene silencing by siRNA

Following these seminal discoveries, the mechanism by which siRNA leads to the cleavage of target messenger RNA (mRNA) and thus post-transcriptional gene silencing could be fully elucidated (Fig. 41). Inside the cytoplasm long ds RNA, derived from cellular genes or infectious pathogens, is degraded into smaller fragments by the nucleolytic activity of an RNase III-like enzyme named Dicer. [294] The generated ds siRNA is hybridized over a region of about 20 nucleotides with a two nucleotides long overhang on each 3'-end. The degradation of long ds RNA, however, can be skipped by the direct delivery of synthetic siRNA. The siRNA is then incorporated in a multi-protein entity. This multi-protein complex assembles from Dicer, the

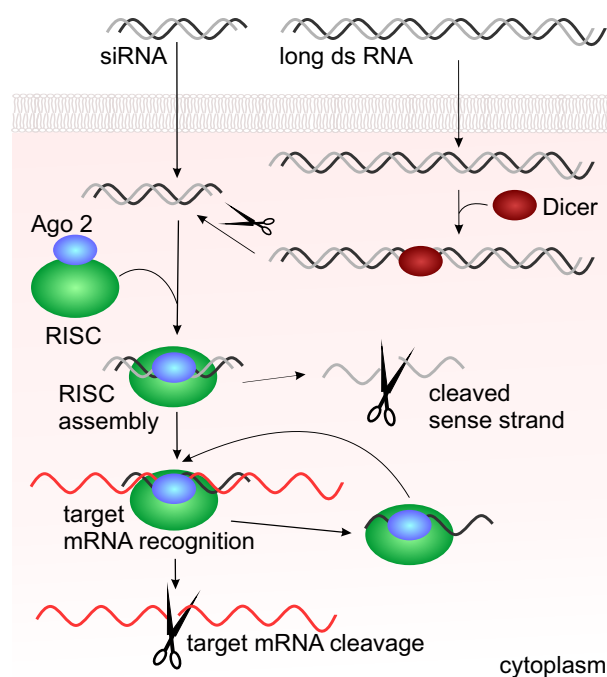


Figure 41: The mechanism of RNAi as described in the main text. Adapted from Ref. [22].

cofactor TRBP (transactivating response RNA-binding protein in HIV) and the catalytic multi-function protein Argonaute 2 (Ago 2). It serves as a loading complex of the actual effective unit, the RNA induced silencing complex (RISC). [295, 296] In the loading complex, the unwinding of the duplex is followed by a sorting into sense and antisense strand. It has been postulated that the thermodynamic stability of the 5'-end is decisive during the asymmetric selection process. The antisense strand was hence found to contain the 5'-end which is less tightly paired with the 3'-end of its complementary strand. [297] The sense strand is subsequently cleaved and the antisense strand resides in the activated RISC from which Dicer and TRBP have detached. [298] By Watson-Crick base-pairing, the antisense strand binds to its target mRNA which is thus captured for nucleolytic degradation by Ago 2. [299] Upon release of the cleaved mRNA, the activated RISC is retained and undergoes its next round of target recognition. [300] This multiple turnover rate renders siRNA mediated gene silencing highly effective. Important contributions for the elucidation of the RNAi mechanism were furthermore achieved by FCS- and FCCS-based investigations in the group of Petra Schwill. These comprised studies on target recognition, RISC assembly and strand selection. [301–303] In addition, they were concerned with identifying similarities and differences of cytoplasmic *vs.* nuclear RNAi and siRNA *vs.* micro RNA, a class of nuclear-encoded small ds RNA. [301, 304, 305]

9.1.2 Need for nanocarrier-based delivery of siRNA

RNAi offers a great advantage over small molecule drug pharmacology because it is highly versatile and can be used to target almost all diseases caused by abnormal gene activity. In 2017, a total of 70 clinical trials comprising 31 drug candidates had been reported. [39] However, only

one formulation, a lipid nanoparticle-delivered siRNA targeted against hereditary transthyretin-mediated amyloidosis (Patisiran), has thus far been submitted to the FDA. [306] In general, the drug candidates are designed to target genes involved in 18 different diseases spanning *e.g.* cancer, viral infections, ocular and metabolic disorders. What limits the applicability of siRNA in many cases, however, is the need for an appropriate delivery vehicle. [22, 307, 308] By itself, siRNA is too large (≈ 14 kDa) and negatively charged to passively diffuse across cellular membranes. Furthermore, a systemic administration of naked siRNA leads to degradation by unspecific RNases in the blood and tissue, rapid clearance by kidneys and liver and the onset of an innate immune response. [309] Immunogenicity and susceptibility to nucleolytic degradation could be reduced by the introduction of chemical modifications to the phosphate backbone (phosphorothioates), the 2'-OH groups of the sugar (substituted by *e.g.* 2'-O-methyl, 2'-F) or the nucleobase (*e.g.* 5-bromo-uridine). [307] Therefore, many therapies that are currently tested in clinical trials involve the local or topical application of naked, chemically modified siRNA to the eye, skin or accessible solid tumors. [310]

Nanocarriers are engineered to overcome many of the aforementioned obstacles, but are themselves exposed to new ones. [22] First of all, they shield the siRNA from recognition by the immune system and from nucleases. But to avoid toxicity they should consist of biodegradable material themselves. A positive surface charge of the nanocarrier system facilitates the passage of membranes, but this comes at the expense of increased interactions with blood proteins. This, however, was shown to be reduced through acquisition of “stealth” properties, for instance by a surface decoration with PEG (Section 1.2). [19] Due to their increased size, nanocarriers avoid glomerular filtration but are still accumulated in organs of the reticuloendothelial system. To benefit from such effects, the accumulating organs are preferentially chosen as targets. For instance, a number of clinical trials is concerned with liver-associated diseases such as hypercholesterolemia, hemophilia, liver fibrosis and other hepatic gene disorders. [310]

9.1.3 siRNA delivery systems

Vehicle-assisted delivery approaches of siRNA include complexation of the polyanionic siRNA *via* electrostatic interactions with cationic material and encapsulation into nanoparticles. [311] Covalent conjugation of siRNA and a targeting ligand is considered another option to transport siRNA to its target site.

Lipid-based formulating agents: Single or multiple cationic or ionizable lipids optionally combined with shielding lipids (*e.g.* PEG-lipid conjugates), cholesterol and targeting ligands associate into fusogenic particles. [312] These particles can incorporate siRNA in their aqueous core. Such lipid nanoparticles were reported to convey successful *in vivo* gene knockdown and are the most widespread delivery vehicles currently tested in clinical trials. [310] Lipid nanoparticles, however, are not to be confused with lipoplexes which constitute amorphous structures with ill-defined size distributions that electrostatically bind nucleic acids. [47, 313] Commercial lipoplex formulations (*e.g.* Lipofectamine[®] or Oligofectamine[®]) are broadly applied for *in vitro*

transfections, but show limited *in vivo* applicability due to high cytotoxicity. [314]

Polymer-based formulating agents: The spectrum of polymeric particles, complexes (termed polyplexes), dendrimers and micelles offers infinite possibilities for the development of custom-fit delivery. Nonetheless, only a small number of polymer-based formulations have thus far entered clinical trials. Commonly used materials are, for instance, chitosan, cyclodextrin, polyethylene imine, poly(lactic-co-glycolic) acid and peptides. [315–317] Polymer-coated metallic core nanoparticles are furthermore investigated.

siRNA conjugates: Covalent constructs with targeting ligands such as tris-N-acetylglucosamine, folic acid, cholesterol, aptamers or antibodies are engineered to convey targeting of certain cell types. [318, 319] Especially, the combination of tris-N-acetylglucosamine and chemically modified siRNA has shown successful gene knockdown in hepatocytes and is clinically tested for a number of hepatic diseases. [310]

Viral vectors have mostly disappeared as delivery systems as they were found to trigger an acute immune response which caused high cytotoxicity. [22] Furthermore, some delivery approaches are limited to *in vitro* transfection. These include direct microinjection of siRNA into the cytoplasm and electroporation. The latter results in siRNA uptake as a consequence of the disruption of the cellular membrane. [320] Despite its restriction to *in vitro* transfection, electroporation has been translated to clinical testing by treating tumor-isolated cells *ex vivo* and subsequently administering them by intradermal injection. [321]

9.2 From cellular uptake to release

Once the nanocarriers have reached their target cells, they have to overcome the plasma membrane and release their siRNA payload into the cytoplasm. [22]

9.2.1 Endocytosis and intracellular trafficking

It has been proposed that most carriers overcome the barrier of the plasma membrane by endocytic uptake. [26, 263, 322] In the active process of endocytosis, the plasma membrane invaginates and engulfs extracellular material into membrane-bound vesicles. [322] In a second step these vesicles are pinched off the membrane and form endosomes. Endosomes were reported to take part in an intracellular routing system of various specialized vesicles. [26] Although linked by this ubiquitous sequence of events, different endocytic pathways have been described. In literature, two main categories are commonly distinguished: (i) phagocytosis which is thought to be specific for certain cell types including some immune cells (macrophages, dendritic cells, neutrophils) and (ii) pinocytosis which has been reported to take place in all cell types. [26] It has been proposed to further subdivide pinocytosis into a variety of pathways for which the involvement of different protein machineries has been reported. Figure 42 provides an overview of the proposed pathways.

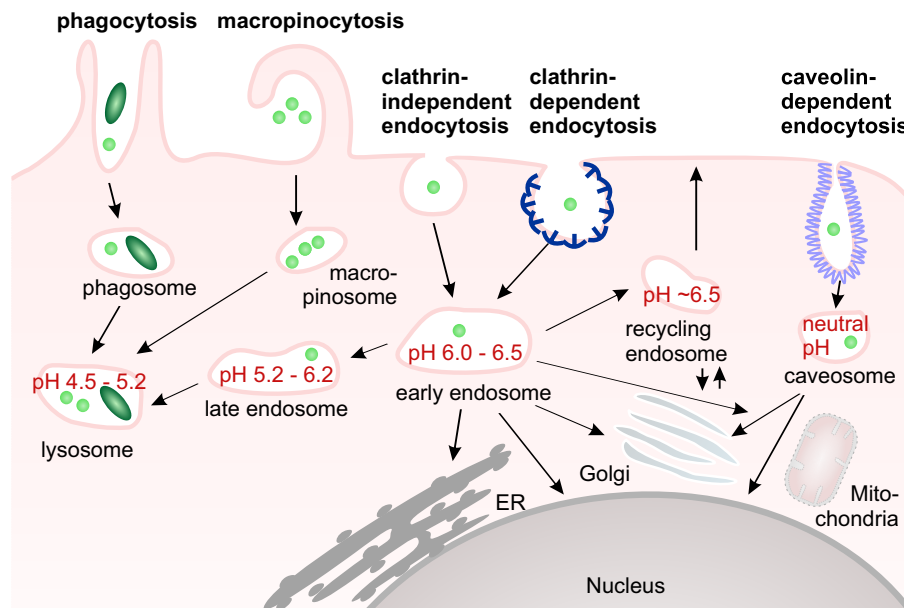


Figure 42: Possible internalization pathways of nanocarriers (light green). [26] Particles, senescent cells or pathogens (dark green) are typically taken up into big vesicles (> 250 nm) by phagocytosis. In the actin-driven process of macropinocytosis great volumes of extracellular fluid are engulfed into large vesicles ($0.5 - 10 \mu\text{m}$). Clathrin-independent endocytosis comprises a number of pathways that are characterized by the involved proteins such as Arf-6, RhoA, Cdc42 and flotillin. In clathrin-dependent endocytosis clathrin-coated pits have been described that are formed by the involvement of an extensive protein machinery. The formed vesicles are intracellularly pinched off by the activity of the GTPase dynamin. This has been suggested as one of the main routes of entry for nanocarriers with a size of ≈ 100 nm. The coat proteins “cavins”, together with other proteins, were found to regulate the formation of vesicles in caveolin-dependent endocytosis which are then severed off by dynamin. Furthermore, intracellular trafficking routes are depicted. The initially formed vesicles can potentially fuse with endosomes which are guided to other organelles or towards degradation in the acidic and hydrolytic environment of late endosomes and lysosomes. Adapted from Ref. [26].

Physicochemical properties such as size, shape and surface charge of the nanocarrier have been suggested to determine the preferred uptake mechanism. Nonetheless, most nanocarriers were found to internalize *via* more than one pathway. [26] It has furthermore been proposed that the endocytic entry route is related to the intracellular fate of the nanocarrier (Fig. 42). With the help of regulatory proteins (*e.g.* RAB proteins) and effector molecules, endosomes were found (i) to traffick towards intracellular compartments such as Golgi or endoplasmic reticulum, (ii) to be routed to the recycling machinery where they delivered their content to the extracellular milieu or (iii) to encounter a number of fusion processes during which they were reported to mature from early endosomes to late endosomes and finally to lysosomes. [322–324] This last-mentioned maturation was found to be accompanied by a gradual decrease in pH from 6 - 6.5 (early endosome) down to ≈ 4.5 (lysosome) mediated by the vacuolar proton pump V-ATPase. [325] The low pH in combination with hydrolytic enzymes contributes to lysosomal degradation of engulfed material.

9.2.2 Endosomal escape and release of payload

It is generally assumed that nanocarriers, or at least their payload, should escape from the endosome to prevent lysosomal degradation and to be available for their physiological mechanism of action, *e.g.* RNAi. Although endosomal escape has been extensively researched, it is still an inadequately mastered challenge in nanocarrier engineering. It has been suggested that the release of siRNA is often interlinked with endosomal escape as both processes involve a destabilization of the carrier system.

Two mechanisms of endosomal escape have been proposed. [26,27] The endosmolytic mechanism was first described for polyamine-based carrier systems and was reported to rely on the differential pH values of cytoplasm and endosomal lumen. [326] Accordingly, luminal acidification would initially lead to the protonation of polyamines. Such buffering would be counteracted by an increased influx of protons into the vesicular lumen which would subsequently trigger the inflow of counter ions and water. A thus caused swelling would eventually result in a rupture of the endosomal membrane concomitant with a release of the endosomal content (so-called “proton sponge effect”). The second mechanism was described for lipid-based formulations. [327,328] It was proposed that cationic or ionizable lipids would interact with anionic lipids of the endosomal membrane. Such interaction, characterized by a transition from the lamellar to the less stable inverted hexagonal phase, was assumed to cause membrane destabilization and pore formation. Consequently, the vesicular content would be emptied into the cytoplasm. [312]

It was reported that pH-responsiveness of a nanocarrier could also be achieved with acid-labile compounds that promoted destabilization upon hydrolytic cleavage. [329,330] Further intrinsic stimuli for triggered release have been proposed. It was reported that disulfide linkers could be reductively cleaved by glutathione. [265,331,332] Intracellular levels of glutathione ($\approx 2 - 10$ mM) were reported to be higher than extracellular ones ($\approx 2 - 10$ μ M). [333,334] Elevated relative glutathione levels (tumor *vs.* healthy tissue) were also found in a number of cancer types.

[335] Furthermore, altered expression levels of some (mostly extracellular) enzymes, including proteases, phospholipases and glycosidases, in conditions such as cancer and inflammation have been tested for triggered release. [334, 336, 337] Possible trigger mechanism can also be initiated externally. For instance, the application of a magnetic field or NIR irradiation were investigated for a controlled disintegration of the nanomaterial and a release of the siRNA in *in vitro* as well as *in vivo* models. [338–340]

9.2.3 Analytical techniques to study intracellular trafficking

Fluorescence microscopy is commonly employed to elucidate endocytic uptake and trafficking in living cells. [322, 341] In general, two approaches are distinguished. The first approach involves spatiotemporal tracking of fluorescently labeled nanocarriers and/or their payloads by co-incubation with a fluorescent probe. The probe, a fusion protein or small molecule, is known to either travel a certain endocytic pathway or reside in specific vesicles that are encountered during a certain uptake route. Colocalization of the fluorescent signals consequently points towards a similar passage. The second approach relies on the inhibition of a certain endocytosis route either by application of pharmacological inhibitors or by the use of knockout strains. Both approaches, however, suffer from a lack of selectivity as probes or inhibitors often utilize or disturb more than one pathway. In general, the same applies to the nanocarriers themselves, for which it was also discussed that they interfere with physiological processes. Several other methods such as immunocytochemistry, in conjunction with fluorimetric, enzymatic or radioactive detection approaches, and electron microscopy are incompatible with living cells. [322] They therefore only provide snapshots of the nanocarrier/payload localization in fixed cells.

Frequently, multiple methods are used to assess a carrier's intracellular behavior. As an example, Cardarelli and colleagues employed colocalization studies with labeled endocytic vesicles, single particle tracking analysis and a quantitative transfection assay which was based on monitoring luciferase expression. [342] Their results suggested that lipoplexes evade lysosomal degradation by preferentially moving through undirected Brownian motion. The authors claim this to be the cause for the reportedly high *in vitro* transfection efficiency of lipoplexes. However, such studies depend critically on the underlying protocols and experimental conduct as the above-mentioned finding is in contradiction to previous papers reporting the cytoskeleton-driven transport of lipoplexes. [343, 344] Furthermore, the endocytic uptake mechanism of lipoplexes still remains a matter of debate. [44, 47]

9.3 Applicability of FCS to study intracellular release

Efficient uptake of an siRNA-loaded nanocarrier does not necessarily lead to efficient gene silencing. Failure to escape lysosomal degradation is a common pitfall of many carrier systems (Section 9.2.2). All the more, an unambiguous analysis of this critical step is crucial. FCS is a potential analytical tool to complement uptake and gene knockdown assays. In the past decades, FCS was advanced and applied to derive quantitative parameters such as concentration,

mobility or inter- and intramolecular reaction kinetics of biomolecules in living cells (Section 2.4.6). [8,10] Thus, the basic requirements for resolving the mobility of intact nanocarriers *vs.* released payload have been established. Indeed, FCS has long been recognized as a standard method to assess release in buffer or serum-containing cell culture medium. [265,272,345]

However, reports on FCS-based studies of intracellular drug release are rare, even beyond the scope of siRNA drug delivery. The only study that involved an autocorrelation analysis was performed by Greco *et al.* who observed cytoplasmic siRNA release from photoresponsive polyplexes. [346] The authors reported that upon irradiation the measured autocorrelation curves were shifted to shorter lag times. Extraction of diffusion parameters revealed the presence of two co-diffusing species that differed by four orders of magnitude. The faster was assigned to free siRNA and the slower to polyplexes. Furthermore, the intracellular diffusion coefficients were found to be reduced compared to their aqueous counterparts.

By contrast, Remaut and colleagues refrained from performing an autocorrelation analysis and instead employed fluorescence fluctuation spectroscopy to study the intracellular fate of microinjected polyplexes. [347] The cationic polymer as well as the nucleic acid payload were labeled with spectrally different dyes. For analysis, the authors measured the average fluorescence intensity in both channels. While the simultaneous appearance of highly intense peaks in both channels indicated the presence of intact complexes, their dissociation became apparent by an increase in the intensity signal of the payload.

In addition, FCS has been used in several studies to investigate either the uptake, intracellular distribution and degradation of drug carriers or the integrity of nucleic acids. [348–353]

10 Results and discussion

10.1 General considerations for FCS measurements in living cells

The interior of a eukaryotic cell is a complex functional unit characterized by a subdivision into specialized organelles and a diverse set of effector biomolecules. The resulting heterogeneity and molecular crowding poses a challenge to intracellular FCS measurements. FCS measurements require equilibrium conditions to investigate the Brownian movement of fluorescent species and derive quantitative parameters from it (Section 2.4.1). To minimize the possibility of artifacts and erroneous interpretation of data, the system under investigation, *i.e.* the cell, must be well known beforehand. Therefore, several points were considered and implemented in a protocol suitable for FCS measurements in living cells (see also Ref. [9, 354, 355]).

10.1.1 Autofluorescent background

To distinguish the fluorescence emission of endogenous fluorophores from that of exogenously introduced fluorophores, the term “autofluorescence” is commonly used to describe the former. [356] Several biomolecules were found to show autofluorescent properties. Cellular autofluorescent molecules include, for instance, NAD(P)H, flavin coenzymes, aromatic amino acids, various porphyrins as well as lipopigments such as ceroids and lipofuscin. These molecules reveal distinct excitation and emission spectra (*e.g.* the emission maxima of flavins, porphyrins and lipopigments lie above 500 nm while the remaining mentioned molecules emit primarily < 500 nm). Furthermore, autofluorescent molecules are not uniformly distributed intracellularly, but some compartments such as mitochondria contain high amounts of NADH and flavin containing enzymes. [7] In fluorescence spectroscopy, autofluorescence leads to a background signal that is considered problematic for two reasons. [9, 86] First, a constant background increases the average fluorescence intensity and lowers the autocorrelation amplitude (Section 2.4.1). This results in an overestimation of the concentration of the fluorescent species and in an underestimation of its fluorescence brightness. Second, a correlating background signal can be mistaken for a positive signal. This misinterpretation is especially dangerous when the diffusion time of the investigated species is unknown. This was the case in the here presented study on the intracellular release of siRNA molecules which could diffuse freely or associated with a protein complex and which could exist as a mixture of fragments at different integrity levels from full length siRNA to free dye.

Therefore, control measurements in cell culture media, in an immortalized endothelial cell line (RBE4 cells) and in primary human macrophages were performed. Three laser lines with excitation wavelengths of 488 nm, 543 nm and 633 nm with their respective typical detection ranges (either long pass or band pass filters) were included. In cell culture media (DMEM + Ham’s F-10/F-12), a correlating signal was prevalent at all wavelengths irrespective of the presence of fetal bovine serum. The derived diffusion coefficients ranged from 60 to 100 $\mu\text{m}^2 \text{s}^{-1}$. The average fluorescent signal was roughly linear with laser intensity and could be reduced by

limiting the detection range. A small detection bandwidth of approximately 50 nm was hence applied, unless otherwise indicated. In cell culture media that contained the pH indicator dye phenol red a high background signal was detected. Consequently, after seeding the cells in chambered microscopy slides phenol red-free medium was used.

A correlating autofluorescent background signal was detected in the cytoplasm of untreated cells. Here, calculated diffusion coefficients typically ranged from 1 to 10 $\mu\text{m}^2 \text{s}^{-1}$. The presence of autofluorescent molecules was furthermore apparent by photobleaching. Upon laser illumination a decrease in the average fluorescence intensity signal at the first seconds indicated photodestruction of the fluorophore. Furthermore, highly intense signal peaks were detected. Their prevalence, however, showed a dependence on excitation wavelength. It was most disturbing for 543 nm excitation followed by 633 nm excitation and least prevalent at 488 nm excitation. At 543 nm excitation, the high peaks presumably derived from autofluorescent molecules with high quantum yields (*e.g.* riboflavins) [357] and yielded a good autocorrelation. At 488 nm, high intensity peaks were extremely rare and at reduced laser intensities the signal remained low and did not correlate. Hence, siRNA was preferentially labeled with fluorescent dyes that were efficiently excited at 488 nm. Laser power was typically chosen as a trade-off between sufficient excitation of the fluorescent species (fluorescence brightness > 1 kHz per molecule) and a minimization of background and photodamage to the cells. It was thus aimed for the lowest possible laser power that still allowed a clear discrimination against background. In addition, intracellular measurements were often preceded by prebleaching. This short sequence (up to one minute) of very high laser power served to inactivate immobile, autofluorescent molecules and to avoid a slow decrease in the average fluorescence signal.

10.1.2 Control of measurement position

The combination with CLSM allowed to perform FCS measurements at selected intracellular positions. Cell outlines and nuclei could be sufficiently identified in transmission mode. However, the additional application of an organelle or structure specific fluorescent stain can be beneficial to position the observation volume with subcellular precision. Here, a nuclear stain (Hoechst dye) was applied in some experiments to facilitate discrimination between nucleus and cytoplasm. To define a suitable position not only in x,y - but also in z -dimension, an image stack of several sections was recorded. V_{obs} could hence be positioned in a section that was clearly located between the lower and upper cell membrane. Measurements were furthermore performed at optimal culturing conditions to sustain cell viability, *i.e.* at a temperature of 37°C and an air / CO₂ mixture of 95% / 5%. Importantly, when the microscopy slide was first placed into the incubation unit, the system needed to adapt to equilibrium conditions for several minutes. During this equilibration time, a thermal drift in z -direction occurred which impeded position-controlled measurements. To account for focal drifts measurement positions were controlled and adjusted on a regular basis, either manually or by automated focus control.

10.1.3 Heterogenous environment of cells

A further point to consider arose from the heterogeneity of the cell's interior. An increased viscosity, molecular crowding and interactions with cellular components are known to affect the mobility of investigated fluorescent species. [9] This hindrance of diffusion has been reported to result in an increase of diffusion time (τ_D) through V_{obs} , and thus decrease in diffusion coefficient, by a factor of 2- to 10-fold with regard to aqueous solutions. [86, 358] The effective intracellular diffusion slowdown was found to depend approximately on the molecular size of the species whereby larger molecules tended to be slowed down by a larger factor. Kalwarczyk *et al.* proposed that the size-dependent scaling factor of the diffusion slowdown was linked to a differently perceived viscosity. [359] The authors determined that molecules below a certain correlation length (≈ 5 nm for HeLa cells) would experience matrix viscosity with values of $\eta_{\text{matrix}} \approx 1.3 \cdot \eta_{\text{water}} \approx 0.9$ mPa·s. Molecules/particles larger than a certain limiting length scale (≈ 86 nm for HeLa cells), in contrast, would experience viscosity at the macroscopic scale ($\eta_{\text{macro}} \approx 64 \cdot \eta_{\text{water}} \approx 44$ mPa·s). For molecules with a size in between those two length scales the experienced viscosity would increase with the hydrodynamic radius of the probe.

In order to determine how great the diffusion slowdown of enhanced green fluorescent protein (EGFP, $M \approx 33$ kDa) would be, diffusion coefficients of EGFP were measured in the cytoplasm of HeLa cells and in a solution of EGFP in PBS. As depicted in Figure 43, EGFP diffusion was slowed down by a factor of three in the cytoplasm with respect to buffer conditions. This slowdown factor as well as the respective diffusion coefficients were in agreement with reported values. [301, 360–363]

Heterogeneity of the cellular environment and deviations from equilibrium conditions were often reflected in the measurement data. As mentioned above, a high concentration of immobile autofluorescent molecules became apparent in a strong decrease in fluorescence intensity due to photobleaching. Moreover, large fluctuations in the count rate were observed when bright objects, either intact nanoparticles presumably transported in endosomes or autofluorescent compartments, crossed V_{obs} . Time segments (repetitions) that were affected by these events were excluded from the average autocorrelation curve and not considered in the autocorrelation analysis. If a large percentage of repetitions ($> 50\%$) did not pass the selection criteria, the measurement was discarded.

10.2 Lipoplex-mediated transfection

Lipoplexes have been broadly applied as transfection agents for nucleic acids and were therefore found suitable to develop an experimental framework for the detection of intracellular siRNA release by FCS. [47, 313] Here, a commercial cationic lipid mixture (Oligofectamine[®]) was used to complex siRNA and deliver it to mammalian cells. In preliminary experiments it was determined that lipoplexes could not be adequately characterized in buffer presumably due to their heterogeneous large size and their high loading efficiency of fluorescently labeled siRNA molecules. Furthermore, the slow diffusion of a strongly fluorescent lipoplex or vesicle through

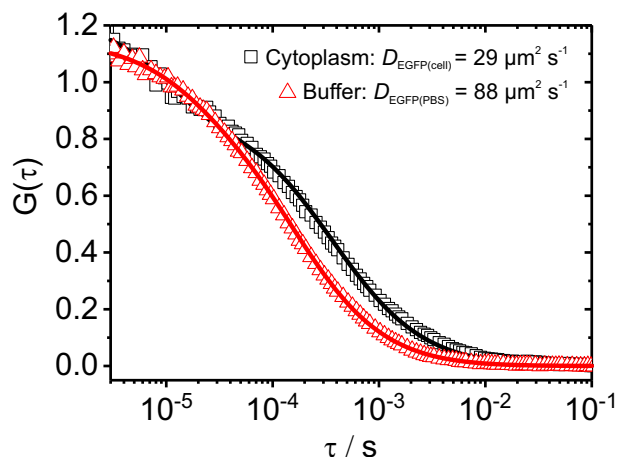


Figure 43: Normalized autocorrelation curves of EGFP in PBS (red triangles) and in HeLa cells (black squares). Prior to the intracellular measurement, the cell was photobleached to reduce the high overall concentration of EGFP. Both autocorrelation curves were fitted (solid lines) with a fit for one freely diffusing species including a triplet contribution (Eq. 2.20). The derived diffusion times were converted into diffusion coefficients assuming equally sized observation volumes in both cases. The fluorescence brightness in solution and in the cytoplasm was 20 kHz and 5 kHz per molecule, respectively.

V_{obs} in intracellular FCS measurements led to an extremely high signal. To prevent damage to the detectors, positioning of V_{obs} in proximity to bright spots was avoided and intracellular FCS measurements were conducted with the aim of detecting fluorescent siRNA after, and not before, the release event.

10.2.1 Lipoplex uptake and siRNA release in immortalized cells

First, an immortalized endothelial (RBE4) cell line was transfected with lipoplexes in order to determine the diffusion coefficient of cytoplasmic siRNA and to establish the time frame of release. The employed ds siRNA was 22 nucleotides in length with a two nucleotides long overhang at the 3'-ends of each strand. It encoded a target sequence for EGFP (Materials 11.1.3) and was labeled with Atto 488 at the 3'-end of the sense strand (Fig. 44A). This labeling has been previously shown not to impair the *in vitro* siRNA knockdown efficiency. [364] FCS measurements of the Atto 488-siRNA in PBS yielded a diffusion coefficient $D_{\text{siRNA(PBS)}} = 152 \mu\text{m}^2 \text{s}^{-1}$ ($\tau_{\text{D}} = 111 \mu\text{s}$) which was translated into a hydrodynamic radius R_{H} of 2.2 nm by Stokes-Einstein equation (Eq. 2.11).

After transfection, the uptake of lipoplexes was observed with confocal imaging. Bright spots inside the cell boundaries started to appear within minutes after the addition of the lipoplexes. These bright spots were assigned to vesicle-encapsulated lipoplexes. Most cells took up several of the lipoplexes and their presence was still apparent after 24 hours. However, a sudden uniform spreading of fluorescence as described in the literature was rarely detected. [40, 41] When studying nanocarrier-based uptake and release, this spreading is often interpreted as a rupture of endosomal membranes and an associated release of the nanocarrier payload.

Conversely, the absence of a burst event cannot prove the absence of release, as the distri-

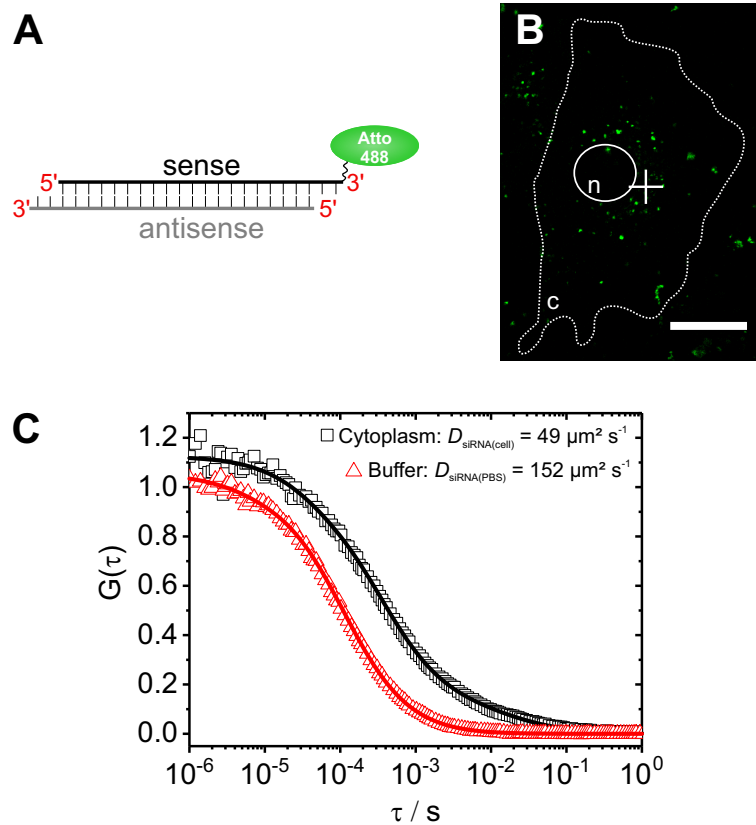


Figure 44: A) siRNA molecule labeled with the fluorescent dye Atto 488. B) RBE4 cell in which FCS (C) was measured at the crosshairs three hours after transfection. Dotted and solid lines indicate the cell outline (c) and nucleus (n), respectively. Atto 488-labeled siRNA was detected by its green fluorescence ($\lambda_{\text{exc}} = 488 \text{ nm}$, $\lambda_{\text{em}} = 508 - 562 \text{ nm}$). Scale bar: $20 \mu\text{m}$. C) Normalized autocorrelation curves of Atto 488-labeled siRNA in PBS (red triangles) and in RBE4 cells (black squares). Autocorrelation data was fitted with a 3D diffusion model for one component (PBS) and two components (cell), including a triplet contribution (Eq. 2.20). The diffusion coefficients are presented in the inset.

bution of a small number of fluorescent molecules might just not be detectable by CLSM. This hypothesis could be supported by a study by Gilleron and colleagues who were able to identify *in vitro* and *in vivo* release events of only 200 siRNA-gold compounds from lipid nanoparticles (about 2000 to 4000 siRNA molecules in total) by tracing them with electron microscopy. [365] The minimum number of cytoplasmic siRNA molecules per cell required to cause a detectable signal in fluorescence microscopy, in contrast, was estimated to range around at least 20,000 molecules. [365] In this respect, it also seems likely that the uptake, trafficking and release of small nanocarriers loaded with a low number of fluorescently labeled molecules would remain undetected by conventional fluorescence microscopy methods.

Within this work, cells for intracellular FCS measurements were selected based on a visual inspection by CLSM. Hereby, cells which indicated lipoplex uptake by the detection of fluorescent spots within the cell boundaries were chosen as suitable release candidates. The time frame in which these imaging and FCS measurements were performed ranged from approximately one to four hours post-transfection with only one cell being analyzed at a time. FCS

was assumed to exhibit an increased sensitivity for the detection of small amounts of released siRNA. However, most of the cells selected by imaging showed either no fluorescent signal above background or a strongly fluctuating signal which indicated the presence of bright objects such as lipoplex-loaded vesicles. In a subset of cells, a steady fluorescent signal was observed and analyzed *via* autocorrelation analysis. Figure 44B depicts a cell that revealed such a signal. Importantly, the corresponding confocal image did not show a clear indication for release. The FCS data, in contrast, indicated the presence of a fluorescent species that diffused at a time scale expected for a relatively small molecule such as siRNA.

In order to assess which fitting model was suited to accurately describe diffusion parameters, two commonly applied models for intracellular FCS were tested (Appendix 11). [354] The first model was a 3D Brownian motion fit of multiple independently diffusing components (Eq. 2.20) to account for transient or permanent interactions of the fluorescent species with cellular components. Correspondingly, the exemplary cell (Fig. 44B) was fitted with two components and yielded a fast and slow diffusing species ($D_{\text{fast}(\text{siRNA})} = 49 \mu\text{m}^2 \text{s}^{-1}$, $D_{\text{slow}(\text{interactions})} = 1.5 \mu\text{m}^2 \text{s}^{-1}$). The second model assumed a deviation from free 3D diffusion resulting in anomalous diffusion where the mean-square displacement is described by $\langle r^2 \rangle = \Gamma t^\alpha$ (Section 2.4.2). [354] Here, Γ denotes the transport coefficient (equivalent to the diffusion coefficient) and t the time. The coefficient α ($0 < \alpha < 1$) yields the degree of diffusion restriction with values close to 1 indicating a low degree of diffusion restriction and smaller values indicating a greater hindrance. For the exemplary autocorrelation curve (Appendix 11), this model rendered $\Gamma_{\text{siRNA}} = 55 \mu\text{m}^2 \text{s}^{-1}$ and $\alpha = 0.69$ indicating that the diffusion was indeed restricted. For both models the exponential term accounting for fast photophysics (triplet state, Eq. 2.19) was fixed to $\tau_T = 30 \mu\text{s}$, as in a number of intracellular measurements conducted in this study τ_T was found to range around this value. This triplet lifetime was remarkably higher than $\tau_T \approx 4 \mu\text{s}$ which had been measured in buffer (Fig. 44C). However, increased triplet lifetimes for measurements in cells have been reported. [301] A direct comparison of the two fitting models and their residuals revealed that both of them could adequately fit the experimental data with only minor differences in the reported diffusion coefficients for the siRNA. For subsequent analysis of intracellular autocorrelation data, the model for multiple freely diffusing components (Eq. 2.20) was chosen.

In Figure 44C, the *in vitro* diffusion of Atto 488-labeled siRNA in PBS buffer and *in cellulo* ($D_{\text{siRNA}(\text{cell})} = 49 \mu\text{m}^2 \text{s}^{-1}$, $\tau_D = 340 \mu\text{s}$) are compared. In the cytoplasm, the diffusion was slowed down by a factor of 3.1 ($D_{\text{siRNA}(\text{PBS})}/D_{\text{siRNA}(\text{cell})}$) which was comparable to the three-fold slowdown of EGFP (Fig. 43). In addition to the cell depicted in Figure 44C, further RBE4 cells revealed comparable diffusion coefficients ($D_{\text{siRNA}(\text{cell})} = 43.3 \pm 8.9 \mu\text{m}^2 \text{s}^{-1}$, mean \pm standard deviation for $N = 10$ cells from two independent experiments). The about three-fold diffusion slowdown furthermore indicated that the fluorescent species was Atto 488-labeled siRNA rather than degradation products or siRNA incorporated into RISC. The question whether the detected species was single- or double-stranded could not be answered by single label FCS as both species differ only marginally in size. However, degradation products (*e.g.* free dye with $D_{\text{Atto 488}(\text{H}_2\text{O})}$)

$= 361 \mu\text{m}^2 \text{s}^{-1}$) would be expected to show higher cytoplasmic diffusion coefficients. In contrast, the siRNA-loaded RISC with its molecular weight of $\approx 3 \text{ MDa}$ as determined by intracellular FCCS would be expected to diffuse at longer time scales. [301] The incorporation of siRNA into RISC was furthermore reported to peak between three and twelve hours after siRNA delivery to the cytoplasm and thus at later time points than studied here. [301] It should also be pointed out that the siRNA used here was labeled on the sense strand (Fig. 44A), *i.e.* the strand that would not be used for mRNA recognition and thus degraded (Section 9.1.1). Importantly, further preliminary experiments conducted within this work revealed that cells neither took up free, uncomplexed siRNA nor free monoanionic Atto 488-azide dye. It was thus assumed that the detected cytoplasmic diffusion corresponded to intact siRNA released from lipoplexes after their cellular uptake. FCS furthermore yielded the concentration of the fluorescent species. This intracellular concentration, however, should be interpreted with care as cellular background hinders an accurate determination unless proper corrections are performed (Section 10.1.1). [86] Nonetheless, a rough estimation revealed that the intracellular concentration spanned a broad range from approximately 10 to 500 nM. Assuming an average cell volume of 2,000 fL this translated into absolute numbers of 12,000 to 600,000 siRNA molecules per cell. This number was in accordance with an estimate of $10^5 - 10^6$ intact siRNA molecules per cell delivered by lipoplexes and determined by FRET-based CLSM 48 hours post-transfection. [40, 366]

It was concluded that i) FCS was suitable to detect the release of siRNA from lipoplexes by the cytoplasmic diffusion of a fast fluorescent species, ii) this release was initiated within a few hours post-transfection and iii) only a small subset of cells showed release while the majority of cells revealed either no fluorescent signal above background or diffusion of bright, large objects. These results were in accordance with Hirsch & Helm who reported that in total 13.8% of all lipoplex-transfected cells showed release over a time span of six hours. [40] The authors furthermore assessed that with an average persistence time of < 1 hour only 1.5 to 2% of the cells were simultaneously affected by siRNA release. Release events in their study were identified by the homogeneous cellular distribution of fluorescence detected by CLSM. From the here presented findings on the increased sensitivity of FCS compared to CLSM, it was assumed that some low-level release events might have been missed. Nonetheless, one important drawback of intracellular FCS was exposed: only one cell at a time could be analyzed and the duration of each measurement (including selection of positions by confocal imaging) spanned several minutes. A low overall probability of release and its asynchronous occurrence therefore led to a low number of analyzable curves and poor statistics.

10.2.2 Lipoplex uptake and siRNA release in primary macrophages

After the release of siRNA from lipoplexes had been successfully detected in an immortalized cell line, the experimental design was transferred to primary macrophages. In general, it has been reported that primary cells retain their *in vivo* functions and markers while immortalized cell lines tend to deviate genotypically and phenotypically from the tissue from which they

originated. [367] Macrophages belong to the mononuclear phagocyte system and are responsible for the phagocytosis of cellular debris and pathogens. They are furthermore part of the innate and adaptive immune system and are involved in inflammation processes. [368] So-called tumor-associated macrophages are found in the tumor microenvironment where they negatively influence the patient's prognosis by promoting tumor growth, metastases and inflammation. Targeting of macrophages by nanocarriers is therefore a promising approach for the treatment of cancer and inflammatory diseases. [369,370]

Similar to the experiment in Figure 44, the release of Atto 488-labeled siRNA from Oligofectamine lipoplexes was investigated by confocal imaging and intracellular FCS measurements one to four hours after the transfection of the macrophages.⁸ Again, a fast uptake of lipoplexes was observed and from those cells identified by imaging as promising candidates for release a subset ($\approx 1/3$) showed a steady fluorescent signal. Autocorrelation analysis of these cells yielded $D_{\text{siRNA}(\text{cell})} = 45.4 \pm 17.5 \mu\text{m}^2 \text{s}^{-1}$ (mean \pm standard deviation for $N = 6$ cells) which is in accordance with the diffusion coefficient of siRNA in the cytoplasm of RBE4 cells. This finding suggested that in macrophages siRNA molecules were released from lipoplexes in a manner similar to that determined for RBE4 cells.

So far, the detection of release events had been the result of a “search” for positive signals among randomly chosen cells at a given time point. To provide a more detailed and time-dependent analysis of release, an experiment was conducted in which four cells were observed at regular intervals in a time span of 45 to 240 min post-transfection. At a time point of 60 min post-transfection, all four cells showed uptake of at least one lipoplex. The signal intensity traces and confocal images for five selected time points are shown in Figure 45 and Appendix 12:

- Cell 1 (Fig. 45): During the first hour the average fluorescent signal intensity equaled background levels. Starting from 75 min, peaks appeared and the average count rate increased. A doubling of the count rate, in this case from background levels of ≈ 4 kHz (background values varied across cells) to levels > 8 kHz, was assumed to indicate release. At 90 min a fluorescent species was detected which showed a diffusion time in the range of small molecules (Appendix 13A) while release was not yet indicated by CLSM. From 120 min onward, a microscopically detected spreading of the fluorescent signal supported the assumption that release had occurred. Autocorrelation analysis continuously evidenced the presence of a small fluorescent species. The corresponding diffusion coefficients, however, were increased with respect to $D_{\text{siRNA}(\text{cell})}$. It was thus assumed that the siRNA was at least partially degraded. The high count rate started to decrease again at 215 min post-transfection.
- Cell 2 (Fig. 45): During the time course of the experiment, fluorescence of the internalized lipoplex prevailed and no burst release was observed by CLSM. Nonetheless, release was indicated by FCS which recorded an increase in the average fluorescent signal starting from

⁸Macrophages were isolated and cultured by Jonathan Schupp.

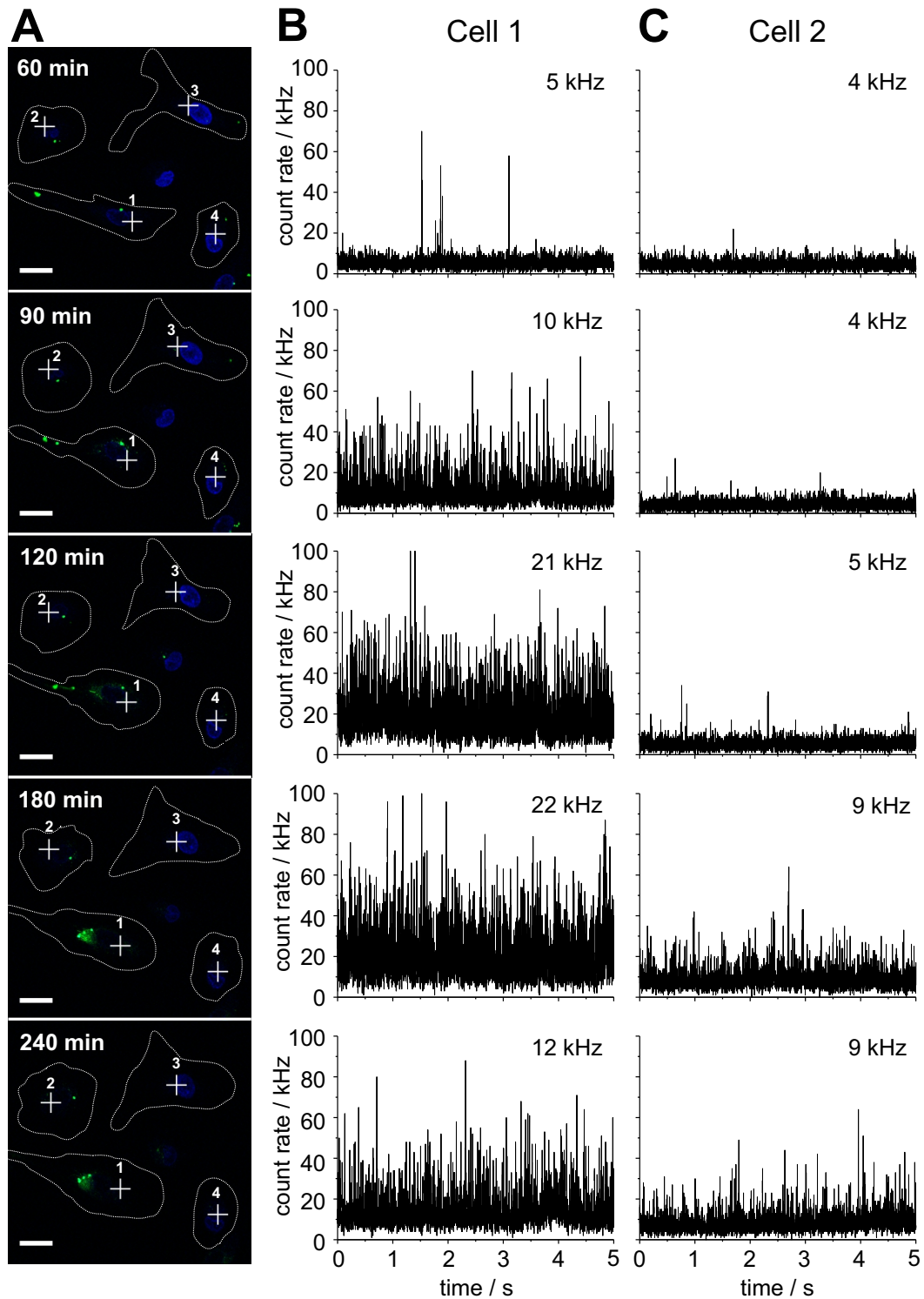


Figure 45: Time-dependent experiment of siRNA release from lipoplexes in four macrophages (cell 1 - 4). A) Confocal images at different time points post-transfection. Dotted lines indicate the cell outline. Blue channel: nuclei stained with Hoechst dye ($\lambda_{\text{exc}} = 405 \text{ nm}$, $\lambda_{\text{em}} = 410 - 482 \text{ nm}$). Green channel: Atto 488-labeled siRNA ($\lambda_{\text{exc}} = 488 \text{ nm}$, $\lambda_{\text{em}} = 500 - 589 \text{ nm}$). Crosshairs indicate positions of FCS measurements. Scale bar: $20 \mu\text{m}$. Excerpts of the fluorescence signal time traces of cell 1 (B) and cell 2 (C). The average count rates are displayed in the insets.

180 min, concomitant with a fast diffusing species detected by autocorrelation analysis (Appendix 13B).

- Cell 3 (Appendix 12): The onset of release starting from 90 min post-transfection was detected by FCS but not by CLSM. Even though the fluorescent spot, *i.e.* the uptaken lipoplex, vanished, the amount of released siRNA presumably remained below the detection limit of confocal microscopy.
- Cell 4 (Appendix 12): Within the time frame of the experiment, release was detected neither by FCS nor by CLSM.

In summary, intracellular FCS measurements revealed that three out of four cells showed diffusion of a small fluorescent species and thus evidence for release of siRNA. In contrast, only one cell showed a sudden spreading of fluorescence as an indication for release detected by CLSM. These results indicated that a higher percentage of cells showed release than originally assumed based on CLSM studies. These “hidden” release events were detectable by FCS in long-term measurements. Thus, FCS offered the perspective of gaining new insights into release statistics. However, this was made possible at the expense of a time-consuming investigation with only single-digit cell numbers analyzed per experiment.

10.2.3 Integrity of intracellularly released siRNA

The release of intact siRNA molecules has been assumed by an about three-fold reduced diffusion coefficient of a cytoplasmic fluorescent species with respect to $D_{\text{siRNA(PBS)}} = 152 \mu\text{m}^2 \text{s}^{-1}$. Nonetheless, the prevalence of an even faster diffusing species, presumably degraded siRNA, was detected in some cells including those analyzed in Figure 45. To gain further insight on the integrity state of released siRNA, intracellular dual color FCCS measurements were performed. To this end, a double-labeled construct was used in which two spectrally distinct dyes (Atto 488 and Atto 647N) were placed at opposite ends of the siRNA, each covalently conjugated to the 5'-end of one strand. In dual color FCCS, the autocorrelation curves of each label are complemented by a cross-correlation analysis which reveals the abundance of the species containing both dye labels, *i.e.* the intact siRNA (Section 2.4.4). Characterization of the siRNA in buffer yielded a cross-correlation amplitude of 67% relative to those of the autocorrelation curves (Fig. 46A). This incomplete cross-correlation for the double-labeled construct could be partly caused by the difference in size of the two observation volumes (Section 2.4.4). There were no indications for degradation of the siRNA, as both autocorrelation curves were adequately fitted with a model for only one diffusing species. Of note, it was assumed that only a substantial amount of completely degraded siRNA, *i.e.* to the level of free dye, would have yielded a two-component fit. A slight excess of one of the strands during hybridization, the omission of a bleed-through correction and FRET between the dyes might have reduced the cross-correlation amplitude. [371] However, a low bleed-through factor had been previously

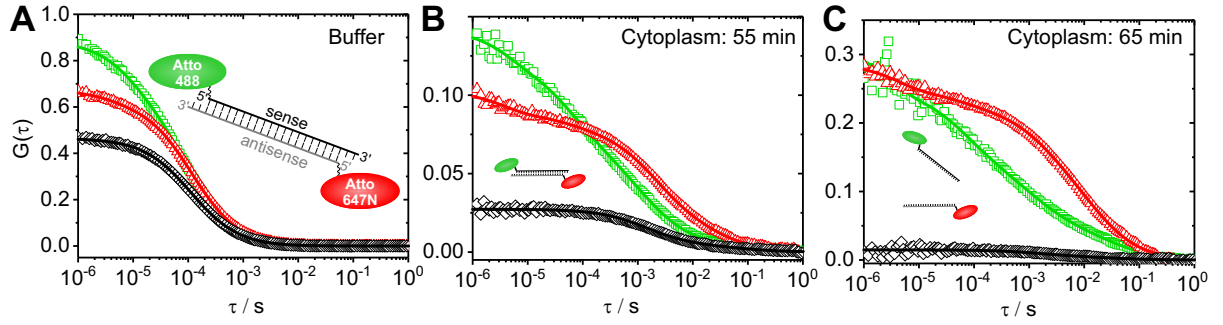


Figure 46: FCCS analysis of Atto 488/Atto 647N-labeled siRNA in PBS (A) and in the cytoplasm of macrophages (B,C). The green and red color indicate autocorrelation data (symbols) and fit (solid lines) registering Atto 488 and Atto 647N labels, respectively. The cross-correlation is displayed in black. A) Curves were obtained from the average of five repetitions of 30 s each. Autocorrelation data were fitted with a one-component fit for free diffusion including triplet (Eq. 2.20). The cross-correlation curve was fitted without a triplet contribution as triplet state dynamics do not give rise to cross-correlation. B,C) Cytoplasmic measurements in the same cell at the indicated time points post-transfection. Autocorrelation data were fitted with a three-component fit for free diffusion including triplet (Eq. 2.20). Besides the cross-correlating species ($\tau_D \approx 1500 \mu\text{s}$) two further species were detected, one with a faster and one with a slower diffusion time. The relative fraction of the cross-correlating species in both autocorrelation curves decreased from B) to C). The cross-correlation curves were fitted with a model for two components without a triplet contribution.

reported for the Atto488/Atto647N FRET pair. [372] Furthermore, the FRET efficiency calculated with Equation 2.5 under the assumption of an approximate distance of the dyes of 7.4 nm and a Förster radius of 4.8 nm yielded a comparatively low value of 0.069. [366, 373] In comparison, if both dyes were located at the same end of the siRNA (distance of 1.7 nm), a calculated E_{FRET} of 0.998 would apply.

To study intracellular release, primary human macrophages were transfected with lipoplexes formed with the double-labeled siRNA. Intracellular FCCS measurements were then performed in individual cells in a time frame of up to 2.5 hours post-transfection. In several cells diffusion of yet unreleased particles was detected by broad and highly intense peaks in both channels. These events gave rise to a positive cross-correlation (Appendix 14). In other cells, however, positive cross-correlation of a fast diffusing species was observed. In Figure 46B, the auto- and cross-correlation curves of such a cell are presented. At the investigated time point, the cross-correlation amplitude (in black) was already decreased to approximately 40% of intact siRNA with the buffer conditions serving as measure for full integrity. The cross-correlation amplitude, however, rapidly dropped within the subsequent ten minutes (Fig. 46C). Interestingly, the cross-correlating species yielded a diffusion coefficient of $D_{\text{Atto488/Atto647N-siRNA}(\text{cell})} \approx 11 \mu\text{m}^2 \text{s}^{-1}$. This value was also found in several other cells thus precluding that it was a coincidental observation. This five-fold decrease in the diffusion coefficient with respect to the cytoplasmic Atto 488-siRNA ($D_{\text{Atto488-siRNA}(\text{cell})} \approx 50 \mu\text{m}^2 \text{s}^{-1}$) could not be explained by a size increase due to the additional dye label but rather indicated an interaction with a cellular component. Taking into consideration the expected imbalance of labeled siRNA molecules ($\approx 10^4 - 10^6$) and the reported number of all Ago1 - 4 molecules ($\approx 10^5$) [374, 375] per cell shared among

siRNA and micro RNA molecules, the association with RISC would presumably have went indistinguishable among other interactions. Importantly, however, these findings gave a first hint that siRNA was released into the cytoplasm at least partially intact and double-stranded. Indications for a subsequent degradation were also found. However, due to the limited accuracy of intracellular diffusion parameters and the low number of analyzed cells, conclusions on the siRNA integrity state should be drawn with care and demand further analysis.

10.3 siRNA release from nanohydrogel particles

In the previous section, the experimental framework to detect intracellular siRNA release by FCS has been set. Therefore, its applicability was tested for a nanocarrier system which revealed promising properties. The employed nanocarrier was a polymeric cationic nanohydrogel particle (NHG) which had already shown efficient delivery of siRNA as well as gene knockdown in several cell types. [33, 45, 329, 376] The nanometer-sized NHG particles were first self-assembled into reactive ester block copolymers micelles.⁹ In a next step, they were core-crosslinked and thus stabilized by the addition of the oligoamine compound spermine. To these cationic NHG particles, siRNA was added in a mass ratio of 10:1 (NHG:siRNA) (Fig. 47A). [329] The formed complexes were characterized by FCS where they yielded a hydrodynamic radius of 17.3 nm in PBS (Fig. 47B).

In preliminary experiments, seeded RBE4 cells were incubated with the complexes and subjected to intracellular FCS measurements. Here, siRNA diffusion in the extracellular medium yielded an autocorrelation curve from which an siRNA concentration of about 10 nM was derived. This finding prompted an investigation on the stability of the complexes in serum-free cell medium. With FCS, a loss of complexed siRNA molecules upon a ten-times dilution with medium was detected (Fig. 47B). A second, fast diffusing species with the size of free siRNA became apparent with a relative fraction of 27% immediately following the dilution. This fraction of free siRNA rose to 100% (one-component fit) when the measurement was repeated 1.5 hours later. Simultaneously, the total concentration of the fluorescent species was increased (not apparent in Fig. 47B due to normalization) which furthermore pointed towards a separation of NHG and siRNA. It was assumed that the dissociation occurred either due to a competition for binding sites with components of the cell culture medium or as a result of re-equilibration upon dilution. In addition, NHG (labeled with Alexa Fluor 647) were found to adhere to the cover glass surface. Therefore, a certain fraction of complexes might still have been intact but inaccessible to FCS due to immobilization. The incubation protocol was subsequently adapted in order to avoid an erroneous interpretation of intracellular release (Fig. 47A.2). Such misinterpretation might occur when the observation volume is accidentally placed not entirely within the cytoplasm. Cells, in this case primary human macrophages, were now first incubated with the complexes, then washed and seeded. Measurements were performed when the cells showed sufficient adherence (after ≈ 30 min). Consequently, the disturbing autocorrelation of

⁹The nanohydrogel particle was synthesized and characterized by Nadine Leber.

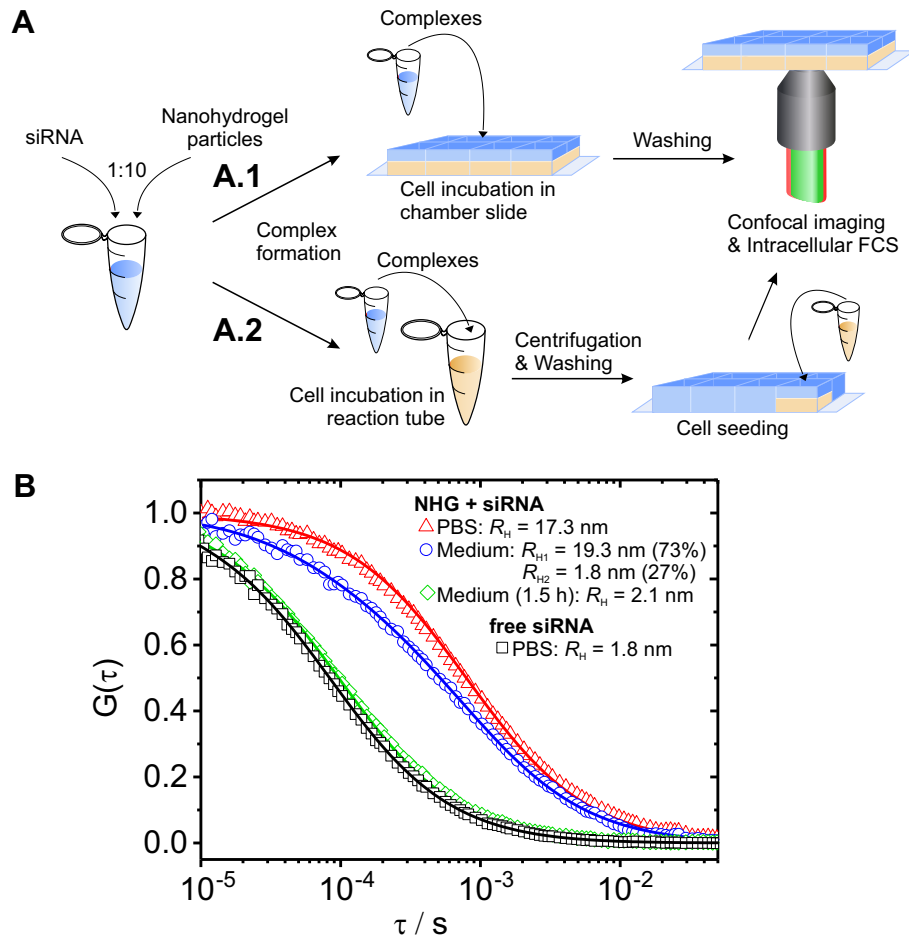


Figure 47: A) Standard (A.1) and adapted (A.2) protocol for the incubation of cells with siRNA-NHG complexes. For the adapted protocol, cells were first transfected with the complexes and afterwards seeded for FCS analysis. Further details can be found in Methods 11.2.7. B) Normalized autocorrelation curves of free Atto 488-labeled siRNA and siRNA-NHG complexes in PBS and cell medium without serum (macrophage transfection medium). Autocorrelation data were fitted with a model for one or two freely diffusing components (Eq. 2.20). For improved comparability the amplitudes were normalized.

extracellularly diffusing siRNA (calculated concentration of about 1 nM) could be reduced.

A second adaptation involved the application of an siRNA construct (siSTABLE-Cy3) that incorporated several proprietary chemical modifications (Dharmacon) (Figure 48A). These modifications were designed to convey an increased resistance against nucleases (Section 9.1.2). An increased stability of siSTABLE-Cy3 in comparison to Atto 488-labeled siRNA could be shown for the treatment with nuclease RNase V1 (Figure 48B). A small difference in size between intact and degraded constructs prevented the application of a two-component fit model and thus direct extraction of the degraded fraction (Section 2.4.2). However, as estimated from the average hydrodynamic radius it was assumed that Atto 488-labeled siRNA was almost completely degraded within the first five minutes. Only a minor fraction of siSTABLE-Cy3, in contrast, appeared to be degraded after one hour as indicated by a drop of R_H from 2.2 to 1.7 nm. In intracellular FCS measurements, siSTABLE-Cy3 delivered by lipoplexes showed a cytoplasmic diffusing species of $D_{\text{siSTABLE-Cy3}(\text{cell})} = 10.8 \pm 2.3 \mu\text{m}^2 \text{s}^{-1}$ (mean \pm standard deviation for $N = 7$ cells). The obtained diffusion coefficient resembled that of the intact, double-labeled ds siRNA (Section 10.2.3).

When the adapted protocol was applied to the transfection of macrophages with NHG-siSTABLE-Cy3, a high uptake of the complexes was observed with CLSM (Figure 48D). The cells were hence searched for release events by FCS. In general, fluorescence intensity traces revealed the presence of large, fluorescent objects. Segments that were not dominated by these broad peaks indicated a fast diffusing species as characteristic for release (Figure 48C). However, due to the multitude of simultaneously occurring events like the diffusion of vesicles, complexes, loaded RISC and released siRNA, autocorrelation data could often not be adequately fitted, even with a multi-component model. In curves that could be fitted the diffusion coefficients of the dominant fast fraction spanned a broad range ($D_{\text{NHG-siSTABLE}(\text{cell})} \approx 6 - 50 \mu\text{m}^2 \text{s}^{-1}$). Figure 48E shows the autocorrelation curve of one such cell.

In summary, the cellular uptake of NHG-siRNA complexes was confirmed and indications of siRNA release were found in several cells. For autocorrelation analysis, this meant that a diffusing species was detected whose diffusion coefficient was assigned to a small molecule rather than an NHG particle or vesicle. In fluorescence intensity traces, a high signal without distinct peaks was assumed to be indicative for release. However, a quantitative and temporally resolved analysis of the release process by FCS could not be obtained. Such analysis was hampered by i) the lack of statistics (single-digit cell numbers within one experimental day) due to the time-consuming measurement mode (about ten minutes per position including z -stack acquisition, V_{obs} positioning and FCS measurement), ii) difficulties to accurately fit the obtained data due to the diversity of simultaneously diffusing fluorescent particles, which iii) complicated the unambiguous assignment of the observed species (*e.g.* intact *vs.* degraded siRNA or RISC *vs.* yet unreleased complexes). Additionally, it was impossible to collect data for multiple cells at the same time point within the same experimental day. Thus, in order to obtain release information on two-digit cell numbers for a given time frame (*e.g.* the first hour after transfection) at least two weeks of experiments would have been necessary while suffering from daily variations in

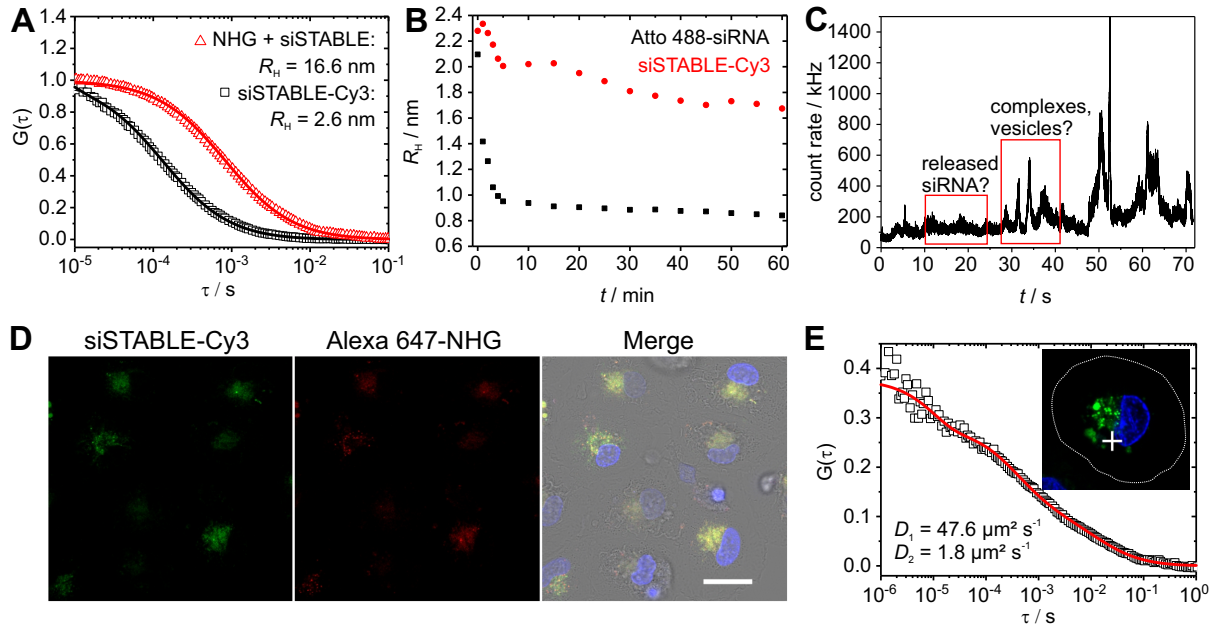


Figure 48: A) Normalized autocorrelation curves of siSTABLE-Cy3 and respective NHG complexes in buffer (PBS). Autocorrelation curves were fitted with a model for one freely diffusing species including a triplet contribution (Eq. 2.20). B) Susceptibility of Atto 488-siRNA and siSTABLE-Cy3 towards RNase V1 nuclease activity. C) Representative fluorescence intensity trace that was recorded in a macrophage 2.5 hours after transfection with siSTABLE-Cy3-NHG complexes. D) Confocal image that shows the uptake of Alexa 647-labeled NHG particles loaded with siSTABLE-Cy3 2.5 hours post-transfection. Merged image represents an overlay of nuclei staining (blue), siSTABLE-Cy3 (green), NHG (red) and the transmission channel. Scale bar: 20 μm . E) Autocorrelation curve measured three hours post-transfection in a macrophage that was treated with siRNA-NHG complexes and which showed release as indicated by the diffusion coefficient D_1 . A second species diffused at a slower time scale (D_2).

parameters such as cell density and viability.

11 Materials and methods

11.1 Materials

11.1.1 Chemicals

Further chemicals that were also employed in Part II and Part III are listed in Materials 5.1.1.

Alexa Fluor [®] 488 carboxylic acid, #A33077	Thermo Fisher Scientific
Alexa Fluor [®] 647 cadaverine, #A30679	Thermo Fisher Scientific
Atto [®] 488 azide, #AD 488-101	Atto-Tec (Siegen, Germany)
D-MEM, indicator-free, 25 mM HEPES, #21063	Thermo Fisher Scientific
D-MEM, #61965	Thermo Fisher Scientific
Ethanol, absolute	Carl Roth
Hoechst 33258 solution, nuclear stain	PromoCell (Heidelberg, Germany)
Oligofectamine [®] transfection reagent, #12252011	Thermo Fisher Scientific
Recombinant EGFP, expressed by <i>E. coli</i>	BioVision (Milpitas, CA, US)
Rhodamine 6G chloride, #R634	Thermo Fisher Scientific
RNase V1, biochemistry grade, 0.1 U/mL	Ambion (Life Technologies, Carlsbad, CA, US)

11.1.2 Fluorophores

Table 15: Fluorophores employed in CLSM and/or FCS measurements.

Name	$\lambda_{\text{exc}}^{\text{max}}$ /nm	$\lambda_{\text{em}}^{\text{max}}$ /nm	Excitation laser /nm	CLSM detection /nm	FCS detection /nm
Hoechst	352	461	405	410 - 470	/
EGFP [†]	488	507	488	LP505	LP488
Alexa 488	500	525	488	/	500 - 562
Atto 488	501	523	488	500 - 562	500 - 562
Rhodamine 6G	528	550	543	/	553 - 606
Cy3	543	547	543	553 - 606	553 - 606
Alexa 647	651	672	633	642 - 696	642 - 696
Atto 647N	644	669	633	/	642 - 696

[†]Measured with Olympus microscope.

11.1.3 siRNA

siRNA single strands targeted against EGFP mRNA were purchased from Iba (Göttingen, Germany). Where indicated, a fluorescent label was added to the 3'- or 5'-end *via* a spacer.

EGFP sense strand: 5'-GCAAGCUGACCCUGAAGUUCAU- 3'

EGFP antisense strand: 5' -GAACUUCAGGGUCAGCUUGCCG- 3'

Chemically modified siRNA (siSTABLE) labeled with Cy3 was a kind gift from Jonathan Schupp (working group of PD Dr. A. Tüttenberg, Dermatology Clinic, University Clinic Medicine, Mainz). It was purchased from Dharmacon (Horizon Discovery Group, Cambridge, UK) and contained a target sequence against the mRNA of peroxisome proliferator-activated receptor gamma (PPARG).

PPARG sense strand: 5'-Cy3-AGACUCAGCUCUACAAUAAUU- 3'

PPARG antisense strand: 5'-UUAUUGUAGAGCUGAGUCUUU- 3'

11.1.4 Buffers and Media

HeLa Maz growth medium: 90% v/v DMEM, 10% v/v FBS, 100 U mL⁻¹ penicillin, 100 µg mL⁻¹ streptomycin

HeLa Maz incubation/microscopy medium: 90% v/v DMEM indicator free + 25 mM HEPES, 10% v/v FBS, 100 U mL⁻¹ penicillin, 100 µg mL⁻¹ streptomycin

HeLa Maz freezing medium: 70% v/v DMEM, 20% v/v FBS, 10% DMSO

Macrophage growth medium: 99% v/v RPMI 1640 indicator free, rh-M-CSF (macrophage colony-stimulating factor), 1% v/v serum

Macrophage transfection medium: 100% RPMI 1640 indicator free, rh-M-CSF

RBE4 pre-transfection medium: 90% v/v DMEM:F-12 indicator free, 10% v/v FBS, 1 ng mL⁻¹ bFGF

RBE4 transfection medium: 100% DMEM:F-12 indicator free + 15 mM HEPES

Cell culture media for the cultivation of RBE4 cells are listed in Materials 5.1.3.

11.1.5 Glassware and Disposables

Glassware and disposables are listed in Materials 5.1.4.

11.1.6 Nanohydrogel particle

The nanohydrogel particle was obtained from Nadine Leber from the working group of Prof. Dr. R. Zentel (Institute of Organic Chemistry, Johannes Gutenberg University, Mainz). The synthesis was performed as described in References [33] and [329].

11.2 Methods

11.2.1 Software and data analysis

Autocorrelation analysis of FCS data was performed with ZEN 2.1 SP3 software. Confocal images were processed with the open-source software ImageJ. [224] Charts and plots were prepared with OriginPro 9.1. Figures were prepared with Corel Draw X7.

11.2.2 Hybridization of siRNA

To determine the appropriate ratio that led to a 1:1 siRNA duplex formation, a titration series of different ratios of the two complementary strands was analyzed by non-denaturing polyacrylamide gel electrophoresis as described in Reference [372]. The single strands were then mixed at the determined ratio at $\approx 5 \mu\text{M}$ concentration in PBS. Prior to the one hour incubation period at 37°C , the mixture was briefly heated (1 min at 90°C). Afterwards, to remove residual free dye the hybridized siRNA was mixed with ammonium acetate to a final concentration of 0.5 M and precipitated with a three-fold volumetric excess of ice-cold ethanol. The mixture was incubated at -20°C for three hours and afterwards centrifuged. After discarding the supernatant, the pellet was washed with 70% ethanol and then dried. Upon resuspension in H_2O , the concentration of the siRNA was determined *via* FCS and Nanodrop (ND-2000, PeqLab, Erlangen, Germany).

11.2.3 CLSM and FCS setup

Intracellular FCS experiments were performed with two different setups, an Olympus / PicoQuant setup and a Zeiss LSM 880 setup. The Olympus microscope was used for the determination of autofluorescence in cell culture media and RBE4 cells and to measure intracellular EGFP diffusion (Sections 10.1.1 and 10.1.3). All other experiments were performed on the Zeiss microscope.

Olympus IX70 / PicoQuant: The commercial setup was based on an inverted Olympus IX70 microscope in combination with a FluoView300 confocal laser scanning unit (Olympus) and a PicoQuant FCS unit that included two separate single photon counting APDs (τ -SPAD, PicoQuant). The instrument was equipped with an argon-ion laser of which the 488 nm laser line was used and helium-neon lasers (543 nm, 633 nm). An Olympus UPLSAPO 60XW 60x/1.2 water immersion objective was used to focus the laser beam into the sample. During

measurements, cells were heated to $\approx 37^\circ\text{C}$ with a remotely controlled Peltier stage (PE100, Linkam Scientific Instruments, Tadworth, UK).

Zeiss LSM 880: A description of the microscope setup can be found in Methods 5.2.5. For this project, the built-in lasers at 488 nm (argon laser line), 543 nm and 633 nm (both helium-neon lasers) excitation wavelengths were used as well as a 405 nm diode laser that was coupled in from a PicoQuant upgrade kit. Furthermore, a C-Apochromat 40x/1.2 water immersion objective was employed. Selection of the main beam splitter depended on the combination of lasers used in the respective experiment. The pinhole diameter was set to one Airy unit. The Quasar spectral detection unit (grating element on a 32 channel array of GaAsP detectors) which shows single photon counting efficiency was used for the detection of photons in CLSM and FCS mode.

11.2.4 Calibration and buffer measurements

Measurements in aqueous solutions were performed in eight-well chambered Nunc microscopy slides. Calibration measurements to obtain size (r_0) and shape (S) of the FCS observation volume were performed using dyes with well-known diffusion coefficients. Precisely, Alexa Fluor 488 ($D = 435 \mu\text{m}^2 \text{s}^{-1}$ at 22.5°C), rhodamine 6G ($D = 414 \mu\text{m}^2 \text{s}^{-1}$ at 25°C) and Alexa Fluor 647 ($D = 330 \mu\text{m}^2 \text{s}^{-1}$ at 25°C) were used. [361, 377] The measurements were carried out at 37°C . Calibration curves were obtained in five repetitions of 30 s each. Upon averaging, a model for one freely diffusing component including a triplet contribution (Eq. 2.20) was applied to retrieve the dimensions of the observation volume. Measurements of siRNA or NHG-siRNA complexes in PBS were comparably obtained. However, where indicated a model for two types of freely diffusing species was applied to fit the autocorrelation data (Eq. 2.20).

11.2.5 Nuclease resistance assay

3 pmol siRNA (10 nM) were reacted with 60 μU RNase V1 in RNA structure buffer (Ambion) in a total volume of 300 μL . FCS was measured over a period of one hour. From the data of five consecutive minutes an autocorrelation curve was calculated which was then fitted with a model for one type of diffusing species including a triplet contribution (Eq. 2.20). The respective hydrodynamic radius was calculated applying Equations 2.10 and 2.11.

11.2.6 Cell culture

The following mammalian cells were employed for intracellular FCS measurements:

RBE4: refer to Methods 5.2.4.

HeLa Maz: The HeLa cell line is derived from epitheloid cervix carcinoma cells (DSMZ #ACC57). The HeLa Maz strain contains the episomal vector pMARS-mODC-AZ (gene bank accession #EU421131), which encodes and expresses destabilized EGFP. [378] The cells were

a kind gift from Dr. A. Khobta (Prof. Dr. B. Epe, Institute for Pharmacy and Biochemistry, Mainz).

Macrophages: Primary human macrophages were cultured by Jonathan Schupp from the working group of PD Dr. A. Tüttenberg (Dermatology Clinic, University Clinic Medicine, Mainz). In short, peripheral blood mononuclear cells were isolated from peripheral blood of healthy volunteers using density gradient centrifugation. [379] The adherent cells were then cultured in macrophage growth medium for several days. Upon harvesting by accutase, the unpolarized macrophages were collected and transported to the MPI-P where they were subjected to the respective transfection protocol (Methods 11.2.7).

General cell culture procedures for the immortalized cell line RBE4 can be found in Methods 5.2.4. HeLa Maz cells were treated similarly using optimized HeLa cell culture media.

11.2.7 Protocol for intracellular FCS measurements

Lipoplex transfection: RBE4 cells or macrophages were seeded one to two days prior to the live cell experiment in 300 μL indicator- and antibiotics-free medium (RBE4 pre-transfection medium or macrophage growth medium) in eight-well Nunc chambered cover slides. On the day of the experiment, lipoplexes were prepared by first mixing (A) 1.6 μL (8 pmol) of siRNA with 29 μL of transfection medium and (B) 1.6 μL of Oligofectamine[®] with 7 μL of transfection medium. Mix (A) and (B) were combined and incubated for 15 min at room temperature to ensure lipoplex formation. Meanwhile, the adherent RBE4 cells were washed and supplied with 261 μL of prewarmed medium (RBE4 transfection medium or macrophage transfection medium). To initiate transfection, 39 μL of lipoplexes were added to each well. Where indicated, macrophages were co-stained with the nuclear dye Hoechst by adding a 0.05% solution during transfection. Cells were then either directly subjected to CLSM and FCS measurements or they were washed 30 to 60 min post-transfection and afterwards analyzed.

Adapted protocol for transfection with NHG particles: Complexes were prepared by mixing NHG particles and siRNA at a 10:1 mass ratio and incubating them for 15 min at room temperature. 25 μL of complexes (containing 50 pmol loaded siRNA) were added to 800 μL of macrophage cells in suspension (10^6 cells per mL) and incubated for 30 min in a 37°C water bath. Afterwards, the cell suspension was centrifuged ($500 \times g$, 5 min) and washed twice with 600 μL of macrophage growth medium. The cells were then resuspended in 600 μL of macrophage growth medium supplemented with 0.05% Hoechst solution. The suspension was distributed to eight-well Nunc microscopy slides (300 μL per well) and the cells were left to adhere for about 30 min inside a cell incubator. Without further washing steps, the cells were subsequently analyzed by CLSM and FCS.

Intracellular data acquisition: First, confocal imaging was employed to search for cells of interest. If such cells were identified, the region of interest, usually accomodating several cells,

was zoomed in and a z -stack was recorded. In the acquired image stack a spot for FCS was selected that, judging from the acquired z -sections, was located within the cell boundaries. Prior to the data acquisition, the average fluorescence intensity of the selected position was observed as a first hint towards a positive signal above background. In some cases, measurements were preceded by either a short period of photobleaching or a z -scan in FCS mode to adjust the selected z -plane to the one with the highest count rate as this often indicated a localization well inside the cell's interior. Typically, for each intracellular position ten correlation curves were recorded over sequential 10 s intervals.

Data analysis: Curves affected either by a decrease in count rate or by the occurrence of large aggregates (fluorescent particles or vesicles) were excluded and the remaining curves were averaged for further data analysis. Fitting models such as Equation 2.20 were applied as indicated in the respective experiment. The thus extracted diffusion times were converted to diffusion coefficients with Equation 2.12 under the assumption that the FCS observation volume had the same dimensions as determined in the corresponding calibration measurement.

Autofluorescence: Autofluorescence measurements in RBE4 cell culture medium were performed on the Olympus setup with the following lasers and emission filters (Semrock, Rochester, NY, US): 488 nm excitation with an LP488 or BP525/50 emission filter, 543 nm excitation with an LP565 or BP585/40 emission filter, 633 nm excitation with an LP635 or BP690/70 emission filter. For the intracellular autofluorescence measurements of untreated RBE4 cells only band pass filters were employed. As the microscope lacked a transmission detector, cellular outlines were identified *via* an altered reflectivity of cellular material *vs.* the aqueous extracellular environment. Macrophage autofluorescence, in contrast, was determined on the Zeiss LSM 880 setup where the detection of transmitted light as well as nuclear staining facilitated accurate intracellular positioning for FCS measurements. The employed emission ranges were 500 to 562 nm ($\lambda_{\text{exc}} = 488$ nm), 553 to 606 nm ($\lambda_{\text{exc}} = 543$ nm) and 642 to 696 nm ($\lambda_{\text{exc}} = 633$ nm).

EGFP diffusion in HeLa Maz cells: HeLa Maz cells were seeded in chambered microscopy slides two days prior to the live cell experiment. On the day of the experiment, the medium was exchanged to HeLa Maz microscopy medium. Cell outlines were identified in CLSM mode by bright EGFP fluorescence. Due to the high EGFP expression level prebleaching of the entire cell was required prior to the intracellular FCS measurement. FCS curves were then acquired upon 488 nm excitation and emission detection with an LP488 filter. The averaged autocorrelation curves were fitted with a model for one type of freely diffusion species including a triplet contribution (Eq. 2.20).

Part V

Conclusion and Outlook

This work set out to investigate the fate of transporting structures based on small molecules and nanocarriers in biological environments. To this end, the application of fluorescently labeled structures offered the possibility of i) *in situ* detection modes which were ii) non-destructive and iii) specific for the labeled structures among their heterogeneous and crowded biological surroundings. The special focus was on the development and application of FCS- and FRET-based protocols that allowed to study the behavior of the transporting structures at a scale below the optical resolution limit of CLSM.

Modulation of mitochondriotropic properties of cyanine dyes by *in organello* copper-free click reaction

This study reported on the covalent formation of a FRET dye inside the mitochondria of living cells. The concept of targeting mitochondria with mitochondriotropic compounds for diagnostic or potential therapeutic purposes has been continuously extended throughout the last decades. [16] However, the exploitation of mitochondria as reaction chambers for exogenously introduced molecules has only recently been shown. In 2016, two studies independently reported on the latter concept, one of which employed LC-MS as an endpoint analysis to detect product formation and the other relied on the detection of an uncaged fluorescent dye by CLSM. [122,206] With the goal of performing a mitochondrial reaction that would be *in situ* traceable at a molecular scale, reaction partners based on the cyanine dye structures of Cy3 and Cy5 had been chosen. Cy3 and Cy5 hence served as targeting domains and imaging reporters which by the detection of FRET proved suitable to report on a successful coupling of Cy3 and Cy5 by strain-promoted azide-alkyne cycloaddition. The mitochondriotropism of Cy3 and Cy5 dyes, as apparent in fluorescent mitochondrial staining of RBE4 cells, was demonstrated to remain unaffected by the functionalization with the reactive moieties of azide or DBCO. Moreover, the $\Delta\Psi_m$ -dependence of mitochondrial accumulation and the reversibility of membrane passage for the functionalized Cy dyes was shown. Hence, both reaction pairs, Cy3-DBCO and Cy5-azide as well as their permutated counterpart of Cy3-azide and Cy5-DBCO, were separately examined with respect to their *in organello* reactivity. The $\Delta\Psi_m$ -dependent formation of the respective products was traceable by FRET in confocal microscopy and could be confirmed by an LC-MS analysis of the re-isolated products. In addition, after the precursors had been exported from the mitochondria upon washing the cells, the mitochondrial FRET staining remained. This finding was attributed to the presence of two delocalized cationic charges in the products' structure which potentially led to a reduced membrane permeation and greater retention in the negative mitochondrial matrix as compared to their building blocks. This assumption could be supported by the observation that the externally preformed products were not able to localize

to mitochondria.

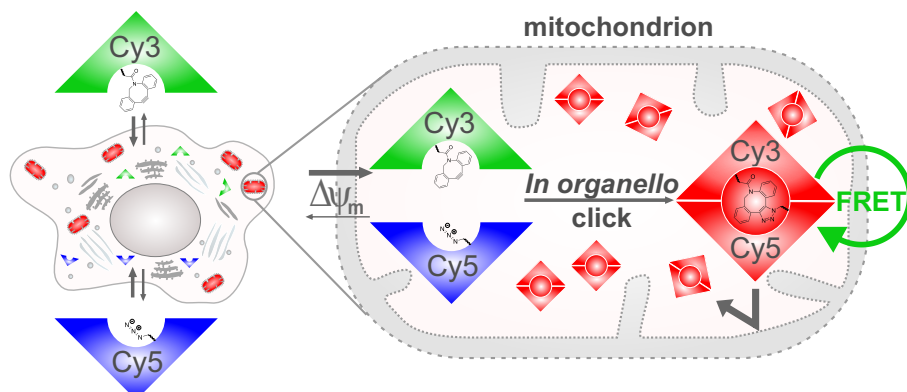


Figure 49: The *in organello* synthesis of the Cy3-Cy5 product revealed the synergistic properties of FRET and a reduced membrane permeability, the latter leading to its effective mitochondrial retention.

Taken together, the new mitochondria-localizing Cy3-Cy5 conjugates possessed synergistic properties which were not present in their respective Cy dye building blocks. These properties comprised an efficient FRET and a reduced membrane permeability. The emergence of either of these two favorable properties by covalent *in organello* reaction had not been demonstrated before. While the FRET effect enabled the detection of product formation at a scale below the optical resolution limit, the altered membrane permeability of the product highlighted the advantage of its *in organello* synthesis rather than its application from the outside.

Future work might explore the application of the washing-resistant FRET dye as a fluorescent redox sensor *e.g.* in ROS imaging. For instance, the strategy of measuring peroxynitrite levels with a Cy3-Cy5 construct as introduced by Jia *et al.* might be improved: The *in organello* synthesis rather than post-synthetic administration of such construct might allow to reduce probe concentration and to increase mitochondrial specificity. [190] Furthermore, these new insights into mitochondrial targeting, membrane permeation and the proceedings of intramitochondrial SPAAC could be used to develop novel therapies for mitochondrial diseases. Acting by this prodrug concept, the assembly of a toxic or non-penetrating active compound directly at the target site might be beneficial with respect to the treatment's efficacy and safety. [380]

Monitoring drug nanocarriers in human blood by near-infrared fluorescence correlation spectroscopy

In this project a new FCS-based method was developed that allowed to investigate the behavior of fluorescently labeled nanocarriers directly in blood. The onset of instabilities such as aggregation, decomposition or substantial loss of drug cargo upon contact with blood can have detrimental effects on the nanocarriers' fate. However, *in situ* blood measurements have not been part of routine examinations in preclinical studies due to a lack of blood-compatible methods. In order to minimize spectroscopic interferences with red blood cells, the presented FCS method employed single photon NIR excitation and emission. NIR-FCS measurements

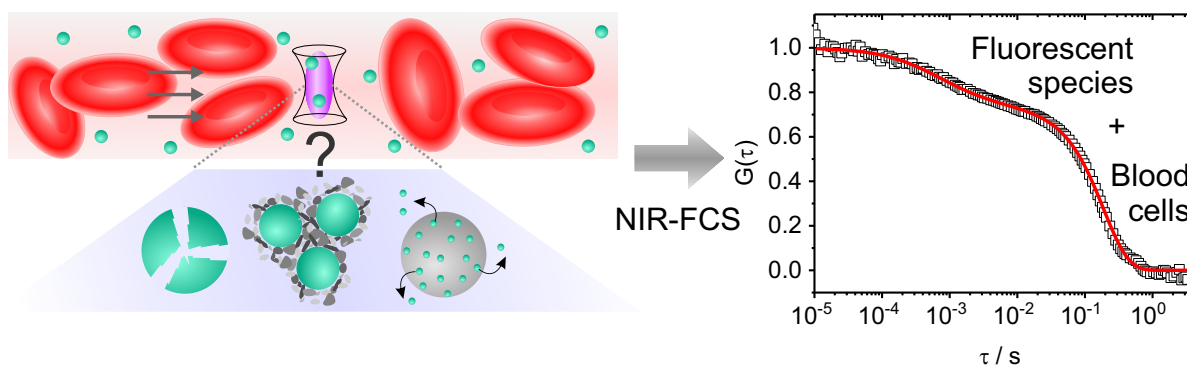


Figure 50: The method of NIR-FCS was developed in order to monitor the onset of nanocarrier instabilities such as disintegration, aggregation or premature drug release directly in blood.

were preceded by a thorough calibration of the NIR-FCS setup. The calibration in aqueous solution was based on an NIR-labeled, monodisperse polymer brush **PB1** and yielded the radial ($r_0 \approx 0.35 \mu\text{m}$) and axial ($z_0 \approx 1.75 \mu\text{m}$) dimensions of the observation volume. **PB1** was furthermore utilized for the subsequent method development in human blood. First measurements in a blood droplet highlighted the necessity for positioning the observation volume at cell-free spots in order to observe unhindered diffusion of **PB1**. Abrogation of such position dependence was achieved by subjecting the blood sample to flow. The autocorrelation curves measured in flowing blood showed two decay times, the faster one caused by diffusion and flow of **PB1** and the slower one caused by the passage of blood cells through the observation volume. An extended fit model was derived that considered both additional effects, the presence of flow and the depletion of tracers in the presence of a blood cell. The thus obtained diffusion coefficient of **PB1** closely matched the diffusion properties in plasma but was markedly slower than diffusion in water. This diffusion slowdown could be attributed to an ≈ 1.4 -fold increase of the effective viscosity of plasma. The NIR-FCS protocol was shown to be sensitive enough to detect low fluorescing single dye molecules in blood. This was an important prerequisite to ensure that events such as dissociation or the loss of complexed dye would be traceable. Detection of the latter event could be confirmed with blood-dispersed polymeric micelles. Here, NIR-FCS was able to reveal the premature loss of non-covalently attached dye from these micelles. In contrast, covalently labeled micelles remained intact in the blood during a 30-hour incubation. Protein adsorption on the nanocarriers' surface, an event that can potentially result in aggregation, was also successfully detected with NIR-FCS.

Altogether, NIR-FCS has been implemented for direct measurements in flowing blood and its applicability has been demonstrated in “proof-of-principle” investigations on single dyes and nanocarriers. Importantly, the measurements in blood did not require any preceding preparation steps besides the addition of an anticoagulant. To the author’s knowledge, this demonstration of a blood-compatible method with individual nanocarrier sensitivity is unprecedented. It shows potential for the detection of stability-related issues early during the development process of nanocarriers which can help in the design of more efficient nanocarrier-based therapeutics.

Further work might engage in performing *ex vivo* kinetic measurements by drawing blood samples at regular intervals and determining the stability and blood circulation half-life of fluorescently labeled nanocarriers. Also, future research might take the NIR-FCS method further towards an *in vivo* adaptation. The measurement mode in the presence of flow already approximates *in vivo* conditions where the blood is set in motion by the heart. Challenges, however, might arise from the pulsation of the blood flow or from too high flow velocities that uncompensably shorten the time segments in which nanocarrier diffusion can be monitored.

Monitoring nanocarrier-based delivery and release of RNA molecules by fluorescence correlation spectroscopy

While cellular uptake and intracellular trafficking of drug-loaded nanocarriers are often investigated by CLSM, the unambiguous detection of payload release is hampered by the optical resolution limit. In this project, the question of intracellular drug release from nanocarriers was explored with FCS. The development of a protocol was carried out using the example of siRNA delivery by lipoplexes. The release of fluorescently labeled siRNA could be detected by two modes of analysis. First, a qualitative indication for release was yielded by an evident increase in the average fluorescence intensity signal. This increase was found to be distinctive from the broad and highly intense signals caused by unreleased carriers diffusing through the observation volume. Second, the detection of a species by autocorrelation analysis, which diffused orders of magnitude faster than vesicles or nanocarriers, was shown to be indicative for release. Both approaches revealed a high sensitivity for the detection of release events of which many would have gone unnoticed by CLSM alone. However, caution had to be applied while attempting to assign the detected diffusing species to intact siRNA. An accurate size determination was complicated by cell-to-cell variations and an increased fluid-phase viscosity. Furthermore, it was assumed that intact as well as degraded siRNA, intact nanocarriers and loaded vesicles could be simultaneously present within a cell and interact with cell components. Hence, it remained difficult to account for the uncertain number of diffusing fluorescent species, even with a multi-component fitting model. Findings from dual color FCCS experiments, however, suggested that the released species at least partially comprised intact siRNA. A further limitation derived from the low occurrence of release events which presumably affected only a subset of cells. Intracellular FCS measurements furthermore demanded a manual, cell-by-cell data acquisition, analysis and interpretation. Thus, the number of analyzable measurements per experiment was limited and returned low statistics. Nonetheless, findings from a number of experiments allowed the tentative conclusion that release events peaked within the first hours after the transfection. Intracellular FCS measurements were also performed to investigate the release of siRNA molecules from nanohydrogel particles. In comparison to lipoplexes, nanohydrogel particles bound a much lower number of siRNA molecules. Consequently, many synchronously releasing nanohydrogel particles would have been required to obtain an autocorrelation curve that was dominated by released siRNA. Most of the measurements, however, revealed a great heterogeneity of fluorescent species suggesting the simultaneous presence of released siRNA and

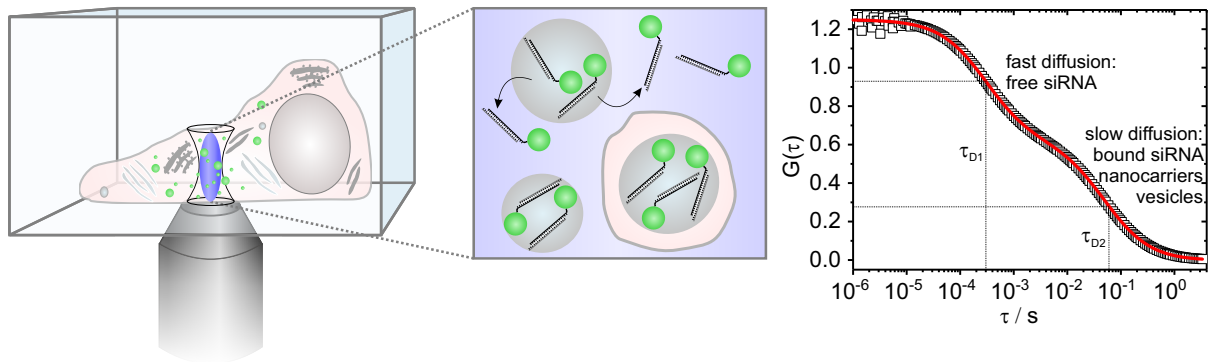


Figure 51: Intracellular FCS measurements provided indications on the release of siRNA molecules from nanocarriers, *i.e.* by the appearance of a fast diffusing species in the autocorrelation curve.

intact particles.

Altogether, in “proof-of-principle” experiments an FCS protocol was established that was able to report on the intracellular release of siRNA molecules from lipoplexes and nanohydrogel particles. The key strength of this protocol is its single-molecule sensitivity by which it is able to complement CLSM-based studies on the intracellular fate of nanocarriers.

Future work might investigate in two directions. First, the protocol might be routinely extended to FCCS. As demonstrated by Ohrt *et al.* on microinjected siRNA, dual color FCCS offers the great potential of resolving the integrity state of siRNA or its interaction with fluorescently labeled protein complexes such as RISC. [301,305] Furthermore, to support investigations on the site and time point of release fluorescent endocytosis markers might be employed. Second, automated high-throughput FC(C)S, as introduced by Wachsmuth *et al.*, might be explored to approach a comprehensive quantitative description of release across a large set of cells. [381] By acquiring and analyzing data from > 10,000 living HeLa cells, the authors studied chromatin-protein interactions between a fluorescent protein-tagged chromatin marker (histone H2B-mCherry) and transiently expressed and fluorescent protein-tagged nuclear proteins by FCCS. Hence, they stated that the method allows for unattended time-lapse measurements and comprises an automated FCS workflow including all steps from image acquisition to data analysis.

Bibliography

- [1] N. S. Claxton, T. J. Fellers, and M. W. Davidson, "Microscopy, Confocal," in *Encyclopedia of Medical Devices and Instrumentation*. John Wiley & Sons, Inc., 2006.
- [2] H. C. Ishikawa-Ankerhold, R. Ankerhold, and G. P. C. Drummen, "Advanced Fluorescence Microscopy Techniques—FRAP, FLIP, FLAP, FRET and FLIM," *Molecules*, vol. 17, no. 4, p. 4047, 2012.
- [3] S. J. Sahl, S. W. Hell, and S. Jakobs, "Fluorescence nanoscopy in cell biology," *Nature Reviews Molecular Cell Biology*, vol. 18, p. 685, 2017.
- [4] T. Förster, "Zwischenmolekulare Energiewanderung Und Fluoreszenz," *Annalen der Physik*, vol. 2, no. 1-2, pp. 55–75, 1948.
- [5] J. R. Lakowicz, *Principles of Fluorescence Spectroscopy*. Springer, 2006.
- [6] R. Rigler and E. Elson, *Fluorescence Correlation Spectroscopy: Theory and Applications*. New York: Springer, 2001.
- [7] E. J. Zander, C. and R. A. Keller, *Single Molecule Detection in Solution - Methods and Applications*. Wiley-VCH, 2002.
- [8] R. Macháň and T. Wohland, "Recent applications of fluorescence correlation spectroscopy in live systems," *FEBS Letters*, vol. 588, no. 19, pp. 3571–3584, 2014.
- [9] J. Mutze, T. Ohrt, and P. Schwille, "Fluorescence correlation spectroscopy in vivo," *Laser & Photonics Reviews*, vol. 5, no. 1, pp. 52–67, 2011.
- [10] P. Schwille and E. Haustein, "Fluorescence Correlation Spectroscopy - An Introduction to its Concepts and Applications," 2006.
- [11] L. F. Yousif, K. M. Stewart, and S. O. Kelley, "Targeting mitochondria with organelle-specific compounds: strategies and applications," *ChemBiochem: A European Journal of Chemical Biology*, vol. 10, no. 12, pp. 1939–50, 2009.
- [12] R. A. J. Smith, R. C. Hartley, H. M. Cochemé, and M. P. Murphy, "Mitochondrial pharmacology," *Trends in Pharmacological Sciences*, vol. 33, no. 6, pp. 341–352, 2012.
- [13] V. Weissig and V. P. Torchilin, "Mitochondriotropic cationic vesicles: a strategy towards mitochondrial gene therapy," *Current Pharmaceutical Biotechnology*, vol. 1, no. 4, pp. 325–46, 2000.

- [14] R. W. Horobin, S. Trapp, and V. Weissig, "Mitochondriotropics: A review of their mode of action, and their applications for drug and DNA delivery to mammalian mitochondria," *Journal of Controlled Release*, vol. 121, no. 3, pp. 125–136, 2007.
- [15] V. Weissig and V. P. Torchilin, "Towards Mitochondrial Gene Therapy: DQAsomes as a Strategy," *Journal of Drug Targeting*, vol. 9, no. 1, pp. 1–13, 2000.
- [16] S. Wisnovsky, E. K. Lei, S. R. Jean, and S. O. Kelley, "Mitochondrial Chemical Biology: New Probes Elucidate the Secrets of the Powerhouse of the Cell," *Cell Chemical Biology*, vol. 23, no. 8, pp. 917–927, 2016.
- [17] B. Alberts, A. Johnson, J. Lewis, M. Raff, K. Roberts, and P. Walter, *Molecular Biology of the Cell*, 4th ed. New York: Garland Science, 2002.
- [18] D. G. Nicholls and S. J. Ferguson, "10 - The Cell Biology of the Mitochondrion," in *Bioenergetics*. Boston: Academic Press, 2013, pp. 303–325.
- [19] E. Blanco, H. Shen, and M. Ferrari, "Principles of nanoparticle design for overcoming biological barriers to drug delivery," *Nature Biotechnology*, vol. 33, no. 9, pp. 941–951, 2015.
- [20] D. Bobo, K. J. Robinson, J. Islam, K. J. Thurecht, and S. R. Corrie, "Nanoparticle-Based Medicines: A Review of FDA-Approved Materials and Clinical Trials to Date," *Pharmaceutical Research*, vol. 33, no. 10, pp. 2373–87, 2016.
- [21] J. Shi, P. W. Kantoff, R. Wooster, and O. C. Farokhzad, "Cancer nanomedicine: progress, challenges and opportunities," *Nature Reviews: Cancer*, vol. 17, no. 1, pp. 20–37, 2017.
- [22] K. A. Whitehead, R. Langer, and D. G. Anderson, "Knocking down barriers: advances in siRNA delivery," *Nature Reviews Drug Discovery*, vol. 8, no. 2, pp. 129–138, 2009.
- [23] K. C. Liu and Y. Yeo, "Extracellular stability of nanoparticulate drug carriers," *Archives of Pharmacal Research*, vol. 37, no. 1, pp. 16–23, 2014.
- [24] Y. Matsumura and H. Maeda, "A new concept for macromolecular therapeutics in cancer chemotherapy: mechanism of tumor-tropic accumulation of proteins and the antitumor agent smancs," *Cancer Research*, vol. 46, no. 12 Pt 1, pp. 6387–92, 1986.
- [25] R. K. Jain and T. Stylianopoulos, "Delivering nanomedicine to solid tumors," *Nature Reviews Clinical Oncology*, vol. 7, no. 11, p. 653, 2010.
- [26] B. Yameen, W. I. Choi, C. Vilos, A. Swami, J. Shi, and O. C. Farokhzad, "Insight into nanoparticle cellular uptake and intracellular targeting," *Journal of Controlled Release*, vol. 190, pp. 485–499, 2014.

- [27] R. Duncan and S. C. W. Richardson, “Endocytosis and Intracellular Trafficking as Gateways for Nanomedicine Delivery: Opportunities and Challenges,” *Molecular Pharmaceutics*, vol. 9, no. 9, pp. 2380–2402, 2012.
- [28] B. Pelaz, C. Alexiou, R. A. Alvarez-Puebla, F. Alves, A. M. Andrews, S. Ashraf, L. P. Balogh, L. Ballerini, A. Bestetti, C. Brendel, S. Bosi, M. Carril, W. C. W. Chan, C. Chen, X. Chen, X. Chen, Z. Cheng, D. Cui, J. Du, C. Dullin, A. Escudero, N. Feliu, M. Gao, M. George, Y. Gogotsi, A. Grünweller, Z. Gu, N. J. Halas, N. Hampp, R. K. Hartmann, M. C. Hersam, P. Hunziker, J. Jian, X. Jiang, P. Jungebluth, P. Kadhiresan, K. Kataoka, A. Khademhosseini, J. Kopeček, N. A. Kotov, H. F. Krug, D. S. Lee, C.-M. Lehr, K. W. Leong, X.-J. Liang, M. Ling Lim, L. M. Liz-Marzán, X. Ma, P. Macchiarini, H. Meng, H. Möhwald, P. Mulvaney, A. E. Nel, S. Nie, P. Nordlander, T. Okano, J. Oliveira, T. H. Park, R. M. Penner, M. Prato, V. Puentes, V. M. Rotello, A. Samarakoon, R. E. Schaak, Y. Shen, S. Sjöqvist, A. G. Skirtach, M. G. Soliman, M. M. Stevens, H.-W. Sung, B. Z. Tang, R. Tietze, B. N. Udugama, J. S. VanEpps, T. Weil, P. S. Weiss, I. Willner, Y. Wu, L. Yang, Z. Yue, Q. Zhang, Q. Zhang, X.-E. Zhang, Y. Zhao, X. Zhou, and W. J. Parak, “Diverse Applications of Nanomedicine,” *ACS Nano*, vol. 11, no. 3, pp. 2313–2381, 2017.
- [29] M. Hemmelmann, D. Kurzbach, K. Koynov, D. Hinderberger, and R. Zentel, “Aggregation behavior of amphiphilic p(HPMA)-co-p(LMA) copolymers studied by FCS and EPR spectroscopy,” *Biomacromolecules*, vol. 13, no. 12, pp. 4065–4074, 2012.
- [30] J. Weyermann, D. Lochmann, C. Georgens, I. Rais, J. Kreuter, M. Karas, M. Wolkenhauer, and A. Zimmer, “Physicochemical characterisation of cationic polybutylcyanoacrylat-nanoparticles by fluorescence correlation spectroscopy,” *European Journal of Pharmaceutics and Biopharmaceutics*, vol. 58, no. 1, pp. 25–35, 2004.
- [31] K. Tappertzhofen, S. Beck, E. Montermann, D. Huesmann, M. Barz, K. Koynov, M. Bros, and R. Zentel, “Bio-reducible Poly-L-Lysine–Poly[HPMA] Block Copolymers Obtained by RAFT-Polymerization as Efficient Polyplex-Transfection Reagents,” *Macromolecular Bioscience*, vol. 16, no. 1, pp. 106–120, 2016.
- [32] I. Tabujew, C. Freidel, B. Krieg, M. Helm, K. Koynov, K. Mullen, and K. Peneva, “The guanidinium group as a key part of water-soluble polymer carriers for siRNA complexation and protection against degradation,” *Macromolecular Rapid Communications*, vol. 35, no. 13, pp. 1191–1197, 2014.
- [33] L. Nuhn, M. Hirsch, B. Krieg, K. Koynov, K. Fischer, M. Schmidt, M. Helm, and R. Zentel, “Cationic nanohydrogel particles as potential siRNA carriers for cellular delivery,” *ACS Nano*, vol. 6, no. 3, pp. 2198–2214, 2012.
- [34] P. Rigler and W. Meier, “Encapsulation of Fluorescent Molecules by Functionalized Polymeric Nanocontainers: Investigation by Confocal Fluorescence Imaging and Fluorescence

- Correlation Spectroscopy,” *Journal of the American Chemical Society*, vol. 128, no. 1, pp. 367–373, 2006.
- [35] T. Fritz, M. Voigt, M. Worm, I. Negwer, S. S. Muller, K. Kettenbach, T. L. Ross, F. Roesch, K. Koynov, H. Frey, and M. Helm, “Orthogonal Click Conjugation to the Liposomal Surface Reveals the Stability of the Lipid Anchorage as Crucial for Targeting,” *Chemistry – A European Journal*, vol. 22, no. 33, pp. 11 578–82, 2016.
- [36] E. I. Altinoglu and J. H. Adair, “Near infrared imaging with nanoparticles,” *Wiley Interdiscip Rev Nanomed Nanobiotechnol*, vol. 2, no. 5, pp. 461–477, 2010.
- [37] A. Haque, M. S. H. Faizi, J. A. Rather, and M. S. Khan, “Next generation NIR fluorophores for tumor imaging and fluorescence-guided surgery: A review,” *Bioorganic and Medicinal Chemistry*, vol. 25, no. 7, pp. 2017–2034, 2017.
- [38] I. Martinić, S. V. Eliseeva, and S. Petoud, “Near-infrared emitting probes for biological imaging: Organic fluorophores, quantum dots, fluorescent proteins, lanthanide(III) complexes and nanomaterials,” *Journal of Luminescence*, vol. 189, no. Supplement C, pp. 19–43, 2017.
- [39] D. Scherman, A. Rousseau, P. Bigey, and V. Escriou, “Genetic pharmacology: progresses in siRNA delivery and therapeutic applications,” *Gene Therapy*, vol. 24, no. 3, pp. 151–156, 2017.
- [40] M. Hirsch and M. Helm, “Live cell imaging of duplex siRNA intracellular trafficking,” *Nucleic Acids Research*, vol. 43, no. 9, pp. 4650–4660, 2015.
- [41] A. Wittrup, A. Ai, X. Liu, P. Hamar, R. Trifonova, K. Charisse, M. Manoharan, T. Kirchhausen, and J. Lieberman, “Visualizing lipid-formulated siRNA release from endosomes and target gene knockdown,” *Nature Biotechnology*, vol. 33, no. 8, pp. 870–876, 2015.
- [42] G. Sahay, W. Querbes, C. Alabi, A. Eltoukhy, S. Sarkar, C. Zurenko, E. Karagiannis, K. Love, D. Chen, R. Zoncu, Y. Buganim, A. Schroeder, R. Langer, and D. G. Anderson, “Efficiency of siRNA delivery by lipid nanoparticles is limited by endocytic recycling,” *Nature Biotechnology*, vol. 31, no. 7, pp. 653–661, 2013.
- [43] K. Kubota, K. Onishi, K. Sawaki, T. Li, K. Mitsuoka, T. Sato, and S. Takeoka, “Effect of the nanoformulation of siRNA-lipid assemblies on their cellular uptake and immune stimulation,” *International journal of nanomedicine*, vol. 12, pp. 5121–5133, 2017.
- [44] M. Lazebnik, R. K. Keswani, and D. W. Pack, “Endocytic Transport of Polyplex and Lipoplex siRNA Vectors in HeLa Cells,” *Pharmaceutical Research*, vol. 33, no. 12, pp. 2999–3011, 2016.

- [45] B. Krieg, M. Hirsch, E. Scholz, L. Nuhn, I. Tabujew, H. Bauer, S. Decker, A. Khobta, M. Schmidt, W. Tremel, R. Zentel, K. Peneva, K. Koynov, A. J. Mason, and M. Helm, “New Techniques to Assess In Vitro Release of siRNA from Nanoscale Polyplexes,” *Pharmaceutical Research*, vol. 32, no. 6, pp. 1957–1974, 2015.
- [46] K. Holmes, C. M. Williams, E. A. Chapman, and M. J. Cross, “Detection of siRNA induced mRNA silencing by RT-qPCR: considerations for experimental design,” *BMC Research Notes*, vol. 3, 2010.
- [47] A. Elouahabi and J.-M. Ruyschaert, “Formation and Intracellular Trafficking of Lipoplexes and Polyplexes,” *Molecular Therapy*, vol. 11, no. 3, pp. 336–347, 2005.
- [48] A. Dominik, D. Steinhilber, and A. Wurglics, *Instrumentelle Analytik kompakt*. Wissenschaftliche Verlagsgesellschaft Stuttgart, 2013.
- [49] Confocal Microscopy - Fluorescence Excitation and Emission Fundamentals. Accessed: 2018/03/06. [Online]. Available: <http://olympus.magnet.fsu.edu/primer/techniques/confocal/fluoroexciteemit.html>
- [50] G. G. Stokes, “XXX. On the change of refrangibility of light,” *Philosophical Transactions of the Royal Society of London*, vol. 142, pp. 463–562, 1852.
- [51] M. Kasha, “Characterization of Electronic Transitions in Complex Molecules,” *Discussions of the Faraday Society*, vol. 9, no. 9, pp. 14–19, 1950.
- [52] J. F. W. Herschel, “IV. On a case of superficial colour presented by a homogeneous liquid internally colourless,” *Philosophical Transactions of the Royal Society of London*, vol. 135, pp. 143–145, 1845.
- [53] M. Minsky, “Microscopy apparatus,” United States Patent 3,013,467, 1961.
- [54] R. H. Webb, “Confocal optical microscopy,” *Reports on Progress in Physics*, vol. 59, no. 3, p. 427, 1996.
- [55] R. Borlinghaus, “The White Confocal: Continuous Spectral Tuning in Excitation and Emission,” in *Optical Fluorescence Microscopy: From the Spectral to the Nano Dimension*, A. Diaspro, Ed. Springer-Verlag Berlin Heidelberg, 2011, pp. 37–54.
- [56] F. Quercioli, “Fundamentals of Optical Microscopy,” in *Optical Fluorescence Microscopy: From the Spectral to the Nano Dimension*, A. Diaspro, Ed. Springer-Verlag Berlin Heidelberg, 2011, pp. 1–36.
- [57] E. Abbe, “VII.—On the Estimation of Aperture in the Microscope,” *Journal of the Royal Microscopical Society*, vol. 1, no. 3, pp. 388–423, 1881.
- [58] Numerical Aperture. Accessed: 2018/03/06. [Online]. Available: <https://www.microscopyu.com/microscopy-basics/numerical-aperture>

- [59] S. Bolte and F. P. Cordelières, “A guided tour into subcellular colocalization analysis in light microscopy,” *Journal of Microscopy*, vol. 224, no. 3, pp. 213–232, 2006.
- [60] L. Schermelleh, R. Heintzmann, and H. Leonhardt, “A guide to super-resolution fluorescence microscopy,” *The Journal of Cell Biology*, vol. 190, no. 2, pp. 165–175, 2010.
- [61] E. Betzig, G. H. Patterson, R. Sougrat, O. W. Lindwasser, S. Olenych, J. S. Bonifacino, M. W. Davidson, J. Lippincott-Schwartz, and H. F. Hess, “Imaging Intracellular Fluorescent Proteins at Nanometer Resolution,” *Science*, vol. 313, no. 5793, pp. 1642–1645, 2006.
- [62] S. T. Hess, T. P. Girirajan, and M. D. Mason, “Ultra-high resolution imaging by fluorescence photoactivation localization microscopy,” *Biophysical Journal*, vol. 91, no. 11, pp. 4258–4272, 2006.
- [63] M. J. Rust, M. Bates, and X. Zhuang, “Sub-diffraction-limit imaging by stochastic optical reconstruction microscopy (STORM),” *Nature Methods*, vol. 3, no. 10, pp. 793–795, 2006.
- [64] S. W. Hell and J. Wichmann, “Breaking the diffraction resolution limit by stimulated emission: stimulated-emission-depletion fluorescence microscopy,” *Optics Letters*, vol. 19, no. 11, pp. 780–782, 1994.
- [65] T. A. Klar, S. Jakobs, M. Dyba, A. Egner, and S. W. Hell, “Fluorescence microscopy with diffraction resolution barrier broken by stimulated emission,” *Proceedings of the National Academy of Sciences of the United States of America*, vol. 97, no. 15, pp. 8206–8210, 2000.
- [66] S. W. Hell, “Fluorescence nanoscopy: Breaking the diffraction barrier by the RESOLFT concept,” *Nanobiotechnology*, vol. 1, no. 3, pp. 296–297, 2005.
- [67] M. Hofmann, C. Eggeling, S. Jakobs, and S. W. Hell, “Breaking the diffraction barrier in fluorescence microscopy at low light intensities by using reversibly photoswitchable proteins,” *Proceedings of the National Academy of Sciences of the United States of America*, vol. 102, no. 49, pp. 17 565–17 569, 2005.
- [68] A. M. Sydor, K. J. Czymmek, E. M. Puchner, and V. Mennella, “Super-Resolution Microscopy: From Single Molecules to Supramolecular Assemblies,” *Trends in Cell Biology*, vol. 25, no. 12, pp. 730–748, 2015.
- [69] D. Baddeley and J. Bewersdorf, “Biological Insight from Super-Resolution Microscopy: What We Can Learn from Localization-Based Images,” *Annual Review of Biochemistry*, vol. 87, no. 1, 2017.
- [70] L. Stryer, “Fluorescence Energy Transfer as a Spectroscopic Ruler,” *Annual Review of Biochemistry*, vol. 47, no. 1, pp. 819–846, 1978.

-
- [71] M. Levitus and S. Ranjit, “Cyanine dyes in biophysical research: the photophysics of polymethine fluorescent dyes in biomolecular environments,” *Quarterly Reviews of Biophysics*, vol. 44, no. 1, pp. 123–151, 2010.
- [72] S. Lee, J. Lee, and S. Hohng, “Single-molecule three-color FRET with both negligible spectral overlap and long observation time,” *PloS One*, vol. 5, no. 8, p. e12270, 2010.
- [73] S. Padilla-Parra and M. Tramier, “FRET microscopy in the living cell: different approaches, strengths and weaknesses,” *Bioessays*, vol. 34, no. 5, pp. 369–376, 2012.
- [74] K. Koynov and H. J. Butt, “Fluorescence correlation spectroscopy in colloid and interface science,” *Current Opinion in Colloid & Interface Science*, vol. 17, no. 6, pp. 377–387, 2012.
- [75] D. Magde, E. Elson, and W. W. Webb, “Thermodynamic Fluctuations in a Reacting System—Measurement by Fluorescence Correlation Spectroscopy,” *Physical Review Letters*, vol. 29, no. 11, pp. 705–708, 1972.
- [76] E. L. Elson and D. Magde, “Fluorescence correlation spectroscopy. I. Conceptual basis and theory,” *Biopolymers*, vol. 13, no. 1, pp. 1–27, 1974.
- [77] D. Magde, E. L. Elson, and W. W. Webb, “Fluorescence correlation spectroscopy. II. An experimental realization,” *Biopolymers*, vol. 13, no. 1, pp. 29–61, 1974.
- [78] R. Rigler, U. Mets, J. Widengren, and P. Kask, “Fluorescence correlation spectroscopy with high count rate and low background: analysis of translational diffusion,” *European Biophysics Journal*, vol. 22, no. 3, pp. 169–175, 1993.
- [79] S. Saffarian and E. L. Elson, “Statistical Analysis of Fluorescence Correlation Spectroscopy: The Standard Deviation and Bias,” *Biophysical Journal*, vol. 84, no. 3, pp. 2030–2042, 2003.
- [80] S. A. Kim and P. Schwille, “Intracellular applications of fluorescence correlation spectroscopy: prospects for neuroscience,” *Current Opinion in Neurobiology*, vol. 13, no. 5, pp. 583–590, 2003.
- [81] K. Starchev, J. Zhang, and J. Buffle, “Applications of Fluorescence Correlation Spectroscopy— Particle Size Effect,” *Journal of Colloid and Interface Science*, vol. 203, no. 1, pp. 189–196, 1998.
- [82] U. Meseth, T. Wohland, R. Rigler, and H. Vogel, “Resolution of fluorescence correlation measurements,” *Biophysical Journal*, vol. 76, no. 3, pp. 1619–1631, 1999.
- [83] R. Macháň and M. Hof, “Lipid diffusion in planar membranes investigated by fluorescence correlation spectroscopy,” *Biochimica et Biophysica Acta (BBA) - Biomembranes*, vol. 1798, no. 7, pp. 1377–1391, 2010.

- [84] J. Korlach, P. Schwille, W. W. Webb, and G. W. Feigensohn, "Characterization of lipid bilayer phases by confocal microscopy and fluorescence correlation spectroscopy," *Proceedings of the National Academy of Sciences*, vol. 96, no. 15, pp. 8461–8466, 1999.
- [85] R. Macháň and M. Hof, "Recent Developments in Fluorescence Correlation Spectroscopy for Diffusion Measurements in Planar Lipid Membranes," *International Journal of Molecular Sciences*, vol. 11, no. 2, pp. 427–457, 2010.
- [86] P. Schwille, U. Haupts, S. Maiti, and W. W. Webb, "Molecular Dynamics in Living Cells Observed by Fluorescence Correlation Spectroscopy with One- and Two-Photon Excitation," *Biophysical Journal*, vol. 77, no. 4, pp. 2251–2265, 1999.
- [87] M. Wachsmuth, W. Waldeck, and J. Langowski, "Anomalous diffusion of fluorescent probes inside living cell nuclei investigated by spatially-resolved fluorescence correlation spectroscopy," *Journal of Molecular Biology*, vol. 298, no. 4, pp. 677–689, 2000.
- [88] T. J. Feder, I. Brust-Mascher, J. P. Slattery, B. Baird, and W. W. Webb, "Constrained diffusion or immobile fraction on cell surfaces: a new interpretation," *Biophysical Journal*, vol. 70, no. 6, pp. 2767–2773, 1996.
- [89] M. Gösch, H. Blom, J. Holm, T. Heino, and R. Rigler, "Hydrodynamic Flow Profiling in Microchannel Structures by Single Molecule Fluorescence Correlation Spectroscopy," *Analytical Chemistry*, vol. 72, no. 14, pp. 3260–3265, 2000.
- [90] R. Kohler, P. Schwille, W. Webb, and M. Hanson, "Active protein transport through plastid tubules: velocity quantified by fluorescence correlation spectroscopy," *Journal of Cell Science*, vol. 113, no. 22, pp. 3921–3930, 2000.
- [91] D. Magde, W. W. Webb, and E. L. Elson, "Fluorescence correlation spectroscopy. III. Uniform translation and laminar flow," *Biopolymers*, vol. 17, no. 2, pp. 361–376, 1978.
- [92] J. Widengren, U. Mets, and R. Rigler, "Fluorescence correlation spectroscopy of triplet states in solution: a theoretical and experimental study," *The Journal of Physical Chemistry*, vol. 99, no. 36, pp. 13 368–13 379, 1995.
- [93] P. Schwille, S. Kummer, A. A. Heikal, W. E. Moerner, and W. W. Webb, "Fluorescence correlation spectroscopy reveals fast optical excitation-driven intramolecular dynamics of yellow fluorescent proteins," *Proceedings of the National Academy of Sciences of the United States of America*, vol. 97, no. 1, pp. 151–156, 2000.
- [94] A. Loman, I. Gregor, C. Stutz, M. Mund, and J. Enderlein, "Measuring rotational diffusion of macromolecules by fluorescence correlation spectroscopy," *Photochemical & Photobiological Sciences*, vol. 9, no. 5, pp. 627–636, 2010.
- [95] M. Ehrenberg and R. Rigler, "Rotational brownian motion and fluorescence intensity fluctuations," *Chemical Physics*, vol. 4, no. 3, pp. 390–401, 1974.

-
- [96] P. Kask, P. Piksarv, M. Pooga, U. Mets, and E. Lippmaa, "Separation of the rotational contribution in fluorescence correlation experiments," *Biophysical Journal*, vol. 55, no. 2, pp. 213–220, 1989.
- [97] T. Basché, W. E. Moerner, M. Orrit, and H. Talon, "Photon antibunching in the fluorescence of a single dye molecule trapped in a solid," *Physical Review Letters*, vol. 69, no. 10, pp. 1516–1519, 1992.
- [98] M. Böhmer, M. Wahl, H.-J. Rahn, R. Erdmann, and J. Enderlein, "Time-resolved fluorescence correlation spectroscopy," *Chemical Physics Letters*, vol. 353, no. 5, pp. 439–445, 2002.
- [99] M. Brinkmeier, K. Dorre, J. Stephan, and M. Eigen, "Two-beam cross-correlation: a method to characterize transport phenomena in micrometer-sized structures," *Analytical Chemistry*, vol. 71, no. 3, pp. 609–616, 1999.
- [100] D. Schaeffel, R. H. Staff, H.-J. Butt, K. Landfester, D. Crespy, and K. Koynov, "Fluorescence Correlation Spectroscopy Directly Monitors Coalescence During Nanoparticle Preparation," *Nano Letters*, vol. 12, no. 11, pp. 6012–6017, 2012.
- [101] P. Schwille, F. J. Meyer-Almes, and R. Rigler, "Dual-color fluorescence cross-correlation spectroscopy for multicomponent diffusional analysis in solution," *Biophysical Journal*, vol. 72, no. 4, pp. 1878–1886, 1997.
- [102] P. Schwille, "Cross-correlation analysis in FCS," in *Fluorescence Correlation Spectroscopy: Theory and Applications*. Berlin, Heidelberg: Springer, 2001, pp. 360–378.
- [103] K. Bacia, S. A. Kim, and P. Schwille, "Fluorescence cross-correlation spectroscopy in living cells," *Nature Methods*, vol. 3, no. 2, pp. 83–89, 2006.
- [104] K. Bacia and P. Schwille, "Practical guidelines for dual-color fluorescence cross-correlation spectroscopy," *Nature Protocols*, vol. 2, no. 11, pp. 2842–2856, 2007.
- [105] B. K. Muller, E. Zaychikov, C. Brauchle, and D. C. Lamb, "Pulsed interleaved excitation," *Biophysical Journal*, vol. 89, no. 5, pp. 3508–3522, 2005.
- [106] S. Wennmalm, P. Thyberg, L. Xu, and J. Widengren, "Inverse-Fluorescence Correlation Spectroscopy," *Analytical Chemistry*, vol. 81, no. 22, pp. 9209–9215, 2009.
- [107] S. Wennmalm, "Potentials and pitfalls of inverse fluorescence correlation spectroscopy," *Methods*, 2018.
- [108] S. Wennmalm and J. Widengren, "Inverse-Fluorescence Cross-Correlation Spectroscopy," *Analytical Chemistry*, vol. 82, no. 13, pp. 5646–5651, 2010.

- [109] E. L. Elson, J. Schlessinger, D. E. Koppel, D. Axelrod, and W. W. Webb, "Measurement of lateral transport on cell surfaces," *Progress in Clinical and Biological Research*, vol. 9, pp. 137–47, 1976.
- [110] J. Schlessinger, D. E. Koppel, D. Axelrod, K. Jacobson, W. W. Webb, and E. L. Elson, "Lateral transport on cell membranes: mobility of concanavalin A receptors on myoblasts," *Proceedings of the National Academy of Sciences*, vol. 73, no. 7, pp. 2409–2413, 1976.
- [111] T. Weidemann and P. Schwille, "Fluorescence Correlation Spectroscopy in Living Cells," in *Handbook of Single-Molecule Biophysics*, P. Hinterdorfer and A. van Oijen, Eds. Springer Science & Business Media, 2009, pp. 217–241.
- [112] I. E. Scheffler, "Metabolic Pathways Inside Mitochondria," in *Mitochondria*. John Wiley & Sons, Inc., 2008.
- [113] D. C. Wallace, W. Fan, and V. Procaccio, "Mitochondrial energetics and therapeutics," *Annual Review of Pathology*, vol. 5, no. 1, pp. 297–348, 2010.
- [114] C. Cottet-Rousselle, X. Ronot, X. Lerverve, and J.-F. Mayol, "Cytometric assessment of mitochondria using fluorescent probes," *Cytometry Part A*, vol. 79A, no. 6, pp. 405–425, 2011.
- [115] J. M. Berg, J. L. Tymoczko, G. J. Gatto, and L. Stryer, *Stryer Biochemie*. Berlin, Heidelberg: Springer, 2018.
- [116] H. M. Wilkins, S. M. Carl, and R. H. Swerdlow, "Cytoplasmic hybrid (cybrid) cell lines as a practical model for mitochondriopathies," *Redox Biology*, vol. 2, pp. 619–631, 2014.
- [117] J. M. Berg, J. L. Tymoczko, G. J. Gatto jr., and L. Stryer, "Der Citratzyklus," in *Stryer Biochemie*. Berlin, Heidelberg: Springer, 2018, pp. 581–611.
- [118] J. M. Berg, J. L. Tymoczko, G. J. Gatto, and L. Stryer, "Proteinumsatz und Aminosäurekatabolismus," in *Stryer Biochemie*. Berlin, Heidelberg: Springer, 2018, pp. 801–837.
- [119] D. G. Nicholls and S. J. Ferguson, "9 - Cellular Bioenergetics," in *Bioenergetics*. Boston: Academic Press, 2013, pp. 255–302.
- [120] J. M. Berg, J. L. Tymoczko, G. J. Gatto, and L. Stryer, "Die oxidative Phosphorylierung," in *Stryer Biochemie*. Berlin, Heidelberg: Springer, 2018, pp. 613–660.
- [121] S. W. Perry, J. P. Norman, J. Barbieri, E. B. Brown, and H. A. Gelbard, "Mitochondrial membrane potential probes and the proton gradient: a practical usage guide," *Biotechniques*, vol. 50, no. 2, pp. 98–115, 2011.

- [122] A. Logan, V. R. Pell, K. J. Shaffer, C. Evans, N. J. Stanley, E. L. Robb, T. A. Prime, E. T. Chouchani, H. M. Cocheme, I. M. Fearnley, S. Vidoni, A. M. James, C. M. Porteous, L. Partridge, T. Krieg, R. A. Smith, and M. P. Murphy, "Assessing the Mitochondrial Membrane Potential in Cells and In Vivo using Targeted Click Chemistry and Mass Spectrometry," *Cell Metabolism*, vol. 23, no. 2, pp. 379–385, 2016.
- [123] J. Zielonka, J. Joseph, A. Sikora, M. Hardy, O. Ouari, J. Vasquez-Vivar, G. Cheng, M. Lopez, and B. Kalyanaraman, "Mitochondria-Targeted Triphenylphosphonium-Based Compounds: Syntheses, Mechanisms of Action, and Therapeutic and Diagnostic Applications," *Chemical Reviews*, vol. 117, no. 15, pp. 10 043–10 120, 2017.
- [124] F. Wang, M. A. Ogasawara, and P. Huang, "Small mitochondria-targeting molecules as anti-cancer agents," *Molecular Aspects of Medicine*, vol. 31, no. 1, pp. 75–92, 2010.
- [125] L. B. Chen, "Mitochondrial membrane potential in living cells," *Annual Review of Cell Biology*, vol. 4, pp. 155–181, 1988.
- [126] G. Solaini, G. Sgarbi, and A. Baracca, "Oxidative phosphorylation in cancer cells," *Biochimica et Biophysica Acta (BBA) - Bioenergetics*, vol. 1807, no. 6, pp. 534–542, 2011.
- [127] S. S. Korshunov, V. P. Skulachev, and A. A. Starkov, "High protonic potential actuates a mechanism of production of reactive oxygen species in mitochondria," *FEBS Letters*, vol. 416, no. 1, pp. 15–18, 1997.
- [128] V. Weissig and V. P. Torchilin, "Cationic bolosomes with delocalized charge centers as mitochondria-specific DNA delivery systems," *Advanced Drug Delivery Reviews*, vol. 49, no. 1, pp. 127–149, 2001.
- [129] B. H. Honig, W. L. Hubbell, and R. F. Flewelling, "Electrostatic interactions in membranes and proteins," *Annual Review of Biophysics and Biophysical Chemistry*, vol. 15, pp. 163–193, 1986.
- [130] B. Ketterer, B. Neumcke, and P. Läuger, "Transport mechanism of hydrophobic ions through lipid bilayer membranes," *The Journal of Membrane Biology*, vol. 5, no. 3, pp. 225–245, 1971.
- [131] R. F. Flewelling and W. L. Hubbell, "The membrane dipole potential in a total membrane potential model. Applications to hydrophobic ion interactions with membranes," *Biophysical Journal*, vol. 49, no. 2, pp. 541–552, 1986.
- [132] M. F. Ross, G. F. Kelso, F. H. Blaikie, A. M. James, H. M. Cocheme, A. Filipovska, T. Da Ros, T. R. Hurd, R. A. Smith, and M. P. Murphy, "Lipophilic triphenylphosphonium cations as tools in mitochondrial bioenergetics and free radical biology," *Biochemistry (Mosc.)*, vol. 70, no. 2, pp. 222–230, 2005.

- [133] M. B. Jackson, "Molecular forces in biological structures," in *Molecular and Cellular Biophysics*. New York: Cambridge University Press, 2006, pp. 25–55.
- [134] R. F. Flewelling and W. L. Hubbell, "Hydrophobic ion interactions with membranes. Thermodynamic analysis of tetraphenylphosphonium binding to vesicles," *Biophysical Journal*, vol. 49, no. 2, pp. 531–540, 1986.
- [135] E. A. Liberman, V. P. Topaly, L. M. Tsofina, A. A. Jasaitis, and V. P. Skulachev, "Mechanism of Coupling of Oxidative Phosphorylation and the Membrane Potential of Mitochondria," *Nature*, vol. 222, p. 1076, 1969.
- [136] L. E. Bakeeva, L. L. Grinius, A. A. Jasaitis, V. V. Kuliene, D. O. Levitsky, E. A. Liberman, I. I. Severina, and V. P. Skulachev, "Conversion of biomembrane-produced energy into electric form. II. Intact mitochondria," *Biochimica et Biophysica Acta*, vol. 216, no. 1, pp. 13–21, 1970.
- [137] M. F. Ross, T. A. Prime, I. Abakumova, A. M. James, C. M. Porteous, R. A. Smith, and M. P. Murphy, "Rapid and extensive uptake and activation of hydrophobic triphenylphosphonium cations within cells," *Biochemical Journal*, vol. 411, no. 3, pp. 633–645, 2008.
- [138] J. Asin-Cayuela, A. R. Manas, A. M. James, R. A. Smith, and M. P. Murphy, "Fine-tuning the hydrophobicity of a mitochondria-targeted antioxidant," *FEBS Letters*, vol. 571, no. 1-3, pp. 9–16, 2004.
- [139] A. A. Gerencser and M. D. Brand, "Exploiting Mitochondria In Vivo as Chemical Reaction Chambers Dependent on Membrane Potential," *Molecular Cell*, vol. 61, no. 5, pp. 642–643, 2016.
- [140] M. F. Ross, T. Da Ros, F. H. Blaikie, T. A. Prime, C. M. Porteous, I. I. Severina, V. P. Skulachev, H. G. Kjaergaard, R. A. Smith, and M. P. Murphy, "Accumulation of lipophilic dicationic probes by mitochondria and cells," *Biochemical Journal*, vol. 400, no. 1, pp. 199–208, 2006.
- [141] P. Mitchell, "Coupling of phosphorylation to electron and hydrogen transfer by a chemiosmotic type of mechanism," *Nature*, vol. 191, pp. 144–8, 1961.
- [142] L. V. Johnson, M. L. Walsh, and L. B. Chen, "Localization of mitochondria in living cells with rhodamine 123," *Proceedings of the National Academy of Sciences of the United States of America*, vol. 77, no. 2, pp. 990–994, 1980.
- [143] Z. Liu, W. R. Bushnell, and R. Brambl, "Potentiometric Cyanine Dyes Are Sensitive Probes for Mitochondria in Intact Plant Cells : Kinetin Enhances Mitochondrial Fluorescence," *Plant Physiology*, vol. 84, no. 4, pp. 1385–1390, 1987.

- [144] A. Lazarow and S. J. Cooperstein, "Studies on the mechanism of Janus Green B staining of mitochondria," *Experimental Cell Research*, vol. 5, no. 1, pp. 56–69, 1953.
- [145] V. C. Keil, F. Funke, A. Zeug, D. Schild, and M. Müller, "Ratiometric high-resolution imaging of JC-1 fluorescence reveals the subcellular heterogeneity of astrocytic mitochondria," *Pflügers Archiv - European Journal of Physiology*, vol. 462, no. 5, pp. 693–708, 2011.
- [146] A. Perelman, C. Wachtel, M. Cohen, S. Haupt, H. Shapiro, and A. Tzur, "JC-1: alternative excitation wavelengths facilitate mitochondrial membrane potential cytometry," *Cell Death & Disease*, vol. 3, p. e430, 2012.
- [147] L. V. Johnson, M. L. Walsh, B. J. Bockus, and L. B. Chen, "Monitoring of relative mitochondrial membrane potential in living cells by fluorescence microscopy," *Journal of Cell Biology*, vol. 88, no. 3, pp. 526–535, 1981.
- [148] W. Pendergrass, N. Wolf, and M. Poot, "Efficacy of MitoTracker Green and CMXRosamine to measure changes in mitochondrial membrane potentials in living cells and tissues," *Cytometry A*, vol. 61, no. 2, pp. 162–169, 2004.
- [149] A. Maftah, J. M. Petit, M. H. Ratinaud, and R. Julien, "10-N nonyl-acridine orange: a fluorescent probe which stains mitochondria independently of their energetic state," *Biochemical and Biophysical Research Communications*, vol. 164, no. 1, pp. 185–190, 1989.
- [150] R. Bleday, M. J. Weiss, R. R. Salem, R. E. Wilson, L. B. Chen, and J. Steele, G., "Inhibition of rat colon tumor isograft growth with dequalinium chloride," *Archives of Surgery*, vol. 121, no. 11, pp. 1272–1275, 1986.
- [151] M. J. Weiss, J. R. Wong, C. S. Ha, R. Bleday, R. R. Salem, G. D. Steele, and L. B. Chen, "Dequalinium, a Topical Antimicrobial Agent, Displays Anticarcinoma Activity Based on Selective Mitochondrial Accumulation," *Proceedings of the National Academy of Sciences of the United States of America*, vol. 84, no. 15, pp. 5444–5448, 1987.
- [152] C. Helige, J. Smolle, G. Zellnig, R. Fink-Puches, H. Kerl, and H. A. Tritthart, "Effect of dequalinium on K1735-M2 melanoma cell growth, directional migration and invasion in vitro," *European Journal of Cancer*, vol. 29a, no. 1, pp. 124–128, 1992.
- [153] K. Makowska, M. C. Estañ, I. Gañán-Gómez, M. C. Boyano-Adánez, A. I. García-Pérez, and P. Sancho, "Changes in mitochondrial function induced by dequalinium precede oxidative stress and apoptosis in the human prostate-cancer cell line PC-3," *Molecular Biology*, vol. 48, no. 3, pp. 359–370, 2014.

- [154] W. L. Bodden, S. T. Palayoor, and W. N. Hai, "Selective antimitochondrial agents inhibit calmodulin," *Biochemical and Biophysical Research Communications*, vol. 135, no. 2, pp. 574–582, 1986.
- [155] R. W. Horobin, "Predicting mitochondrial targeting by small molecule xenobiotics within living cells using QSAR models," *Methods in Molecular Biology*, vol. 1265, pp. 13–23, 2015.
- [156] K. L. Horton, K. M. Stewart, S. B. Fonseca, Q. Guo, and S. O. Kelley, "Mitochondria-Penetrating Peptides," *Chemistry and Biology*, vol. 15, no. 4, pp. 375–382, 2008.
- [157] L. F. Yousif, K. M. Stewart, K. L. Horton, and S. O. Kelley, "Mitochondria-Penetrating Peptides: Sequence Effects and Model Cargo Transport," *Chembiochem: A European Journal of Chemical Biology*, vol. 10, no. 12, pp. 2081–2088, 2009.
- [158] K. Zhao, G. M. Zhao, D. Wu, Y. Soong, A. V. Birk, P. W. Schiller, and H. H. Szeto, "Cell-permeable peptide antioxidants targeted to inner mitochondrial membrane inhibit mitochondrial swelling, oxidative cell death, and reperfusion injury," *Journal of Biological Chemistry*, vol. 279, no. 33, pp. 34 682–90, 2004.
- [159] H. H. Szeto, "Mitochondria-targeted peptide antioxidants: novel neuroprotective agents," *AAPS Journal*, vol. 8, no. 3, pp. E521–31, 2006.
- [160] H. H. Szeto and P. W. Schiller, "Novel therapies targeting inner mitochondrial membrane—from discovery to clinical development," *Pharmaceutical Research*, vol. 28, no. 11, pp. 2669–79, 2011.
- [161] M. P. Fink, C. A. Macias, J. Xiao, Y. Y. Tyurina, R. L. Delude, J. S. Greenberger, V. E. Kagan, and P. Wipf, "Hemigramicidin-TEMPO conjugates: novel mitochondria-targeted antioxidants," *Critical Care Medicine*, vol. 35, no. 9 Suppl, pp. S461–467, 2007.
- [162] M. P. Fink, C. A. Macias, J. Xiao, Y. Y. Tyurina, J. Jiang, N. Belikova, R. L. Delude, J. S. Greenberger, V. E. Kagan, and P. Wipf, "Hemigramicidin-TEMPO conjugates: novel mitochondria-targeted anti-oxidants," *Biochemical Pharmacology*, vol. 74, no. 6, pp. 801–809, 2007.
- [163] J. Fernández-Carneado, M. Van Gool, V. Martos, S. Castel, P. Prados, J. de Mendoza, and E. Giralt, "Highly Efficient, Nonpeptidic Oligoguanidinium Vectors that Selectively Internalize into Mitochondria," *Journal of the American Chemical Society*, vol. 127, no. 3, pp. 869–874, 2005.
- [164] K. K. Maiti, W. S. Lee, T. Takeuchi, C. Watkins, M. Fretz, D. C. Kim, S. Futaki, A. Jones, K. T. Kim, and S. K. Chung, "Guanidine-containing molecular transporters: sorbitol-based transporters show high intracellular selectivity toward mitochondria," *Angewandte Chemie International Edition*, vol. 46, no. 31, pp. 5880–5884, 2007.

- [165] W. S. Lee, C. N. Im, Q. Y. Teng, Y. T. Chang, D. C. Kim, K. T. Kim, and S. K. Chung, "Synthesis and cellular uptake properties of guanidine-containing molecular transporters built on the sucrose scaffold," *Molecular Biosystems*, vol. 5, no. 8, pp. 822–825, 2009.
- [166] T. Lithgow, B. S. Glick, and G. Schatz, "The protein import receptor of mitochondria," *Trends in Biochemical Sciences*, vol. 20, no. 3, pp. 98–101, 1995.
- [167] E. Schleiff and T. Becker, "Common ground for protein translocation: access control for mitochondria and chloroplasts," *Nature Reviews: Molecular Cell Biology*, vol. 12, no. 1, pp. 48–59, 2011.
- [168] A. B. Harbauer, R. P. Zahedi, A. Sickmann, N. Pfanner, and C. Meisinger, "The protein import machinery of mitochondria—a regulatory hub in metabolism, stress, and disease," *Cell Metabolism*, vol. 19, no. 3, pp. 357–372, 2014.
- [169] S. E. Weinberg and N. S. Chandel, "Targeting mitochondria metabolism for cancer therapy," *Nature Chemical Biology*, vol. 11, no. 1, pp. 9–15, 2015.
- [170] R. A. Smith, R. C. Hartley, and M. P. Murphy, "Mitochondria-targeted small molecule therapeutics and probes," *Antioxid Redox Signal*, vol. 15, no. 12, pp. 3021–3038, 2011.
- [171] S. R. Jean, M. Ahmed, E. K. Lei, S. P. Wisnovsky, and S. O. Kelley, "Peptide-Mediated Delivery of Chemical Probes and Therapeutics to Mitochondria," *Accounts of Chemical Research*, vol. 49, no. 9, pp. 1893–1902, 2016.
- [172] S. Rin Jean, D. V. Tulumello, S. P. Wisnovsky, E. K. Lei, M. P. Pereira, and S. O. Kelley, "Molecular Vehicles for Mitochondrial Chemical Biology and Drug Delivery," *ACS Chemical Biology*, vol. 9, no. 2, pp. 323–333, 2014.
- [173] Y. Yamada, H. Akita, H. Kamiya, K. Kogure, T. Yamamoto, Y. Shinohara, K. Yamashita, H. Kobayashi, H. Kikuchi, and H. Harashima, "MITO-Porter: A liposome-based carrier system for delivery of macromolecules into mitochondria via membrane fusion," *Biochimica et Biophysica Acta*, vol. 1778, no. 2, pp. 423–32, 2008.
- [174] V. Weissig, J. Lasch, G. Erdos, H. W. Meyer, T. C. Rowe, and J. Hughes, "DQAsomes: a novel potential drug and gene delivery system made from Dequalinium," *Pharmaceutical Research*, vol. 15, no. 2, pp. 334–7, 1998.
- [175] H. S. Jung, J. Han, J.-H. Lee, J. H. Lee, J.-M. Choi, H.-S. Kweon, J. H. Han, J.-H. Kim, K. M. Byun, J. H. Jung, C. Kang, and J. S. Kim, "Enhanced NIR Radiation-Triggered Hyperthermia by Mitochondrial Targeting," *Journal of the American Chemical Society*, vol. 137, no. 8, pp. 3017–3023, 2015.
- [176] L. Zhao, H. Yang, T. Amano, H. Qin, L. Zheng, A. Takahashi, S. Zhao, I. Tooyama, T. Murakami, and N. Komatsu, "Efficient delivery of chlorin e6 into ovarian cancer cells

- with octalysine conjugated superparamagnetic iron oxide nanoparticles for effective photodynamic therapy,” *Journal of Materials Chemistry B*, vol. 4, no. 47, pp. 7741–7748, 2016.
- [177] P. K. B. Nagesh, N. R. Johnson, V. K. N. Boya, P. Chowdhury, S. F. Othman, V. Khalilzad-Sharghi, B. B. Hafeez, A. Ganju, S. Khan, S. W. Behrman, N. Zafar, S. C. Chauhan, M. Jaggi, and M. M. Yallapu, “PSMA targeted docetaxel-loaded superparamagnetic iron oxide nanoparticles for prostate cancer,” *Colloids and Surfaces B - Biointerfaces*, vol. 144, pp. 8–20, 2016.
- [178] S. Biswas, N. S. Dodwadkar, A. Piroyan, and V. P. Torchilin, “Surface conjugation of triphenylphosphonium to target poly(amidoamine) dendrimers to mitochondria,” *Biomaterials*, vol. 33, no. 18, pp. 4773–82, 2012.
- [179] S. B. Fonseca, M. P. Pereira, R. Mourtada, M. Gronda, K. L. Horton, R. Hurren, M. D. Minden, A. D. Schimmer, and S. O. Kelley, “Rerouting chlorambucil to mitochondria combats drug deactivation and resistance in cancer cells,” *Chemistry and Biology*, vol. 18, no. 4, pp. 445–53, 2011.
- [180] G. R. Chamberlain, D. V. Tulumello, and S. O. Kelley, “Targeted delivery of doxorubicin to mitochondria,” *ACS Chemical Biology*, vol. 8, no. 7, pp. 1389–1395, 2013.
- [181] S. P. Wisnovsky, J. J. Wilson, R. J. Radford, M. P. Pereira, M. R. Chan, R. R. Laposa, S. J. Lippard, and S. O. Kelley, “Targeting mitochondrial DNA with a platinum-based anticancer agent,” *Chemistry and Biology*, vol. 20, no. 11, pp. 1323–1328, 2013.
- [182] S. Marrache, R. K. Pathak, and S. Dhar, “Detouring of cisplatin to access mitochondrial genome for overcoming resistance,” *Proceedings of the National Academy of Sciences*, vol. 111, no. 29, pp. 10 444–10 449, 2014.
- [183] H. Xu, S. Z. DeLuca, and P. H. O’Farrell, “Manipulating the metazoan mitochondrial genome with targeted restriction enzymes,” *Science*, vol. 321, no. 5888, pp. 575–577, 2008.
- [184] S. R. Bacman, S. L. Williams, M. Pinto, S. Peralta, and C. T. Moraes, “Specific elimination of mutant mitochondrial genomes in patient-derived cells by mitoTALENs,” *Nature Medicine*, vol. 19, no. 9, pp. 1111–1113, 2013.
- [185] P. A. Gammage, J. Rorbach, A. I. Vincent, E. J. Rebar, and M. Minczuk, “Mitochondrially targeted ZFNs for selective degradation of pathogenic mitochondrial genomes bearing large-scale deletions or point mutations,” *EMBO Molecular Medicine*, vol. 6, no. 4, pp. 458–466, 2014.
- [186] B. H. Kang, J. Plescia, H. Y. Song, M. Meli, G. Colombo, K. Beebe, B. Scroggins, L. Neckers, and D. C. Altieri, “Combinatorial drug design targeting multiple cancer signaling

- networks controlled by mitochondrial Hsp90,” *The Journal of Clinical Investigation*, vol. 119, no. 3, pp. 454–464, 2009.
- [187] M. Škrtić, S. Sriskanthadevan, B. Jhas, M. Gebbia, X. Wang, Z. Wang, R. Hurren, Y. Jitkova, M. Gronda, N. Maclean, C. Lai, Y. Eberhard, J. Bartoszko, P. Spagnuolo, A. Rutledge, A. Datti, T. Ketela, J. Moffat, B. Robinson, J. Cameron, J. Wrana, C. Eaves, M. Minden, J. Y. Wang, J. Dick, K. Humphries, C. Nislow, G. Giaever, and A. Schimmer, “Inhibition of Mitochondrial Translation as a Therapeutic Strategy for Human Acute Myeloid Leukemia,” *Cancer Cell*, vol. 20, no. 5, pp. 674–688, 2011.
- [188] F. N. Bralha, S. U. Liyanage, R. Hurren, X. Wang, M. H. Son, T. A. Fung, F. B. Chingcuanco, A. Y. W. Tung, A. C. Andrezza, P. Psarianos, A. D. Schimmer, L. Salmena, and R. R. Laposa, “Targeting mitochondrial RNA polymerase in acute myeloid leukemia,” *Oncotarget*, vol. 6, no. 35, pp. 37 216–37 228, 2015.
- [189] I. G. Kirkinezos and C. T. Moraes, “Reactive oxygen species and mitochondrial diseases,” *Seminars in Cell and Developmental Biology*, vol. 12, no. 6, pp. 449–457, 2001.
- [190] X. Jia, Q. Chen, Y. Yang, Y. Tang, R. Wang, Y. Xu, W. Zhu, and X. Qian, “FRET-Based Mito-Specific Fluorescent Probe for Ratiometric Detection and Imaging of Endogenous Peroxynitrite: Dyad of Cy3 and Cy5,” *Journal of the American Chemical Society*, vol. 138, no. 34, pp. 10 778–10 781, 2016.
- [191] J. J. Hu, N.-K. Wong, S. Ye, X. Chen, M.-Y. Lu, A. Q. Zhao, Y. Guo, A. C.-H. Ma, A. Y.-H. Leung, J. Shen, and D. Yang, “Fluorescent Probe HKSOX-1 for Imaging and Detection of Endogenous Superoxide in Live Cells and In Vivo,” *Journal of the American Chemical Society*, vol. 137, no. 21, pp. 6837–6843, 2015.
- [192] G. F. Kelso, C. M. Porteous, C. V. Coulter, G. Hughes, W. K. Porteous, E. C. Ledgerwood, R. A. Smith, and M. P. Murphy, “Selective targeting of a redox-active ubiquinone to mitochondria within cells: antioxidant and antiapoptotic properties,” *Journal of Biological Chemistry*, vol. 276, no. 7, pp. 4588–96, 2001.
- [193] Z. Zou, H. Chang, H. Li, and S. Wang, “Induction of reactive oxygen species: an emerging approach for cancer therapy,” *Apoptosis*, vol. 22, no. 11, pp. 1321–1335, 2017.
- [194] N. J. Agard, J. A. Prescher, and C. R. Bertozzi, “A Strain-Promoted [3 + 2] Azide-Alkyne Cycloaddition for Covalent Modification of Biomolecules in Living Systems,” *Journal of the American Chemical Society*, vol. 126, no. 46, pp. 15 046–15 047, 2004.
- [195] I. Nikić, J. H. Kang, G. E. Girona, I. V. Aramburu, and E. A. Lemke, “Labeling proteins on live mammalian cells using click chemistry,” *Nature Protocols*, vol. 10, no. 5, pp. 780–791, 2015.

- [196] A. Niederwieser, A.-K. Späte, L. D. Nguyen, C. Jüngst, W. Reutter, and V. Wittmann, "Two-Color Glycan Labeling of Live Cells by a Combination of Diels–Alder and Click Chemistry," *Angewandte Chemie International Edition*, vol. 52, no. 15, pp. 4265–4268, 2013.
- [197] H. E. Murrey, J. C. Judkins, C. W. am Ende, T. E. Ballard, Y. Fang, K. Riccardi, L. Di, E. R. Guilmette, J. W. Schwartz, J. M. Fox, and D. S. Johnson, "Systematic Evaluation of Bioorthogonal Reactions in Live Cells with Clickable HaloTag Ligands: Implications for Intracellular Imaging," *Journal of the American Chemical Society*, vol. 137, no. 35, pp. 11 461–11 475, 2015.
- [198] K. Yamagishi, K. Sawaki, A. Murata, and S. Takeoka, "A Cu-free clickable fluorescent probe for intracellular targeting of small biomolecules," *Chemical Communications*, vol. 51, no. 37, pp. 7879–7882, 2015.
- [199] T. Carell and M. Vrabel, "Bioorthogonal Chemistry-Introduction and Overview," *Topics in Current Chemistry*, vol. 374, no. 1, p. 9, 2016.
- [200] J. Dommerholt, F. P. Rutjes, and F. L. van Delft, "Strain-Promoted 1,3-Dipolar Cycloaddition of Cycloalkynes and Organic Azides," *Topics in Current Chemistry*, vol. 374, no. 2, p. 16, 2016.
- [201] R. Huisgen, "1,3-Dipolar Cycloadditions. Past and Future," *Angewandte Chemie International Edition*, vol. 2, no. 10, pp. 565–598, 1963.
- [202] V. V. Rostovtsev, L. G. Green, V. V. Fokin, and K. B. Sharpless, "A Stepwise Huisgen Cycloaddition Process: Copper(I)-Catalyzed Regioselective "Ligation" of Azides and Terminal Alkynes," *Angewandte Chemie International Edition*, vol. 41, no. 14, pp. 2596–2599, 2002.
- [203] C. W. Tornøe, C. Christensen, and M. Meldal, "Peptidotriazoles on solid phase: [1,2,3]-triazoles by regiospecific copper(i)-catalyzed 1,3-dipolar cycloadditions of terminal alkynes to azides," *Journal of Organic Chemistry*, vol. 67, no. 9, pp. 3057–64, 2002.
- [204] K. Hoogewijs, A. M. James, R. A. Smith, M. J. Gait, M. P. Murphy, and R. N. Lightowlers, "Assessing the Delivery of Molecules to the Mitochondrial Matrix Using Click Chemistry," *Chembiochem: A European Journal of Chemical Biology*, vol. 17, no. 14, pp. 1312–1316, 2016.
- [205] K. Hoogewijs, A. M. James, R. A. J. Smith, F. Abendroth, M. J. Gait, M. P. Murphy, and R. N. Lightowlers, "ClickIn: a flexible protocol for quantifying mitochondrial uptake of nucleobase derivatives," *Interface Focus*, vol. 7, no. 2, p. 7, 2017.

- [206] M. Tomas-Gamasa, M. Martinez-Calvo, J. R. Couceiro, and J. L. Mascarenas, "Transition metal catalysis in the mitochondria of living cells," *Nature Communications*, vol. 7, p. 12538, 2016.
- [207] I. Negwer, M. Hirsch, S. Kaloyanova, T. Brown, K. Peneva, H. J. Butt, K. Koynov, and M. Helm, "Modulation of Mitochondriotropic Properties of Cyanine Dyes by in Organello Copper-Free Click Reaction," *Chembiochem: A European Journal of Chemical Biology*, vol. 18, no. 18, pp. 1814–1818, 2017.
- [208] S. Tomcin, G. Baier, K. Landfester, and V. Mailänder, "Pharmacokinetics on a microscale: visualizing Cy5-labeled oligonucleotide release from poly(n-butylcyanoacrylate) nanocapsules in cells," *International journal of nanomedicine*, vol. 9, pp. 5471–5489, 2014.
- [209] W. J. Rhee and G. Bao, "Slow non-specific accumulation of 2'-deoxy and 2'-O-methyl oligonucleotide probes at mitochondria in live cells," *Nucleic Acids Research*, vol. 38, no. 9, p. e109, 2010.
- [210] L. A. Ernst, R. K. Gupta, R. B. Mujumdar, and A. S. Waggoner, "Cyanine dye labeling reagents for sulfhydryl groups," *Cytometry*, vol. 10, no. 1, pp. 3–10, 1989.
- [211] M. Gerowska, L. Hall, J. Richardson, M. Shelbourne, and T. Brown, "Efficient reverse click labeling of azide oligonucleotides with multiple alkynyl Cy-Dyes applied to the synthesis of HyBeacon probes for genetic analysis," *Tetrahedron*, vol. 68, no. 3, pp. 857–864, 2012.
- [212] E. M. M. Manders, F. J. Verbeek, and J. A. Aten, "Measurement of co-localization of objects in dual-colour confocal images," *Journal of Microscopy*, vol. 169, no. 3, pp. 375–382, 1993.
- [213] M. Henary and M. Mojzych, "Stability and Reactivity of Polymethine Dyes in Solution," in *Heterocyclic Polymethine Dyes: Synthesis, Properties and Applications*. Springer, 2008, vol. 14, pp. 221–238.
- [214] B. Dinda, "Cycloaddition Reactions," *Essentials of Pericyclic and Photochemical Reactions*, vol. 93, pp. 37–106, 2017.
- [215] J. D. Wikstrom, G. Twig, and O. S. Shirihai, "What can mitochondrial heterogeneity tell us about mitochondrial dynamics and autophagy?" *International Journal of Biochemistry and Cell Biology*, vol. 41, no. 10, pp. 1914–1927, 2009.
- [216] S. Jakobs, S. Stoldt, and D. Neumann, "Light microscopic analysis of mitochondrial heterogeneity in cell populations and within single cells," *Advances in Biochemical Engineering/Biotechnology*, vol. 124, pp. 1–19, 2011.
- [217] L. D. Zorova, V. A. Popkov, E. Y. Plotnikov, D. N. Silachev, I. B. Pevzner, S. S. Jankauskas, V. A. Babenko, S. D. Zorov, A. V. Balakireva, M. Juhaszova, S. J. Sollott, and D. B. Zorov, "Mitochondrial membrane potential," *Analytical Biochemistry*, 2017.

- [218] T. J. Collins, M. J. Berridge, P. Lipp, and M. D. Bootman, “Mitochondria are morphologically and functionally heterogeneous within cells,” *The EMBO Journal*, vol. 21, no. 7, pp. 1616–1627, 2002.
- [219] R. Benz and S. McLaughlin, “The molecular mechanism of action of the proton ionophore FCCP (carbonylcyanide p-trifluoromethoxyphenylhydrazone),” *Biophysical Journal*, vol. 41, no. 3, pp. 381–398, 1983.
- [220] L. D. Hughes, R. J. Rawle, and S. G. Boxer, “Choose Your Label Wisely: Water-Soluble Fluorophores Often Interact with Lipid Bilayers,” *PloS One*, vol. 9, no. 2, p. e87649, 2014.
- [221] C. E. Dieteren, S. C. Gielen, L. G. Nijtmans, J. A. Smeitink, H. G. Swarts, R. Brock, P. H. Willems, and W. J. Koopman, “Solute diffusion is hindered in the mitochondrial matrix,” *Proceedings of the National Academy of Sciences of the United States of America*, vol. 108, no. 21, pp. 8657–8662, 2011.
- [222] S. Smith, C. Cianci, and R. Grima, “Macromolecular crowding directs the motion of small molecules inside cells,” *Journal of the Royal Society Interface*, vol. 14, no. 131, 2017.
- [223] Z. Konkoli, “Diffusion-controlled reactions in small and structured spaces as a tool for describing living cell biochemistry,” *Journal of Physics: Condensed Matter*, vol. 19, no. 6, p. 065149, 2007.
- [224] C. A. Schneider, W. S. Rasband, and K. W. Eliceiri, “NIH Image to ImageJ: 25 years of image analysis,” *Nature Methods*, vol. 9, no. 7, pp. 671–675, 2012.
- [225] P. Kankaanpää, L. Paavolainen, S. Tiitta, M. Karjalainen, J. Paivarinne, J. Nieminen, V. Marjomäki, J. Heino, and D. J. White, “BioImageXD: an open, general-purpose and high-throughput image-processing platform,” *Nature Methods*, vol. 9, no. 7, pp. 683–689, 2012.
- [226] F. Roux, O. Durieu-Trautmann, N. Chaverot, M. Claire, P. Mailly, J. M. Bourre, A. D. Strosberg, and P. O. Couraud, “Regulation of gamma-glutamyl transpeptidase and alkaline phosphatase activities in immortalized rat brain microvessel endothelial cells,” *Journal of Cellular Physiology*, vol. 159, no. 1, pp. 101–113, 1994.
- [227] “Blood,” in *Biology and Mechanics of Blood Flows: Part I: Biology*. New York, NY: Springer New York, 2008, pp. 265–294.
- [228] C. Weiss and W. Jelkmann, “Functions of the Blood,” in *Human Physiology*, R. F. Schmidt and G. Thews, Eds. Berlin, Heidelberg: Springer, 1989, pp. 402–438.
- [229] E. Mutschler, *Mutschler Arzneimittelwirkungen: Lehrbuch der Pharmakologie und Toxikologie ; mit einführenden Kapiteln in die Anatomie, Physiologie und Pathophysiologie ; 264 Tabellen*. Wiss. Verlag-Ges., 2008.

- [230] E. J. Cho, H. Holback, K. C. Liu, S. A. Abouelmagd, J. Park, and Y. Yeo, "Nanoparticle Characterization: State of the Art, Challenges, and Emerging Technologies," *Molecular Pharmaceutics*, vol. 10, no. 6, pp. 2093–2110, 2013.
- [231] T. Cedervall, I. Lynch, S. Lindman, T. Berggard, E. Thulin, H. Nilsson, K. A. Dawson, and S. Linse, "Understanding the nanoparticle-protein corona using methods to quantify exchange rates and affinities of proteins for nanoparticles," *Proceedings of the National Academy of Sciences of the United States of America*, vol. 104, no. 7, pp. 2050–2055, 2007.
- [232] D. Docter, D. Westmeier, M. Markiewicz, S. Stolte, S. K. Knauer, and R. H. Stauber, "The nanoparticle biomolecule corona: lessons learned - challenge accepted?" *Chemical Society Reviews*, vol. 44, no. 17, pp. 6094–6121, 2015.
- [233] A. Salvati, A. S. Pitek, M. P. Monopoli, K. Prapainop, F. B. Bombelli, D. R. Hristov, P. M. Kelly, C. Åberg, E. Mahon, and K. A. Dawson, "Transferrin-functionalized nanoparticles lose their targeting capabilities when a biomolecule corona adsorbs on the surface," *Nat Nanotechnol*, vol. 8, p. 137, 2013.
- [234] S. Schöttler, K. Landfester, and V. Mailänder, "Controlling the Stealth Effect of Nanocarriers through Understanding the Protein Corona," *Angewandte Chemie International Edition*, vol. 55, no. 31, pp. 8806–8815, 2016.
- [235] A. N. Ilinskaya and M. A. Dobrovolskaia, "Nanoparticles and the blood coagulation system. Part II: safety concerns," *Nanomedicine (London, England)*, vol. 8, no. 6, pp. 969–981, 2013.
- [236] A. Gabizon, H. Shmeeda, and Y. Barenholz, "Pharmacokinetics of pegylated liposomal Doxorubicin: review of animal and human studies," *Clinical Pharmacokinetics*, vol. 42, no. 5, pp. 419–436, 2003.
- [237] J. M. Harris and R. B. Chess, "Effect of pegylation on pharmaceuticals," *Nature Reviews Drug Discovery*, vol. 2, no. 3, pp. 214–221, 2003.
- [238] S. Schöttler, G. Becker, S. Winzen, T. Steinbach, K. Mohr, K. Landfester, V. Mailänder, and F. R. Wurm, "Protein adsorption is required for stealth effect of poly(ethylene glycol)- and poly(phosphoester)-coated nanocarriers," *Nat Nanotechnol*, vol. 11, no. 4, pp. 372–377, 2016.
- [239] D. F. Moyano, K. Saha, G. Prakash, B. Yan, H. Kong, M. Yazdani, and V. M. Rotello, "Fabrication of Corona-Free Nanoparticles with Tunable Hydrophobicity," *ACS Nano*, vol. 8, no. 7, pp. 6748–6755, 2014.
- [240] V. Mirshafiee, R. Kim, S. Park, M. Mahmoudi, and M. L. Kraft, "Impact of protein pre-coating on the protein corona composition and nanoparticle cellular uptake," *Biomaterials*, vol. 75, pp. 295–304, 2016.

- [241] L. K. Müller, J. Simon, S. Schöttler, K. Landfester, V. Mailänder, and K. Mohr, “Pre-coating with protein fractions inhibits nano-carrier aggregation in human blood plasma,” *RSC Advances*, vol. 6, no. 99, pp. 96 495–96 509, 2016.
- [242] S. Ritz, S. Schöttler, N. Kotman, G. Baier, A. Musyanovych, J. Kuharev, K. Landfester, H. Schild, O. Jahn, S. Tenzer, and V. Mailänder, “Protein Corona of Nanoparticles: Distinct Proteins Regulate the Cellular Uptake,” *Biomacromolecules*, vol. 16, no. 4, pp. 1311–1321, 2015.
- [243] P. L. Rodriguez, T. Harada, D. A. Christian, D. A. Pantano, R. K. Tsai, and D. E. Discher, “Minimal "Self" peptides that inhibit phagocytic clearance and enhance delivery of nanoparticles,” *Science*, vol. 339, no. 6122, pp. 971–975, 2013.
- [244] C.-M. J. Hu, L. Zhang, S. Aryal, C. Cheung, R. H. Fang, and L. Zhang, “Erythrocyte membrane-camouflaged polymeric nanoparticles as a biomimetic delivery platform,” *Proceedings of the National Academy of Sciences*, vol. 108, no. 27, pp. 10 980–10 985, 2011.
- [245] A. Parodi, N. Quattrocchi, A. L. van de Ven, C. Chiappini, M. Evangelopoulos, J. O. Martinez, B. S. Brown, S. Z. Khaled, I. K. Yazdi, M. V. Enzo, L. Isenhardt, M. Ferrari, and E. Tasciotti, “Synthetic nanoparticles functionalized with biomimetic leukocyte membranes possess cell-like functions,” *Nat Nanotechnol*, vol. 8, no. 1, pp. 61–8, 2013.
- [246] C. M. Hu, R. H. Fang, K. C. Wang, B. T. Luk, S. Thamphiwatana, D. Dehaini, P. Nguyen, P. Angsantikul, C. H. Wen, A. V. Kroll, C. Carpenter, M. Ramesh, V. Qu, S. H. Patel, J. Zhu, W. Shi, F. M. Hofman, T. C. Chen, W. Gao, K. Zhang, S. Chien, and L. Zhang, “Nanoparticle biointerfacing by platelet membrane cloaking,” *Nature*, vol. 526, no. 7571, pp. 118–121, 2015.
- [247] F. Pederzoli, G. Tosi, M. A. Vandelli, D. Belletti, F. Forni, and B. Ruozi, “Protein corona and nanoparticles: how can we investigate on?” *Wiley Interdisciplinary Reviews: Nanomedicine and Nanobiotechnology*, p. e1467, 2017.
- [248] V. Mirshafiee, R. Kim, M. Mahmoudi, and M. L. Kraft, “The importance of selecting a proper biological milieu for protein corona analysis in vitro: Human plasma versus human serum,” *International Journal of Biochemistry and Cell Biology*, vol. 75, pp. 188–95, 2016.
- [249] U. Sakulkhu, L. Maurizi, M. Mahmoudi, M. Motazacker, M. Vries, A. Gramoun, M.-G. Ollivier Beuzelin, J.-P. Vallee, F. Rezaee, and H. Hofmann, “Ex situ evaluation of the composition of protein corona of intravenously injected superparamagnetic nanoparticles in rats,” *Nanoscale*, vol. 6, no. 19, pp. 11 439–11 450, 2014.
- [250] R. Savic, T. Azzam, A. Eisenberg, and D. Maysinger, “Assessment of the Integrity of Poly(caprolactone)-b-poly(ethylene oxide) Micelles under Biological Conditions: A Fluorogenic-Based Approach,” *Langmuir*, vol. 22, no. 8, pp. 3570–3578, 2006.

- [251] P. Opanasopit, M. Yokoyama, M. Watanabe, K. Kawano, Y. Maitani, and T. Okano, "Influence of serum and albumins from different species on stability of camptothecin-loaded micelles," *Journal of Controlled Release*, vol. 104, no. 2, pp. 313–321, 2005.
- [252] H. Chen, S. Kim, W. He, H. Wang, P. S. Low, K. Park, and J.-X. Cheng, "Fast Release of Lipophilic Agents from Circulating PEG-PDLLA Micelles Revealed by in Vivo Förster Resonance Energy Transfer Imaging," *Langmuir*, vol. 24, no. 10, pp. 5213–5217, 2008.
- [253] Y. Shi, T. Lammers, G. Storm, and W. E. Hennink, "Physico-chemical strategies to enhance stability and drug retention of polymeric micelles for tumor-targeted drug delivery," *Macromolecular Bioscience*, vol. 17, no. 1, 2017.
- [254] K. Letchford and H. M. Burt, "Copolymer micelles and nanospheres with different in vitro stability demonstrate similar paclitaxel pharmacokinetics," *Molecular Pharmaceutics*, vol. 9, no. 2, pp. 248–60, 2012.
- [255] Y. Shi, R. van der Meel, B. Theek, E. Oude Blenke, E. H. E. Pieters, M. H. A. M. Fens, J. Ehling, R. M. Schiffelers, G. Storm, C. F. van Nostrum, T. Lammers, and W. E. Hennink, "Complete Regression of Xenograft Tumors upon Targeted Delivery of Paclitaxel via π - π Stacking Stabilized Polymeric Micelles," *ACS Nano*, vol. 9, no. 4, pp. 3740–3752, 2015.
- [256] Y. Mochida, H. Cabral, Y. Miura, F. Albertini, S. Fukushima, K. Osada, N. Nishiyama, and K. Kataoka, "Bundled assembly of helical nanostructures in polymeric micelles loaded with platinum drugs enhancing therapeutic efficiency against pancreatic tumor," *ACS Nano*, vol. 8, no. 7, pp. 6724–6738, 2014.
- [257] Z. Su, Y. Liang, Y. Yao, T. Wang, and N. Zhang, "Polymeric complex micelles based on the double-hydrazone linkage and dual drug-loading strategy for pH-sensitive docetaxel delivery," *Journal of Materials Chemistry B*, vol. 4, no. 6, pp. 1122–1133, 2016.
- [258] S. McRae Page, M. Martorella, S. Parelkar, I. Kosif, and T. Emrick, "Disulfide cross-linked phosphorylcholine micelles for triggered release of camptothecin," *Molecular Pharmaceutics*, vol. 10, no. 7, pp. 2684–2692, 2013.
- [259] P. Xu, E. Gullotti, L. Tong, C. B. Highley, D. R. Errabelli, T. Hasan, J. X. Cheng, D. S. Kohane, and Y. Yeo, "Intracellular drug delivery by poly(lactic-co-glycolic acid) nanoparticles, revisited," *Molecular Pharmaceutics*, vol. 6, no. 1, pp. 190–201, 2009.
- [260] Z. Amoozgar, J. Park, Q. Lin, and Y. Yeo, "Low molecular-weight chitosan as a pH-sensitive stealth coating for tumor-specific drug delivery," *Molecular Pharmaceutics*, vol. 9, no. 5, pp. 1262–1270, 2012.

- [261] K. Kono, T. Ozawa, T. Yoshida, F. Ozaki, Y. Ishizaka, K. Maruyama, C. Kojima, A. Harada, and S. Aoshima, “Highly temperature-sensitive liposomes based on a thermosensitive block copolymer for tumor-specific chemotherapy,” *Biomaterials*, vol. 31, no. 27, pp. 7096–7105, 2010.
- [262] Study of ThermoDox With Standardized Radiofrequency Ablation (RFA) for Treatment of Hepatocellular Carcinoma (HCC). Accessed: 2018/02/15. [Online]. Available: <https://clinicaltrials.gov/ct2/show/NCT02112656>
- [263] L. Shang, K. Nienhaus, and G. U. Nienhaus, “Engineered nanoparticles interacting with cells: size matters,” *Journal of Nanobiotechnology*, vol. 12, p. 5, 2014.
- [264] G. R. Dakwar, E. Zagato, J. Delanghe, S. Hobel, A. Aigner, H. Denys, K. Braeckmans, W. Ceelen, F. C. De Smedt, and K. Remaut, “Colloidal stability of nano-sized particles in the peritoneal fluid: Towards optimizing drug delivery systems for intraperitoneal therapy,” *Acta Biomaterialia*, vol. 10, no. 7, pp. 2965–2975, 2014.
- [265] L. Nuhn, L. Braun, I. Overhoff, A. Kelsch, D. Schaeffel, K. Koynov, and R. Zentel, “Degradable cationic nanohydrogel particles for stimuli-responsive release of siRNA,” *Macromol Rapid Commun*, vol. 35, no. 24, pp. 2057–2064, 2014.
- [266] M. A. Hood, U. Paiphansiri, D. Schaeffel, K. Koynov, M. Kappl, K. Landfester, and R. Muñoz-Espí, “Hybrid Poly(urethane–urea)/Silica Nanocapsules with pH-Sensitive Gateways,” *Chemistry of Materials*, vol. 27, no. 12, pp. 4311–4318, 2015.
- [267] P. Maffre, K. Nienhaus, F. Amin, W. J. Parak, and G. U. Nienhaus, “Characterization of protein adsorption onto FePt nanoparticles using dual-focus fluorescence correlation spectroscopy,” *Beilstein Journal of Nanotechnology*, vol. 2, pp. 374–83, 2011.
- [268] H. Wang, L. Shang, P. Maffre, S. Hohmann, F. Kirschhofer, G. Brenner-Weiss, and G. U. Nienhaus, “The Nature of a Hard Protein Corona Forming on Quantum Dots Exposed to Human Blood Serum,” *Small*, vol. 12, no. 42, pp. 5836–5844, 2016.
- [269] L. Shang and G. U. Nienhaus, “In Situ Characterization of Protein Adsorption onto Nanoparticles by Fluorescence Correlation Spectroscopy,” *Accounts of Chemical Research*, vol. 50, no. 2, pp. 387–395, 2017.
- [270] S. Milani, F. Baldelli Bombelli, A. S. Pitek, K. A. Dawson, and J. Rädler, “Reversible versus Irreversible Binding of Transferrin to Polystyrene Nanoparticles: Soft and Hard Corona,” *ACS Nano*, vol. 6, no. 3, pp. 2532–2541, 2012.
- [271] L. Novo, K. M. Takeda, T. Petteta, G. R. Dakwar, J. B. van den Dikkenberg, K. Remaut, K. Braeckmans, C. F. van Nostrum, E. Mastrobattista, and W. E. Hennink, “Targeted Decationized Polyplexes for siRNA Delivery,” *Molecular Pharmaceutics*, vol. 12, no. 1, pp. 150–161, 2015.

- [272] J. J. Mittag, B. Kneidl, T. Preiß, M. Hossann, G. Winter, S. Wuttke, H. Engelke, and J. O. Rädler, “Impact of plasma protein binding on cargo release by thermosensitive liposomes probed by fluorescence correlation spectroscopy,” *European Journal of Pharmaceutics and Biopharmaceutics*, vol. 119, pp. 215–223, 2017.
- [273] K. Fischer and M. Schmidt, “Pitfalls and novel applications of particle sizing by dynamic light scattering,” *Biomaterials*, vol. 98, pp. 79–91, 2016.
- [274] L. Nuhn, S. Gietzen, K. Mohr, K. Fischer, K. Toh, K. Miyata, Y. Matsumoto, K. Kataoka, M. Schmidt, and R. Zentel, “Aggregation Behavior of Cationic Nanohydrogel Particles in Human Blood Serum,” *Biomacromolecules*, vol. 15, no. 4, pp. 1526–1533, 2014.
- [275] L. K. Muller, L. Kaps, D. Schuppan, A. Brose, W. Chai, K. Fischer, S. Muller, H. Frey, M. Schmidt, and K. Mohr, “Physicochemical and Preclinical Evaluation of Spermine-Derived Surfactant Liposomes for in Vitro and in Vivo siRNA-Delivery to Liver Macrophages,” *Molecular Pharmaceutics*, vol. 13, no. 11, pp. 3636–3647, 2016.
- [276] S. L. Jacques, “Optical properties of biological tissues: a review,” *Physics in Medicine and Biology*, vol. 58, no. 11, pp. R37–61, 2013.
- [277] W. F. Cheong, S. A. Prahl, and A. J. Welch, “A review of the optical properties of biological tissues,” *IEEE Journal of Quantum Electronics*, vol. 26, no. 12, pp. 2166–2185, 1990.
- [278] R. Weissleder, “A clearer vision for in vivo imaging,” *Nature Biotechnology*, vol. 19, no. 4, pp. 316–317, 2001.
- [279] S. Guldbrand, V. Kirejev, C. Simonsson, M. Goksör, M. Smedh, and M. B. Ericson, “Two-photon fluorescence correlation spectroscopy as a tool for measuring molecular diffusion within human skin,” *European Journal of Pharmaceutics and Biopharmaceutics*, vol. 84, no. 2, pp. 430–436, 2013.
- [280] I. Negwer, A. Best, M. Schinnerer, O. Schäfer, M. Schmidt, V. Mailänder, M. Helm, M. Barz, H.-J. Butt, and K. Koynov, “Monitoring Drug Nanocarriers in Human Blood by Near-Infrared Fluorescence Correlation Spectroscopy,” *in preparation*, 2018.
- [281] C. E. Leroux, I. Wang, J. Derouard, and A. Delon, “Adaptive optics for fluorescence correlation spectroscopy,” *Optics Express*, vol. 19, no. 27, pp. 26 839–49, 2011.
- [282] Y. Park, M. Diez-Silva, G. Popescu, G. Lykotrafitis, W. Choi, M. S. Feld, and S. Suresh, “Refractive index maps and membrane dynamics of human red blood cells parasitized by *Plasmodium falciparum*,” *Proceedings of the National Academy of Sciences of the United States of America*, vol. 105, no. 37, pp. 13 730–5, 2008.

- [283] J. Szymanski, A. Patkowski, A. Wilk, P. Garstecki, and R. Holyst, "Diffusion and viscosity in a crowded environment: from nano- to macroscale," *Journal of Physical Chemistry. B*, vol. 110, no. 51, pp. 25 593–7, 2006.
- [284] T. Cherdhirankorn, A. Best, K. Koynov, K. Peneva, K. Muellen, and G. Fytas, "Diffusion in polymer solutions studied by fluorescence correlation spectroscopy," *Journal of Physical Chemistry. B*, vol. 113, no. 11, pp. 3355–3359, 2009.
- [285] R. J. Williams, M. Lipowska, G. Patonay, and L. Strekowski, "Comparison of covalent and noncovalent labeling with near-infrared dyes for the high-performance liquid chromatographic determination of human serum albumin," *Analytical Chemistry*, vol. 65, no. 5, pp. 601–605, 1993.
- [286] A. S. Tatikolov, "Polymethine dyes as spectral-fluorescent probes for biomacromolecules," *Journal of Photochemistry and Photobiology C: Photochemistry Reviews*, vol. 13, no. 1, pp. 55–90, 2012.
- [287] M. Y. Berezin, H. Lee, W. Akers, G. Nikiforovich, and S. Achilefu, "Ratiometric analysis of fluorescence lifetime for probing binding sites in albumin with near-infrared fluorescent molecular probes," *Photochemistry and Photobiology*, vol. 83, no. 6, pp. 1371–1378, 2007.
- [288] S. Palchetti, D. Pozzi, A. L. Capriotti, G. Barbera, R. Z. Chiozzi, L. Digiaco, G. Peruzzi, G. Caracciolo, and A. Lagana, "Influence of dynamic flow environment on nanoparticle-protein corona: From protein patterns to uptake in cancer cells," *Colloids and Surfaces B - Biointerfaces*, vol. 153, pp. 263–271, 2017.
- [289] K. Klinker, O. Schafer, D. Huesmann, T. Bauer, L. Capelo, L. Braun, N. Stergiou, M. Schinnerer, A. Dirisala, K. Miyata, K. Osada, H. Cabral, K. Kataoka, and M. Barz, "Secondary-Structure-Driven Self-Assembly of Reactive Polypept(o)ides: Controlling Size, Shape, and Function of Core Cross-Linked Nanostructures," *Angewandte Chemie International Edition*, vol. 56, no. 32, pp. 9608–9613, 2017.
- [290] C. J. F. Rijcken, M. Talelli, C. F. van Nostrum, G. Storm, and W. E. Hennink, "Therapeutic Nanomedicine: Cross linked micelles with transiently linked drugs – a versatile drug delivery system," *European Journal of Nanomedicine*, vol. 3, no. 1, pp. 19–24, 2010.
- [291] A. Fire, S. Xu, M. K. Montgomery, S. A. Kostas, S. E. Driver, and C. C. Mello, "Potent and specific genetic interference by double-stranded RNA in *Caenorhabditis elegans*," *Nature*, vol. 391, no. 6669, pp. 806–811, 1998.
- [292] S. M. Elbashir, J. Harborth, W. Lendeckel, A. Yalcin, K. Weber, and T. Tuschl, "Duplexes of 21-nucleotide RNAs mediate RNA interference in cultured mammalian cells," *Nature*, vol. 411, no. 6836, pp. 494–498, 2001.

-
- [293] A. P. McCaffrey, L. Meuse, T.-T. T. Pham, D. S. Conklin, G. J. Hannon, and M. A. Kay, “RNA interference in adult mice,” *Nature*, vol. 418, p. 38, 2002.
- [294] E. Bernstein, A. A. Caudy, S. M. Hammond, and G. J. Hannon, “Role for a bidentate ribonuclease in the initiation step of RNA interference,” *Nature*, vol. 409, no. 6818, pp. 363–366, 2001.
- [295] T. A. Rand, K. Ginalski, N. V. Grishin, and X. Wang, “Biochemical identification of Argonaute 2 as the sole protein required for RNA-induced silencing complex activity,” *Proceedings of the National Academy of Sciences of the United States of America*, vol. 101, no. 40, pp. 14 385–9, 2004.
- [296] R. I. Gregory, T. P. Chendrimada, N. Cooch, and R. Shiekhattar, “Human RISC couples microRNA biogenesis and posttranscriptional gene silencing,” *Cell*, vol. 123, no. 4, pp. 631–640, 2005.
- [297] D. S. Schwarz, G. Hutvagner, T. Du, Z. Xu, N. Aronin, and P. D. Zamore, “Asymmetry in the assembly of the RNAi enzyme complex,” *Cell*, vol. 115, no. 2, pp. 199–208, 2003.
- [298] T. A. Rand, S. Petersen, F. Du, and X. Wang, “Argonaute2 cleaves the anti-guide strand of siRNA during RISC activation,” *Cell*, vol. 123, no. 4, pp. 621–629, 2005.
- [299] S. L. Ameres, J. Martinez, and R. Schroeder, “Molecular basis for target RNA recognition and cleavage by human RISC,” *Cell*, vol. 130, no. 1, pp. 101–112, 2007.
- [300] G. Hutvagner and P. D. Zamore, “A microRNA in a multiple-turnover RNAi enzyme complex,” *Science*, vol. 297, no. 5589, pp. 2056–2060, 2002.
- [301] T. Ohrt, J. Mutze, W. Staroske, L. Weinmann, J. Hock, K. Crell, G. Meister, and P. Schwill, “Fluorescence correlation spectroscopy and fluorescence cross-correlation spectroscopy reveal the cytoplasmic origination of loaded nuclear RISC in vivo in human cells,” *Nucleic Acids Research*, vol. 36, no. 20, pp. 6439–6449, 2008.
- [302] T. Ohrt, W. Staroske, J. Mutze, K. Crell, M. Landthaler, and P. Schwill, “Fluorescence cross-correlation spectroscopy reveals mechanistic insights into the effect of 2'-O-methyl modified siRNAs in living cells,” *Biophysical Journal*, vol. 100, no. 12, pp. 2981–2990, 2011.
- [303] T. Ohrt and P. Schwill, “siRNA modifications and sub-cellular localization: a question of intracellular transport?” *Current Pharmaceutical Design*, vol. 14, no. 34, pp. 3674–3685, 2008.
- [304] T. Ohrt, D. Merkle, K. Birkenfeld, C. J. Echeverri, and P. Schwill, “In situ fluorescence analysis demonstrates active siRNA exclusion from the nucleus by Exportin 5,” *Nucleic Acids Research*, vol. 34, no. 5, pp. 1369–1380, 2006.

- [305] T. Ohrt, J. Muetze, P. Svoboda, and P. Schwillle, "Intracellular Localization and Routing of miRNA and RNAi Pathway Components," *Current Topics in Medicinal Chemistry*, vol. 12, no. 2, pp. 79–88, 2012.
- [306] C. Morrison, "Alynlam prepares to land first RNAi drug approval," *Nature Reviews Drug Discovery*, vol. 17, p. 156, 2018.
- [307] K. Gavrilov and W. M. Saltzman, "Therapeutic siRNA: Principles, Challenges, and Strategies," *The Yale Journal of Biology and Medicine*, vol. 85, no. 2, pp. 187–200, 2012.
- [308] S. F. Dowdy, "Overcoming cellular barriers for RNA therapeutics," *Nature Biotechnology*, vol. 35, no. 3, pp. 222–229, 2017.
- [309] V. Hornung, M. Guenther-Biller, C. Bourquin, A. Ablasser, M. Schlee, S. Uematsu, A. Noronha, M. Manoharan, S. Akira, A. de Fougerolles, S. Endres, and G. Hartmann, "Sequence-specific potent induction of IFN- α by short interfering RNA in plasmacytoid dendritic cells through TLR7," *Nature Medicine*, vol. 11, no. 3, pp. 263–270, 2005.
- [310] M. L. Bobbin and J. J. Rossi, "RNA Interference (RNAi)-Based Therapeutics: Delivering on the Promise?" *Annual Review of Pharmacology and Toxicology*, vol. 56, no. 1, pp. 103–122, 2016.
- [311] E. Wagner, "Biomaterials in RNAi therapeutics: quo vadis?" *Biomaterials Science*, vol. 1, no. 8, pp. 804–809, 2013.
- [312] R. Kanasty, J. R. Dorkin, A. Vegas, and D. Anderson, "Delivery materials for siRNA therapeutics," *Nature Materials*, vol. 12, no. 11, pp. 967–977, 2013.
- [313] P. L. Felgner, T. R. Gadek, M. Holm, R. Roman, H. W. Chan, M. Wenz, J. P. Northrop, G. M. Ringold, and M. Danielsen, "Lipofection: a highly efficient, lipid-mediated DNA-transfection procedure," *Proceedings of the National Academy of Sciences of the United States of America*, vol. 84, no. 21, pp. 7413–7417, 1987.
- [314] Y. Omid, A. J. Hollins, M. Benboubetra, R. Drayton, I. F. Benter, and S. Akhtar, "Toxicogenomics of non-viral vectors for gene therapy: a microarray study of lipofectin- and oligofectamine-induced gene expression changes in human epithelial cells," *Journal of Drug Targeting*, vol. 11, no. 6, pp. 311–323, 2003.
- [315] A. Mokhtarzadeh, A. Alibakhshi, M. Hashemi, M. Hejazi, V. Hosseini, M. de la Guardia, and M. Ramezani, "Biodegradable nano-polymers as delivery vehicles for therapeutic small non-coding ribonucleic acids," *Journal of Controlled Release*, vol. 245, pp. 116–126, 2017.
- [316] S. Mao, W. Sun, and T. Kissel, "Chitosan-based formulations for delivery of DNA and siRNA," *Advanced Drug Delivery Reviews*, vol. 62, no. 1, pp. 12–27, 2010.

- [317] J. Li, S. Xue, and Z.-W. Mao, "Nanoparticle delivery systems for siRNA-based therapeutics," *Journal of Materials Chemistry B*, vol. 4, no. 41, pp. 6620–6639, 2016.
- [318] S. Kruspe and P. H. Giangrande, "Aptamer-siRNA Chimeras: Discovery, Progress, and Future Prospects," *Biomedicines*, vol. 5, no. 3, p. 45, 2017.
- [319] M. Gooding, M. Malhotra, J. C. Evans, R. Darcy, and C. M. O'Driscoll, "Oligonucleotide conjugates – Candidates for gene silencing therapeutics," *European Journal of Pharmaceutics and Biopharmaceutics*, vol. 107, pp. 321–340, 2016.
- [320] C. Luft and R. Ketteler, "Electroporation Knows No Boundaries: The Use of Electrostimulation for siRNA Delivery in Cells and Tissues," *Journal of Biomolecular Screening*, vol. 20, no. 8, pp. 932–942, 2015.
- [321] J. Nemunaitis, M. Barve, D. Orr, J. Kuhn, M. Magee, J. Lamont, C. Bedell, G. Wallraven, B. O. Pappen, A. Roth, S. Horvath, D. Nemunaitis, P. Kumar, P. B. Maples, and N. Senzer, "Summary of bi-shRNA/GM-CSF augmented autologous tumor cell immunotherapy (FANG) in advanced cancer of the liver," *Oncology*, vol. 87, no. 1, pp. 21–29, 2014.
- [322] G. Sahay, D. Y. Alakhova, and A. V. Kabanov, "Endocytosis of nanomedicines," *Journal of Controlled Release*, vol. 145, no. 3, pp. 182–195, 2010.
- [323] C. C. Scott, F. Vacca, and J. Gruenberg, "Endosome maturation, transport and functions," *Seminars in Cell and Developmental Biology*, vol. 31, pp. 2–10, 2014.
- [324] H. Stenmark, "Rab GTPases as coordinators of vesicle traffic," *Nature Reviews: Molecular Cell Biology*, vol. 10, no. 8, pp. 513–525, 2009.
- [325] C. Lafourcade, K. Sobo, S. Kieffer-Jaquinod, J. Garin, and F. G. van der Goot, "Regulation of the V-ATPase along the Endocytic Pathway Occurs through Reversible Subunit Association and Membrane Localization," *PLoS One*, vol. 3, no. 7, p. e2758, 2008.
- [326] O. Boussif, F. Lezoualc'h, M. A. Zanta, M. D. Mergny, D. Scherman, B. Demeneix, and J. P. Behr, "A versatile vector for gene and oligonucleotide transfer into cells in culture and in vivo: polyethylenimine," *Proceedings of the National Academy of Sciences of the United States of America*, vol. 92, no. 16, pp. 7297–7301, 1995.
- [327] I. M. Hafez, N. Maurer, and P. R. Cullis, "On the mechanism whereby cationic lipids promote intracellular delivery of polynucleic acids," *Gene Therapy*, vol. 8, pp. 1188–1196, 2001.
- [328] Y. Xu and J. Szoka, F. C., "Mechanism of DNA release from cationic liposome/DNA complexes used in cell transfection," *Biochemistry*, vol. 35, no. 18, pp. 5616–5623, 1996.

- [329] N. Leber, L. Kaps, M. Aslam, J. Schupp, A. Brose, D. Schäffel, K. Fischer, M. Diken, D. Strand, K. Koynov, A. Tuettenberg, L. Nuhn, R. Zentel, and D. Schuppan, “SiRNA-mediated in vivo gene knockdown by acid-degradable cationic nanohydrogel particles,” *Journal of Controlled Release*, vol. 248, pp. 10–23, 2017.
- [330] K. K. Hou, H. Pan, L. Ratner, P. H. Schlesinger, and S. A. Wickline, “Mechanisms of Nanoparticle-Mediated siRNA Transfection by Melittin-Derived Peptides,” *ACS Nano*, vol. 7, no. 10, pp. 8605–8615, 2013.
- [331] K. L. Kozielski, S. Y. Tzeng, B. A. De Mendoza, and J. J. Green, “Bioreducible cationic polymer-based nanoparticles for efficient and environmentally triggered cytoplasmic siRNA delivery to primary human brain cancer cells,” *ACS Nano*, vol. 8, no. 4, pp. 3232–3241, 2014.
- [332] S. An, D. He, E. Wagner, and C. Jiang, “Peptide-like Polymers Exerting Effective Glioma-Targeted siRNA Delivery and Release for Therapeutic Application,” *Small*, vol. 11, no. 38, pp. 5142–5150, 2015.
- [333] F. Q. Schafer and G. R. Buettner, “Redox environment of the cell as viewed through the redox state of the glutathione disulfide/glutathione couple,” *Free Radical Biology and Medicine*, vol. 30, no. 11, pp. 1191–1212, 2001.
- [334] S. Mura, J. Nicolas, and P. Couvreur, “Stimuli-responsive nanocarriers for drug delivery,” *Nat Mater*, vol. 12, no. 11, pp. 991–1003, 2013.
- [335] M. P. Gamcsik, M. S. Kasibhatla, S. D. Teeter, and O. M. Colvin, “Glutathione Levels in Human Tumors,” *Biomarkers : biochemical indicators of exposure, response, and susceptibility to chemicals*, vol. 17, no. 8, pp. 671–691, 2012.
- [336] H.-X. Wang, X.-Z. Yang, C.-Y. Sun, C.-Q. Mao, Y.-H. Zhu, and J. Wang, “Matrix metalloproteinase 2-responsive micelle for siRNA delivery,” *Biomaterials*, vol. 35, no. 26, pp. 7622–7634, 2014.
- [337] H. Li, S. S. Yu, M. Miteva, C. E. Nelson, T. Werfel, T. D. Giorgio, and C. L. Duvall, “Matrix Metalloproteinase Responsive, Proximity-Activated Polymeric Nanoparticles for siRNA Delivery,” *Advanced Functional Materials*, vol. 23, no. 24, pp. 3040–3052, 2013.
- [338] G. Salzano, D. F. Costa, and V. P. Torchilin, “siRNA Delivery by Stimuli-Sensitive Nanocarriers,” *Current Pharmaceutical Design*, vol. 21, no. 31, pp. 4566–4573, 2015.
- [339] Y. Liu, V. Gunda, X. Zhu, X. Xu, J. Wu, D. Askhatova, O. C. Farokhzad, S. Parangi, and J. Shi, “Theranostic near-infrared fluorescent nanoplatfom for imaging and systemic siRNA delivery to metastatic anaplastic thyroid cancer,” *Proceedings of the National Academy of Sciences*, vol. 113, no. 28, pp. 7750–7755, 2016.

- [340] G. Chen, B. Ma, R. Xie, Y. Wang, K. Dou, and S. Gong, "NIR-induced spatiotemporally controlled gene silencing by upconversion nanoparticle-based siRNA nanocarrier," *Journal of Controlled Release*, 2017.
- [341] T.-G. Iversen, T. Skotland, and K. Sandvig, "Endocytosis and intracellular transport of nanoparticles: Present knowledge and need for future studies," *Nano Today*, vol. 6, no. 2, pp. 176–185, 2011.
- [342] F. Cardarelli, L. Digiacomo, C. Marchini, A. Amici, F. Salomone, G. Fiume, A. Rossetta, E. Gratton, D. Pozzi, and G. Caracciolo, "The intracellular trafficking mechanism of Lipofectamine-based transfection reagents and its implication for gene delivery," *Scientific Reports*, vol. 6, p. 25879, 2016.
- [343] V. Ondrej, E. Lukasova, M. Falk, and S. Kozubek, "The role of actin and microtubule networks in plasmid DNA intracellular trafficking," *Acta Biochimica Polonica*, vol. 54, no. 3, pp. 657–663, 2007.
- [344] S. Coppola, L. C. Estrada, M. A. Digman, D. Pozzi, F. Cardarelli, E. Gratton, and G. Caracciolo, "Intracellular trafficking of cationic liposome-DNA complexes in living cells," *Soft Matter*, vol. 8, no. 30, pp. 7919–7927, 2012.
- [345] K. Buyens, B. Lucas, K. Raemdonck, K. Braeckmans, J. Vercaemmen, J. Hendrix, Y. Engelborghs, S. C. De Smedt, and N. N. Sanders, "A fast and sensitive method for measuring the integrity of siRNA-carrier complexes in full human serum," *Journal of Controlled Release*, vol. 126, no. 1, pp. 67–76, 2008.
- [346] C. T. Greco, T. H. Epps, and M. O. Sullivan, "Mechanistic Design of Polymer Nanocarriers to Spatiotemporally Control Gene Silencing," *ACS Biomaterials Science & Engineering*, vol. 2, no. 9, pp. 1582–1594, 2016.
- [347] K. Remaut, B. Lucas, K. Raemdonck, K. Braeckmans, J. Demeester, and S. C. De Smedt, "Can we better understand the intracellular behavior of DNA nanoparticles by fluorescence correlation spectroscopy?" *Journal of Controlled Release*, vol. 121, no. 1–2, pp. 49–63, 2007.
- [348] A. Sasaki and M. Kinjo, "Monitoring intracellular degradation of exogenous DNA using diffusion properties," *Journal of Controlled Release*, vol. 143, no. 1, pp. 104–111, 2010.
- [349] J. R. LaRochelle, G. B. Cobb, A. Steinauer, E. Rhoades, and A. Schepartz, "Fluorescence Correlation Spectroscopy Reveals Highly Efficient Cytosolic Delivery of Certain Penta-Arg Proteins and Stapled Peptides," *Journal of the American Chemical Society*, vol. 137, no. 7, pp. 2536–2541, 2015.

- [350] A. Sasaki and M. Kinjo, “Fluorescence Cross-Correlation Spectroscopy for Real-Time Monitoring of Exogenous DNA Behavior in Living Cells,” in *Gene Therapy Applications*, C. Kang, Ed. Rijeka: InTech, 2011.
- [351] R. Rezgui, K. Blumer, G. Yeoh-Tan, A. J. Trexler, and M. Magzoub, “Precise quantification of cellular uptake of cell-penetrating peptides using fluorescence-activated cell sorting and fluorescence correlation spectroscopy,” *Biochimica et Biophysica Acta*, vol. 1858, no. 7 Pt A, pp. 1499–1506, 2016.
- [352] A. Silvestri, D. Di Silvio, I. Llarena, R. A. Murray, M. Marelli, L. Lay, L. Polito, and S. E. Moya, “Influence of surface coating on the intracellular behaviour of gold nanoparticles: a fluorescence correlation spectroscopy study,” *Nanoscale*, vol. 9, no. 38, pp. 14 730–14 739, 2017.
- [353] K. Quach, J. LaRochelle, X. H. Li, E. Rhoades, and A. Schepartz, “Unique arginine array improves cytosolic localization of hydrocarbon-stapled peptides,” *Bioorganic and Medicinal Chemistry*, vol. 26, no. 6, pp. 1197–1202, 2018.
- [354] S. A. Kim, K. G. Heinze, and P. Schuille, “Fluorescence correlation spectroscopy in living cells,” *Nature Methods*, vol. 4, no. 11, pp. 963–973, 2007.
- [355] N. Altan-Bonnet and G. Altan-Bonnet, “Fluorescence correlation spectroscopy in living cells: a practical approach,” *Current Protocols in Cell Biology*, 2009.
- [356] G. A. Wagnieres, W. M. Star, and B. C. Wilson, “In vivo fluorescence spectroscopy and imaging for oncological applications,” *Photochemistry and Photobiology*, vol. 68, no. 5, pp. 603–632, 1998.
- [357] W. R. Zipfel, R. M. Williams, R. Christie, A. Y. Nikitin, B. T. Hyman, and W. W. Webb, “Live tissue intrinsic emission microscopy using multiphoton-excited native fluorescence and second harmonic generation,” *Proceedings of the National Academy of Sciences*, vol. 100, no. 12, pp. 7075–7080, 2003.
- [358] M. Arrio-Dupont, G. Foucault, M. Vacher, P. F. Devaux, and S. Cribier, “Translational diffusion of globular proteins in the cytoplasm of cultured muscle cells,” *Biophysical Journal*, vol. 78, no. 2, pp. 901–907, 2000.
- [359] T. Kalwarczyk, N. Ziebacz, A. Bielejewska, E. Zaboklicka, K. Koynov, J. Szymanski, A. Wilk, A. Patkowski, J. Gapinski, H. J. Butt, and R. Holyst, “Comparative analysis of viscosity of complex liquids and cytoplasm of mammalian cells at the nanoscale,” *Nano Lett*, vol. 11, no. 5, pp. 2157–2163, 2011.
- [360] Y. Chen, J. D. Müller, Q. Ruan, and E. Gratton, “Molecular brightness characterization of EGFP in vivo by fluorescence fluctuation spectroscopy,” *Biophysical Journal*, vol. 82, no. 1 Pt 1, pp. 133–144, 2002.

- [361] Z. Petrasek and P. Schwille, “Precise measurement of diffusion coefficients using scanning fluorescence correlation spectroscopy,” *Biophysical Journal*, vol. 94, no. 4, pp. 1437–1448, 2008.
- [362] M. A. Hink, R. A. Griep, J. W. Borst, A. van Hoek, M. H. Eppink, A. Schots, and A. J. Visser, “Structural dynamics of green fluorescent protein alone and fused with a single chain Fv protein,” *Journal of Biological Chemistry*, vol. 275, no. 23, pp. 17 556–60, 2000.
- [363] G. Vámosi, N. Mücke, G. Müller, J. W. Krieger, U. Curth, J. Langowski, and K. Tóth, “EGFP oligomers as natural fluorescence and hydrodynamic standards,” *Scientific Reports*, vol. 6, p. 33022, 2016.
- [364] S. Seidu-Larry, B. Krieg, M. Hirsch, M. Helm, and O. Domingo, “A modified guanosine phosphoramidite for click functionalization of RNA on the sugar edge,” *Chemical Communications (Cambridge, England)*, vol. 48, no. 89, pp. 11 014–6, 2012.
- [365] J. Gilleron, W. Querbes, A. Zeigerer, A. Borodovsky, G. Marsico, U. Schubert, K. Manygoats, S. Seifert, C. Andree, M. Stoter, H. Epstein-Barash, L. Zhang, V. Kotliansky, K. Fitzgerald, E. Fava, M. Bickle, Y. Kalaidzidis, A. Akinc, M. Maier, and M. Zerial, “Image-based analysis of lipid nanoparticle-mediated siRNA delivery, intracellular trafficking and endosomal escape,” *Nature Biotechnology*, vol. 31, no. 7, pp. 638–46, 2013.
- [366] A. Jarve, J. Muller, I. H. Kim, K. Rohr, C. MacLean, G. Fricker, U. Massing, F. Eberle, A. Dalpke, R. Fischer, M. F. Trendelenburg, and M. Helm, “Surveillance of siRNA integrity by FRET imaging,” *Nucleic Acids Research*, vol. 35, no. 18, p. e124, 2007.
- [367] G. Kaur and J. M. Dufour, “Cell lines: Valuable tools or useless artifacts,” *Spermatogenesis*, vol. 2, no. 1, pp. 1–5, 2012.
- [368] J. Schupp, F. K. Krebs, N. Zimmer, E. Trzeciak, D. Schuppan, and A. Tuettenberg, “Targeting myeloid cells in the tumor sustaining microenvironment,” *Cellular Immunology*, 2017.
- [369] S. Jain and M. Amiji, “Macrophage-Targeted Nanoparticle Delivery Systems,” in *Multifunctional Nanoparticles for Drug Delivery Applications: Imaging, Targeting, and Delivery*, S. Svenson and R. K. Prud’homme, Eds. Boston, MA: Springer US, 2012, pp. 47–83.
- [370] K. Binnemars-Postma, G. Storm, and J. Prakash, “Nanomedicine Strategies to Target Tumor-Associated Macrophages,” *International Journal of Molecular Sciences*, vol. 18, no. 5, p. 979, 2017.
- [371] H. Sahoo and P. Schwille, “FRET and FCS—Friends or Foes?” *Chemphyschem*, vol. 12, no. 3, pp. 532–541, 2011.

- [372] M. Hirsch, D. Strand, and M. Helm, “Dye selection for live cell imaging of intact siRNA,” *Biological Chemistry*, vol. 393, no. 1-2, pp. 23–35, 2012.
- [373] Förster radius of selected Atto-dye pairs. Accessed: 2018/04/03. [Online]. Available: http://www.atto-tec.com/fileadmin/user_upload/Katalog_Flyer_Support/R_0_-Tabelle_2016_web.pdf
- [374] D. Wang, Z. Zhang, E. O’Loughlin, T. Lee, S. Houel, D. O’Carroll, A. Tarakhovsky, N. G. Ahn, and R. Yi, “Quantitative functions of Argonaute proteins in mammalian development,” *Genes and Development*, vol. 26, no. 7, pp. 693–704, 2012.
- [375] X. Zhang, X. Zuo, B. Yang, Z. Li, Y. Xue, Y. Zhou, J. Huang, X. Zhao, J. Zhou, Y. Yan, H. Zhang, P. Guo, H. Sun, L. Guo, Y. Zhang, and X. D. Fu, “MicroRNA directly enhances mitochondrial translation during muscle differentiation,” *Cell*, vol. 158, no. 3, pp. 607–619, 2014.
- [376] L. Nuhn, S. Tomcin, K. Miyata, V. Mailänder, K. Landfester, K. Kataoka, and R. Zentel, “Size-Dependent Knockdown Potential of siRNA-Loaded Cationic Nanohydrogel Particles,” *Biomacromolecules*, vol. 15, no. 11, pp. 4111–4121, 2014.
- [377] C. B. Müller, A. Loman, V. Pacheco, F. Koberling, D. Willbold, W. Richtering, and J. Enderlein, “Precise measurement of diffusion by multi-color dual-focus fluorescence correlation spectroscopy,” *EPL (Europhysics Letters)*, vol. 83, no. 4, p. 46001, 2008.
- [378] N. Kitsera, A. Khobta, and B. Epe, “Destabilized green fluorescent protein detects rapid removal of transcription blocks after genotoxic exposure,” *Biotechniques*, vol. 43, no. 2, pp. 222–227, 2007.
- [379] F. Foerster, D. Bamberger, J. Schupp, M. Weilbacher, L. Kaps, S. Strobl, L. Radi, M. Diken, D. Strand, A. Tuettenberg, P. R. Wich, and D. Schuppan, “Dextran-based therapeutic nanoparticles for hepatic drug delivery,” *Nanomedicine: Nanotechnology, Biology, and Medicine*, vol. 11, no. 20, pp. 2663–2677, 2016.
- [380] D. Rideout, “Self-Assembling Drugs: A New Approach to Biochemical Modulation in Cancer Chemotherapy,” *Cancer Investigation*, vol. 12, no. 2, pp. 189–202, 1994.
- [381] M. Wachsmuth, C. Conrad, J. Bulkescher, B. Koch, R. Mahen, M. Isokane, R. Pepperkok, and J. Ellenberg, “High-throughput fluorescence correlation spectroscopy enables analysis of proteome dynamics in living cells,” *Nature Biotechnology*, vol. 33, no. 4, pp. 384–9, 2015.

List of abbreviations

Acetyl CoA	Acetyl coenzyme A
ADP	Adenosine diphosphate
Ago2	Argonaute protein 2
APD	Avalanche photodiode
ATP	Adenosine triphosphate
a.u.	Arbitrary units
BP	Band pass
CLSM	Confocal laser scanning microscopy
CMC	Critical micellar concentration
Cy	Cyanine
DBCO	Dibenzocyclooctyne
DLS	Dynamic light scattering
DMSO	Dimethyl sulfoxide
ds	Double-stranded
EGFP	Enhanced green fluorescent protein
EPR	Enhanced permeability and retention
ESI-MS	Electrospray ionization mass spectrometry
FADH ₂	Flavine adenine dinucleotide
FB	Fluorescence brightness
FBS	Fetal bovine serum
FCCP	Carbonyl cyanide <i>p</i> -trifluoromethoxyphenylhydrazone
FCS	Fluorescence correlation spectroscopy
FCCS	Fluorescence cross-correlation spectroscopy
FRET	Förster resonance energy transfer
HSA	Human serum albumin
LC-MS	Liquid chromatography mass spectrometry
LP	Long pass
MPS	Mononuclear phagocyte system
mRNA	Messenger ribonucleic acid
mtDNA	Mitochondrial deoxyribonucleic acid
MTS	Mitochondrial targeting sequence
NADH	Nicotinamide dinucleotide
NHG	Nanohydrogel
NIR	Near-infrared
OXPHOS	Oxidative phosphorylation
PB	Polymer brush
PBS	Phosphate buffered saline
PEG	Polyethylene glycol

PM	Polymeric micelle
PMT	Photomultiplier tube
PPARG	Peroxisome proliferator-activated receptor gamma
Qdot	Quantum dot
RBC	Red blood cells
RBE4	Rat brain endothelial
RISC	RNA-induced silencing complex
RNAi	RNA interference
ROS	Reactive oxygen species
RP-HPLC	Reversed phase high performance liquid chromatography
rRNA	Ribosomal ribonucleic acid
SD	Standard deviation
siRNA	Small interfering ribonucleic acid
SPAAC	Strain-promoted azide-alkyne cycloaddition
TMRM/E	Tetramethylrhodamine methyl/ethyl ester
TPP	Triphenylphosphonium
TRBP	Transactivating response RNA-binding protein in HIV
tRNA	Transfer ribonucleic acid

Publications

Peer-reviewed publications

- T. Fritz, M. Voigt, M. Worm, I. Negwer, S. S. Muller, K. Kettenbach, T. L. Ross, F. Roesch, K. Koynov, H. Frey, and M. Helm, “Orthogonal Click Conjugation to the Liposomal Surface Reveals the Stability of the Lipid Anchorage as Crucial for Targeting,” *Chemistry – A European Journal*, vol. 22, no. 33, pp. 11 578–82, 2016.
- E. Wüstenhagen, L. Hampe, F. Boukhallouk, M. A. Schneider, G. A. Spoden, I. Negwer, K. Koynov, W. M. Kast, and L. Florin, “The cytoskeletal adaptor obscurin-like 1 interacts with the HPV16 capsid protein L2 and is required for HPV16 endocytosis,” *Journal of Virology*, 2016.
- I. Negwer, M. Hirsch, S. Kaloyanova, T. Brown, K. Peneva, H. J. Butt, K. Koynov, and M. Helm, “Modulation of Mitochondriotropic Properties of Cyanine Dyes by in Organello Copper-Free Click Reaction,” *Chembiochem: A European Journal of Chemical Biology*, vol. 18, no. 18, pp. 1814–1818, 2017.
- J. Petit, L. Thomi, J. Schultze, M. Makowski, I. Negwer, K. Koynov, S. Herminghaus, F. R. Wurm, O. Baumchen, and K. Landfester, “A modular approach for multifunctional polymersomes with controlled adhesive properties,” *Soft Matter*, vol. 14, no. 6, pp. 894–900, 2018.
- E. Wüstenhagen, F. Boukhallouk, I. Negwer, K. Rajalingam, F. Stubenrauch, and L. Florin, “The Myb-related protein MYPOP is a novel intrinsic host restriction factor of oncogenic human papillomaviruses,” *Oncogene, under revision*, 2018.
- I. Negwer, A. Best, M. Schinnerer, O. Schäfer, M. Schmidt, V. Mailänder, M. Helm, M. Barz, H.-J. Butt, and K. Koynov, “Monitoring Drug Nanocarriers in Human Blood by Near- Infrared Fluorescence Correlation Spectroscopy,” *in preparation*, 2018.

Poster presentations

- SFB 1066 Mini-Symposium, Mainz, September 2016. “Fluorescence correlation spectroscopy studies of nanocarrier-based drug delivery systems.”

-
- Building the Cell, Paris (France), September 2016. “Fluorescence Correlation Spectroscopy Studies for Nanocarrier-based siRNA Gene Therapy.”
 - Workshop FCS in Polymer Science, Garching, October 2017. “Direct monitoring of drug nanocarriers in human blood by near-infrared fluorescence correlation spectroscopy (NIR-FCS).”

Appendices

Part II

1 Born energy

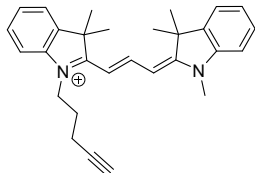
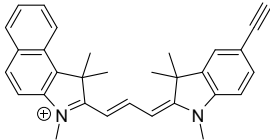
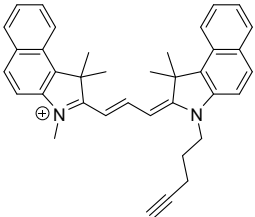
The Born energy derives the free energy of solvation and is described by:

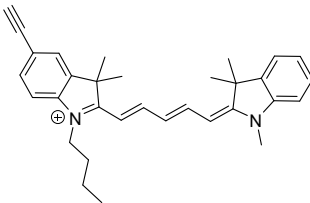
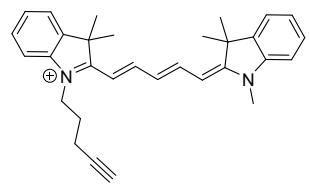
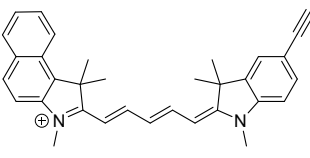
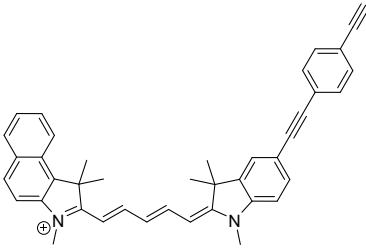
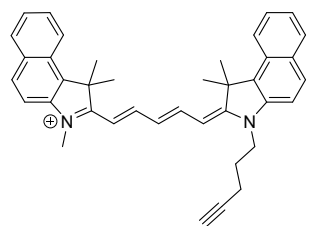
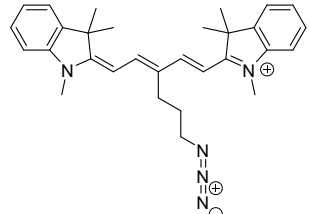
$$W_B = \frac{q^2}{8\pi\epsilon_0 r} * \left(\frac{1}{\epsilon_1} - \frac{1}{\epsilon_2} \right)$$

Here, ϵ_0 denotes the vacuum permittivity. ϵ_1 and ϵ_2 are the dielectric constants of the core of the membrane (≈ 2) and water (≈ 80), respectively. The electrical charge (per mole of cation) is given by q and the radius of the ion is denoted by r .

2 Colocalization study of alkynylated Cy dyes with MitoTracker Green FM

Table A.1: Alkyne-functionalized Cy dyes and Cy5-azide tested for colocalization with MitoTracker Green FM.

Cyanine dye	Chemical structure	Pearson's coefficient	Manders' coefficient (M ₁ ;M ₂)
<i>N</i> -pentynyl-Cy3		0.96	0.76; 0.84
Ethynyl-Cy3.25		0.93	0.85; 0.56
<i>N</i> -pentynyl-Cy3.5		0.93	0.86; 0.43

Ethynyl-Cy5		0.96	0.99; 1
<i>N</i> -pentynyl-Cy5		0.93	0.89; 0.83
Ethynyl-Cy5.25		0.93	0.7; 0.67
Phenyl-ethynyl-Cy5.25		0.91	0.82; 0.63
<i>N</i> -pentynyl-Cy5.5		0.92	0.79; 0.57
Cy5 propyl azide		0.92	0.4; 0.68

3 Sulfonated Cy dyes

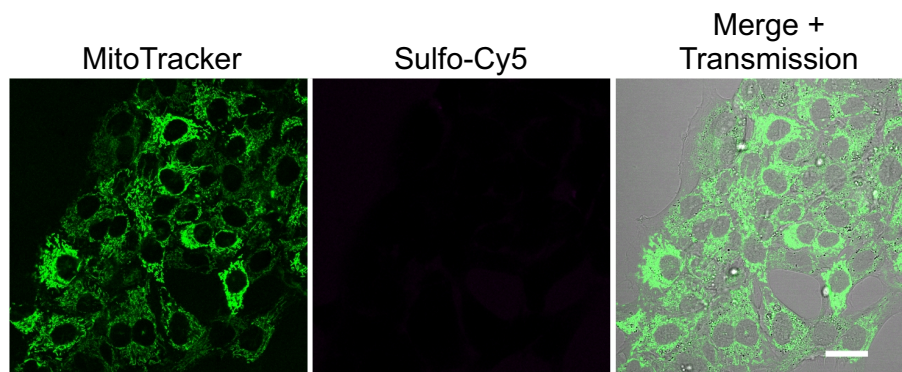


Figure A.1: Confocal images for co-incubation of RBE4 cells with 250 nM of sulfonated Cy5 dye with 250 nM MitoTracker Green FM. Cells were incubated for two hours. MitoTracker channel: $\lambda_{exc} = 488$ nm and $\lambda_{em} = 500 - 544$ nm. Sulfo-Cy5 channel: $\lambda_{exc} = 633$ nm and $\lambda_{em} = 659 - 696$ nm. Scale bar: 25 μm

4 Chemical names of SPAAC products 1 and 2

The full chemical names of SPAAC product **1** and **2** as shown in Figure 18 are 2-((E)-3-((E)-1-(6-((3-(1-(3-(6-((E)-3,3-dimethyl-2-((2E,4E)-5-(1,3,3-trimethyl-3H-indol-1-ium-2-yl)penta-2,4-dien-1-ylidene)indolin-1-yl)hexanamido)propyl)-1,9-dihydro-8H-dibenzo[b,f][1,2,3]triazolo[4,5-d]azocin-8-yl)-3-oxopropyl)amino)-6-oxohexyl)-3,3-dimethylindolin-2-ylidene)prop-1-en-1-yl)-1-ethyl-3,3-dimethyl-3H-indol-1-ium and 2-((E)-3-((E)-1-(6-((3-(8-(6-(6-((E)-3,3-dimethyl-2-((2E,4E)-5-(1,3,3-trimethyl-3H-indol-1-ium-2-yl)penta-2,4-dien-1-ylidene)indolin-1-yl)hexanamido)hexanoyl)-8,9-dihydro-1H-dibenzo[b,f][1,2,3]triazolo[4,5-d]azocin-1-yl)propyl)amino)-6-oxohexyl)-3,3-dimethylindolin-2-ylidene)prop-1-en-1-yl)-1,3,3-trimethyl-3H-indol-1-ium, respectively.

5 Copper-free click reaction of Cy3-azide and Cy5-DBCO

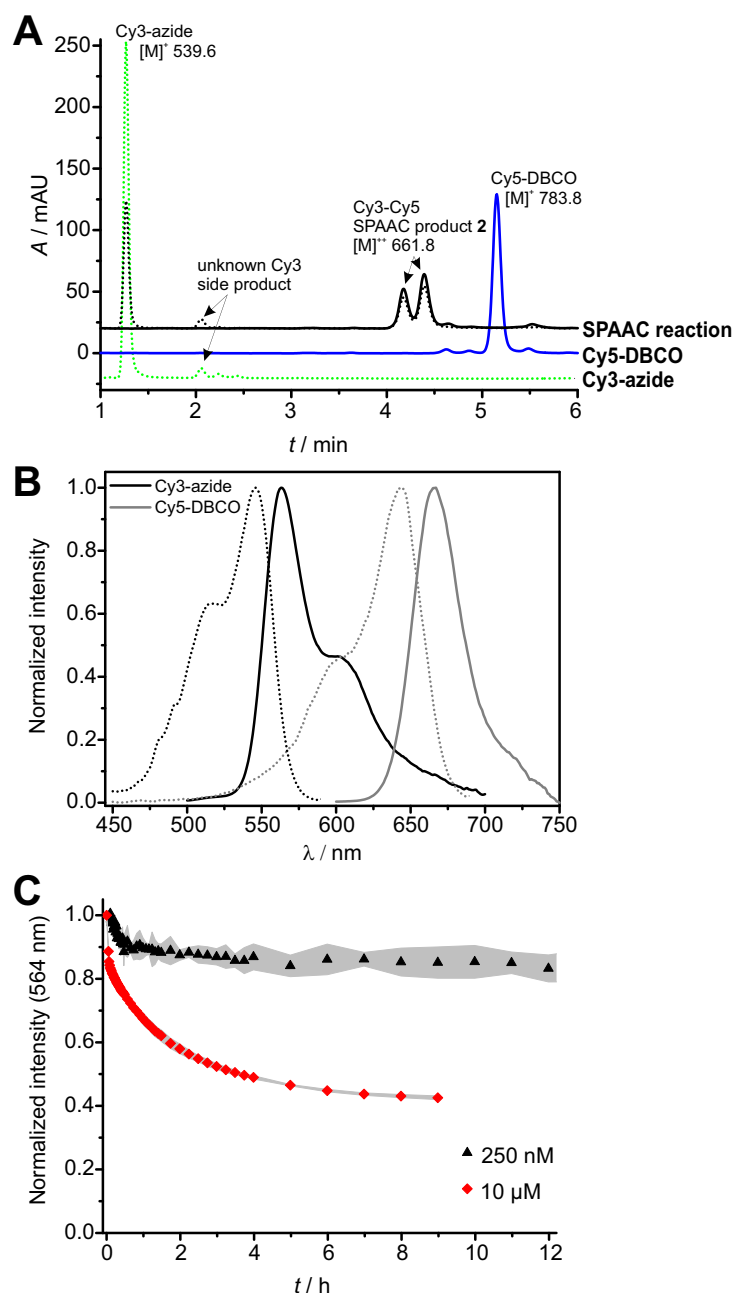


Figure A.2: A) RP-HPLC analysis of Cy3-azide, Cy5-DBCO and the reaction mixture for which the reactants (final concentration 250 μM each) were mixed in PBS, 40% DMSO at room temperature for four hours and diluted to 25 μM concentration before the measurement. Solid and dotted lines represent absorbance detection at 632 nm and 542 nm, respectively. Coupling to ESI-MS allowed the assignment of peaks to Cy3-azide, Cy5-DBCO and SPAAC product **2**. The product was detected in a double peak, presumably consisting of regioisomers **2.1** and **2.2** (Fig. 18B). B) Excitation (dotted line) and emission (solid line) spectra of Cy3-azide ($\lambda_{\text{exc}}^{\text{max}} = 546 \text{ nm}$, $\lambda_{\text{em}}^{\text{max}} = 563 \text{ nm}$) and Cy5-DBCO ($\lambda_{\text{exc}}^{\text{max}} = 643 \text{ nm}$, $\lambda_{\text{em}}^{\text{max}} = 667 \text{ nm}$). C) Kinetics of Cy3-azide and Cy5-DBCO reaction. Reactants were mixed at high (10 μM , red diamonds) and low (250 nM, black triangles) concentration. Donor emission at 564 nm upon $\lambda_{\text{exc}} = 488 \text{ nm}$ was normalized to the intensity at the starting concentration and plotted as mean \pm SD (in gray) of three independent experiments. PMT detector gain was adapted for high and low concentrations.

6 Mitochondrial accumulation of Cy3-azide and Cy5-DBCO

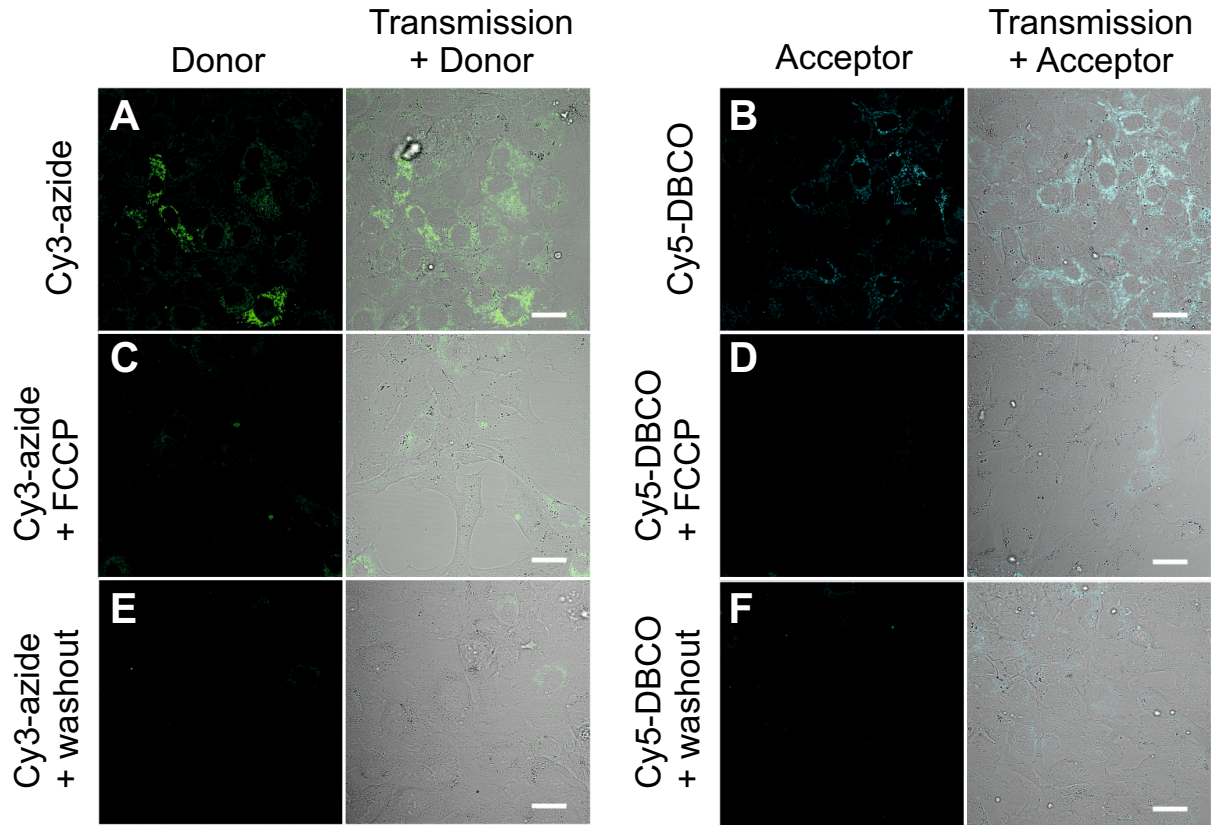


Figure A.3: Confocal images for incubation with the single dyes Cy3-azide (A,C,E) or Cy5-DBCO (B,D,F). RBE4 cells were incubated with the dyes (final concentration 250 nM) for two hours. Co-treatment with FCCP (5 μM) (C,D) led to dissipation of $\Delta\Psi_m$ and reduced fluorescent signal. Performing two washing cycles (E,F) led to a loss of fluorescent signal. Donor channel: $\lambda_{exc} = 488$ nm and $\lambda_{em} = 544 - 598$ nm. Acceptor channel: $\lambda_{exc} = 633$ nm and $\lambda_{em} = 659 - 696$ nm. Scale bar: 25 μm.

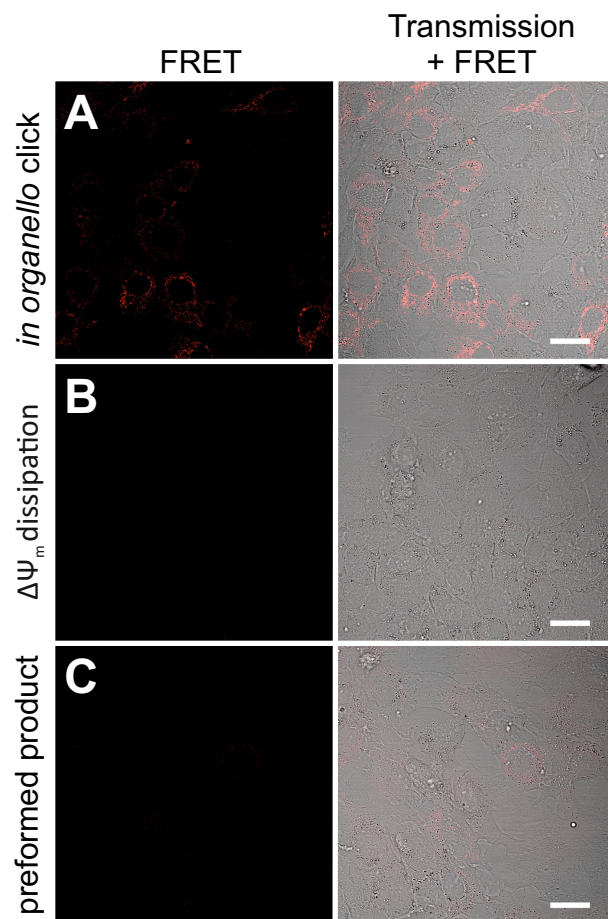
7 *In organello* copper-free click reaction between Cy3-azide and Cy5-DBCO

Figure A.4: Confocal images for synchronous incubation with 250 nM of Cy3-azide and Cy5-DBCO (A) and control reactions: *in organello* SPAAC in the presence of 5 μ M FCCP (B) and incubation with preformed product **2** (C). RBE4 cells were treated for four hours followed by two washing cycles. FRET channel: Cy5 signal (659 - 696 nm) upon $\lambda_{\text{exc}} = 488$ nm. Scale bar: 25 μ m.

8 Reaction kinetics of copper-free click reaction

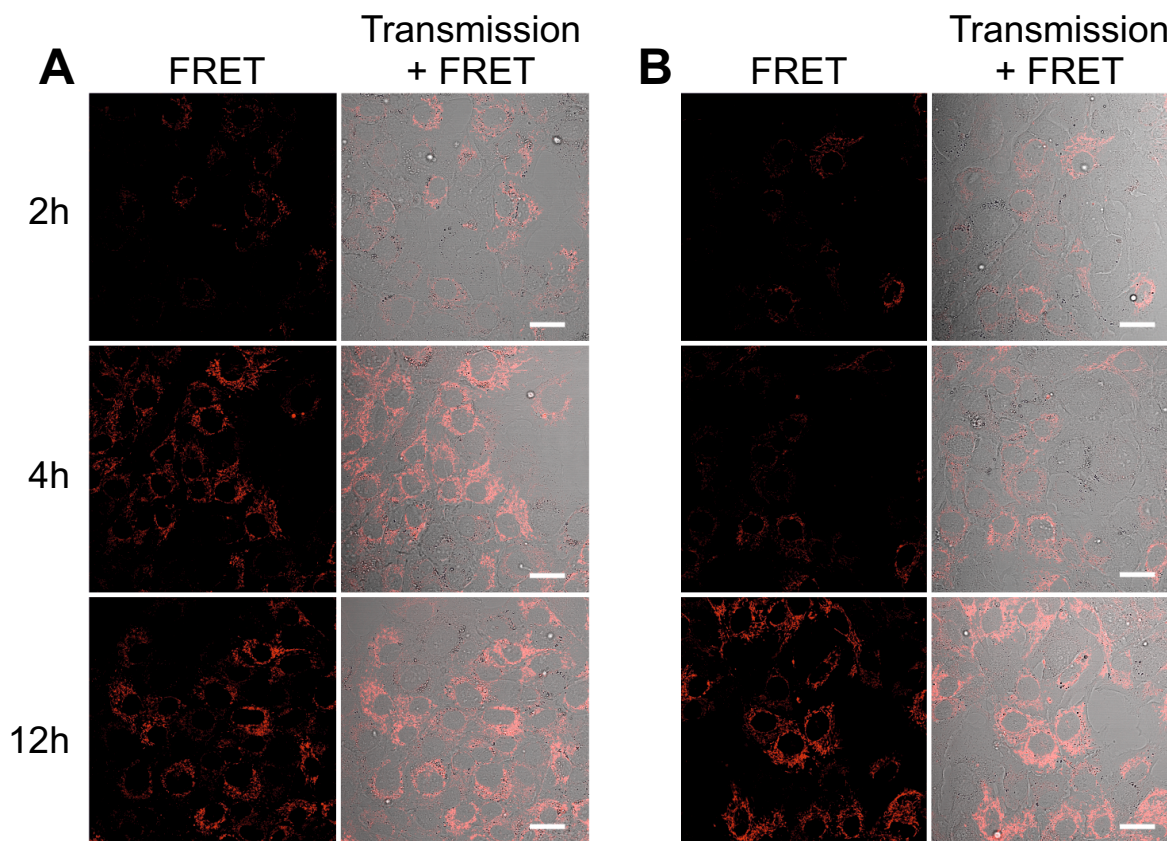


Figure A.5: Confocal images of time-dependent SPAAC reaction inside mitochondria forming SPAAC products **1** (A) or **2** (B). RBE4 cells were incubated at 250 nM concentration with precursors (Cy3-DBCO and Cy5-azide for product **1**; Cy3-azide and Cy5-DBCO for product **2**) for two, four and twelve hours followed by two washing cycles. FRET channel: Cy5 signal (659 - 696 nm) upon $\lambda_{\text{exc}} = 488$ nm. Scale bar: 25 μm .

Part III

9 Characterization of polymer brushes and polymeric micelles

Table A.2: Characterization of polymer brushes **PB1** and **PB2** and unlabeled polymeric micelles **PM**.

Sample	R_H / nm*	Mw / g mol ⁻¹ †	R_G / nm†	D_{HFIP} ‡	Side chain length NMR/SLS§	ζ / mV#	Aspect ratio (AFM) Δ
PB1	11 ± 1	$2.2 \cdot 10^5$ $\pm 0.1 \cdot 10^5$	10.4 ± 1.0	1.2	30 / 27	-6 ± 4	1.6
PB2	21 ± 1	$10.4 \cdot 10^5$ $\pm 0.5 \cdot 10^5$	22.7 ± 2.3	1.2	66 / 63	-3 ± 5	3.3
PM	45 ± 1					-1 ± 4	

Characterization was performed by Meike Schinnerer (polymer brushes) and Olga Schäfer (polymeric micelles).

* determined by dynamic light scattering in PBS

† determined by static light scattering in PBS

‡ determined by size exclusion chromatography in hexafluoroisopropanol

§ determined by ¹H-NMR in D₂O and static light scattering in PBS

determined by zeta potential measurements in 10 mM NaCl

Δ determined by atomic force microscopy on mica substrates

10 NIR-FCS of NIR dyes in aqueous solution

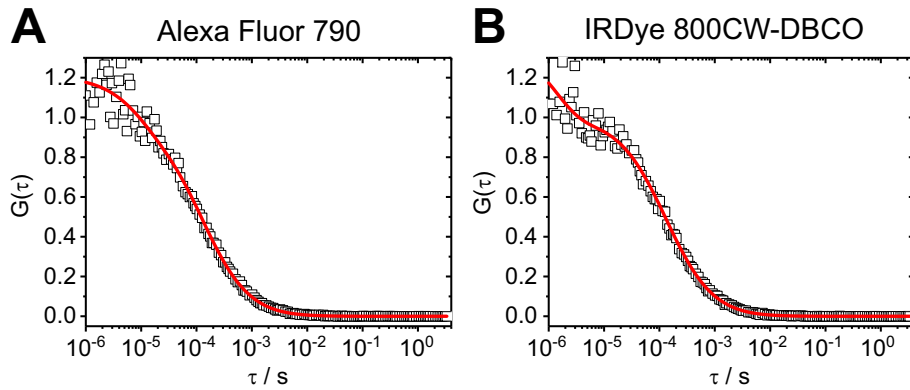


Figure A.6: NIR-FCS calibration measurements of Alexa Fluor 790 (A) and IRDye 800CW-DBCO (B) in water. The autocorrelation curves (squares) were fitted with an analytical model for 3D diffusion of one fluorescent species including triplet (Eq. 2.20)(line).

Part IV

11 Comparison of fitting models for intracellular measurements

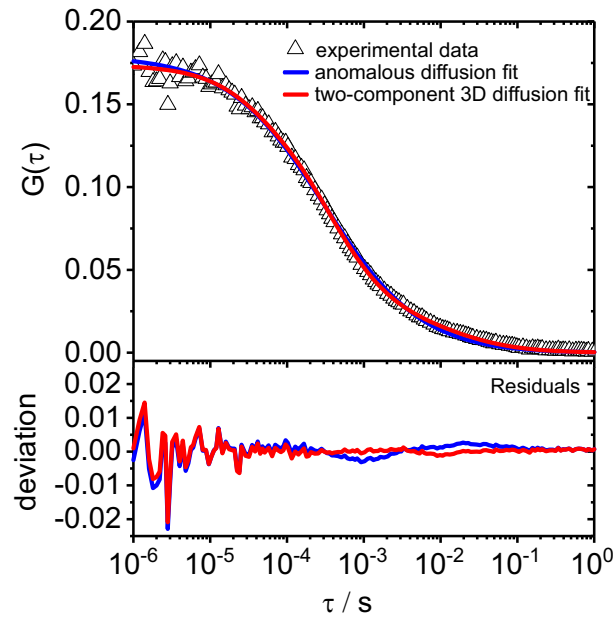


Figure A.7: The normalized autocorrelation curve of intracellular Atto 488-labeled siRNA was fitted with two models: an anomalous diffusion model (blue, Eq. 2.17) and a model for 3D diffusion of two independently diffusing components (red, Eq. 2.16). Below, the residuals of the respective fits are presented.

12 Time-dependent measurement of siRNA release in primary macrophages

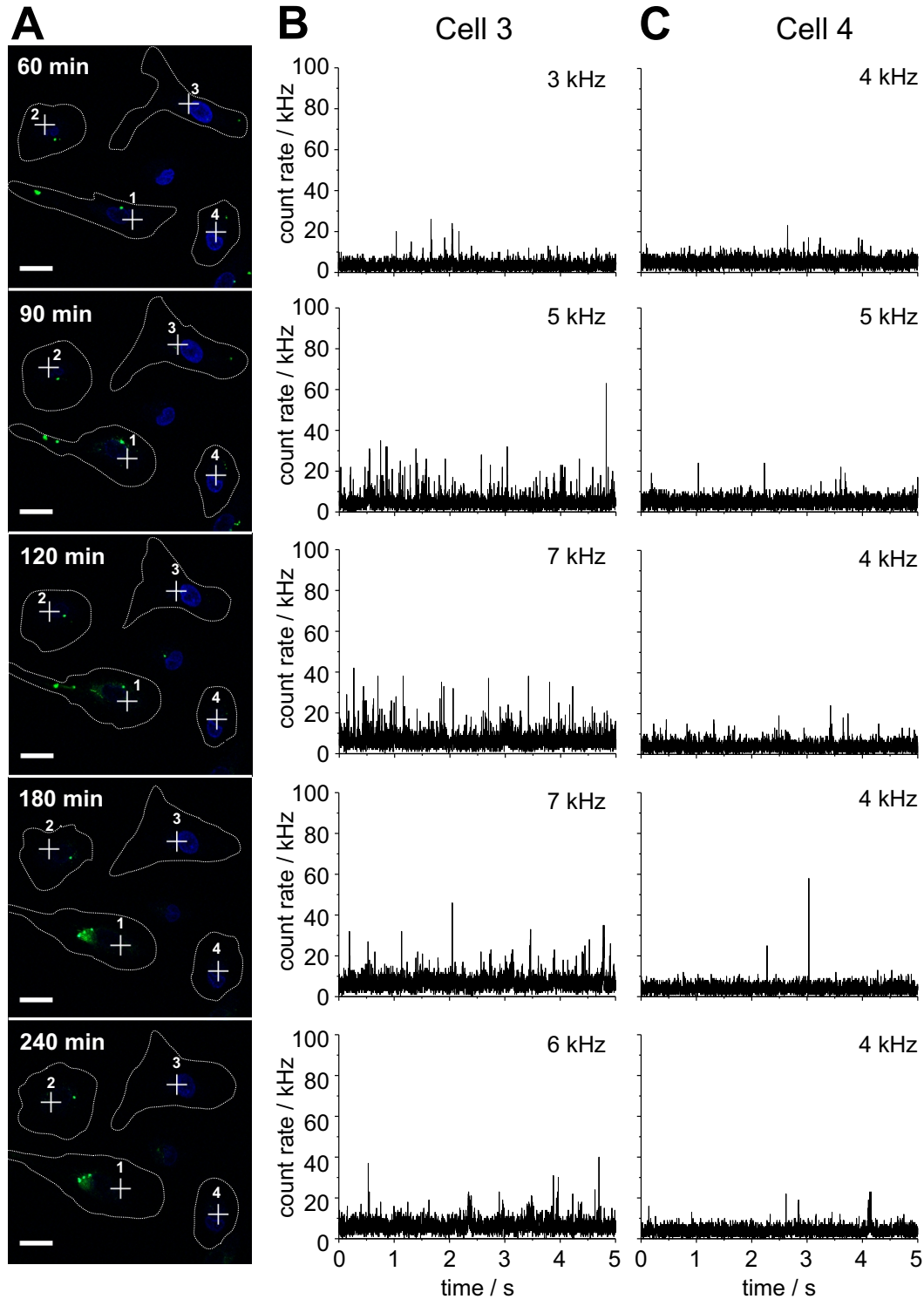


Figure A.8: Time-dependent experiment of siRNA release from lipoplexes in macrophages. A) Confocal images at different time points post-transfection. Dotted lines indicate the cell outline. Blue channel: nuclei stained with Hoechst dye ($\lambda_{\text{exc}} = 405 \text{ nm}$, $\lambda_{\text{em}} = 410 - 482 \text{ nm}$). Green channel: Atto 488-labeled siRNA ($\lambda_{\text{exc}} = 488 \text{ nm}$, $\lambda_{\text{em}} = 500 - 589 \text{ nm}$). Crosshairs indicate positions of FCS measurements. Scale bar: $20 \mu\text{m}$. Excerpts of the fluorescence signal time traces of cell 3 (B) and cell 4 (C). The average count rates are displayed in the insets.

13 Autocorrelation analysis of released siRNA in macrophages

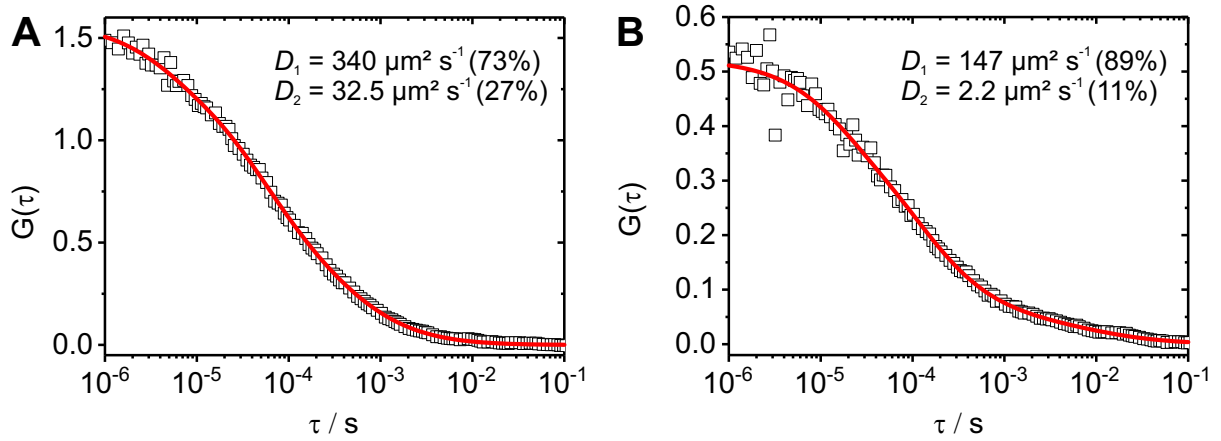


Figure A.9: Autocorrelation curves (black squares) measured in cell 1 (A) after 90 min (Fig. 45) and in cell 2 (B) after 180 min (Appendix 12) post-transfection. A fit model (red line) for two independently diffusing components including a triplet contribution (Eq. 2.20) was applied. The diffusion coefficients as well as the apparent relative fractions for each diffusing species are inserted. The predominance of a fast diffusing species indicative of free siRNA is apparent in both measurements.

14 Diffusion of a lipoplex assessed by FCCS

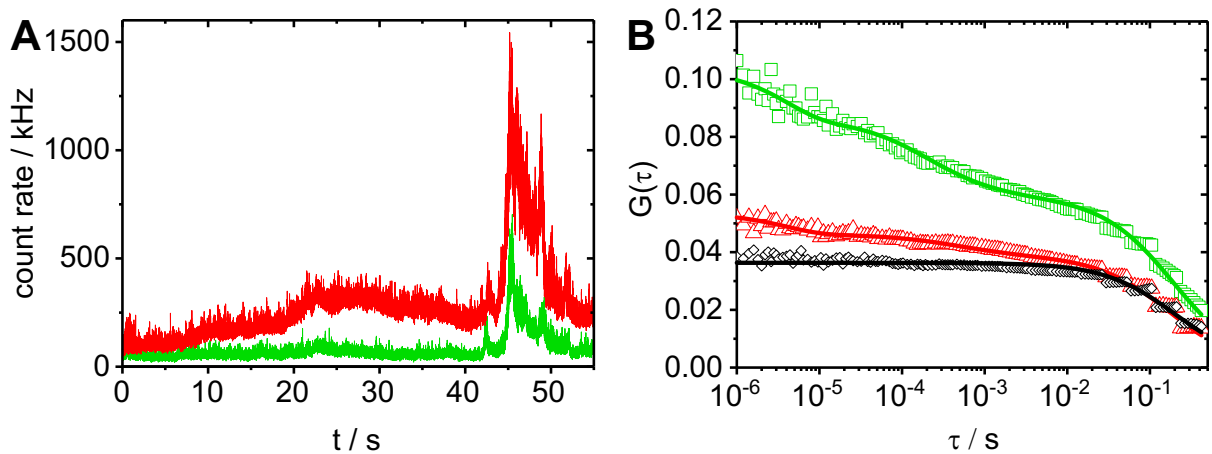


Figure A.10: FCCS measurement in the cytoplasm of a macrophage registering the diffusion of a lipoplex. A) Fluorescence signal traces of the green channel (Atto 488) and red channel (Atto 647N) show a large peak. B) Corresponding auto- (green, red) and cross-correlation (black) analysis. Autocorrelation data were fitted with a three-component fit (solid lines) including triplet (Eq. 2.20). The cross-correlation curve was fitted with a model of two components without a triplet contribution (black line). The curves are dominated by the slow diffusion of the lipoplex with a diffusion coefficient of $0.6 \mu\text{m}^2 \text{s}^{-1}$. But the time trace and autocorrelation analysis indicate the co-existence of a fast diffusing species which presumably consisted of released siRNA.

Curriculum vitae

This part was removed from the electronic version of the document.